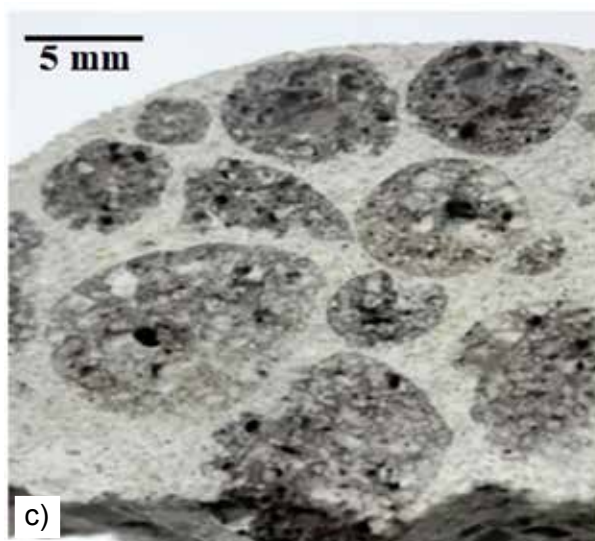
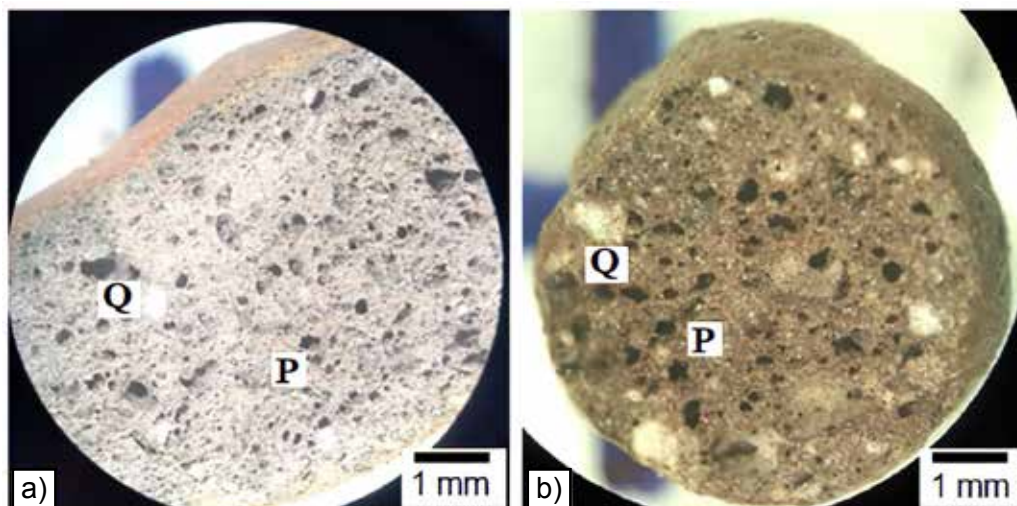


Cerâmica

ISSN-0366-6913

ÓRGÃO OFICIAL DA ASSOCIAÇÃO BRASILEIRA DE CERÂMICA - ANO LXIX - VOL. 69, 389 - JAN/FEV/MAR 2023

A S S O C I A Ç Ã O
B R A S I L E I R A



D E C E R Â M I C A

Cerâmica

A revista Cerâmica, órgão oficial da Associação Brasileira de Cerâmica (ABCeram), publica contribuições originais (e artigos revisão) de interesse na área de cerâmica, compreendendo arte cerâmica, abrasivos, biocerâmicas, cerâmicas avançadas, cerâmica branca, cerâmica de mesa, cerâmica eletroeletrônica, cerâmica estrutural, cerâmica magnética, cerâmica nuclear, cerâmica óptica, cerâmica química, cerâmica termomecânica, cerâmica vermelha, cimento, compósitos de matriz cerâmica, materiais refratários, materiais de revestimento, matérias-primas, vidrados, vidros e vitrocerâmicas, análise microestrutural, instrumentação, processos de fabricação, síntese de pós, técnicas de caracterização, etc. Todas as contribuições são submetidas independentemente a análise por relatores, pertencente ou não ao Conselho de Editores. Cerâmica é publicada trimestralmente. Os artigos publicados podem ser acessados por meio de: www.scielo.br/ce. Cópias impressas são distribuídas aos sócios da ABCeram e a bibliotecas do Brasil e de outros países.

Cerâmica, the official journal of the Brazilian Ceramic Society, accepts original (and review) articles in the entire field of ceramic science and technology, including ceramic art, bioceramics, advanced ceramics, electro-electronic ceramics, magnetic ceramics, optical ceramics, nuclear ceramics, structural ceramics, ceramic raw materials, cements, sanitaryware and porcelain, thermal insulators, ceramic tiles, refractories, glazes and ceramic pigments, glasses and glass-ceramics, ceramic matrix composites, characterization techniques, ceramic equipments, microstructural analysis, manufacturing processes, powder synthesis, etc. All contributions are independently refereed. Cerâmica is published every three months. Published papers can be accessed by: www.scielo.br/ce. Printed copies are distributed to members of the Brazilian Ceramic Society and to libraries worldwide.

Editores Associados (Associate Editors)

Editor Principal (Principal Editor)

H. N. Yoshimura
CECS - UFABC
Av. dos Estados, 5001
Santo André, SP 09210-580
humberto.yoshimura@ufabc.edu.br
ceram.abc@gmail.com

D. Z. de Florio
CECS - UFABC
Av. dos Estados, 5001
Santo André, SP 09210-580
daniel.florio@ufabc.edu.br

R. Salomão
SMM - EESC - USP
Av. João Dagnone, 1100
São Carlos, SP 13563-120
rsalomao@sc.usp.br

Editores Associados (Associate Editors)

F. M. B. Marques
DEMaC - Univ. Aveiro
Aveiro 3810-193
Portugal
fmarques@ua.pt

A. M. Segadães
DEMaC - Univ. Aveiro
Aveiro 3810-193
Portugal
segadaes@ua.pt

A. E. Martinelli
DEMat - CT - UFRN
Campus Lagoa Nova s/n
Natal, RN 59072-970
martinelli.ufrn@gmail.com

Conselho de Editores (Editorial Board)

Acchar W. - UFRN - RN
Berg E.A.T. - PR
Bergmann C.P. - UFRGS - RS
Bezerra U.T. - IFPB - PB
Bressiani A.H.A. - IPEN - SP
Fonseca F.C. - IPEN - SP
Holanda J.N.F. - UENF - RJ
Hotza D. - UFSC - SC
Kiminami R.H.G.A. - UFSCar - SP
Lameiras F.A. - CDTN - MG
Longo E. - UNESP - SP
Melo D.M.A. - UFRN - RN
Muccillo E.N.S. - IPEN - SP
Muccillo R. - IPEN - SP
Nascimento R.M. - UFRN - RN

Pandolfelli V.C. - UFSCar - SP
Pianaro S.A. - UEPG - PR
Pulcinelli S.H. - UNESP - SP
Resende W.S. - IBAR - SP
Riella H.G. - UFSC - SC
Rodrigues J.A. - UFSCar - SP
Santilli C.V. - UNESP - SP
Santos I.M.G. - UFPA - PA
Silva C.R.M. - UNB - DF
Vasconcelos W.L. - UFMG - MG
Vieira C.M.F. - UENF - RJ
Zanotto E.D. - UFSCar - SP
Baptista J.L. - Univ. Aveiro - Portugal
Carda J.B. - Univ. Castellón - Spain
Castro M.S. - Univ. Mar del Plata - Argentina

Castro R.H.R. - Univ. California, Davis - USA
Clemens F.J. - EMPA - Switzerland
Esposito V. - DTU - Denmark
Fernandez J.F. - ICV-CSIC - Spain
Greil P. - F-Alexander-U. Erlangen - Germany
Prado F.D. - Univ. Nacional del Sur - Argentina
Sakka Y. - NIMS - Japan
Sin A. - Pirelli Labs - Italy
Steil M.C. - Univ. Grenoble Alpes - France
Studart A.R. - ETH Zürich - Switzerland
Sun Z. - Queensland Univ. Technol. - Australia
Traversa E. - Univ. Roma "Tor Vergata" - Italy
Velez M. - Univ. Missouri-Rolla - USA
Watari K. - AIST - Japan
Yoshimura M. - NCKU - Taiwan; TIT - Japan

Editores Principais Anteriores (Previous Principal Editors): P. S. Santos (in memoriam); R. Muccillo (1997-2015)

Cerâmica – Revista trimestral editada pela Associação Brasileira de Cerâmica ABCERAM, ISSN 0366-6913, registro nº 1004/P209/73 no DPF, fundada em 09/09/1953 - CFMO 0255 - CNPJ: 61.615.977/0001-08. Associação Brasileira de Cerâmica - IPT - prédio 36 - 2. Andar, Av. Prof. Almeida Prado 532, Cidade Universitária, S. Paulo, 05508-901, Brasil. tel: 11-3768-4284, fax: 11-3768-7101 abceram@abceram.org.br, <http://www.abceram.org.br>

Projeto Gráfico: TWA Studio Gráfico - contato@twastudio.com.br <http://www.twastudio.com.br>

- Toda correspondência destinada à revista Cerâmica deve ser endereçada ao Editor Principal.

- Os trabalhos técnicos publicados pela revista Cerâmica são de total responsabilidade dos autores. Artigos assinados não expressam necessariamente a opinião da publicação ou da ABCERAM.

- Any correspondence to Cerâmica should be addressed to the Principal Editor.

- The Brazilian Ceramic Society and the Editors assume no responsibility for the contents of the technical papers and for the statements and opinions advanced by the contributors.

Cerâmica, ISSN-0366-6913, é indexada em (is indexed in): Web of Science (isiknowledge.com), Scopus, Ceramic Abstracts, British Ceramic Abstracts, Chemical Abstracts, Engineered Materials Abstracts, INIS Atomindex, Chemical Engineering and Biotechnology Abstracts (CEABA-VtB), Directory of Open Access Journals (DOAJ), Scimago Journal & Country Rank (SJR), SciELO (www.scielo.br/ce).

COVER: Optical micrographs of cross-sections of: A) commercial aggregate AAE-1506 (P: pore, Q: quartz); B) expanded aggregate (EA-AG) prepared by firing clay from Arroio Grande-RS, Brazil, at 1250 °C; and C) lightweight concrete prepared with EA-AG showing the interaction between aggregate and mortar. See article by A. V. Rodrigues, S. R. Bragança, p. 6.

CAPA: Micrografias ópticas de seções transversais de: A) agregado comercial AAE-1506 (P: poro, Q: quartzo); B) agregado expandido (EA-AG) preparado pela queima de argila de Arroio Grande-RS, Brasil, a 1250 °C; e C) concreto leve preparado com EA-AG mostrando interação entre agregado e argamassa. V. artigo de A. V. Rodrigues, S. R. Bragança, p. 6.





Associação Brasileira de Cerâmica

Tel: 11 3768 4284

Fax: 11 3768 7101

abceram@abceram.org.br

http://www.abceram.org.br

DIRETORIA

Presidente

José Carlos Bressiani

Vice-Presidente

Luis Leonardo Horne Curimbaba Ferreira

Diretor Administrativo-Financeiro

Juliana Marchi

Diretor de Publicações

Humberto Naoyuki Yoshimura

Diretor de Assuntos Empresariais

Edmilson Ricelli dos Passos

Diretor de Assuntos Especiais

Fábio dos Santos Bernardo

Diretora de Comissões Técnicas

Ulisses Soares do Prado

Diretora de Comunicações

Edgar Dutra Zanotto

Diretor de Eventos

Rafael Salomão

CONSELHO

Presidente do Conselho

Antonio Carlos de Camargo

Categorias Patrocinador / Coletivo

Ecio Rodrigues de Araujo

Leandro Cesar Ribeiro

Categorias Individual, Júnior e Instituição

Carlos Mauricio Fontes Vieira

Carolina Del Roveri

Dolores Ribeiro Ricci Lazar

Fernando dos Santos Ortega

Gelmires de Araújo Neves

Luiz Fenando Grespan Setz

Mauro Akerman

Luis Antonio Genova

Renata Ayres Rocha

Ruth Herta Goldschmidt Aliaga Kiminami

Editorial

Este número inicia o volume 69, mantendo a tradição de 69 anos de publicação ininterrupta da revista Cerâmica. Neste número, 389, são apresentados 10 artigos escritos em inglês com autoria de 46 pesquisadores. Considerando a localização da instituição do autor correspondente, 2 artigos são provenientes de países do exterior (1 da Indonésia e 1 da Nigéria) e 8 artigos são de seis diferentes estados brasileiros: 2 da Bahia, 2 do Ceará, 1 do Maranhão, 1 de Minas Gerais, 1 do Rio Grande do Sul e 1 de Sergipe.

Convidamos os leitores a participarem do 67º Congresso Brasileiro de Cerâmica, que será realizado no hotel Costão do Santinho, na cidade de Florianópolis - Santa Catarina, entre 12 e 15 de junho de 2023. A submissão de trabalhos pode ser realizada pelo site do evento (<https://metallum.com.br/67cbc/>). Informações adicionais podem ser obtidas no website da Associação Brasileira de Cerâmica (<https://abceram.org.br/>).

Aproveitamos para parabenizar os alunos do PPG-CEM do Departamento de Engenharia de Materiais da Universidade Federal de São Carlos que foram premiados pelos trabalhos apresentados na área de materiais cerâmicos para alta temperatura no 42nd Latin-American Congress - ALAFAR 2022 realizado em Foz de Iguaçu entre 06 e 10/11/2022: i) prêmio de melhor trabalho: “*In-situ* spinelization of alumina-based castables containing ZnO”, O.H. Borges (PPG-CEM), J.A. Sardelli (RHI-Magnesita/PPG-CEM), C. Pagliosa Neto (RHI-Magnesita), V.C. Pandolfelli (DEMA); ii) prêmio de segundo melhor trabalho: “*In-situ* Al₂O₃-MgO and Al₂O₃-spinel formation: effect on the physical and mechanical properties of unfired alumina brick”, J.A. Sardelli, O.H. Borges, C. Pagliosa Neto, V.C. Pandolfelli. O Prof. Dr. Victor C. Pandolfelli, membro do Conselho de Editores da revista Cerâmica, ministrou a Key-Note Speech: “Refractory eco design” neste congresso.

Humberto N. Yoshimura
Editor



Synthesis of delafossite CuCrO_2 via solution combustion method and its acid functionalization for biodiesel production

M. C. Viegas¹, G. P. de Figueredo¹, S. F. Rodrigues², A. A. Cabral², M. A. M. Castro³, M. M. Oliveira^{1*}

¹Instituto Federal do Maranhão, PPGQ/DAQ, Av. Getúlio Vargas 4, 65025-001, São Luís, MA, Brazil

²Instituto Federal do Maranhão, PPGEM, São Luís, MA, Brazil

³Universidade Federal do Rio Grande do Norte, PPGCEM, Natal, RN, Brazil

Abstract

CuCrO_2 was synthesized by solution combustion synthesis (SCS) and applied as a heterogeneous catalyst to produce soybean biodiesel. The combustion reaction was carried out using urea as a fuel, and copper (II) and chromium (III) nitrates as precursors. After the powders' obtention, these were calcined and functionalized in an acidic medium. The powders were characterized by thermogravimetry (TG), X-ray diffraction (XRD), scanning electron microscopy (SEM), and infrared spectroscopy (IR) techniques. The TG curve revealed that the formation of the CuCrO_2 in the combustion reaction remained stable up to 1000 °C. The XRD results confirmed the formation of the CuCrO_2 compound. The SEM images showed that the crystallinity of the samples increased after the calcination process. The IR spectra showed the presence of delafossite characteristic bands. After the transesterification reaction, biodiesel was obtained with a yield of around 80%. Thus, catalysts based on delafossite synthesized through the combustion method and functionalized showed to be promising for the transesterification reaction of vegetable oils.

Keywords: delafossite, solution combustion synthesis, heterogeneous catalyst, transesterification reaction.

INTRODUCTION

Delafossites are a class of minerals formed by ternary oxides that present a general formula of the type ABO_2 , where A and B represent metallic cations [1]. The A elements have a 1⁺ charge (such as Cu, Pt, and Ag), while the B elements have a 3⁺ charge (Fe, Cr, Al, and Ga being more common) [1, 2]. These compounds have a crystalline structure of hexagonal or rhombohedral type displayed in layer forms. Additionally, their arrangement depends on the type of orientation that each layer is disposed of in the compound structure [3]. The layers are formed by A⁺ cations-bound oxygen, which forms O-A-O. These are coupled to the BO_6 octahedron that is formed by the trivalent ions B³⁺ bonded to the oxygen atoms [3, 4]. Delafossite CuCrO_2 is an oxide semiconductor that has excellent electrical, magnetic, and optical properties. The oxide is used mainly to produce electrodes and sensors for the photocatalysis process and other applications [1-5]. This material is also widely studied for transparent conducting oxide (TCO) applications due to its unique combination of electrical conductivity and optical transparency [5, 6]. These properties are directly related to its particle size and surface characteristics, which mainly depend on the synthesis process. Some ceramic powder synthesis method details can be found in the literature [7]. It is worth highlighting the solution combustion synthesis that stands out for its versatility, simplicity, cost, and process speed. It has been shown that this method led to particles that present good chemical homogeneity results [7, 8].

Compounds based on CuCrO_2 are promising for

application in heterogeneous catalytic systems, such as the transesterification process to produce biodiesel. In such a process, a basic or acidic catalyst is used to improve the reaction rate and yield. On the other hand, when mainly homogeneous basic catalysts (NaOH and KOH) are used [9-11], the presence of these compounds leads to the contamination of the final product, which requires expensive washing and refining steps. Instead, heterogeneous acid catalysts do not present these problems and are still able to be recycled and reused for new reactions [9-12]. The performance of CuCrO_2 for the transesterification of vegetable oils can be significantly improved by increasing its acidic character. This is a requirement to subject it to a chemical functionalization in an acidic medium [13-15]. According to Zhong et al. [16], functionalization modifies the surface of the solid, promoting the addition of acid sites that remove impurities and decrease the hydrophobicity.

In this study, ceramic powders based on delafossite CuCrO_2 were obtained using the solution combustion method. This was followed by chemical functionalization in order to verify its behavior as a heterogeneous catalyst for the production of biodiesel from soybean oil. It is noteworthy that the solution combustion method is a cheap method in terms of energy expenditure, as it takes advantage of the heat of the reaction to synthesize the material and the reagents involved in the process have relatively low cost.

EXPERIMENTAL

Synthesis of delafossite by solution combustion method (SCS): the ceramic powders were synthesized by combustion reaction, using metallic nitrates as precursors and urea as fuel. To obtain 5 g (0.034 mol) of delafossite

*marcelo@ifma.edu.br

https://orcid.org/0000-0003-4991-8157

CuCrO_2 , stoichiometric quantities of the reagents were used as follows: 8.18 g (0.034 mol) of copper nitrate [$\text{Cu}(\text{NO}_3)_2 \cdot 3\text{H}_2\text{O}$, Isifar], 13.56 g (0.034 mol) of chromium nitrate [$\text{Cr}(\text{NO}_3)_3 \cdot 9\text{H}_2\text{O}$, Sigma Aldrich] and 8.47 g (0.141 mol) of urea [$(\text{NH}_2)_2\text{CO}$, Synth], all of them of analytical grade. The mixture of reagents (in 20 mL of deionized water) was previously heated at $\sim 65^\circ\text{C}$ and stirred in a magnetic stirrer until an emulsion was formed. Then, the mixture was taken into a muffle furnace, heated to 400°C , and held there for 10 min for the total completion of the reaction. The powder resulting from the reaction was deagglomerated in an agate mortar, heated at a rate of $10^\circ\text{C}\cdot\text{min}^{-1}$ to be calcined at 1100°C for a period of 2 h in a muffle furnace.

Functionalization: after the synthesis process, a part of the powder was functionalized in an acidic medium. The employed chemical treatment was carried out according to the methodology shown elsewhere [16]. Initially, 250 mL of a solution $1\text{ mol}\cdot\text{L}^{-1}$ of H_2SO_4 (>95%, Merck) was prepared. Then, 100 mL of the H_2SO_4 solution was transferred to a flat bottom flask, to which 1.0 g of the obtained oxide (CuCrO_2) was added. For this treatment, a reflux system was installed using a magnetic stirring with a heater. The mixture was kept in this apparatus at a temperature range of approximately 80°C for 2 h. After this period, the mixture was filtered, washed with deionized water up to $\text{pH}=5.0$, and dried in an oven at 100°C for 4 h. Table I shows the identification of the non-calcined, calcined, and functionalized samples, and their corresponding obtaining temperatures.

Table I - Identification code of the samples.

Description	Temperature ($^\circ\text{C}$)	Sample
Non-calcined	400	$\text{CuCrO}_2\text{-NC}$
Calcined	1100	$\text{CuCrO}_2\text{-CC}$
Functionalized	1100	$\text{CuCrO}_2\text{-FC}$

Transesterification reaction: for this reaction, refined soybean oil and ethanol were used as reagents for biodiesel production. The reactions were conducted by using 5% in mol of the functionalized catalyst in relation to the oil mass (0.5 g), alcohol:oil molar ratio of 12:1 (38 mL of ethanol:50 mL of oil) at 150°C during 6 h of reaction in a reactor (4848, Parr). The reaction was kept under constant agitation while the soybean biodiesel was obtained. The biodiesel composition was analyzed through the gas chromatography technique. The reaction yield was calculated according to:

$$\text{Yield (\%)} = \frac{M_{\text{biodiesel}}}{M_{\text{oil}}} \cdot 100 \quad (\text{A})$$

where $M_{\text{biodiesel}}$ represents the obtained biodiesel mass and M_{oil} is the soybean oil mass used in the reaction [17]. Analyzes of the biodiesel were also carried out by gas chromatography (GC) in order to evaluate the conversion rate of triglycerides to alkyl esters. The experiments were carried out in a gas chromatograph analyzer (CG-2010, Shimadzu), coupled

with a mass spectrometer (CG-EM QP2010 Plus, Shimadzu). A capillary column (30 m x 0.25 mm x 0.25 μm , ZB-FFAP, Phenomenex) with a flow of carrier gas (He) at a linear speed of $47.5\text{ cm}\cdot\text{s}^{-1}$ and column flow of $1.0\text{ mL}\cdot\text{min}^{-1}$ was used.

Characterizations: the samples were characterized by thermogravimetry (TG), X-ray diffraction (XRD), scanning electron microscopy (SEM), infrared spectroscopy (IR), and gas chromatography (GC). TG was carried out so that variations in the mass of the compound CuCrO_2 as a function of temperature were observed. The analyzes were carried out in a thermal analyzer (STA 409, Netzsch) by the dynamic method of analysis with a heating rate of $10^\circ\text{C}\cdot\text{min}^{-1}$ in static air and at a temperature range of 25 to 1000°C . The XRD characterization was performed to determine the structure and crystalline phases presented in the samples. The technique was done by using an X-ray diffractometer (XRD-6100, Shimadzu), with $\text{CuK}\alpha$ radiation (1.5406 \AA), scanning speed of $2^\circ\cdot\text{min}^{-1}$, and angle of 2θ from 10° to 80° . SEM was employed to analyze the morphological characteristics of the sample surfaces. The analyzes were carried out using a microscope (Vega3 LMU, Tesca) in secondary electron mode. The identification and characterization of the groups present in the samples were carried out by infrared absorption spectroscopy. For this, a spectrophotometer (Prestige 2, Shimadzu) was used. Here, the transmittance spectra of the samples were obtained in a range of 4000 to 400 cm^{-1} , resolution of 4 cm^{-1} , and an average of 40 scans.

RESULTS AND DISCUSSION

Thermogravimetry (TG): the thermogravimetric curves obtained from the $\text{CuCrO}_2\text{-NC}$ sample are shown in Fig. 1a and TG/DSC in Fig. 1b. It is possible to observe in Fig. 1a that there was a small loss in mass of the material, less than 1%, as the temperature varied. This showed that the synthesis proved to be efficient because it was possible to obtain a stable material. Nevertheless, three distinct events are shown in Fig. 1b, evidenced by the peaks in the DSC (differential scanning calorimetry) curve. In region I, the initial mass loss was due to the loss of water that is part of the delafossite structure [18, 19]. In regions II and III (600 and 800°C , respectively), the mass loss process may be associated with the elimination of organic residues formed during the synthesis, derived from urea [20].

X-ray diffraction (XRD): the diffractograms obtained for the non-calcined ($\text{CuCrO}_2\text{-NC}$), calcined ($\text{CuCrO}_2\text{-CC}$), and functionalized ($\text{CuCrO}_2\text{-FC}$) samples are depicted in Fig. 2. The delafossite phase was obtained for the three analyzed samples, but with different diffraction profiles. For the non-calcined sample (NC), the formation of the delafossite phase occurred with the presence of secondary phases such as Cr_2O_3 (PDF 038-1479) and CuO (PDF 041-0254). The functionalized sample ($\text{CuCrO}_2\text{-FC}$) exhibited a similar profile when compared to the non-calcined material, also with the presence of secondary phases. In the calcined sample

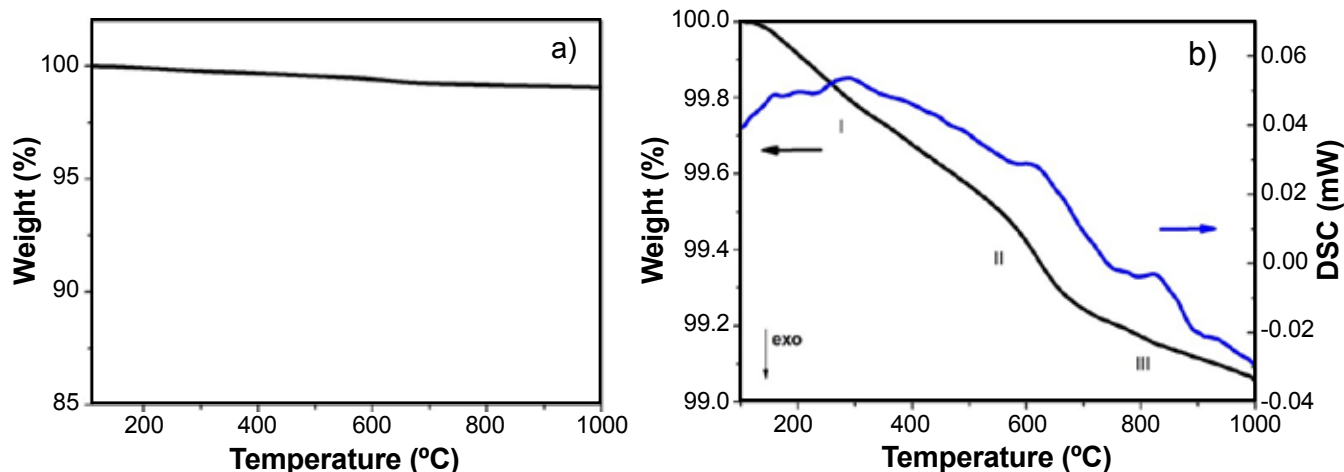


Figure 1: Thermogravimetric curves of $\text{CuCrO}_2\text{-NC}$ sample: a) original curve; and b) scale enlargement of TG/DSC curves.

($\text{CuCrO}_2\text{-CC}$), the pure phase of delafossite (PDF 039-0247), of rhombohedral structure (R-3M), was observed. According to Martins et al. [21], the increase of the calcination temperature up to 1100 °C favors the transition from the secondary phases to the CuCrO_2 . Furthermore, chemical functionalization in an acidic medium may result in structural defects of the compounds which lead to the conversion of Cu and Cr oxides during the acidification process [22, 23]. The high-intensity peaks in relation to the $\text{CuCrO}_2\text{-NC}$ material were due to the fact that the $\text{CuCrO}_2\text{-FC}$ sample was previously calcined.

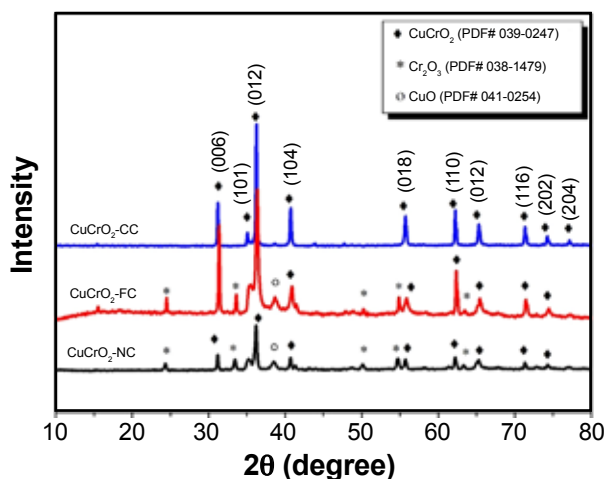


Figure 2: X-ray diffractograms of CuCrO_2 samples: $\text{CuCrO}_2\text{-NC}$, $\text{CuCrO}_2\text{-FC}$, and $\text{CuCrO}_2\text{-CC}$.

Scanning electron microscopy (SEM): the morphologies of the CuCrO_2 compound before and after heat treatment are shown in Figs. 3a and 3b, respectively. It was possible to observe a clear difference in the morphology and particle sizes. The $\text{CuCrO}_2\text{-NC}$ sample showed a pronounced porous appearance, with poorly defined particle morphology. On the other hand, the $\text{CuCrO}_2\text{-CC}$ sample exhibited a more homogeneous morphological aspect, with the formation of particles in the form of irregular polyhedral. These resulted from the applied temperature which represents

a determining factor for the crystallinity of the material [24]. Coelho et al. [9] pointed out that, increasing the temperature, particles tend to coalesce leading to morphologies of polyhedral irregular shapes. Temperatures up to 1100 °C also contribute to the formation of hexagonal shape particles and plate type. These morphologies are an indication of delafossite phase formation. Similar results are presented in the literature [21, 25].

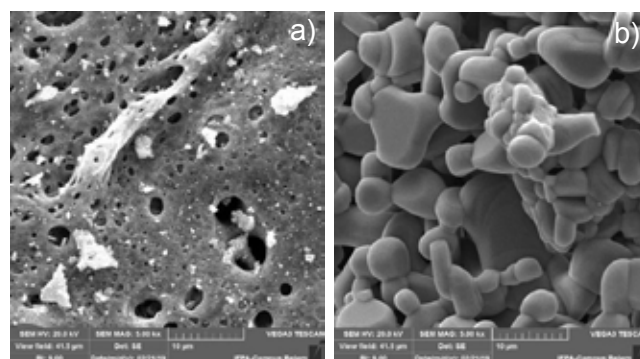


Figure 3: SEM micrographs of CuCrO_2 compound samples before, NC (a), and after, CC (b), heat treatment.

Infrared spectroscopy (IR): through infrared analysis, information about the bonds and functional groups present in the compound (CuCrO_2) was obtained. The infrared spectra of the non-calcined and calcinated material at 1100 °C are shown in Fig. 4. $\text{CuCrO}_2\text{-NC}$ and $\text{CuCrO}_2\text{-CC}$ samples exhibited similar spectral profiles. The bands of strong intensity located at 552 and 730 cm^{-1} were associated with the vibrational frequencies of Cu-O and $\text{Cr}^{\text{III}}\text{-O}$ bonds, respectively [19, 26]. At 946 cm^{-1} , the stretching band present was related to the $\text{Cr}^{\text{IV}}\text{-O}$ bonds [27]. According to Ahmad et al. [27], the presented absorption bands in these regions are characteristic of the CuCrO_2 phase. In the $\text{CuCrO}_2\text{-FC}$ sample, there was a slight deviation of the bands in relation to the other spectral profiles. This behavior may be related to the presence of acidic functional groups in the structure of the CuCrO_2 compound. Functional groups from organic compounds were not detected, indicating that the

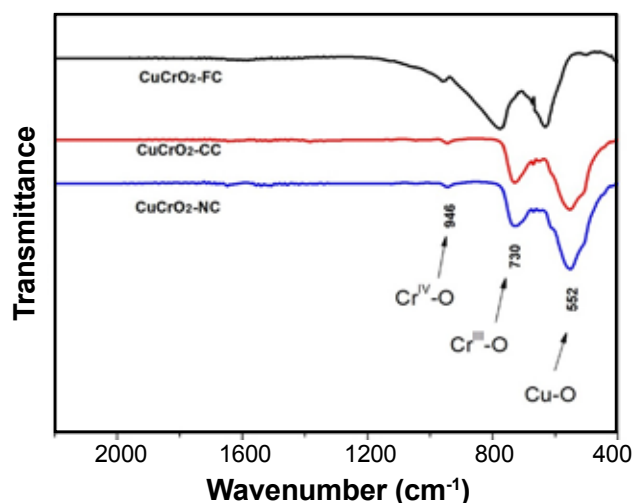


Figure 4: Infrared spectra of the CuCrO_2 compounds.

urea used as fuel during the synthesis of the specimens was entirely consumed during combustion, with the consequent formation of gases.

Catalytic test: this test was carried out in order to evaluate the efficiency of the compound CuCrO_2 as a catalyst in the ethyl transesterification reaction of soybean oil. The tests were performed with a CuCrO_2 -FC sample with an alcohol:oil ratio of 12:1 at 150 °C for 6 h. In the reaction, ethyl esters were produced using the functionalized catalyst (CuCrO_2 -FC). The results of the chromatographic analysis of this reaction are shown in Fig. 5. The chromatogram was characteristic of the soybean biodiesel pattern [27, 28]. The highest intensity peaks were related to the ethyl palmitate ester (peak 1), ethyl stearate (peak 3), ethyl oleate (peak 4), ethyl linoleate (peak 6), and ethyl linolenate (peak 9). The contents of these esters and other information are shown in Table II. Among the major esters, it was observed that ethyl linoleate was the main constituent (40%, $T_r=20.94$ min), followed by ethyl oleate (25%, $T_r=19.79$ min), ethyl palmitate (14%, $T_r=14.83$ min), ethyl linolenate (8.76%, $T_r=22.37$ min), and ethyl stearate (6.64%, $T_r=19.32$ min).

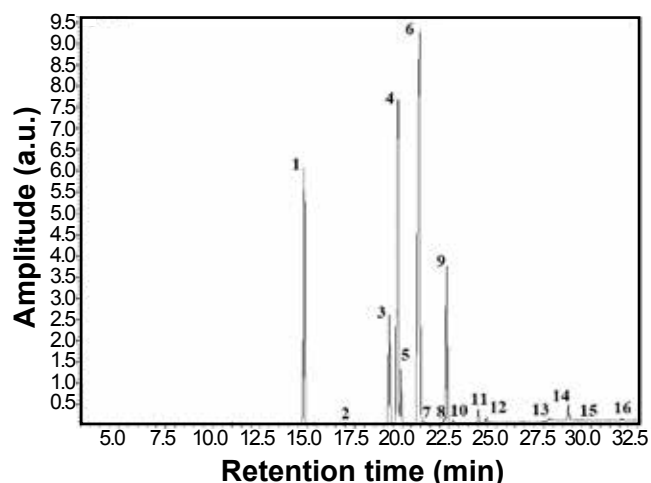


Figure 5: Chromatogram of soybean oil biodiesel.

Table II - Obtained ethyl esters in soybean biodiesel from the transesterification reaction and their characteristics.

Fatty acid ester	N° of carbon	$T_{\text{retention}}$ (min)	Composition (%)
Ethyl palmitate	C 16:0	14.83	14.0
Ethyl stearate	C 18:0	19.32	6.6
Ethyl oleate	C 18:1	19.79	25.0
Ethyl linoleate	C 18:2	20.94	40.0
Ethyl linolenate	C 18:3	22.37	8.8

These data agreed with other studies found in the literature [11, 29, 30]. Soybean biodiesel is characterized by the predominance of esters derived from unsaturated fatty acids.

The yield was calculated using Eq. A. In the reaction, 46 g (50 mL) of soybean oil was initially used. At the end of the reaction, 37 g (42 mL) of biodiesel was obtained and reached a yield of 80%. The yield value was considered satisfactory since the highest yields are achieved with basic catalysts in the methanolic reaction of vegetable oils. Other studies have reported similar results, such as Quintella et al. [31] who used mesoporous silica as a heterogeneous catalyst in the ethyl transesterification of soybean oil. In their investigation, 1% catalyst mass and 20:1 alcohol:oil molar ratio were employed in which 80% yield was obtained after 6 h of reaction at 100 °C. Yuan et al. [32] developed acid-based carbon catalysts which are utilized in the transesterification of soybean oil. In this research, an 8:1 molar ratio of ethanol to oil, 7% of catalyst, and a reaction period of 8 h at 80 °C were employed. As a result, there was a 70% conversion into ethyl esters. In contrast, for the non-calcined (CuCrO_2 -NC) and calcined (CuCrO_2 -CC) samples under the same reaction conditions (alcohol:oil ratio of 12:1 at 150 °C for 6 h), satisfactory reaction results were not possible and no conversion occurred. This result suggested that the pure delafossite compound does not perform as a catalyst for the transesterification reaction. The functionalization of the catalysts was essential for the conversion process, which can be associated with the modification of the structure and surface of the solid product. Additionally, it raises the acid character, removes impurities, and decreases hydrophobicity, thus increasing its catalytic activity for the transesterification reaction [33-35].

CONCLUSIONS

Combustion synthesis followed by calcination proved to be an efficient process to produce delafossite CuCrO_2 . The results of the thermogravimetric analysis showed that the phase of the compound CuCrO_2 was stable up to 1000 °C. This observation was confirmed by the XRD analysis, which revealed that after the synthesis process, the obtained compound presented a mixture of oxides and after calcination, it exhibited greater crystallinity. The predominance of the CuCrO_2 crystalline phase was revealed by the well-defined peaks and their intensities. Porous morphology was presented

when the compound did not experience thermal treatment and irregularly shaped polygons were obtained when treated at 1100 °C. Absorption bands associated with the main connections of the delafossite were identified through the infrared spectra which characterized the formation of the oxide. The chromatographic analysis confirmed the conversion of soybean oil into biodiesel, with a yield of 80%. This revealed that the acidification process increased the activity of the catalyst, resulting in a good reaction yield.

ACKNOWLEDGMENTS

To IFMA for the financial support through the Public Notice PRPGI n° 106 (Selection of Student Dissertation Projects Linked to the IFMA *Stricto Sensu* Graduate Program), to FAPEMA for granting a scholarship and project financing, to the Fuel, Catalysis and Environmental Nucleus and to the Central Analítica of UFMA, for carrying out the analyzes and Prof. Cáritas Mendonça, Ph.D., from UFMA, for their collaboration from chromatographic analysis test.

REFERENCES

- [1] S. Kumar, S. Marinel, M. Miclau, C. Martin, *Mater. Lett.* **70** (2012) 40.
- [2] M.A. Marquardt, N.A. Ashmore, D.P. Cann, *Thin Solid Films* **496** (2006) 146.
- [3] J.F.H. Monteiro, A.R. Jurelo, F.C. Monteiro, D.R. Mosca, *Ceram. Int.* **44** (2018) 14101.
- [4] H.F. Jiang, C.Y. Gui, Y.Y. Zhu, D.J. Wu, S.P. Sun, C. Xiong, X.B. Zhu, *J. Alloys Compd.* **582** (2014) 64.
- [5] A.P. Amrute, Z. Lodziana, C. Mondelli, F. Krumeich, J.P. Ramírez, *Chem. Mater.* **25** (2013) 4423.
- [6] C. Taddee, T. Kamwanna, V. Amornkitbamrung, *Appl. Surf. Sci.* **380** (2016) 237.
- [7] J. Wang, P. Zheng, D. Li, Z. Deng, W. Dong, R. Tao, X. Fang, *J. Alloys Compd.* **509** (2011) 5715.
- [8] B.R. Vahid, M. Haghighi, *Energy Convers. Manag.* **126** (2016) 362.
- [9] M.B.M. Coelho, M.M. Oliveira, I.C. Nogueira, J.H.G. Rangel, J.S. Vasconcelos, E. Azevedo, A.P. Maciel, E. Longo, *Cerâmica* **64**, 369 (2018) 49.
- [10] M.E. Borges, L. Díaz, *Renew. Sust. Energ. Rev.* **16** (2012) 2839.
- [11] C. Kordulis, K. Bourikas, M. Gousi, E. Kordouli, A. Lycourghiotis, *Appl. Catal. B* **18** (2016) 156.
- [12] R.A. Ferrari, V.S. Oliveira, A. Scabio, *Quim. Nova* **28** (2005) 19.
- [13] G.F. Ghesti, J.L. de Macedo, J.A. Dias, S.C.L. Dias, *Quim. Nova* **35** (2012) 119.
- [14] T.C. dos Santo, E.C.S. Santos, J.P. Dias, J. Barreto, F.L. Stavale, C.M. Ronconi, *Fuel* **256** (2019) 115793.
- [15] Y. Nian, H. Teng, *J. Electrochem. Soc.* **8** (2002) 149.
- [16] Y. Zhong, Q. Deng, P. Zhang, J. Wang, R. Wang, Z. Zeng, S. Deng, *Fuel* **240** (2019) 270.
- [17] J.L. Figueiredo, *J. Mater. Chem. A* **1** (2013) 9351.
- [18] W. Ketir, G. Rekhila, M. Trari, A. Amrane, *J. Environ. Sci.* **24** (2012) 2173.
- [19] D. Ursu, M. Miclau, *J. Nanopart. Res.* **16** (2014) 2160.
- [20] W. Li, H. Cheng, *J. Cent. South Univ. Technol.* **14** (2007) 291.
- [21] F.D.A.B.L. Martins, M.B.M. Coelho, R.N.R.D. Silva, J.S. Vasconcelos, J.H.G. Rangel, E. Longo, J.M.R. Mercury, *Matéria* **24** (2019) 24.
- [22] A. Figarol, J. Pourchez, D. Boudard, V. Forest, J.M. Tulliani, J.P. Lecompte, P. Grosseau, *J. Nanopart. Res.* **16** (2014) 2507.
- [23] E.L. Foletto, C. Volzone, A.F. Morgado, L.M. Porto, *Cerâmica* **47**, 304 (2001) 208.
- [24] J.F.H.L. Monteiro, A.R. Jurelo, E.C. Siqueira, *Solid State Commun.* **252** (2017) 64.
- [25] Z.Y. Liu, G.Y. Wang, X.P. Liu, Y.J. Wang, *J. Fuel Chem. Technol.* **41** (2013) 1473.
- [26] Y.H. Chuai, X. Wang, H.Z. Shen, Y.D. Li, C.T. Zheng, Y.D. Wang, *J. Mater. Sci.* **51** (2016) 3592.
- [27] T. Ahmad, R. Phul, P. Alam, I.H. Lone, M. Shahazad, J. Ahmed, S.M. Alshehri, *RSC Adv.* **7** (2017) 27549.
- [28] M. Stefanescu, M. Barbu, T. Vlase, P. Barvinschi, L. Barbu-Tudoran, M. Stoia, *Thermochim. Acta* **526** (2011) 130.
- [29] S.T. Keera, S.M. El Sabagh, A.R. Taman, *Fuel* **90** (2017) 42.
- [30] M.V. Marques, F.F. Naciuk, A.M.D.S. Mello, N.M. Seibel, L.A.M. Fontoura, *Quím. Nova* **33** (2010) 978.
- [31] S.A. Quintella, R.M. Saboya, D.C. Salmin, D.S. Novaes, A.S. Araújo, M.C. Albuquerque, C.L. Cavalcante, *Renew. Energ.* **38** (2012) 136.
- [32] L. Yuan, X.L. Zhang, W.Y. Gao, L.G. Ren, *J. Liaoning Univ. Petrol. Chem. Technol.* **2** (2018) 156.
- [33] C.M. Garcia, S. Teixeira, L.L. Marciniuk, U. Schuchardt, *Bioresour. Technol.* **14** (2008) 6608.
- [34] D. Zuo, J. Lane, D. Culy, M. Schultz, A. Pullar, M. Waxman, *Appl. Catal. B* **129** (2013) 342.
- [35] M. Ramos, A.P.S. Dias, J.F. Puna, J. Gomes, J.C. Bordado, *Energies* **12** (2019) 4408.

(Rec. 26/03/2022, Rev. 14/09/2022, Ac. 11/10/2022)



Technological properties of a self-bloating clay and expanded-clay aggregate for the production of lightweight concrete

A. V. Rodrigues^{1*}, S. R. Bragança¹

¹Federal University of Rio Grande Sul, DEMAT/PPGEM, 90035-190,
Av. Osvaldo Aranha 99/711, Porto Alegre, RS, Brazil

Abstract

The global interest in an increasingly sustainable economy, with a reduction in the consumption of raw materials and energy, can be supported by the growth in the use of lightweight concrete (LC) produced with expanded-clay aggregates (EA). The main qualities of natural self-bloating clay for the production of EA were studied, analyzing the parameters that determine the expansion during firing, which influence EA size, mechanical strength, density, and water absorption. After this step, the production and characterization of the LC were carried out. EA characteristics showed a strong influence on the mechanical strength and the main technological properties of the LC. The results pointed out the necessary attributes that clay (and EA) must have for LC production. These attributes can also be achieved by mixing different clays (blend type), which can enhance the production and use of LC with EA worldwide.

Keywords: clay, expanded-clay aggregate, lightweight concrete.


INTRODUCTION

Concrete is one of the most important materials today and its consumption on a world scale is a reason for concern when it comes to sustainable production. Many studies have proposed the replacement of the cement binder since its manufacture is responsible for the emission of large amounts of gases that cause the greenhouse effect [1, 2]. In addition, the environmental impact of aggregates and steel consumption, in the case of reinforced concrete, must also be considered [3]. Thus, a clear solution is to reduce the consumption of concrete, which can be achieved by reducing the weight of structures when using lightweight concrete. The world consumption of aggregates for concrete production is in the order of 28 billion tons per year, and this amount could double in the next decade [1]. Given this scenario, deposits of rocks such as limestone, granite, basalt, etc., are becoming more and more distant from the large consumption centers, increasing transportation costs. The search for alternative aggregates becomes necessary for the production of sustainable concrete [2, 3]. Among several sustainable actions, there is the replacement of coarse and fine aggregates by construction and demolition waste. Nevertheless, this practice has been shown to be limited, with a reduction in concrete strength in the order of 60% to 75%. Studies indicate that impurities such as textile materials, wood, plaster, and polymeric materials cause high water absorption and directly affect the strength of concrete and its durability [4, 5]. However, some studies show success in the use of waste, such as coal ash and blast furnace slag [6], and

aggregates from recycled materials, such as crushed bricks and glass [5]. On the other hand, the most critical issue is the distance from where the materials are extracted/obtained to the concrete factory, and, above all, the reliability in the quantity supplied and the quality of recycled materials. A well-known alternative is the use of lightweight concrete with expanded-clay aggregates, as demonstrated by several projects in the world, such as the Chase-Park Plaza hotel in the city of St. Louis (USA), which is considered the first building with all its lightweight concrete structure and with 28 floors.

There are advantages of lightweight concrete when compared to regular concrete which is noteworthy, such as higher thermoacoustic insulation, which generates superior comfort in the environment. In addition, thermal insulation provides energy savings that are also translated into environmental gain. There are specific standards that address thermoacoustic comfort [7], and studies that demonstrate performance in buildings [8-10]. Lightweight concrete (LC) is defined as concrete with a density of less than 2000 kg/m³ [11], being structural lightweight concrete when the compressive strength is higher than 17 MPa, according to ASTM 330-05 standard [12, 13], and higher to 20 MPa, according to Brazilian standard (NBR 6118:2014). LC allows the use of smaller sections of columns, beams, and slabs, providing savings on cement and aggregates and also the reduction of steel consumption, or the construction of more floors, in the case of buildings [8, 14]. Expanded-clay aggregates (EA) are produced with plastic clays that facilitate the pelletizing process. At the same time, expansion of the raw aggregate must occur at temperatures from 1200 to 1300 °C [14, 15]. It is believed that, for example, in many of the 7000 ceramic industries producing blocks and bricks

*viana.adalberto1914@gmail.com

 <https://orcid.org/0000-0002-4704-0320>

in Brazil [16], some of them, with the necessary technical adaptations, could be used for the production of EA [17]. However, the adaptation of the redware ceramic industries requires, in addition to technical learning, a considerable financial investment, mainly for the manufacture of high-quality expanded lightweight aggregates, such as those produced in rotary kilns (at high temperatures, between 1000 and 1350 °C [13]). The moving grate process produces an aggregate with higher open porosity and irregular shape, requiring crushing for use in lightweight concrete [13]. As ceramic industries are usually closer to urban areas than rock deposits, there would be savings in transport, which would partially offset the cost of firing the EA [13, 18].

The use of LC in bridges and buildings is an effective solution to reduce 'self-weight', also called 'dead weight' in a structure since LC has a minimum weight reduction of 20% when compared to regular concrete; this also allows the use of larger spans in the structure or the construction of more floors. Other uses stand out, such as LC artifacts: precast structures, barbecue grills, guides, blocks (structural or not), pergolas, benches, and various applications with thermoacoustic insulation properties. LC is also widely used in filling and/or leveling floors, subfloors, and slabs [18-21]. The global panorama indicates that Brazil is among the 6 countries with the largest cement production, reaching 56 million tons in 2019 [22]. However, the country has only one expanded-clay aggregate industrial plant, located in the State of São Paulo, so the cost of transportation to other Brazilian States and regions sometimes makes it impracticable to use these lightweight aggregates [17]. This means that the country has a large underproduction and underutilization of lightweight concrete with EA and, therefore, a need to stimulate new production centers. As in Brazil, the use of LC could increase significantly in other countries if the necessary attributes of clay for the production of expanded aggregates were better known. This would allow the production of EA preferably close to consumption centers, with the aim of economic and environmental costs would be reduced, boosting the utilization of LC.

The aim of this work was to study the characteristics of a clay from the South Region of Brazil for the production of expanded aggregates, also analyzing the main qualities of non-structural lightweight concrete. Therefore, as a novelty, the performance of the selected clay is analyzed from clay characteristics, EA and LC properties, and their relationship. The preparation of these materials was carried out under laboratory conditions so that the comparison with the industrialized product must be done with due care. The self-bloating clay used to produce expanded-clay aggregate (EA) in this research comes from a clay mine strategically located in the country. The deposit is located 1500 km from the single producer in Brazil and is relatively close to Uruguay and Argentina. The work presents clay characterization through the evaluation of its physical and chemical properties, and the relationship of these with the EA production during firing at 1250 °C. The performance of this aggregate was evaluated in the production of lightweight concrete. The

results obtained were compared with experimental data from a commercial EA and with LC data from the research of other authors.

MATERIALS AND METHODS

The experiment began with the characterization of the clay from Arroio Grande-RS, located in the South Region of Brazil, which was named AGC. It was manually formed into clay bodies (spheres or pellets) and fired, producing the expanded-clay aggregates, called EA-AG. The evaluation of the results was carried out by comparing data from aggregates from a unique manufacturer in Brazil (Cinexpan), which uses the code AAE-1506 (for the chosen aggregate used in this work). Lastly, the production and evaluation of lightweight concrete (LC-AG) with the EA-AG was accomplished. From preliminary results, it was possible to conclude that AGC was a self-bloating clay, i.e., the ability to produce expanded aggregates without the need to use pyro-expanding additives.

AGC was characterized using the following tests: i) plasticity limit (LP), liquid limit (LL), and plasticity index (PI) by the Atterberg method using the Casagrande apparatus [23, 24]; ii) laser particle size distribution (mod. 1180, Cilas): the sample was dispersed in water and passed through an ultrasound bath; iii) X-ray fluorescence spectroscopy (XRF, XRF-1800, Shimadzu): the sample was prepared in pellets or tablets, obtained from a mixture of 3 g of powder (passed through an ABNT 325 mesh sieve) and 3 g of binder (boric acid), being compacted at 20 MPa of pressure; iv) optical microscopy and scanning electron microscopy (SEM): samples were prepared by polishing with sandpaper in decreasing granular size, ending with a suspension of alumina in water on fabric wool. For X-ray diffraction (XRD) tests, the clay sample was kept in a muffle at 110±5 °C for 24 h, then disaggregated in a mortar and passed through an ABNT 325 mesh sieve (45 µm opening). The quantification and identification of the crystalline phases were done using the Rietveld method with GOF=3.67 and $R_{wp}=14.52$ in a diffractometer (D8, Bruker) with a θ goniometer, radiation of 1.54184 Å $K\alpha$ from a copper tube (slits of 3 and 0.6 mm with nickel $K\beta$ filter) under 40 kV and 40 mA conditions. The speed and the scan interval were 3 s at 0.02° and 2° to 72° (2 θ), respectively. The thermogravimetric and differential thermal analyses (TGA/DTA, TGA/SDTA 851, Mettler Toledo) were performed using air and a heating rate of 5 °C/min between 25 and 1300 °C.

The clay was humidified (~20% by weight) until it reached the plasticity necessary for its manual molding, and forming small spheres according to the desired granulometry. Subsequently, the clay spheres remained at room temperature for 24 h and, after this period, they were placed in a muffle for another 24 h at 50±5 °C. The firing of the AGC spheres was realized at 1250 °C at a heating rate of 5 °C/min with a holding time of 20 min. The firing cycle had a time of 4.41 h. The maximum temperature chosen was obtained through pre-tests. Normally, in industrial production, temperatures of

~1250 °C are used [25]. However, the differences between laboratory and industrial firing, which are not considered here, must be evaluated. The EA-AG underwent a slow cooling, estimated at 12 h, inside a furnace (TB-9665, Jung) using silicon carbide resistors, and the entire cycle lasted 24 h. The particle size distribution of the EA-AG was analyzed with standardized sieves of 12.5, 9.5, 6.3, and 4.8 mm [26]. The amount of material retained in each sieve was chosen to approximate the distribution found in the material Cinexpan AAE-1506. The evaluated properties of the EA-AG were compressive strength, density, absorption ratio, water absorption, and aggregate expansion rate. For this last parameter, the volume of the EA-AG was taken into account before and after the firing, using as reference 12 spheres with diameters of 12.5, 9.5, and 6.3 mm. The maximum diameter of the EA-AG was 12.5 mm. A compressive strength test of the aggregates was realized using a thin layer (cream) of cement (1:1), only to promote a weak bond between the EAs, in a 10x20 cm cylindrical container [27]. Water absorption and its absorption rate were analyzed after the immersion of the samples in periods of 1, 3, 5, 24, and 72 h.

In the production of lightweight concrete (LC-AG), Portland cement type III (CPV-ARI in Brazil) with a density of 3.12 kg/dm³ was used. As for the fine aggregate (sand), the granulometry, fineness modulus (MF), and density tests were carried out, in accordance with current standards [28-30]. The sand utilized had a density of 2.58 kg/dm³ and a fineness modulus equal to 2.31, classified as medium sand, with its particle size distribution within the optimal zone for concrete production according to ABNT NBR 7211 standard [28]. The sand was dried at ~110 °C. A concrete mix of 1:2.4:1.6:0.8 was prepared by weight basis, following the order of cement, sand, clay, and water/cement factor of 0.8; this ratio was based on literature [12, 31] and previous tests [32]. This mix had a dry mortar content of 68%. 21 cylindrical bodies were molded (10x20 cm), and 6 of them were used for the compressive strength test at the ages of 3, 7, and 28 days [30]. The following tests were carried out: compressive strength, density, absorption ratio, and water absorption by immersion at a time of 24 and 72 h. The compressive strength test was based on the ABNT NBR 5739 standard [27], using a mechanical testing machine (DL 20000 N10741 NS 078, Emic) at a compression speed of 0.45 MPa/s. The Ø10x20 cm cylindrical molds were chosen. The molds were previously lubricated with Vaseline. The mixing sequence was: cement, sand, and half of the water. After mixing, the sample was mechanically mixed for 3 min, then the expanded lightweight aggregate was added with water and homogenized for 4 min and, after a pause of approximately 3 min, molding was carried out. The bodies were molded in 2 layers and each layer received 12 strikes. After molding, the bodies were taken to a humid chamber and kept for 24 h. For each age, 6 bodies were tested, and part of them was also used for density and water absorption tests.

In the LC-AG, an apparent water/cement ratio of 0.80 was used. This high amount is justified because the EA

absorbs part of this water. According to ABNT NBR 12655 standard [30], the maximum water/cement weight ratio (w/c) is 0.65 for regular concrete. Therefore, there is the apparent w/c factor ($w/c_{ap}=0.8$) which deals with the direct relationship between water/cement, and the real w/c factor (w/c_{real}). This influences the concrete moldability and is mainly dictated by the absorption capacity of each EA and by the amount of water in its matrix (concrete mix): $w/c_{real} < w/c_{ap}$. The actual w/c factor or w/c_{real} of the LC-AG was 0.60, corrected after 24 h. This justified the utilization of an apparently high w/c factor when compared to regular concrete since 'excess' water was absorbed by the EA, which returned the water, a process called internal cure [10, 12, 13]. Table I shows the consumption of materials in mass and volume basis for 1 m³ of concrete. For the chosen mix, the cement consumption per m³ of the LC-AG did not obey the minimum recommendation for the production of structural lightweight concrete: 260 kg/m³ for aggressiveness class I. However, this concrete proved to be practical for general use, which was the purpose of this work.

Table I - Material consumption for 1 m³ of concrete in weight (kg per m³) and volume (dm³ per m³).

Parameter	Mix (weight)	LC-AG (kg/m ³)	LC-AG (dm ³ /m ³)
Cement	1.0	255	255 (kg)*
Sand	2.4	612	416
EA	1.6	408	680
w/c (apparent)	0.8	204	204

*: reference unit.

RESULTS AND DISCUSSION

Self-bloating clay (AGC)

Table II shows the chemical composition of clay from Arroio Grande-RS (AGC) and other clays used in other studies. The composition of clays for the production of expanded aggregates (EA) in Table II varies greatly: SiO₂ from 43.9% to 75.5%; Al₂O₃ from 8.5% to 15.74%; Fe₂O₃ from 3.3% to 10.3%; and CaO from 0.4% to 20.0%. There is no pattern of composition between the analyzed contents, including alkali oxides and alkaline earth oxides, which vary widely. In one of the clays (D in Table II), the SiO₂ and CaO contents are quite different from the others. The contents of flux oxides such as alkali, alkaline earth, and iron oxide play a significant role in the firing temperature of aggregates (and other ceramic products) at ~1250 °C. A parameter of the 'swelling potential' of the EA indicates the ratio of SiO₂/flux oxides (Fe₂O₃, Na₂O, K₂O, CaO, and MgO) [18, 35]. Based on this criterion, the results show that EA-AG had the highest ratio (9.5) when compared to other clays (Table II). This could mean a higher melting temperature for AGC. The SiO₂ content was high in AGC (Table II) due to the presence of quartz, as can be seen in Fig. 1.

Table II - Chemical composition (wt%) by XRF of Arroio Grande clay (AGC) and comparison with clays from other researches.

Oxide	AGC	A [13]	B [33]	C [34]	D [35]
SiO ₂	75.05	62.3	64.83	61.05	43.9
Al ₂ O ₃	10.95	17.7	15.05	15.74	8.5
Fe ₂ O ₃	3.55	10.3	7.45	6.10	3.3
Na ₂ O	0.98	0.3	1.10	5.62	0.2
K ₂ O	1.94	4.1	2.55	2.67	1.6
TiO ₂	0.64	1.0	0.63	0.00	0.4
CaO	0.59	0.4	2.98	3.92	20.0
MgO	0.83	2.8	3.67	2.52	2.1
Others	0.67	0.4	0.37	0.84	0.0
LOI	4.80	0.7	1.37	1.51	19.9
Total	100.00	100.00	100.00	100.03	100.10
SiO ₂ /ΣFlux	9.5	3.5	3.6	2.9	1.6



Figure 1: Image of AGC particles retained in the ABNT 200 mesh sieve, showing quartz particles with a vitreous shine.

The particle size distribution data of the AGC (as-received) are shown in Table III. Fine granulometry is one of the factors that explained the ease of molding when using AGC. In addition, it should be noted that the average particle diameter of AGC was one-half to one-third of the average diameter used in other studies [33] and much finer than clay

B in Table II. Therefore, the smaller particle diameter can compensate for the lower concentration of fluxes presented in Table II. As is well known, a smaller particle diameter means a larger surface area and, consequently, a much greater reactivity of a material [36]. An important characteristic of a clay to be used in the production of EA is its plasticity, which is fundamental to the forming process, normally done by extrusion/cutting or pelletizing in the industry. Table III presents good results for the characterization of the plastic limit (PL), liquid limit (LL), and plasticity index (PI). The quantification of the phases by XRD/Rietveld can be seen in Table III. The results indicated a significant amount of quartz, good content of montmorillonite, and the presence of albite and microcline.

In Fig. 2, it is possible to observe the mass loss up to ~160 °C, and, at this temperature, 4.5% of the mass of the AGC was lost, due to the loss of water adsorbed by the clay. The TGA curve had a small loss between 200 to 400 °C, when then there was an abrupt loss from 400 to 550 °C, due to organic matter oxidation and structural water loss, projecting a smoother loss from 550 to 900 °C, after which an almost stable slope was observed up to 1300 °C. The decomposition of organic material was accompanied by an exothermic peak and the decomposition of clay minerals by an endothermic peak in the DTA curve. The behavior in TGA/DTA was typical of clay firing.

Now the main factors for a clay to be used for the production of EA are discussed. The results of plasticity, particle size distribution, and analysis of crystalline phases (Table III) are fundamental parameters for the characterization of a clay for the production of EA. These properties can be related to the good characteristics of AGC in forming, drying, and firing. As stated, plasticity is fundamental for the forming of clay spheres. The presence of quartz in this clay facilitates its drying, as quartz has a low affinity with water and large quartz particles help the formation of a structure in the body and the development of an open porosity [37]. These three factors allow water to escape without damaging the body. The presence of alkali silicates counteracts the presence of quartz, which is a refractory phase, and lowers the firing temperature. Some works [18, 35] highlight three topics about the study of clays for EA production: a high proportion of phyllosilicates improves plasticity, but can favor the breakage (burst) of the aggregate during firing; higher firing temperatures are required for clays with high quartz content,

Table III - Results of tests of consistency, particle size distribution, and quantitative analysis of phases (XRD-Rietveld) of AGC.

Atterberg test (%)		Phase content (%)		Particle diameter (µm)	
Liquid limit (LL)	53.3	Quartz	55.68	Mean diameter	7.51
Plastic limit (PL)	22.1	Montmorillonite	20.94	D ₉₀	19.19
Plasticity index (PI)	33.2	Microcline	12.95	D ₅₀	4.48
		Albite	10.43	D ₁₀	0.86
		Total	100.00		

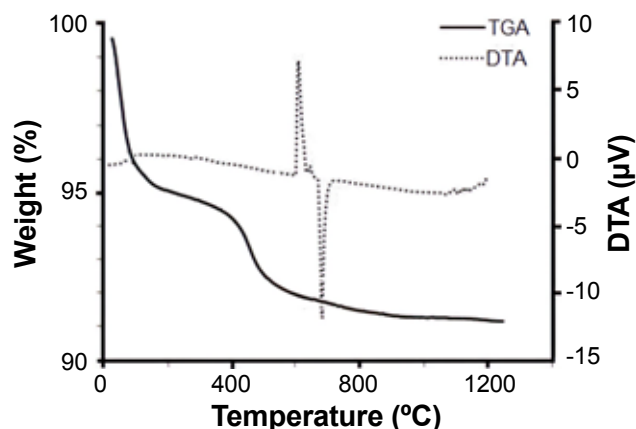


Figure 2: TGA and DTA curves of AGC.

high $\text{SiO}_2/\Sigma\text{Flux}$ ratio, and low MgO content; and a high iron content promotes the expansion (swelling) of the aggregate due to the decomposition of ferric oxide and formation of a gas phase at high temperature ($\text{Fe}_2\text{O}_3 \rightarrow 2\text{FeO} + \frac{1}{2}\text{O}_2$). According to Moreno-Maroto et al. [38], values from 0.2% to 1% of Fe_2O_3 contribute to an increase in the expansion of the aggregate.

The temperature/viscosity relationship is a more important factor than a gas generation for EA expansion [38]. Therefore, the presence of organic material and carbonates, or other compounds that generate gases in the firing, does not affect the expansion, when these compounds decompose in the initial heating phase of the aggregate (until $\sim 900^\circ\text{C}$). The increase in temperature leads to higher gas pressure within the closed pores and this gas pressure is responsible for the increase in the pore size and the expansion of the body's volume. The macroscopic effect of expansion or 'swelling' is strongly dependent on the viscosity and surface tension of the vitreous phase [39]. Accordingly, the characterization analysis showed that the chosen clay has a good potential to be used in the production of EA. Basically, AGC has a good proportion of flux oxides ($\text{Na}_2\text{O} + \text{K}_2\text{O} + \text{Fe}_2\text{O}_3 + \text{CaO} + \text{MgO} = \sim 8\%$), is fine ($10\% < \sim 1\ \mu\text{m}$), and has good plasticity (high plasticity index and presence of a phase such as montmorillonite). The composition of AGC is quite different from other clays studied by other authors, e.g., the study of nine European clays [35] and the clays mentioned in Table II. The chemical composition of AGC is outside the zone recommended by the Riley diagram and the bloating index ($\text{SiO}_2/\Sigma\text{Flux}$ ratio) is much higher than the clays mentioned in Table II, which could indicate a very refractory clay. However, as previously stated in the literature, both the Riley diagram and the bloating index are indicative only [35]. As a differential, AGC has a high content of montmorillonite, a high content of quartz, and fine granulometry, which allow an easy evaluation of these three factors.

It should be noted that a chemical composition rich in fluxes, quartz, fine particle size and the presence of phases that promote plasticity are desirable characteristics in clay for the production of expanded aggregates. Nevertheless, in general, to be used as raw material for the production

of EA, a clay must necessarily have good plasticity. Fluxes and particle size must be studied in relation to the firing temperature so that the composition can be adjusted according to the desired temperature. The study of the quartz/phyllsilicates content ratio must also be considered to avoid excessive flaws in drying and breakage (burst) of aggregates in firing. Therefore, the characterization of AGC shows that an ideal composition for EA production comes from the balance between the content of clay minerals (which provide plasticity), alkali silicates (which provide the flux), quartz (which provides the structural strength in drying and firing), hematite (helps in body expansion) and fine particle size. Certainly, these characteristics when not found in a single clay can be achieved through different clay mixtures (a blended mix). Alternatively, the characteristics of natural clay (run of mine), for example, with a high firing temperature, can be improved by processing the clay, such as milling and/or classifying by sieving. Accordingly, the firing behavior and the bloating behavior are strongly dependent on the composition and the finer grain size fraction of a clay. It is expected that the information presented here will increase the number of clays (and deposits) that can be used for the production of expanded clay aggregates. This information can help increase EA production and LC usage around the world.

Expanded-clay aggregate

Expansion behavior, morphology, and granulometry of aggregates: EA-AG showed an average expansion of 415% from its volume before firing. This result was compatible with expandable clays of excellent quality, for example, in the work of Ozguven and Gunduz [40]. Other authors point out that EA can expand up to 7 times its initial volume [13, 41]. It is important to point out that in the preparation of the EA-AG, no pyro-expansive additives were used, as is added in the production of the AAE-1506 [25]. Aluminum slag, vermiculite, and silicon carbide are additives employed in other works [42, 43]. Fig. 3 shows the morphology of the EA-AG after firing, compared to the AAE-1506, both fired at 1250°C . However, in this analysis, it should be

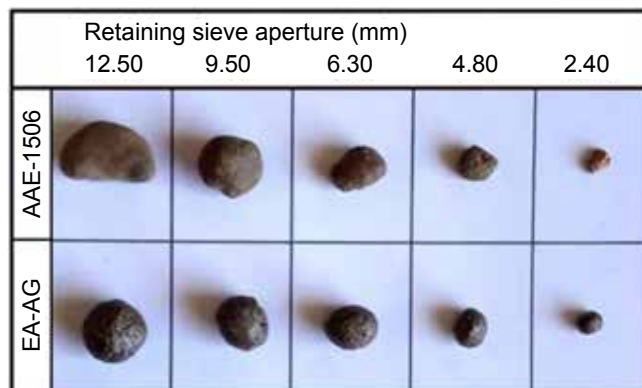


Figure 3: Images of aggregates comparing the AAE-1506 and EA-AG morphology after firing, according to the aperture of the retaining sieve.

noted that the production and firing processes are different; the AAE-1506 was extruded and made in industrial rotary kilns, whereas the EA-AG was manually formed and fired in a laboratory furnace. The sphericity of the AAE-1506 is markedly smaller. In such a manner, the properties of clays and, mainly, the differences presented between the raw aggregates justify the properties achieved, which are described later.

In the firing of clay spheres (aggregates), the increase in temperature initially promotes the decomposition of organic compounds and the transformation of minerals (loss of structural water, calcination of carbonates, etc.). Then, there is the softening of the siliceous phases, forming the liquid phase or vitreous phase. This phenomenon is well known in the so-called liquid phase sintering of ceramic products [14, 44]. The viscous flow fills the porosity and takes the particles together by capillary effect, which leads to retraction at the beginning of the firing. The viscous flow mechanism is strongly dependent on the viscosity and surface tension of the glass phase and on the firing temperature and clay composition. In the final stage of firing, the air is trapped inside the closed porosity in the vitreous phase, while the increase in temperature promotes an increase in pressure inside the pores. At the same time, the reduction in viscosity (and surface tension) at higher temperatures facilitates the growth of pore size and volume expansion of the body (aggregate). In the industrial process, after the firing process, the temperature is reduced to 300 °C in a matter of minutes [35]. In the laboratory, the cooling time was ~12 h. Therefore, many differences are expected in aggregates when produced industrially or in the laboratory, due to differences in forming and firing. These differences explain the distinct characteristics seen in Fig. 3. In addition to the more spherical morphology, the EA-AG had some small cavities on the surface. The 'potato' shape of AAE-1506 is a consequence of the kiln's circular movement [45].

In Fig. 4, a cross-section area of the EAs is shown. It is observed that the AAE-1506 had visible pores, but a clear color differentiation between the external surface and the internal volume (due to low oxygen content in industrial firing), and presented a more homogeneous internal appearance, with a higher number of micropores. The EA-AG, on the other hand, had rough nodulation, with the depth of the superficial cavities or concavities in the order of 0.5 mm. There was also a higher presence of quartz grains (Q) and the number of pores (P) was lower, but the pore size was larger, compared to AAE-1506. The XRD pattern of the fired aggregate (Fig. 5) showed a low peak count with a predominance of quartz and amorphous phase. This analysis confirmed that the firing of the aggregate was adequate since there was no (significant) presence of the albite and microcline phases (Table III) that contributed to the formation of the glassy phase. As previously mentioned, the high silica content in the AGC did not prevent a good firing of the aggregate.

Water absorption and absorption ratio of aggregates: Table IV shows the water absorption and the absorption

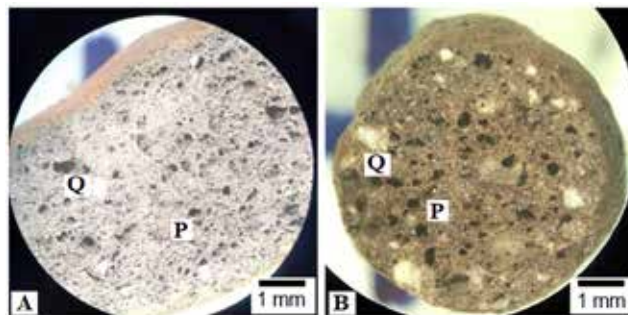


Figure 4: Optical micrographs of the cross-section of aggregates after firing at 1250 °C: a) AAE-1506; and b) EA-AG. P: pore; Q: quartz.

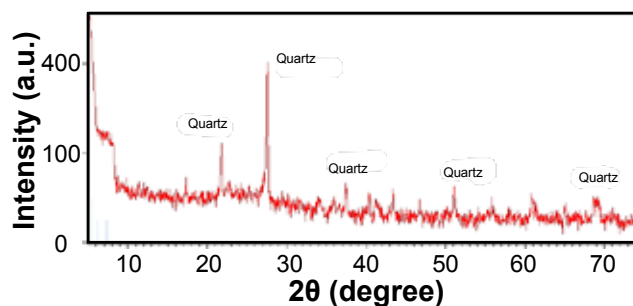


Figure 5: XRD pattern of EA-AG.

ratio of the aggregates. These data are important to evaluate the quality of the aggregate, which can influence the performance of the concrete when in contact with the cement paste. EA absorption depends on the outer shell characteristics of the EA, which are determined by the clay chemical composition and the firing conditions. Increasing the firing temperature by 50 °C reduced the water absorption of the EA after 72 h of immersion in water from 12.7% (1250 °C) to 4.2% (1300 °C) [46]. Water absorption data show the capacity that aggregates have to absorb water from the system. Water is needed for concrete curing and molding and must be carefully balanced. The absorption capacity is an important parameter for the corrections in the mix, which is not necessary with rocky aggregates (gravel), which practically do not absorb water.

An excessive amount of water absorption by the aggregates directly influences the rationalized dosage and affects the consistency of the concrete. This fact requires two possible solutions: i) preceding pre-humidification (saturation) of the EA, or ii) an increase in the w/c (water/cement) factor, taking into account that part of the dosage water is absorbed by the aggregate during the preparation of the concrete. The second option was adopted in this study, but some authors recommend previous humidification when the EA absorption is higher than 15% [10, 12]. Although the concrete production process and its mixing, transport, and casting cycle may vary, the entire cycle tends to be less than 5 h. Table IV shows that the WA of the EA-AG was lower than the absorption of the AAE-1506, but both had an absorption well below the aforementioned 15% limit in the 5 h preparation time. It is noteworthy that, in the period

Table IV - EA water absorption, WA (%), and water absorption ratio, WAR (%), as a function of immersion time.

Aggregate		1 h	3 h	5 h	24 h	72 h
EA-AG	WA	4.1±1.1	5.5±0.9	7.7±0.4	12.5±0.3	12.7±0.3
	WAR	32	43	62	98	100
AAE-1506	WA	8.1±1.8	9.9±1.4	11.0±0.9	18.8±0.3	18.8±0.4
	WAR	43	52	59	100	100

of 24 h and even in 72 h, the EA-AG remained below the limit, unlike what occurred with the AAE-1506. As for the water absorption ratio, an important factor to establish work strategies in the production of lightweight concrete, it was observed that, for the period of 5 h, the two EA had practically the same ratio, 62% and 59% for the EA-AG and the AAE-1506, respectively (Table IV). It is possible to conclude that although Fig. 3 presents superficial cavities or concavities in the EA-AG, these, for the most part, do not present connectivity with the interior of the aggregate, since the absorption of the EA-AG was lower than the absorption of the AAE-1506 (Table IV). Table V presents the results of studies performed by some authors with EA after an immersion period of 24 h. Note that the EA-AG had the lowest WA (12.5%). This demonstrated that, in laboratory firing, the AGC provided the EA-AG with a good firing temperature (1250 °C) that was expected, according to the previous chemical and physical characterization of the clay (AGC).

Table V - Water absorption, WA (%), of EA-AG and aggregates from other authors after 24 h of immersion.

EA-AG	E [47]	F [48]	G [8]	H [49]
12.5±0.3	15.00	18.20	16.20	16.42

Density and mechanical strength of aggregates: the results of density analysis and its relationship with mechanical strength are shown in Table VI. The AAE-1506 presented a compressive strength of 1.21 MPa and a density of 1.10 kg/dm³. The EA-AG showed a lower compressive strength (0.80 MPa). This was predictable since its density was 0.85 kg/dm³. Therefore, EA-AG had a higher porosity, and possibly, larger pores as the critical crack, as shown in Fig. 4. The EA-AG loses in strength but gains in terms of lightness, compared to AAE-1506. The UNE-EN-13055-1 standard [50] establishes that the EA must have a density ≤1.2 g/cm³. Both studied aggregates met this directive. On the other hand, the EA-AG had the potential to achieve higher mechanical strength, as it could be fired at a different time

Table VI - Compressive strength and density of EAs.

EA	Strength (MPa)	Density (kg/dm ³)
EA-AG	0.80±0.02	0.85±0.04
AAE-1506	1.21±0.05	1.10±0.11

and/or temperature and remain within the specified density limit, considering that this would reduce porosity and pore size.

Lightweight concrete

Water absorption, density, and compressive strength: the results of these properties for the concrete formulated with EA-AG are shown in Table VII. Water absorption of the LC-AG bodies after immersion for 24 and 72 h was 4.76% and 5.42%, respectively. Concrete absorption is an important criterion for investigating the durability of concrete when exposed to weather and constant humidification flows. It is known that the control of open porosity is important for the production of more durable concrete against bad weather, avoiding, among other pathologies, efflorescence [41]. In general, EA has a higher open porosity than gravel aggregates, and this can lead to higher absorption of water and can increase chloride penetration in the concrete [45]. One of the most restrictive criteria, regarding the WA, cited in the NBR 6136 standard [51] for the production of concrete blocks, considers that WA must be lower than 10%. In this case, the LC-AG complies with this guideline, presenting good quality, and can be used for the production of this type of artifact. As can be seen in Table VII, LC-AG can be considered a good lightweight concrete, since its density is well below 2.00 kg/dm³ [11]. It is important to point out that, unlike regular concrete, the main characteristic of LC is not its strength, but its lightness. However, good strength benefits the design, from installation to the final structure. At the same time, LC with expanded-clay aggregates have qualities typical of this type of aggregate, such as chemical resistance and fire resistance, providing a much higher mechanical strength than lightweight concrete with polymer, such as expanded polystyrene (EPS) [12].

Table VII - Water absorption (after 24 and 72 h of immersion), compressive strength, and density of LC-AG.

WA _{24h} (%)	WA _{72h} (%)	Strength (MPa)	Density (kg/dm ³)
4.76±0.23	5.42±0.07	12.5±0.4	1.48±0.07

Fig. 6 shows the cross-section area of the body produced with the LC-AG, presenting the interaction between the EA-AG and the mortar. It is possible to observe the penetration of the mortar in the porosity of the EA-AG, promoting a good

anchorage in the aggregate-mortar interaction zone. Some authors emphasize that the characteristics of the interaction zone must always be observed for the study of stress gradient distribution, since this region may have the lowest strength in concrete. This is because lightweight concretes (with clay aggregates) tend to be weaker when compared to regular concrete [12, 17, 41]. In an LC, the failure (crack path) occurs mainly in the aggregate-mortar neighborhood, and

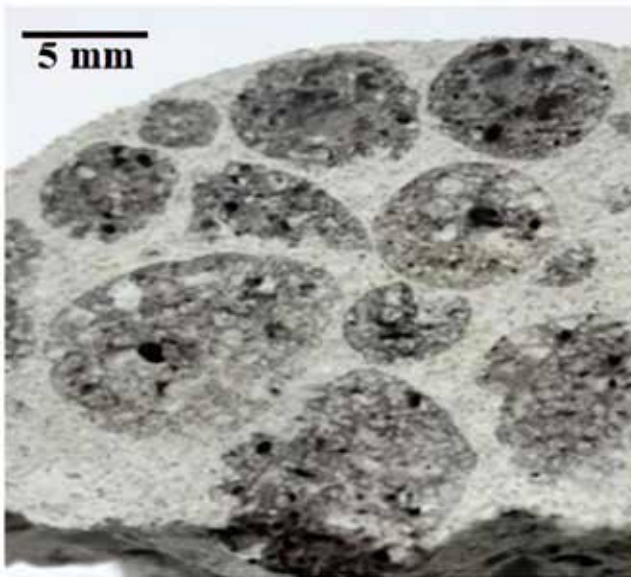


Figure 6: Optical micrograph of the cross-section of the LC-AG body, showing the interaction between the EA and the mortar. At the bottom, the crack path through an aggregate.

sometimes the aggregate breaks, as can be seen in Fig. 6 and stated by Rossignolo [13]. It is worth noting that in a recent work by the authors [46], the production of EA at a higher firing temperature led to an increase in the expansion of the aggregate, with a consequent decrease in its mechanical strength. The lower strength of the EA led, in turn, to the production of LC with lower mechanical strength [46].

In the SEM micrographs of Fig. 7, it is possible to observe the difference in texture between aggregate and mortar phases, whose interface is quite clear. There are no significant defects in the interface region, such as pores or macrocracks, as seen in Fig. 6. However, it is possible to observe some discontinuity when observing the entire segment of the interface 'line' (Fig. 7a). Thus, the fracture path can follow the interface line, the matrix or even break the aggregate (Fig. 6). SEM micrograph with results of chemical analysis by EDS (energy dispersive spectroscopy) in Fig. 7b shows the difference in composition between mortar and aggregate, highlighting a higher calcium content of the mortar.

Table VIII shows the increase in the mechanical strength of the LC-AG at the ages of 3, 7, and 28 days. Note that, on the third day, the LC-AG reached 57% of its total strength; the value was high enough for the handling and application of concrete artifacts. The importance of relative strength is not only in the control and progress of cement hydration but in the use of this concrete at earlier ages. Thus, changing gravel aggregate to the EA-AG in the production of LC-AG does not change the behavior in the curing process.

Table IX presents the characteristics of the LC-AG

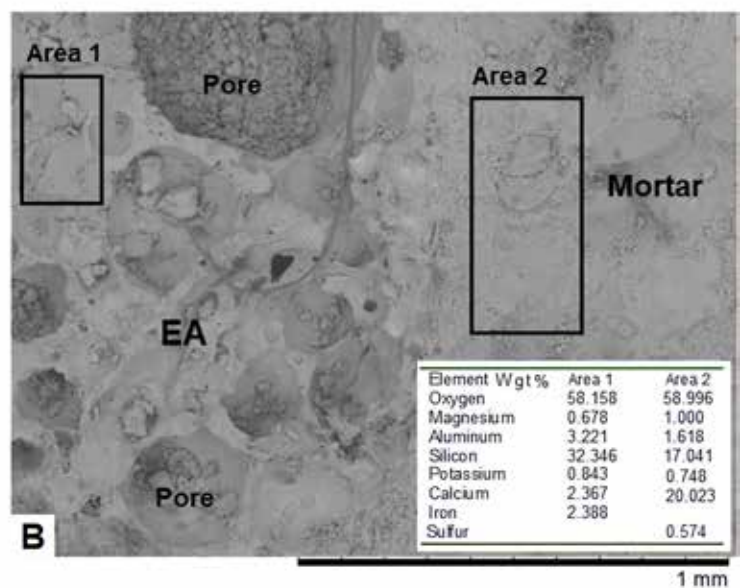
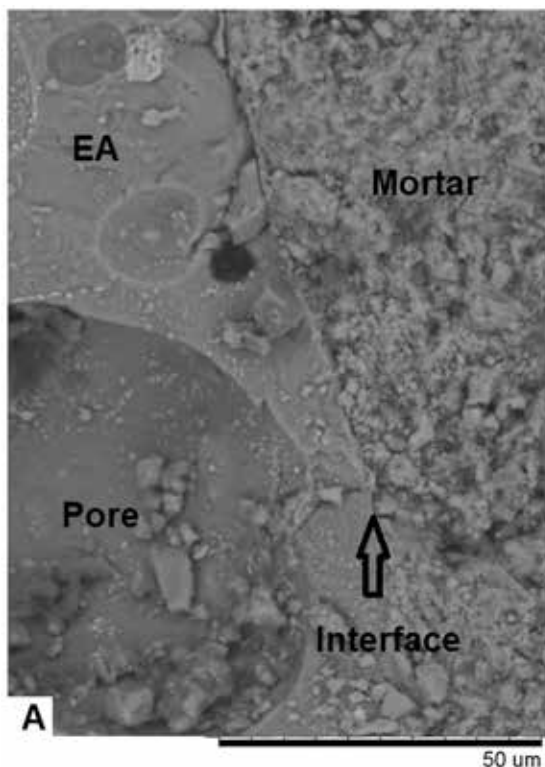


Figure 7: SEM micrographs of the cross-section of LC-AG body: a) interface between the EA and the mortar; and b) results of EDS of indicated areas showing higher Ca content in the mortar.

Table VIII - Compressive strength and relative strength as a function of LC-AG concrete age.

Property	3 days	7 days	28 days
Strength (MPa)	7.1±1.4	9.5±0.9	12.5±0.3
Rel. strength (%)	57	76	100

compared to other LCs produced by other authors that utilize expanded-clay aggregate. In order for the comparisons to be closer, LCs with relatively close densities were sought. The densities between the LCs ranged from 1.46 to 1.73 kg/dm³. However, some restrictions must be considered in a direct comparison of values. For example, it was observed that many authors use different times and methods of the contribution of water absorption from the aggregate when mixing water is added to produce LC, which makes it difficult to compare the results, as already stated in the literature [13]. Another issue is that some compositions take additives and/or additions and others do not, and the amount of cement is variable. LC-AG presented values close to the mean values of density and water absorption of the other authors, which were 1.56 kg/dm³ and 3.67%, respectively (Table IX), although LC-AG density was lower (1.48 kg/dm³) and the absorption was higher (4.76%). In addition, the strength of the LC-AG (12.5 MPa) was considerably lower than the average (24.7 MPa). In Table IX, it is observed that the cement quantity added in the LC-AG was much smaller than the amount added in the others LCs and, at the same time, the LC-AG formulation did not use additives/additions. LC-AG water absorption was higher, as mentioned. These three factors perfectly explain the difference in the LC-AG strength. On the other hand, the LC-AG achieved its production purpose, which was the development of lightweight concrete with low density, strength higher than that required by the standards, and low cement content. As it is well known, the production of cement (clinker) generates a high amount of greenhouse gases. Furthermore, the reduction of cement also means a lower cost of the LC.

The study carried out by Rodrigues [32], using the

Cinexpan aggregate, presented some data similar to those found with the LC-AG. This comparison is interesting since no additives or additions were used in both LCs. However, the cement consumption per m³ was higher (286 kg) when compared to the LC-AG, and, therefore, the water absorption was lower; this result justifies a higher strength of 20.92 MPa achieved in Rodrigues' work. It can be highlighted in Table IX that in some studies the formulated concrete was prepared with high consumption of cement and, at the same time, with the utilization of additives and additions. For example, in the studies by Rossignolo [13] and Lotfy et al. [8], the authors obtained a strength, respectively, of 39.5 and 37.6 MPa, which are values of a structural LC. In general, in Table IX, it is observed that as the amount of cement and the cement/aggregate ratio increases, the higher the strength. The methodologies showed that for the development of lightweight high-performance concrete, there would naturally be a significant cost in cement, just as it occurs in normal concrete. The development and use of lightweight concrete can significantly increase in the world, and this would contribute to the design of lighter structures, with savings on cement (and steel), consequently, lower generation of greenhouse gases. The information presented here can help to promote the use of EA and LC around the world and is especially important in Brazil, where there is only one EA manufacturer, which makes the cost of long-distance transport for the use of LC unfeasible.

CONCLUSIONS

The clay (AGC) analyzed in the present work showed good qualities for the production of expanded-clay aggregates (EA). This clay had: good plasticity, due to the presence of mineral phases that provided plasticity (montmorillonite) and fine granulometry; a considerable amount of quartz, which is an important phase to avoid excessive flaws in drying and breakage (burst) of aggregates in firing; and a suitable amount of fluxes and ferric oxide for firing at temperatures similar to those used in other studies with a significant

Table IX - Comparison of characteristics of LC-AG and LCs produced by other authors.

Parameter	LC-AG	I [32]	J [52]	K [53]	L [31]	M [54]	N [8]	O [13]
Density (kg/dm ³)	1.48	1.52	1.73	1.65	1.49	1.62	1.47	1.46
Strength (MPa)	12.5	20.92	7.37	31.6 [#]	17.7	17.9	37.6	39.5
Water absorption (%)	4.76	3.43	3.4	-	-	2.51	4.29	4.7
Cement (kg/m ³)	255	286	320	426	199	315 ^{&}	416	440
Additives	No	No	No	No	Yes	Yes	Yes	Yes
Additions	No	No	No	No	No	Yes	Yes	Yes
Cement/EA ratio	0.25	0.25	0.24	0.37	0.20	0.38	0.47	0.53
Concrete mix (c:s:EA:w/c)	1:2.4:1.6:0.8	1:2.4:1.6:0.8	1:3.17:0.95:0.65	1:1.82:0.87:0.45	1:3.0:2.0:0.96 [*]	1:2.11:0.53:0.46	1:1.18:0.97:0.44	1:0.57:1.32:0.60

Notes: additives: plasticizers, superplasticizers, set accelerators, air-entraining agent, microsilica, etc.; additions: blast furnace slag, silica fume, metakaolin, etc.; concrete mix in weight basis: c-cement, s-sand, EA-expanded-clay aggregate, w/c-water/cement ratio; #: at 90 days; *: additive was included in the mix; &: cement consumption calculated indirectly.

expansion of the EA. Therefore, the characterization of AGC showed an ‘ideal composition’ of a self-bloating clay for EA production, i.e. the ability to yield lightweight aggregates without the need for pyro-expansive additives. The produced aggregate (EA-AG) presented an expansion of 415 vol%. The AGC bloating index ($\text{SiO}_2/\Sigma\text{Flux}=9$) was relatively (too) high, due to the high silica (quartz) content, and did not reflect the high expansion presented by the EA-AG. As the EA-AG presented a significant amount of residual quartz (part of the quartz present in the coarse fraction of the clay did not dissolve in firing), as seen in its microstructure and in the X-ray diffraction pattern, it can be inferred that the expansion of a clay aggregate depends mainly on the amount and composition of the finer fraction of clay, in addition to the firing conditions. Thus, ideally, a correction factor that considers the particle diameter should be added to the bloating index. The lightweight concrete (LC-AG) prepared with EA-AG was lighter than LCs produced in the studies by other authors, which showed higher strength than LC-AG. However, these concretes were produced with the use of additives/additions and/or much higher amounts of cement, since many works aimed at the production of a structural LC. The amount of cement was considered the key factor in determining the strength of concrete when comparing the results from several studies; a comparative and accurate analysis depends on the same dosage of the components. The increase in the strength of LC-AG depends on a higher amount of cement, that is, its formulation did not reach the peak of strength in relation to the increase in cement. LC-AG showed good properties, in terms of water absorption, density, and mechanical strength, with better values compared to those recommended by the technical standards for non-structural lightweight concrete. LC-AG has, potentially, many applications, such as concrete artifacts, non-structural blocks, void filling, and in thermal and acoustic insulation applications. It has the typical advantages of an LC with expanded-clay aggregates (chemical inertness and fireproof) and with higher strength than commercial lightweight concrete with polymeric aggregates.

ACKNOWLEDGMENTS

We thank Cinexpan for donating the clay aggregates. We thank Geol. J. Pedrassani for selecting and donating AG clay. We acknowledge Eng. Carlos Alberto Pereira from Cinexpan for valuable information. We thank CNPq and CAPES for Adalberto’s scholarship and research funding.

REFERENCES

- [1] A.I. Fares, K.M.A. Sohel, K. Al-Jabri, A. Al-Mamun, *Constr. Build. Mater.* **294**, 2 (2021) 123552.
- [2] P. Ren, T.-C. Ling, K.H. Mo, *J. Clean. Prod.* **291** (2021) 125215.
- [3] B. Monalisa, S.K. Bhattacharyya, A.K. Minocha, R. Deoliya, S. Maiti, *Constr. Build. Mater.* **68** (2014) 501.
- [4] J. Brito, R. Kurda, *J. Clean. Prod.* **281** (2021) 123558.
- [5] A.A. Bahsandy, F.M. Eid, E.H. Abdou, *J. Constr. Eng. Manag.* **6**, 2 (2017) 35.
- [6] M. Gesoglu, E. Güneyisi, H.O. Oz, in *Int. Conf. Solid Waste Technol. Manag.*, Philadelphia (2012) 609.
- [7] ABNT, NBR 15575, “Edificações habitacionais: desempenho”, Ass. Bras. Normas Técn., S. Paulo (2013).
- [8] A. Lotfy, Khandaker, K.M.A. Hossain. M. Lachemi, *Constr. Build. Mater.* **106** (2016) 43.
- [9] A.A. Abouhussien, A.A.A. Hassan, M.K. Ismail, *Constr. Build. Mater.* **75** (2015) 63.
- [10] S. Chandra, L. Berntsson, *Lightweight aggregate concrete: science technology and applications*, Elsevier (2002).
- [11] ABNT, NBR 8953, “Concreto para fins estruturais: classificação pela massa específica, por grupo de resistência e consistência”, Ass. Bras. Normas Técn., S. Paulo (2015).
- [12] A.M. Neville, J.J. Brooks, *Tecnologia do concreto*, Bookman, Porto Alegre (2013).
- [13] J.A. Rossignolo, *Concreto leve estrutural: produção, propriedades, microestrutura e aplicações*, Pini (2009).
- [14] M.S. Nadesan, P. Dinakar, *Constr. Build. Mater.* **154** (2017) 928.
- [15] L. Huang, Z. Yang, Z. Li, Y. Xu, L. Yu, *J. Clean. Prod.* **275** (2020) 123099.
- [16] ANICER, “Relat. anual 2020”, Ass. Nac. Produt. Cerâm. (2021).
- [17] B.C. Santis, E.P. Sichiari, J.A. Rossignolo, G. Ferreira, J. Fiorelli, *Cerâmica* **59**, 350 (2013) 198.
- [18] B. Ayati, V. Ferrándiz-Mas, D. Newport, C. Cheeseman, *Constr. Build. Mater.* **162** (2018) 124.
- [19] M. Loutou, M. Hajjaji, *Appl. Clay Sci.* **150** (2017) 56.
- [20] A.P. Fantilli, A.D. Cavallo, G. Pistone, *Eng. Struct.* **99** (2015) 184.
- [21] F.C. Mamede, M.R.S. Corrêa, M.A. Ramalho, in VII Int. Sem. Struct. Masonry Develo. Countr., CEFET, Belo Horizonte (2002).
- [22] SNIC, “Relat. 2019/2020”, Sind. Nac. Ind. Cimento (2021).
- [23] ABNT, NBR 6459, “Determinação do limite de liquidez”, Ass. Bras. Normas Técn., S. Paulo (2016).
- [24] ABNT, NBR 7180, “Determinação do limite de plasticidade”, Ass. Bras. Normas Técn., S. Paulo (2016).
- [25] Cinexpan, Catálogo, www.cinexpan.com.br, ac. 26/08/2021.
- [26] ABNT, NBR NM 248, “Agregados: determinação da composição granulométrica”, Ass. Bras. Normas Técn., S. Paulo (2003).
- [27] ABNT, NBR 5739, “Ensaio de compressão de corpos de prova cilíndricos”, Ass. Bras. Normas Técn., S. Paulo (2018).
- [28] ABNT, NBR 7211, “Agregados para concreto: especificações”, Ass. Bras. Normas Técn., S. Paulo (2009).
- [29] ABNT, NBR NM 53, “Agregado graúdo: determinação da massa específica, massa aparente e absorção de água”, Ass. Bras. Normas Técn., S. Paulo (2009).
- [30] ABNT, NBR 12655, “Concreto de cimento Portland:

- preparo, controle, recebimento e aceitação: procedimento”, Ass. Bras. Normas Técn., S. Paulo (2015).
- [31] J. Maycá, in 51th Congr. Bras. Concreto, IBRACON, S. Paulo (2009).
- [32] A.V. Rodrigues, “Application of expanded clay from a deposit in Rio Grande do Sul in lightweight concrete and structural lightweight concrete”, M.Sc. thesis, Fed. Univ. Rio Grande Sul (2018).
- [33] M. Zendezhaban, S. Sharifnia, N.H. Seyed, Korean J. Chem. Eng. **30**, 3 (2013) 574.
- [34] M.S. Islam, S. Nahid, M. Moniruzzaman, U.S. Akhtar, Int. J. Sci. Eng. Res. **7**, 4 (2016) 149.
- [35] J.M. Moreno-Maroto, M.U. Rodríguez, C.J.C. Ceacero, T.C. Palomino, C.M. García, J.A. Azcárate, Constr. Build. Mater. **237** (2020) 117583.
- [36] J. Reed, *Principles of ceramic processing*, 2nd ed., Wiley-Intersci., New York (1995).
- [37] A. Barba, V. Beltrán, C. Felú, J. Garcia, F. Ginés, E. Sánchez, V. Sanz, *Materias primas para la fabricación de soportes de baldosas cerámicas*, 2nd ed., Inst. Tecnol. Cerám., Castellón (2002).
- [38] J.M. Moreno-Maroto, C.J.C. Ceacero, M.U. Rodríguez, T.C. Palomino, C.M. García, C. Javier, J.A. Azcárate, Constr. Build. Mater. **247** (2020) 1.
- [39] W.M. Carty, Ceram. Eng. Sci. Proc. **23**, 2 (2002) 79.
- [40] A. Ozguven, L. Gunduz, Cem. Concr. Compos. **34** (2012) 781.
- [41] P.K. Mehta, P.J.M. Monteiro, *Concrete: microstructure, properties and materials*, IBRACON, S. Paulo (2008).
- [42] S.Y. Chung, M.A. Elrahman, D. Stephan, P.H. Kamm, Constr. Build. Mater. **189** (2018) 314.
- [43] M. Dondi, P. Cappelletti, M. D’Amore, R. de Gennaro, S.F. Graziano, A. Langella, M. Raimondo, C. Zanelli, Constr. Build. Mater. **127** (2016) 394.
- [44] M.N. Rahaman, *Sintering of ceramics*, CRC Press, Boca Raton (2007).
- [45] A.M. Rashad, Constr. Build. Mater. **170** (2018) 757.
- [46] A.V. Rodrigues, S.R. Bragança, Bol. Soc. Esp. Ceram. V. **62** (2023) 56.
- [47] Q.A.H. Ateeq, P.D. Maneeth, S. Brijbhushan, Int. J. Innov. Technol. Explor. Eng. **9** (2020) 323.
- [48] K. Heiza, F. Eid, T. Masoud, MATEC Web Conf. **162** (2018) 2031.
- [49] A. Kumar, P. Prakash, Int. Adv. Res. J. Sci. Eng. Technol. **2** (2015) 64.
- [50] UNE-EN13055-1, “Lightweight aggregates for concrete, mortar and grout”, Eur. Stand. (2016).
- [51] ABNT, NBR 6136, “Blocos vazados de concreto simples para alvenaria: requisitos”, Ass. Bras. Normas Técn., S. Paulo (2014).
- [52] C.B. Garcia, A. Hurtado, Y.F. Silva, S. Delvasto, A. Gerardo, Constr. Build. Mater. **273** (2021) 121677.
- [53] G. Roufael, A. Beaucour, J. Eslami, D. Hoxha, A. Noumowé, Constr. Build. Mater. **268** (2021) 12122.
- [54] G.S. Araújo, L.C. Iwamoto, R.C.C. Lintz, L.A. Gachet, Mater. J. **118**, 1 (2021) 79.
- (Rec. 14/01/2022, Rev. 27/05/2022, 11/10/2022, Ac. 17/10/2022)



Impact of fuel quantity on luminescence properties of $\text{Sr}_3\text{Al}_2\text{O}_6:\text{Eu}$ by combustion synthesis

W. T. Barbosa^{1,2*}, C. M. Álvarez-Docio³, R. Garcia-Carrodeguas⁴, M. V. L. Fook²,
M. A. Rodríguez³, R. E. Rojas-Hernandez⁵

¹University Center SENAI CIMATEC, Salvador, BA, Brazil

²Federal University of Campina Grande, Academic Unit of Materials Engineering, Campina Grande, PB, Brazil

³Instituto de Cerámica y Vidrio, Madrid, Spain

⁴Noricum S.L., Madrid, Spain

⁵Tallinn University of Technology, Department of Mechanical and Industrial Engineering, Tallinn, Estonia

Abstract

The photoluminescent behavior of Eu-doped $\text{Sr}_3\text{Al}_2\text{O}_6$ obtained by highly efficient solution combustion synthesis is reported. In order to understand the influence of the fuel on the synthesis, the stoichiometric quantity and an excess of fuel were evaluated. By adjusting the amount of fuel, different luminescence responses were obtained, allowing europium cations incorporation into the $\text{Sr}_3\text{Al}_2\text{O}_6$ lattice to serve as effective luminescence activators in such a short time during the rapid combustion synthesis process. The higher amount of fuel in the presence of the oxidizing agent produced $\text{Sr}_3\text{Al}_2\text{O}_6:\text{Eu}$ particles with higher phosphorescence brightness, owing to the increase of the reduction process from Eu^{3+} to Eu^{2+} . The synthesized phosphor showed an intense band emission centered at 515 nm and could be excited over a broad spectral range in the UV-visible region. Particles having nanostructured flake-type morphology were obtained, which was considered a micro-nanofunctional candidate for practical applications.

Keywords: combustion, aluminate, luminescence.

INTRODUCTION


Phosphors are materials that have the ability to absorb high energy (short wavelength) and down-convert them into lower energy (longer wavelength) [1]. Usually, phosphors are composed of two parts, one part is the lattice and another part is an activator or dopant. Activator ions are the chief luminescent center of the host lattice [2, 3]. The commonly used activators are $\text{Eu}^{3+}/\text{Eu}^{2+}$, Ce^{3+} , Tb^{3+} , Gd^{3+} , Yb^{3+} , Dy^{3+} , Sm^{3+} , Tm^{3+} , Er^{3+} , Nd^{3+} , etc. [4]. The luminescence properties of Eu^{2+} -doped strontium aluminates have been widely studied since it has good luminescent properties such as high initial luminescent intensity, long afterglow, good stability, and can reveal broad-band emission because of the electronic transitions between the fundamental state of $4f^7$ and the excited state of $4f^65d^1$ [5, 6]. The rare earth ions act as luminescent centers in strontium aluminates host [7]; these phosphors are known as efficient green and blue emitters, and for their long-persistent luminescence [8].

The undoped $\text{Sr}_3\text{Al}_2\text{O}_6$ material does not show any luminescence but the emission spectra of europium-doped material show luminescence in the wavelength range from 580 to 620 nm. The $\text{Sr}_3\text{Al}_2\text{O}_6:\text{Eu}^{2+}$ phosphor shows green emission peaking at 538 nm excited at 377 nm with an additional broad band at a longer wavelength. Under lower energy excitation the red emission centered at 625 nm

can be observed. Clearly, multiple emission bands/colors can be observed depending on the excitation wavelength. According to structural data, six different strontium sites exist in $\text{Sr}_3\text{Al}_2\text{O}_6$. Therefore, one can expect that substitution of Sr^{2+} sites by Eu^{2+} ions should lead to six different types of luminescent Eu^{2+} centers. The $\text{Sr}_3\text{Al}_2\text{O}_6:\text{Eu}^{3+}$ phosphor exhibits narrow emission at 580, 592, 595, 613, and 617 nm instead of characteristic 520 nm emission which is the case for divalent europium [6, 9]. The duration of the photoluminescence from a phosphor is affected by a number of parameters such as the type and amount of activators or dopants, the structure of the host lattice, the method of preparation or growth conditions, the particle size and other post-treatments. These parameters play a significant role in inducing a crystal field effect within the host matrix which in turn influences the emission wavelength, intensity, and lifetime [10].

Strontium aluminate can be synthesized by different techniques, such as sol-gel, solid-state, hydrothermal, and combustion methods [11]. Some of these routes require a multi-step process and long calcination treatments at high temperatures to prepare crystalline materials [12] and their heterogeneity is inevitable [13], in addition to a low surface area [14]. Commonly, for large-scale production of luminescent powders, the conventional solid-state reaction process is used [15]. However, this process has the disadvantages previously reported. Currently, solution combustion is being considered a promising approach due to its several advantages, providing a nanostructured powder with high purity, better homogeneity, and high surface area

*willamsteles@yahoo.com.br

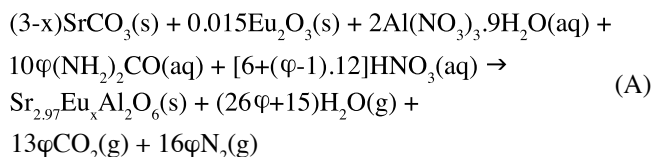
 <https://orcid.org/0000-0002-3019-3195>

in a rapid, inexpensive single-step operation; the materials obtained by this route can be used in different advanced applications, including catalysts, fuel cells, biotechnology, radiation detector, and photoluminescent properties [16-19]. According to Rojas et al. [18], SrAl₂O₄ doped with Eu²⁺ and Dy³⁺ are successfully synthesized by the combustion method avoiding thermal treatments in a reducing atmosphere. They established that the amount of urea as a fuel has an important influence on phase composition and determines the presence of an oxidizing agent such as HNO₃ to complete the reaction, when the fuel content employed is greater than the stoichiometric ones.

The objective of this work is to evaluate the effect of the amount of fuel on the properties of Sr₃Al₂O₆:Eu synthesized by the solution combustion method. Herein, we describe the effect of stoichiometric quantity and excess fuel on the properties of the Sr₃Al₂O₆:Eu. The use of a complementary oxidizing agent could improve the reaction completion, as also influence the microstructural characteristics of the compound. The correlation between the combustion process, morphology, and optical properties of strontium aluminate-based particles is discussed.

EXPERIMENTAL

Procedure: the Sr₃Al₂O₆:Eu was prepared by solution combustion synthesis (SCS) method using strontium carbonate (SrCO₃, >98%, Cinética Reag. Sol.), europium oxide (Eu₂O₃, 99.5%, Metal Rare Earth), aluminum nitrate [Al(NO₃)₃·9H₂O, >98%, Sigma-Aldrich] and nitric acid (HNO₃, 65%, Merck) for the dissolution of the carbonate into nitrate, increasing the oxidizing character of the reaction. These reagents were dissolved in 50 mL of deionized water. The amount of each reagent was calculated according to



with a doping concentration of $x=0.03$ using the calculation proposed by Jain et al. [20]. Urea [(NH₂)₂CO, >99.5%, Sigma-Aldrich] was used as a fuel, in a stoichiometric oxidizing/reducing ratio of 1:1 ($\varphi=1$). In the second route, excess urea was tested with a stoichiometric oxidizing/reducing ratio of 1:2 ($\varphi=2$), which implied that the amount of fuel was twice as stoichiometric. For all the routes, we looked for the synthesis of 5 g of Sr_{2.97}Eu_{0.03}Al₂O₆ powder. For $\varphi=1$, the amount of urea required gave a stoichiometric ratio of fuel to oxidant, considering as oxidant only the aluminum nitrate; $\varphi=2$ implied that the amount of fuel was twice the stoichiometric one, in this case, the stoichiometric amount of HNO₃ was added to balance the total amount of fuel. The reactant mixtures were partially dried under magnetic stirring for 120 min at 80 °C in a porcelain crucible, then placed in the furnace at 600 °C for about 10 min; during

this time, ignition took place.

Characterization: the products obtained by SCS were crushed with an agate mortar obtaining a fine powder. For X-ray characterization, this powder was ground in a pulverizing mill (MM2, Retsch, Germany) for 5 min. Identification of crystalline phases in synthesized powders was carried out by X-ray diffraction analysis using a diffractometer (D8, Bruker, Germany) with CuK α radiation ($\lambda=1.5406$ Å), working at 40 kV and 40 mA. For the acquisition of the diffractograms, they were recorded in step mode in a range of Bragg angle (θ), scanning angles between 15-60° 2 θ , with a step of 0.02° and accumulation time of 4 s. A software (X'Pert HighScore Plus, PANalytical, Netherlands) was used for qualitative phase analysis. The morphology of the nanostructured powders was evaluated using field-emission scanning electron microscopy (FE-SEM, S-4700, Hitachi) with images of secondary electrons. Surface area measurements were performed using a single point isotherm technique (Monosorb Surface Area MS-13, Quantachrome Instr., USA) and applying the Brunauer, Emmett, and Teller (BET) model. The equivalent particle size was calculated based on the BET surface area as follows [21]:

$$D_{\text{BET}} = \frac{6}{S_{\text{BET}} \cdot \rho} \quad (\text{B})$$

where D_{BET} is the equivalent particle size (μm), S_{BET} (specific surface area), and ρ (theoretical density of Sr₃Al₂O₆ - 3.57 g/cm³). The optical properties of these materials by measuring emission and excitation spectra were investigated. The photoluminescence spectra of the phosphor particles were recorded with a spectrofluorometer (Fluorolog-3, Horiba Jobin Yvon) at room temperature. The luminescence intensity was measured over the wavelength 260-700 nm; a xenon arc lamp was used as the excitation source ($\lambda_{\text{exc}} = 365$ and 464 nm), and slits of 2.00 and 10.00 nm bandpass were used for measurements of the emission and excitation spectrum, respectively.

RESULTS AND DISCUSSION

Obtaining powders: solution combustion synthesis consisted of three main steps (Fig. 1), such as: a) homogenization of the precursors by dissolution; b) formation of the gel with the fusion of nitrates; and c) combustion of the gel, obtaining at the end a voluminous and fragile solid. The synthesized products were ground and



Figure 1: Images for a schematic description of the main steps in solution combustion synthesis (SCS).

characterized by XRD for their phase compositions.

Structural characterization: X-ray diffractograms of phosphors obtained by combustion under stoichiometric urea quantity and with twice the quantity ($\varphi=1$ and 2) are shown in Fig. 2. The results for samples in the stoichiometric amount of urea ($\varphi=1$) led mainly to the main formation of the $\text{Sr}_3\text{Al}_2\text{O}_6$ cubic phase, space group Pa3, characterized by three peaks at angles (2θ) of 31.949° , 45.765° and 56.890° accordingly with JCPDS file n° 24-1187 and a minority

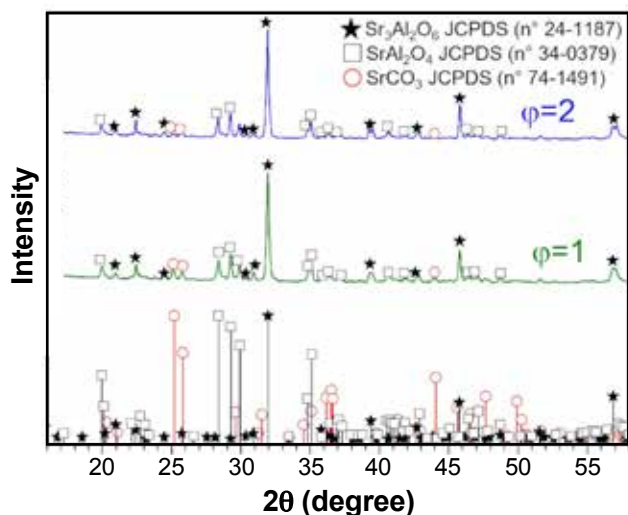


Figure 2: XRD patterns of synthesized $\text{Sr}_3\text{Al}_2\text{O}_6$ phosphors synthesized with the stoichiometric amount of fuel ($\varphi=1$) and with excess fuel ($\varphi=2$). The symbols highlight $\text{Sr}_3\text{Al}_2\text{O}_6$ (black stars), SrCO_3 (open red circles), and SrAl_2O_4 (open black squares).

phase SrAl_2O_4 (monoclinic phase) accordingly with JCPDS file n° 34-0379. The presence of crystalline phases having different Sr/Al ratios revealed the lack of homogeneity in the system during the combustion process [18], as could also be related to the proximity between these two phases as can be seen in the equilibrium phase diagram of SrO- Al_2O_3 system according to Hanic *et al.* [22]. On the other hand, the formation of strontium carbonate may be assigned to high SrO basicity and the presence of CO_2 (slightly acid gas) generated during the combustion [23]. With the excess of fuel ($\varphi=2$), the main phases present in stoichiometric synthesis ($\varphi=1$) were identified, having as the major phase $\text{Sr}_3\text{Al}_2\text{O}_6$ and SrAl_2O_4 as the minor phase. The presence of these phases was again attributed to the characteristic lack of energy homogeneity during the combustion reaction [24]. There was less presence of the strontium carbonate phase, indicating that the increase of oxidant (HNO_3) in equilibrium with the fuel [$(\text{NH}_2)_2\text{CO}$] resulted in a greater decomposition of SrCO_3 .

Microstructural characterization: the FE-SEM analysis was carried out to investigate the morphology of synthesized products. FE-SEM images at different (low and high) magnifications have been taken, as shown in Fig. 3. In Figs. 3a and 3d, the morphology of the products is observed (for $\varphi=1$ and 2, respectively); they present a typical synthesis microstructure due to the combustion of the flake form [25] with many voids attributed to the large volume of gases generated during combustion reaction; by analyzing the micrographs in more detail, it was noted that these flakes were nanostructured. In Figs. 3e and 3f,

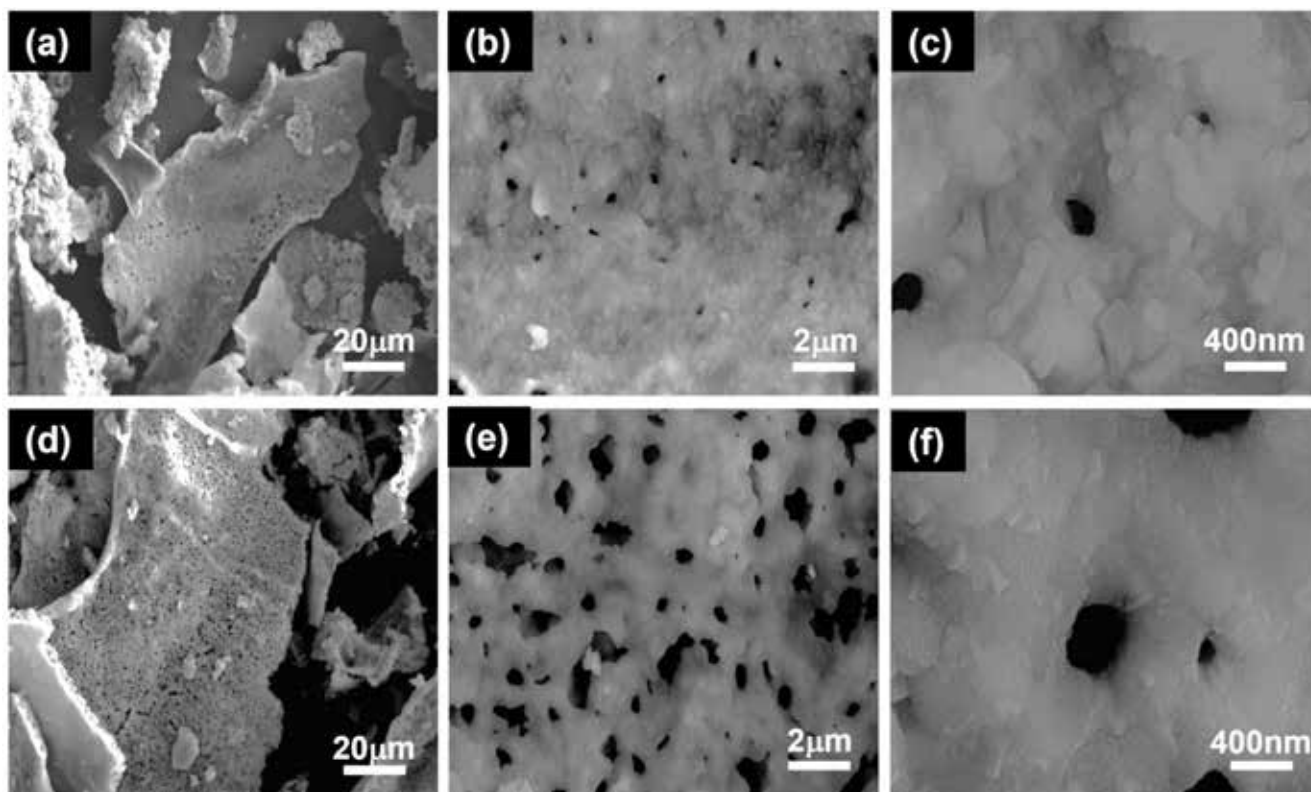


Figure 3: FE-SEM micrographs at different magnifications (low and high) of the products obtained for $\varphi=1$ (a,b,c) and $\varphi=2$ (d,e,f).

Table I - Dependence of specific surface area (S_{BET}) and equivalent particle size (D_{BET}) on amount of fuel (φ).

Sample	S_{BET} (m ² /g)	D_{BET} (μm)
$\varphi=1$	0.15	11.2
$\varphi=2$	0.07	24.0

it is observed the morphology of the powder synthesized with excess fuel ($\varphi=2$), thus occurring an increase in the synthesis temperature that provided greater sintering between the particles, resulting in more porous flakes in relation to the stoichiometric amount of fuel synthesis. These morphological characteristics are the result of the effervescence in the combustion process combined with the short reaction time, preventing the growth of particles [26]. In addition, these nanostructured flakes are interesting for various applications. Table I shows the results of the specific surface area (S_{BET}) of the crushed samples. The phosphors synthesized with the stoichiometric amount of urea ($\varphi=1$) had an S_{BET} of 0.15 m²/g due to a nanostructured flake shape formed by the union between particles as seen in Fig. 3a after efficient combustion. The sample obtained with excess urea ($\varphi=2$) showed an S_{BET} of 0.07 m²/g showing that increasing fuel resulted in greater sintering of this product, leading to the formation of agglomerations and consequently reducing the S_{BET} of the product [24].

Optical characterization: in the crystal lattice of $\text{Sr}_3\text{Al}_2\text{O}_6$, there were six possible sites to accommodate Eu by taking place of Sr. The analysis based on the effective bond valence theory showed that the active valence of Sr in each site was different. Eu entered into the different sites of Sr, thus, the energy barrier that Eu had to overcome was different, since the coordination number and the average length of neighboring-coordination bonds for each site of

Sr were different. Accordingly, the reduction-ability of the Eu was diverse depending on its site occupation. If all Eu ions were completely reduced to Eu^{2+} , it would emit green luminescence [27]. Despite the contradictory results for $\text{Sr}_3\text{Al}_2\text{O}_6$ doped with europium, the observed differences in emission spectra are caused by differences in excitation wavelengths and different crystallographic sites for Eu^{2+} and Eu^{3+} as were explained by Huang *et al.* [28] and Zhang *et al.* [29] and also due to the coexistence of Eu^{2+} and Eu^{3+} in the samples. In order to see Eu^{3+} contribution, the emission spectra of samples with the stoichiometric amount of urea ($\varphi=1$, green open circles) and with the excess of fuel ($\varphi=2$, blue open squares) were taken under 464 nm excitation as shown in Fig. 4a. The 464 nm was chosen to be the excitation wavelength, taking in account the results obtained in excitation spectrum fixing the emission at 611 nm (Fig. 4b). For the emission wavelength at 611 nm, the transitions at ${}^7\text{F}_{0,1} \rightarrow {}^5\text{D}_2$ are clearly seen at 464 nm [9]. As seen in Fig. 4b, the strongest peak is located at 464 nm. Effectively, the emission intensity centered at 611 nm increased in the sample with lower fuel content due to the lack of reduction of europium. If Eu^{3+} was completely reduced to Eu^{2+} , it would give green luminescence in the crystal lattice of $\text{Sr}_3\text{Al}_2\text{O}_6$ and the excitation and emission originate from the real $4f^7 \rightarrow 4f^6 5d$ transition of Eu^{2+} [27].

The excitation spectra fixing the emission at 515 nm are shown in Fig. 5a for the samples with the stoichiometric amount of urea ($\varphi=1$, green open circles) and with the excess of fuel ($\varphi=2$, blue open squares) showing a broad band in UV range with the maxima around 365 nm. The emission spectrum of the sample with $\varphi=1$ under 365nm excitation is shown in Fig. 5b. The emission band centered at 425 nm can be assigned to an anomalous Eu^{2+} trapped exciton emission [6] and the emission bands located at 588, 596, and 611 nm corresponded to the transition of ${}^5\text{D}_0 \rightarrow {}^7\text{F}_1$,

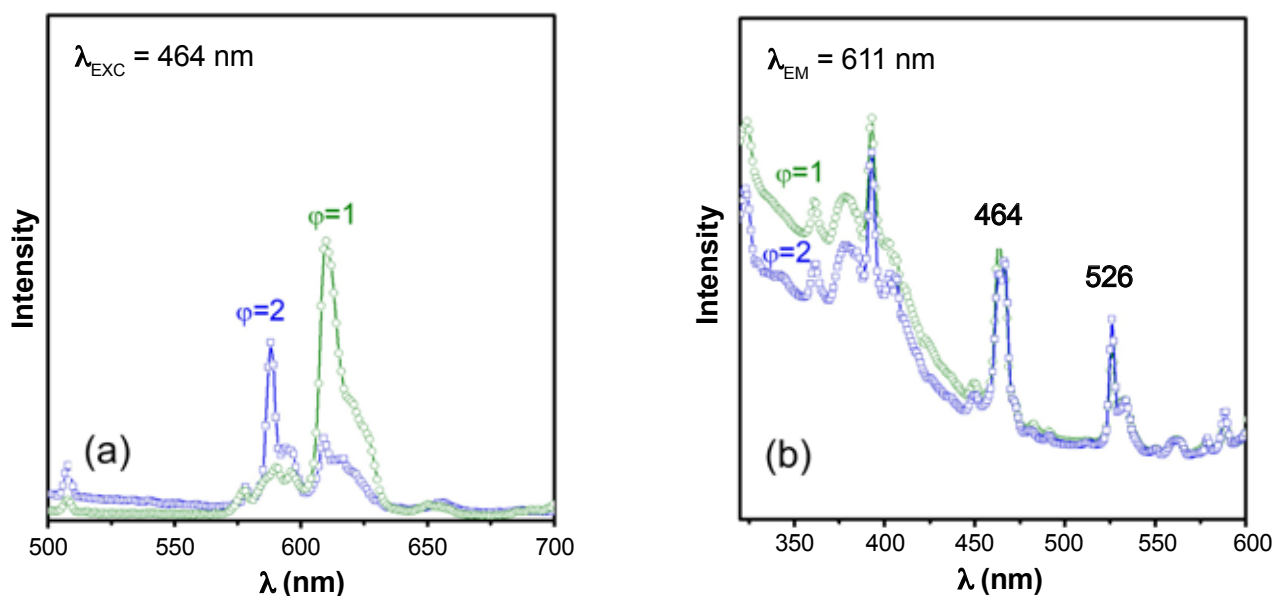


Figure 4: Emission spectra of the samples with the stoichiometric amount of urea ($\varphi=1$) and with the excess of fuel ($\varphi=2$) under 464 nm excitation (a), and excitation spectra of the samples with $\varphi=1$ and 2 fixing the emission at 611 nm (b).

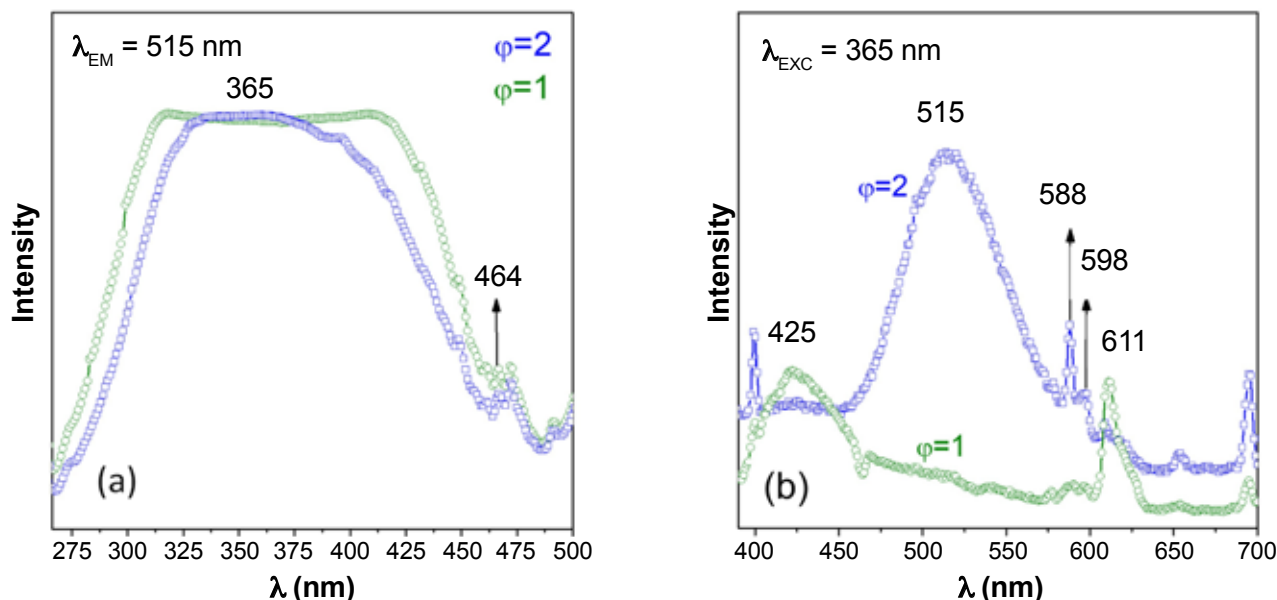


Figure 5: Excitation spectra of the samples with the stoichiometric amount of urea ($\varphi=1$) and with the excess of fuel ($\varphi=2$) fixing the emission at 515 nm (a), and emission spectra of the samples with $\varphi=1$ and 2 under 365 nm excitation (b).

$^5D_0 \rightarrow ^7F_1$, and $^5D_0 \rightarrow ^7F_2$ for the Eu^{3+} ions, respectively [27, 30–32]. The emission spectrum of the sample with $\varphi=2$ is shown also in Fig. 5b. The emission band centered at 515 nm was assigned to the transition of $4f^65d^1/4f_7(8S_{7/2})$ of Eu^{2+} ions and the emission bands located at 588, 598, and 611 nm corresponded to the transition of $^5D_0 \rightarrow ^7F_1$, $^5D_0 \rightarrow ^7F_1$, and $^5D_0 \rightarrow ^7F_2$ for the Eu^{3+} ions, respectively. The emission at 611 nm was more relevant in the sample with the stoichiometric amount of urea ($\varphi=1$) than in the sample with the excess of fuel ($\varphi=2$). It is important to remark that the combustion method avoids the use of a reducing atmosphere during the thermal treatment due to fuel burnout, a creation of suitable atmospheric conditions to reduce the Eu^{3+} to Eu^{2+} [18]. For this reason, the intensity of the peaks corresponded to Eu^{3+} decreased for $\varphi=2$. However, there was not a total reduction of Eu^{3+} . The results indicated that the excitation spectrum (Fig. 5a) of the sample with the excess of fuel ($\varphi=2$) had a peak position in the band from 275 to 475 nm corresponding to the crystal field splitting of the Eu^{2+} d-orbital, being located in the main peak at 365 nm under an emission of 515 nm, which meant that it can be effectively excited by ultraviolet light.

During the last few years, a number of publications have appeared on the luminescence properties of Eu^{2+} in $\text{Sr}_3\text{Al}_2\text{O}_6$. The reported results concerning the position of Eu^{2+} emission in $\text{Sr}_3\text{Al}_2\text{O}_6:1\% \text{Eu}^{2+}$ are confusing or even in contradiction to each other [6]. Some authors [33–35] have reported green emission of $\text{Sr}_3\text{Al}_2\text{O}_6:\text{Eu}^{2+}$ peaking around 510 nm, under 360 nm excitation. Other authors [36] reported broad green band emission but peaking at 518 nm. Studies have shown a broad red emission peak at 604 nm under the excitation wavelength of 460 nm [29]. Additionally, emissions at 405 and 435 nm from $\text{Sr}_3\text{Al}_2\text{O}_6:\text{Eu}^{2+}$ have been reported [37]. The differences in emission spectra of $\text{Sr}_3\text{Al}_2\text{O}_6:\text{Eu}^{2+}$ are caused by differences in excitation wavelengths [28]. The green and red

emissions originate from different crystallographic sites for Eu^{2+} . The $\text{Sr}_3\text{Al}_2\text{O}_6:\text{Eu}^{2+}/\text{Dy}^{3+}$ phosphor emits a yellow-green light upon UV illumination and bright red light upon visible light illumination. The peak positions in the emission spectra depend strongly on the nature of the Eu^{2+} surroundings, and therefore, Eu^{2+} ions can emit different visible lights in the various crystal fields [38]. According to Zhu et al. [39], the red luminescence of $\text{Sr}_3\text{Al}_2\text{O}_6:\text{Eu}$ could be improved by doping with Dy^{3+} and be further improved by co-doping with Li^+ . As also, there is a correlation between the luminescent responses of the materials processed in the presence of the oxidizing agent. The higher fuel content produces different $\text{Eu}^{2+}/\text{Eu}^{3+}$ ratios that account for photoluminescence centered at different wavelengths.

CONCLUSIONS

By solution combustion synthesis method avoiding thermal treatments in a reducing atmosphere, $\text{Sr}_3\text{Al}_2\text{O}_6:\text{Eu}$ phosphors were successfully synthesized. The amount of urea had an important influence on the luminescence response; a urea content larger than the stoichiometric one required the presence of an oxidant agent such as HNO_3 to complete the reaction. The synthesized phosphor showed an intense band emission centered at 515 nm. The optical properties correlated with the $\text{Eu}^{2+}/\text{Eu}^{3+}$ ratio and their emissions. Particles having nanostructured flake-type morphology were obtained. The combustion method avoided the standard requirements of post-thermal treatments in a reducing atmosphere to promote the appearance of Eu^{2+} cations. The fuel content had two roles: the effective chelation of the cations and the creation of suitable atmospheric conditions to reduce the Eu^{3+} to Eu^{2+} . The optimized synthesis and processing conditions by the solution combustion method in presence of oxidizing agent provided a micro-nanofunctional

candidate for practical applications.

ACKNOWLEDGEMENTS

This work was supported by the Ministry of Economy and Competitiveness of Spain under project MAT2013-48426-C2-1R and the Brazilian Program “Science Without Borders” through Project N° 401220/2014-1. The financial support from the Estonian Research Council (grant PSG-466) is gratefully acknowledged by R.E Rojas- Hernandez.

REFERENCES

- [1] G. Balachandran, *Treat. Process Metall.* **3** (2014) 1291.
- [2] I. Gupta, S. Singh, S. Bhagwan, D. Singh, *Ceram. Int.* **47** (2021) 19282.
- [3] S.K. Gupta, R.M. Kadam, P.K. Pujari, *Coord. Chem. Rev.* **420** (2020) 213405.
- [4] V.B. Pawade, S.J. Dhoble, *Luminescence* **26** (2011) 722.
- [5] X. Li, Y. Liang, F. Yang, Z. Xia, W. Huang, Y. Li, J. Mater. Sci. Mater. Electron. **24** (2013) 3199.
- [6] D. Dutczak, T. Jüstel, C. Ronda, A. Meijerink, *Phys. Chem. Chem. Phys.* **17** (2015) 15236.
- [7] J. Qi, X. Zhang, X. Han, Y. Li, X. Wu, R. Zhong, R. Guo, *J. Alloys Compd.* **678** (2016) 421.
- [8] P. Zhang, L. Li, M. Xu, L. Liu, *J. Alloys Compd.* **456** (2008) 216.
- [9] P. Page, R. Ghildiyal, K.V.R. Murthy, *Mater. Res. Bull.* **41** (2006) 1854.
- [10] A.H. Wako, F.B. Dejene, H.C. Swart, *Phys. B Condens. Matter.* **480** (2015) 116.
- [11] P. Ptáček, in “Strontium aluminate: cem. fundam. manuf. hydration, setting behav. appl.”, IntechOpen (2014) 236.
- [12] B. Farin, A.H.A. Monteverde Videla, S. Specchia, E.M. Gaigneaux, *Catal. Today* **257** (2015) 11.
- [13] Y. Xu, Y. He, X. Yuan, *Powder Technol.* **172** (2007) 99.
- [14] P. Zhang, M. Xu, Z. Zheng, B. Sun, Y. Zhang, *Trans. Nonferrous Met. Soc. China* **16** (2006) s423.
- [15] P. Zhang, M. Xu, L. Liu, L. Li, *J. Sol-Gel Sci. Technol.* **50** (2009) 267.
- [16] M.A. Aghayan, M.A. Rodríguez, *Mater. Sci. Eng. C* **32** (2012) 2464.
- [17] A.S. Mukasyan, P. Epstein, P. Dinka, *Proc. Combust. Inst.* **31** (2007) 1789.
- [18] R.E. Rojas-Hernandez, M.A. Rodriguez, J.F. Fernandez, *R. Soc. Chem.* **5** (2015) 3104.
- [19] M. Kavitha, R. Subramanian, K.S. Vinoth, R. Narayanan, G. Venkatesh, N. Esakkiraja, *Powder Technol.* **271** (2015) 167.
- [20] S.R. Jain, K.C. Adiga, V.R. Pai Verneker, *Combust. Flame* **40** (1981) 71.
- [21] W.T. Barbosa, I.V.S.R. Nascimento, R. Garcia-Carrodegua, M.V.L. Fook, M.A. Rodríguez, *Int. J. Appl. Ceram. Technol.* **16** (2019) 595.
- [22] F. Hanic, T.Y. Chemekova, Y.P. Udalov, *Zh. Neorg. Khim.* **24** (1979) 471.
- [23] R. Ianoş, R. Istrate, C. Păcurariu, R. Lazău, *Phys. Chem. Chem. Phys.* **18** (2016) 1150.
- [24] M.A. Rodríguez, C.L. Aguilar, M.A. Aghayan, *Ceram. Int.* **38** (2012) 395.
- [25] R.E. Rojas-Hernandez, M.A. Rodriguez, F. Rubio-Marcos, A. Serrano, J.F. Fernandez, *J. Mater. Chem. C* **3** (2015) 1268.
- [26] L.L. Petschnig, G. Fuhrmann, D. Schildhammer, M. Tribus, H. Schottenberger, H. Huppertz, *Ceram. Int.* **42** (2015) 4262.
- [27] L. Chen, Z. Zhang, Y. Tian, M. Fei, L. He, P. Zhang, W. Zhang, *J. Rare Earths* **35** (2017) 127.
- [28] P. Huang, Q. Zhang, C.E. Cui, J. Li, *Opt. Mater.* **33** (2011) 1252.
- [29] J. Zhang, X. Zhang, J. Shi, M. Gong, *J. Lumin.* **131** (2011) 2463.
- [30] X. Li, H. Pan, A. Tang, J. Zhang, L. Guan, H. Su, G. Dong, Z. Yang, H. Wang, F. Teng, *J. Nanosci. Nanotechnol.* **16** (2016) 3474.
- [31] K. Binnemans, *Coord. Chem. Rev.* **295** (2015) 1.
- [32] J.A. Capobianco, P.P. Proulx, M. Bettinelli, F. Negrisolo, *Phys. Rev. B* **42** (1990) 5936.
- [33] C. Chang, W. Li, X. Huang, Z. Wang, X. Chen, X. Qian, R. Guo, Y. Ding, D. Mao, *J. Lumin.* **130** (2010) 347.
- [34] D. Gingasu, I. Mindru, A. Ianculescu, S. Preda, C. Negrila, M. Secu, *J. Lumin.* **214** (2019) 116540.
- [35] Y. Li, Y. Wang, Y. Xiong, T. Peng, M. Mo, *J. Rare Earths* **30** (2012) 105.
- [36] A. Yu, D. Zhang, Y. Hu, R. Yang, *J. Mater. Sci. Mater. Electron.* **25** (2014) 4434.
- [37] D. Si, B. Geng, S. Wang, *CrystEngComm* **12** (2010) 2722.
- [38] P. Huang, C.E. Cui, S. Wang, *Opt. Mater.* **32** (2009) 184.
- [39] M. Zhu, Y. Tian, J. Chen, M. Fei, L. He, L. Chen, F. Peng, Q. Zhang, T.-S. Chan, *Funct. Mater. Lett.* **11** (2018) 1850012.

(*Rec. 11/07/2022, Rev. 18/10/2022, Ac. 25/10/2022*)



The influence of compositional variability of dimension stone residues on the properties of rustic porous ceramic tiles

A. C. A. Prado^{1*}, R. L. M. Feitosa², M. A. Neves³, S. P. Taguchi⁴

¹Universidade Federal do Cariri, Centro de Ciências e Tecnologia, Av. Ten. Raimundo Rocha, Juazeiro do Norte, CE, Brazil

²Universidade Federal de Pernambuco, 50670-901, Recife, PE, Brazil

³Universidade Federal do Espírito Santo, Departamento de Geologia, CCENS, 29500-000, Alegre, ES, Brazil

⁴Universidade Federal Rural do Rio de Janeiro, Departamento de Engenharia Química, Seropédica, RJ, Brazil

Abstract

This study analyzed how the compositional variability of dimension stone residues influences the characteristics of rustic porous ceramic tiles. The specimens were prepared by adding 20 wt% of dimension stone residue to the clay and sintered at 1000 °C for 1 h. The testing assays performed were physical properties and structural analysis through scanning electron microscopy. The results indicate that water absorption was lower (~9% to 14%) in samples containing silicate residues compared to carbonate residues (~16%). Apparent porosity of ~21% to 25% and shrinkage of 0.5% to 1.6% were measured in silicate samples while higher apparent porosity of ~30% and expansion of -0.04% were found in carbonate samples. Flexural strength and modulus of rupture were similar, ~16 MPa and ~330 N, respectively, for both sample sets. The samples containing silicate residues whose SiO₂ content was between 48% and 58% and the sum of alkaline and alkaline earth oxides was less than 18% were suitable for manufacturing rustic porous ceramic tile, while residues with high SiO₂ or carbonate contents impaired the properties of the ceramic bodies. Therefore, it is recommended that the dimension stone residues intended for use in ceramic tiles be previously separated according to chemical and mineralogical characteristics.

Keywords: processing sludge, dimension stone residue, rustic porous ceramic tile, terracotta, technological properties.


INTRODUCTION

Brazil stands out in the dimension stone sector worldwide. In 2020, the Brazilian export of natural rock materials for ornamentation and coating reached US\$ 987.40 million and 2.16 million tons [1]. The State of Espírito Santo (ES), in Southeastern Brazil, is the main producer in this country. Between January and July 2021, ES was responsible for 76.09% of the dimension stone mass exported by Brazil (in financial terms, the State portion corresponded to 82.12% of the total). Considering only the exports from ES in this period, a little more than 400 thousand tons of granite rocks, marbles, and similar were exported as non-processed blocks while plates and other parts reached 628.4 thousand tons. Among the processed rocks, granite composition products are exported in much higher quantities than marble products [2]. Most of the exported materials undergo beneficiation processes before leaving the country (about 55% by volume) [1], such as cutting blocks into sheets. The quantity of residue generated during the sawing of rock blocks to compose semi-finished sheets is remarkable [3, 4]. This residue consists of very thin mud containing rock dust, steel

shot, lime, and water when conventional looms are used in the process whereas the residue contains rock dust and water when diamond wire looms are used [5]. The dimension stone residue from silicate rocks generally consists of quartz, feldspars, calcite, and micaceous minerals [6] in different quantities while the residue from carbonate rocks contains calcite and dolomite. Using byproducts such as mining and ore processing residues can minimize the environmental impacts and reduce costs when manufacturing red ceramic products. The residues can be added to the product when their composition is similar to the traditional raw material used and/or when their properties are similar or better than the products existing on the market.

To this end, many works investigated including dimension stone residues in red ceramics products [6-13]. The term 'red ceramic' includes several products with clays that contain iron oxides and hydroxides, responsible for the reddish color of the pieces after firing. Among the products are roof tiles, blocks, bricks, and red ceramic tiles used on floors. Despite being extremely variable, the mineralogical composition of Brazilian clays contains non-plastic minerals that are also part of the main types of rocks used for ornamental purposes. Therefore, dimension stone residues present a great potential to be used in red ceramic products [7]. But, while some studies show that mixtures containing residue from the cutting of the dimension stone using

*ana.prado@ufca.edu.br

 <https://orcid.org/0000-0003-4337-9404>

diamond wire looms can be used to manufacture roofing tiles and structural red ceramic blocks [6], other works [8] report that mechanical resistance and water absorption decrease with the increasing percentage of dimension stone residue added to the ceramic mixture. From an economic point of view, red ceramic tile for floors (also known as ‘porous rustic tile’, ‘terracotta’, or ‘baked earth’) has greater added value than other red ceramic products [9]. Additionally, the manufacturing process of rustic porous ceramic coating is simpler than those employed in other ceramic types. The first product is shaped through extrusion, not enameled, and sintered at ~ 1000 °C, and, generally, the rustic coating has high water absorption as well as varying color and size. Although the Brazilian Association of Technical Standards (ABNT) does not establish a specific requirement for this kind of product, and some rustic porous coatings are made by pressing, their properties can be correlated with the class AIII parameters detailed in the ABNT ISO 13006/2020 standard [14].

The authors [10] that investigated the incorporation of residues from gneisses for producing rustic porous tiles recommend new tests at a sintering temperature of ~ 1000 °C. Another research [11] added residues from granitic rocks and kaolin to the ceramic mixture and reported that the specimens met the ABNT standard requirements for semi-porous ceramics at the sintering temperature of 1150 °C. The use of carbonate residues was also tested with different types of clays and various sintering temperatures, confirming the possibility of producing porous ceramic coatings when using kaolinitic clay and carbonate residues [12]. In the literature, a review article [7] analyzing the use of residues in red ceramic reports that, despite generating products that comply with the regulations and contribute to reducing environmental impacts, knowledge gaps still exist in the incorporation field during the manufacturing process. Nonetheless, major research investigated mixed residues, composed of mixing wastes that originated from different types of materials. In Cachoeiro

de Itapemirim, a city in the South of Espírito Santo-Brazil, the only two works that studied the residues segregated according to rock type report that the compositional variability of residues is substantial, therefore requiring to select residues according to the lithological types to obtain more valuable raw materials [5, 13]. Therefore, the present work aims to investigate how the compositional differences of the rocks processed in the Cachoeiro de Itapemirim region (ES) influence the properties of rustic porous ceramic tiles.

MATERIALS AND METHODS

The raw material used in this research was the conventional clay used to manufacture bricks in the red ceramic industry and residues from the sawing of dimension stone blocks in companies in Cachoeiro de Itapemirim (ES, Brazil). The characteristics of the clay used here have already been published [12]. The wide variety of chemical and mineralogical compositions observed in the field of dimension stones consequently generates different residue types [5]. Therefore, we characterized previously several residues from the sawing of dimension stone blocks and selected one residue per group, according to the chemical characteristics (Table I) determined by an X-ray fluorescence spectrometer (XRF, PW-2400, Philips). The mineralogical composition of the samples was determined by X-ray diffraction (XRD) using a diffractometer (X’Pert, Panalytical) that allowed measurements in the 12 to 310 K range, equipped with a copper anode ($K\alpha$ 1.5418 Å); the range of 2θ was from 4° to 70° , with a 0.05° step.

Silicate and carbonate rock residues were collected on conventional and diamond wire looms, respectively. Grinding was not necessary because these particles were very fine, thus, they were just dried and crushed in a mortar. The clay was wet ground for 24 h in a ball mill. Then, the clay paste obtained was first left to air dry, followed by oven drying for 24 h, and sieved through an ASTM #200

Table I - Commercial names of the dimension stones and characteristics of the sawdust residues resulting from the cutting of plates.

Commercial name of the rock	Characteristics of the sawdust residue
Crema Bordeaux	Silicate composition with high silica content and low LOI
Verde Peacock	Silicate composition with intermediate SiO_2 level, relatively high percentages of Al_2O_3 , $\text{Na}_2\text{O}+\text{K}_2\text{O}$, and low LOI
Ocre Itabira	Silicate composition with intermediate SiO_2 level, relatively high percentages of Al_2O_3 , $\text{MgO}+\text{CaO}$, $\text{Na}_2\text{O}+\text{K}_2\text{O}$, and low LOI
Nero Marinace	Silicate composition with intermediate SiO_2 level, a high percentage of $\text{MgO}+\text{CaO}$, and high LOI
Marrom Bahia	Silicate composition with low SiO_2 content, relatively high percentages of Al_2O_3 , $\text{Na}_2\text{O}+\text{K}_2\text{O}$, and low LOI
Preto Aracruz	Silicate composition with low SiO_2 level, a high percentage of $\text{MgO}+\text{CaO}$, and an atypically high percentage of P_2O_5
Mármore Aquarela	Carbonate composition with very high levels of CaO , MgO , and high LOI

LOI: loss on ignition.

sieve (less than 75 μm) to de-agglomerate and improve conditions for the compaction process. Ten specimens were produced for each residue type by mixing it with 80% of clay on a weight basis. The mixtures were humidified using 10% water on a weight basis and formed using a uniaxial hydraulic manual press, with a mold of approximately 80x25x6 mm, and a pressure of 25 MPa for 30 s. In the beginning, the specimens were left to dry in the open air for 24 h, followed by oven drying at 110 °C for 24 h, and then heat treated in an electric oven at 1000 °C, with 1 h isotherm and 10 °C/min heating rate. The residue added in the clay mixture, and the temperature and sintering time used in this work were based on the best conditions obtained in previous work, with samples containing clay and 0, 20%, 40%, 60%, and 80% of ornamental rock residue, fired at 900, 1000 and 1100 °C for 1 and 2 h [6]. Other authors [10, 12, 15] also indicated this firing temperature/time (1000 °C/1 h) for red ceramics due to the resulting good physical and mechanical properties. Good mechanical properties were also obtained after durability testing at 900 °C, compared to ceramics sintered at lower temperatures [16]. In addition, 1000 °C is a consistent value compared to those used in industries that produce ceramic building materials.

After firing, the following technological properties were determined: water absorption (WA), apparent porosity (AP), bulk density (BQ), modulus of rupture (MR), and flexural strength (FS) while adapting the ABNT NBR ISO 10545-3 [17] and 10545-4 [18] standards to the size of laboratory specimens. To determine WA, AP, and BQ, the specimens were oven dried at 110 °C, followed by a thorough water impregnation and immersion. The parameters were calculated using the equations found in the ABNT NBR ISO 10545-3 standard [17]. The FS and MR were determined in a flexometer (Flexi 1000 LX-650, Gabbrilli). The modulus of rupture is the force necessary to break the specimen multiplied by the ratio distance between supports/width of the specimen and flexural strength is the value obtained from 3/2 of the modulus of rupture divided by the square of the minimum thickness along the fractured side of the specimen. In addition to these tests, linear shrinkage (LS) was determined by subtracting the length of the specimen before and after the firing divided by its initial length. The

results presented are the mean and standard deviation of the individual values obtained for a total of 10 specimens. Additionally, after the FS test, microstructural analysis of a cross-section of the specimens was performed in a scanning electron microscope (SEM) at different magnifications.

RESULTS AND DISCUSSION

The chemical compositions of the residues and clay used are shown in Table II. The results showed a difference between the chemical composition of silicate rock residues and marble residue and variability among the silicate residue samples as well. The SiO_2 content varied from 48.27% to 70.19% and the sum of $\text{Na}_2\text{O}+\text{K}_2\text{O}+\text{CaO}+\text{MgO}$ ranged from 10.37% to 19.28% in the silicate residues; additionally, their loss on ignition (LOI) was relatively small, except for the Nero Marinace residue. The marble residue, on the other hand, had low SiO_2 (1.67%) and higher CaO (38.78%) contents, MgO content (15.83%) typical of carbonate rocks, and consequently higher LOI (42.46%) corresponding to the decomposition of the carbonate content.

The clay used to produce the ceramic mass was highly plastic, consisting of clay minerals from the montmorillonite and/or vermiculite and kaolinite groups, in addition to feldspar and quartz [12]. The mineralogical composition of residues (Fig. 1) from the silicate rocks indicated the presence of quartz (SiO_2), microcline (KAlSi_3O_8), plagioclase [$(\text{Na,Ca})\text{Al}(\text{Si,Al})\text{Si}_2\text{O}_8$], and mica [$(\text{K,Na,Ca})_2(\text{Al,Mg,Fe,Li})_{4-6}(\text{Si,Al})_8\text{O}_{20}(\text{OH,F})_4$]. Calcite was also identified in the Nero Marinace residue (corroborating the high LOI). In addition to quartz, mica, microcline, and pyroxene [$(\text{Ca,Na,Fe,Mg,Zn,Mn,Li})(\text{Cr,Al,Fe,Mg,Mn,Ti,P})(\text{Si,Al})_2\text{O}_6$] were present in Verde Peacock while plagioclase, edenite [$\text{NaCa}_2\text{MgSi}_7\text{O}_{22}(\text{OH})_2$] and enstatite [$(\text{Mg,Fe})_2\text{Si}_2\text{O}_6$] were observed in the Ocre Itabira sample. The Mármore Aquarela carbonate residue consisted mainly of calcite (CaCO_3) and dolomite [$\text{CaMg}(\text{CO}_3)_2$]. In the silicate residues, the K_2O came from K-feldspars and micas, while Na_2O was derived from both sodium feldspar and plagioclase. The CaO came mainly from the lime used in the sawing process on conventional looms, but plagioclase can also provide this mineral. In

Table II - Chemical composition (wt%) of the materials used to prepare the ceramic mass (data compiled from [5, 12]).

Material	SiO_2	TiO_2	Al_2O_3	Fe_2O_3	MnO	MgO	CaO	Na_2O	K_2O	P_2O_5	LOI
Crema Bordeaux ¹	70.19	0.05	11.87	6.66	0.06	0.05	2.97	3.34	4.01	0.01	0.81
Verde Peacock ¹	57.86	0.60	15.02	12.29	0.11	0.36	4.83	2.93	5.43	0.24	0.33
Ocre Itabira ¹	53.07	0.82	15.42	10.85	0.14	2.62	7.93	3.47	5.26	0.34	0.09
Nero Marinace ¹	56.45	0.32	8.28	14.32	0.18	0.67	10.25	2.03	1.57	0.11	5.82
Marrom Bahia ¹	51.16	1.21	14.77	15.59	0.25	1.19	5.95	4.95	3.91	0.70	0.32
Preto Aracruz ¹	48.27	3.06	14.00	13.89	0.16	4.41	8.64	2.58	2.26	1.81	0.93
Mármore Aquarela ²	1.67	0.02	0.65	0.51	0.01	15.83	38.78	0.01	0.03	0.04	42.46
Clay	59.14	0.95	24.12	7.79	0.08	2.90	1.03	n.d.	3.36	n.d.	n.d.

¹: silicate rock residue; ²: carbonate rock residue; LOI: loss on ignition; n.d.: not determined.

carbonate rocks, the CaO and MgO contents came from carbonates (calcite and dolomite) whereas iron oxide came from some minerals of the mica and plagioclase group that were present in some of the processed rocks, but mainly it came from the shot and steel blades used in the sawing process. Generally, the presence of alkali metals (such as K and Na) and alkaline earth metals induce the formation of a liquid phase during ceramic firing [10, 19]. Iron gives color and acts in the sintering process by reducing the viscosity of the liquid phase formed during firing, which can lead to pyroplastic deformation [12, 19]. In the burning process, attention is needed to the temperature for starting the liquid phase formation, which depends on the minerals formed by these chemical elements [8-13, 15, 16, 19].

This work investigated the effects of adding residues to

ceramic pieces fired at 1000 °C. The results of the physical tests performed with samples containing 80% clay and 20% residue on a weight basis are compiled in Table III. The physical properties of the specimens and the composition of the residues used to produce the ceramic mass were correlated, as shown in Figs. 2 and 3. The LS and BQ were noticeably lower in the bodies whose residues had higher LOI (Fig. 2a). In these materials, the LOI was associated with the carbonates present that during burning released CO₂, leaving pores in its structure and possibly causing the part to expand. These pores decreased the density, as well as, occupied internal spaces in the samples, that were perceived by a smaller shrinkage during firing. Linear shrinkage is a property that indicates the densification degree during firing and is important for the dimensional control of the final

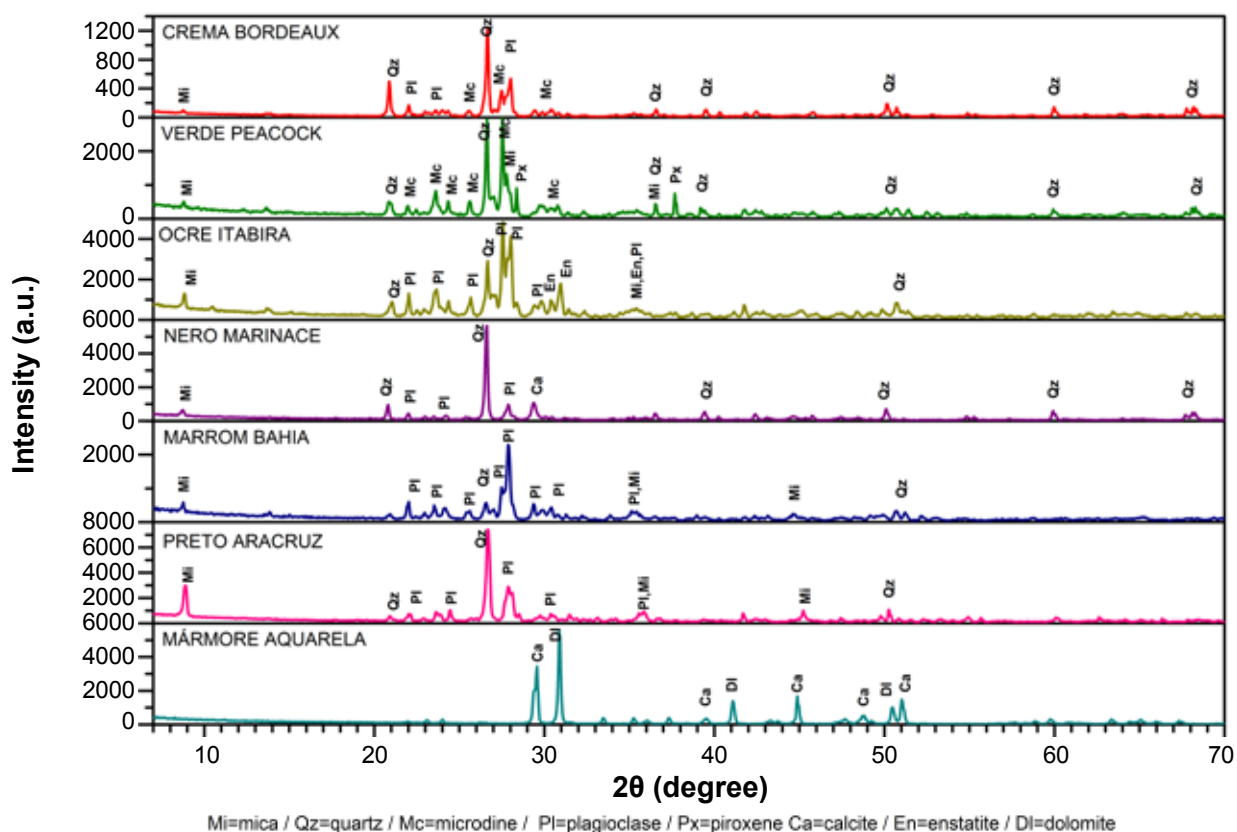


Figure 1: XRD patterns showing mineralogical compositions of the dimension stone residues used to prepare the ceramic mass.

Table III - Means and standard deviations of water absorption (WA), apparent porosity (AP), bulk density (BQ), linear shrinkage (LS), flexural strength (FS), and modulus of rupture (MR) of clay samples with added dimension stone residue.

Sample	WA (%)	AP (%)	BQ (g.cm ⁻³)	LS (%)	FS (MPa)	MR (N)
Crema Bordeaux	12.0±0.3	24.1±0.4	2.03±0.01	1.28±0.09	14.7±1.2	306±5
Verde Peacock	12.3±0.3	24.8±0.5	2.02±0.01	1.60±0.15	17.5±1.5	351±4
Nero Marinace	14.4±0.9	28.0±1.1	1.95±0.03	0.48±0.24	14.9±2.6	321±2
Ocre Itabira	9.7±0.5	21.3±0.8	2.18±0.02	1.34±0.20	17.6±2.2	353±4
Marrom Bahia	12.7±0.6	25.5±0.9	2.01±0.02	1.24±0.17	16.5±2.1	350±3
Preto Aracruz	11.4±0.4	23.7±0.6	2.08±0.01	1.56±0.24	16.9±1.7	343±3
Mármore Aquarela	16.7±0.3	30.6±0.4	1.83±0.01	-0.04±0.11	16.3±1.1	337±5

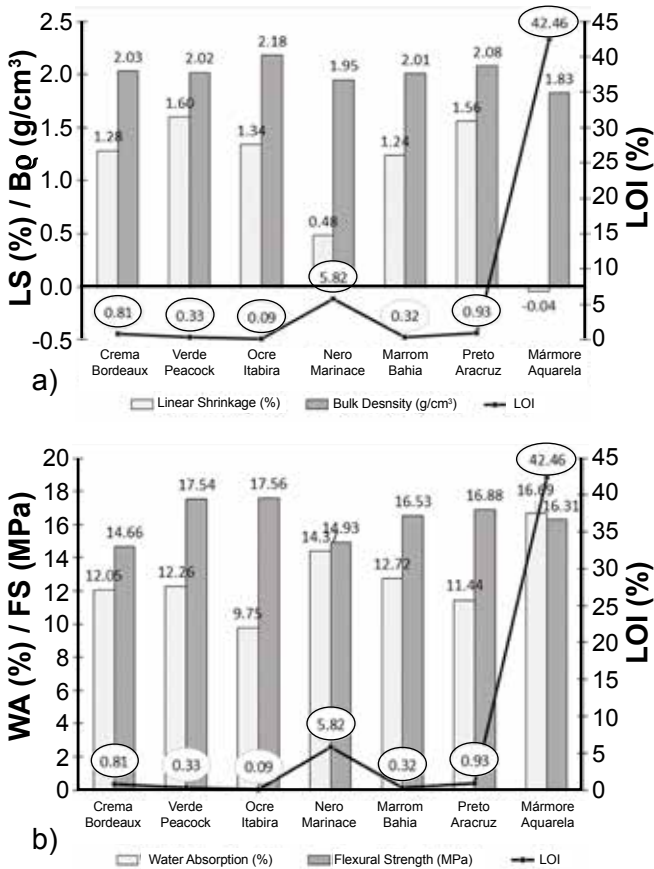


Figure 2: Relationship between linear shrinkage, LS, bulk density, B₀ (a), water absorption, WA, and flexural strength, FS (b), of ceramic pieces with the loss on ignition (LOI) of the residue.

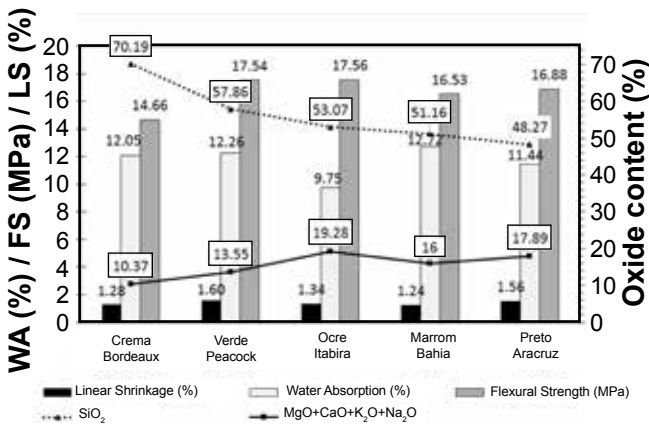


Figure 3: Relationship between water absorption (WA), flexural strength (FS), and linear shrinkage (LS) of the ceramic pieces with SiO₂ and MgO+CaO+K₂O+Na₂O contents in the silicate residues with low percentages of carbonates.

product. Previous works [20, 21] relate that linear shrinkage values between 1.5% and 3.0% are recommended for red ceramics while values less than 1.5% are considered ideal. In this work, the silicate residue samples presented 0.48% to 1.83% shrinkage while carbonate samples expanded to -0.04%, both results within the recommended value. For the AIII ceramic group, the ABNT ISO 13006/2020 standard

[14] requires that the dimensions of any ceramic body stay inside the ±1.5% range of the mean obtained for 10 specimens. Nonetheless, the manufacturers of rustic porous ceramic tiles inform in their catalogs that these product sizes can vary. Therefore, according to such information, the measured linear shrinkage variations and their standard deviations did not disqualify the studied material for being used as this type of red ceramic.

Using residues with very high (Mármore Aquarela) and a relatively high (Nero Marinace) LOI resulted in ceramic bodies with higher WA values. On the other hand, flexural strength did not present the same relationship with the LOI, indicating that other factors interfered with this mechanical property (Fig. 2b). Research investigating the effect of adding 10% of carbonate rock residue (with more than 95% of CaO) in clays used for producing rustic ceramic tiles [12] showed that the added residue increased both, WA and FS, while LS decreased. The increase in FS was probably due to the newly formed calcic solid phases [19]. Also, the SiO₂ content and the sum of alkali and alkaline earth elements and iron oxide affected the properties of the specimens that did not have high or very high LOI (Fig. 3). The sample containing the Crema Bordeaux residue had more than 70% of SiO₂, partially occurring as free silica, which damaged the sintering of the specimen; therefore, the WA value was intermediate, while the LS and mechanical strength were low compared to the other samples. Furthermore, in the silicate residue sample with lower SiO₂ levels (53% or less), the sum of fluxing oxides (Na₂O+K₂O+CaO+MgO) became decisive for densification. So much so that the sample containing the Ocre Itabira residue exhibited the lowest WA and the highest mechanical strength among all the analyzed samples (Fig. 3). According to ABNT ISO 13006 standard [14], ceramic tiles classified as AIII must have minimum mechanical strength values of 8 MPa, breaking load greater than 600 N, and WA greater than 10%. It is noteworthy that ABNT does not have specific values for rustic porous coating, but class AIII is the most appropriate category to evaluate this product type.

The MR values of all samples were lower than the minimum established in the ABNT ISO 13006 standard [14], and the FS values were above the ABNT requirements. In addition, the WA of the Ocre Itabira sample was lower than 10%, which classified this material in another class of ceramic tile regarding this parameter. The Crema Bordeaux residue had relatively lower percentages of alkali and alkaline earth

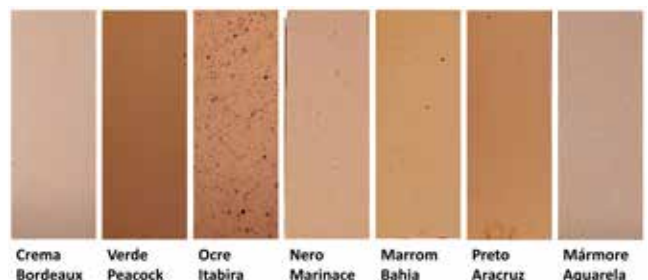


Figure 4: Images showing the aspects of the ceramic specimens made with clay and different residues sintered at 1000 °C.

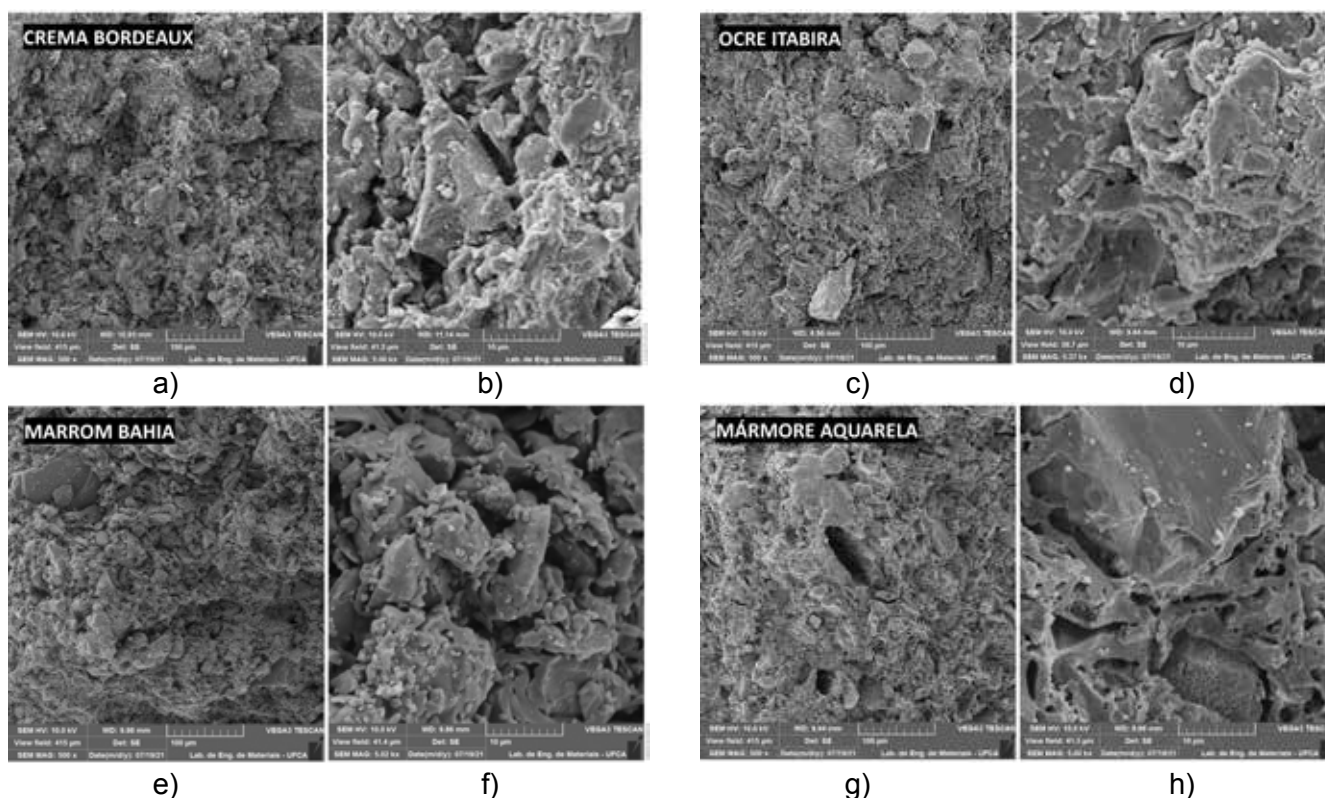


Figure 5: SEM micrographs of ceramic pieces containing 80% clay and 20 wt% of the following residues: a,b) Crema Bordeaux; c,d) Ocre Itabira; e,f) Marrom Bahia; and g,h) Mármore Aquarela.

elements and higher SiO_2 content, thus indicating higher quartz and lower feldspars levels. Feldspars are known to form a liquid phase at eutectic temperatures. Thus, the lower levels of these minerals in the residue probably justify the lower FS and MR compared to the other samples. On the other hand, the Ocre Itabira residue had the highest levels of alkali and alkaline earth oxides, which generated greater densification and reduced the WA to a value lower than that of porous ceramic tiles type AIII.

Fig. 4 shows the difference in color and surface porosity of the samples containing different types of dimension stone residue. All samples were reddish while the sample with Ocre Itabira residue showed dark dots on the surface due to the higher Fe_2O_3 content from the steel shot used for rock sawing.

Fig. 5 shows the micrographs of sample specimens obtained by SEM at different magnifications, whose physical properties met the WA and FS requirements (clay and added Marrom Bahia and Mármore Aquarela residues), the Ocre Itabira sample with WA below the limit for porous ceramic tile and the Crema Bordeaux sample with lower FS and MR. All micrographs showed the typical porous structure of traditional clay ceramic, with a small portion of particles larger than $10\ \mu\text{m}$ and angular morphology. In the microstructure of the Crema Bordeaux sample, for example, some weakly bound regions indicated that sintering did not occur via the liquid phase, and others, with apparently well-cohesive particles, showed that fluxes had better performance. These microstructure characteristics

were evenly distributed throughout the sample. Despite the similar micrographs of the Ocre Itabira and Marrom Bahia samples, the micrographs at low magnification showed that the quantity of intergranular pores was lower in the first, consistent with the higher BQ ($2.18\ \text{g}\cdot\text{cm}^{-3}$) and lower WA (9.75%) compared to the other sample ($2.01\ \text{g}\cdot\text{cm}^{-3}$, 12.72%). The microstructure of the sample containing the Mármore Aquarela residue, in addition to residual intergranular pores from the sintering process, showed some porous channels probably formed by the CO_2 released during the calcination of carbonates present in the residue. The burning temperature of $1000\ ^\circ\text{C}$ was enough to liberate the CO_2 present in the carbonates, leaving pores in the structure but not enough for the alkaline earth oxides (CaO, MgO) to actively participate in the liquid phase formation reactions, which would help the densification of the ceramic piece.

CONCLUSIONS

It was shown that the compositional variability of dimension stone residues from rocks sawed in the Cachoeiro de Itapemirim region (ES-Brazil) influenced the technological properties of rustic porous ceramic tiles. Besides the expected compositional differences between silicate and carbonate residues, from different rock types, there were relevant variations in chemical and mineralogical compositions within the group composed of silicate residues. Samples with higher carbonate contents and, consequently, higher loss on ignition (LOI), presented higher water

absorption values, lower linear shrinkage, and lower bulk density, indicating lower densification. The microstructure of the specimens prepared with Aquarela Marble residue and clay confirmed the lower densification at the sintering temperature of 1000 °C for 1 h. In the silicate residue samples with low LOI, the SiO₂ content and the sum of oxides of alkali and alkaline earth elements and iron oxide affected the ceramic properties. The Crema Bordeaux residue had the highest SiO₂ content (>70%) among the studied samples. Part of SiO₂ occurred as free silica, which generated relatively lower linear shrinkage and flexural strength. The Crema Bordeaux sample showed heterogeneous microstructure regarding the densification. On the other hand, the highest fluxing oxides' content in the Ocre Itabira residue induced lower water absorption and higher flexural strength, indicating that the liquid phase generated during the sintering process was effective in wetting the particles and promoting good rearrangement and lower porosity in the ceramic. The dimension stone residues with intermediate SiO₂ content and fluxing oxide levels not very high were the most suitable for manufacturing a porous ceramic tile. Thus, separating different types of residues may give them greater added value when used as raw material.

ACKNOWLEDGMENT

The authors thank the Espírito Santo Research Foundation (*Fundação de Amparo à Pesquisa e Inovação do Espírito Santo* - FAPES) for the financial support.

REFERENCES

- [1] ABIROCHAS, “Informe 1”, Ass. Bras. Rochas Ornament., Brasília (2021).
 - [2] SINDIROCHAS, “Informativo mensal exportações de rochas 7”, Sind. Ind. Rochas Ornament., Serra (2021).
 - [3] B.C. Moreira, M.A. Neves, M.M. Pinheiro, W.A.R. Nascimento, J.L.B. Barbosa, A.H. Horn, *Geociências* **40**, 2 (2021) 525.
 - [4] A.M.V. González, J.D. Pastor, V. Barrientos, R. Juncosa, *Rev. Soc. Esp. Mineral.* **2** (2004) 75.
 - [5] M.A. Neves, A.C.A. Prado, R.A. Marques, A.B. Fonseca, M.E.S. Machado, *Geociências* **40**, 1 (2021) 123.
 - [6] S.P. Taguchi, J.C. Santos, T.M. Gomes, N.A. Cunha, *Cerâmica* **60**, 354 (2014) 291.
 - [7] K.S. Almeida, R.A.L. Soares, J.M.E. Matos, *Matéria* **25**, 1 (2020) e-12568.
 - [8] L.F. Amaral, J.P.R.G. de Carvalho, B.M. da Silva, G.C.G. Delaqua, S.N. Monteiro, C.M.F. Vieira, *J. Mater. Res. Technol.* **8**, 4 (2019) 599.
 - [9] M.C. de Azevedo, M.T. Marvila, G.C.G. Delaqua, L.F. Amaral, H. Colorado, C.M.F. Vieira., *Int. J. Appl. Ceram. Technol.* **18**, 6 (2021) 1876.
 - [10] A.T. Pacheco, S.N. Monteiro, R.A. Gama, C.M.F. Vieira, in *Proc. 55th Congr. Bras. Cerâm., Porto de Galinhas* (2011) 2652.
 - [11] F.F. Farias, G.A. Neves, L.N.L. Santana, H.L. Lira, H.C. Ferreira, in *Proc. 50th Congr. Bras. Cerâm., Blumenau* (2006).
 - [12] A.M.M. Santos, A.C.A. Prado, M.B.M. Matos, P.H.A. Feitosa, J.H.A. Feitosa, T.M.E. Alves, *Mater. Sci. Forum* **1012** (2020) 221.
 - [13] A.C.A. Prado, S.P.T. Borges, M.A. Neves, R.H. Soares, A.B. Fonseca, *Mater. Sci. Forum* **727-728** (2012) 703.
 - [14] ABNT, NBR 13006, “Placas cerâmicas: definições, classificação, características e marcação”, Ass. Bras. Normas Técn., Rio Janeiro (2020).
 - [15] B.C.A. Pinheiro, J.N.F. Holanda, *Cerâmica* **56**, 339 (2010) 237.
 - [16] D.V. Rodrigues, G.C. Xavier, F. Saboya, P.C.A. Maia, J. Alexandre, *Cerâmica* **58**, 347 (2012) 286.
 - [17] ABNT, NBR 10545-3, “Placas cerâmicas, parte 3: determinação da absorção de água, porosidade aparente, densidade relativa aparente e densidade aparente”, Ass. Bras. Normas Técn., Rio Janeiro (2020).
 - [18] ABNT, NBR 10545-4, “Placas cerâmicas, parte 4: determinação da carga de ruptura e módulo de resistência à flexão”, Ass. Bras. Normas Técn., Rio Janeiro (2020).
 - [19] A. Barba, V. Beltran, C. Feliu, J. Garcia, F. Ginés, E. Sanchez, V. Sanz, *Materias primas para la fabricación de soportes de baldosas cerámicas*, Inst. Tecnol. Cerám., Castellón (2002) 181.
 - [20] M. Dondi, *Cerâm. Ind.* **11**, 3 (2006) 36.
 - [21] L.Z.M. Damazio, M. Peterson, P.S. Camila, A. Zaccaron, F. Rosso, V.S. Nandi, C.M. Oliveira, *Cerâm. Ind.* **22**, 4 (2017).
- (*Rec.* 14/07/2022, *Rev.* 27/09/2022, 23/10/2022, *Ac.* 31/10/2022)



Bioactive $\text{SiO}_2\text{-K}_2\text{O-CaO-P}_2\text{O}_5$ glass-ceramic scaffold prepared using polyurethane foam template

E. R. Essien^{1*}, D. O. Nwude¹, V. E. Okolie¹, L. A. Adams²

¹Bells University of Technology, Department of Chemical and Food Sciences, Ota, 112103, Nigeria

²University of Lagos, Chemistry Department, Akoka, Yaba, 100213, Nigeria

Abstract

A glass-ceramic in the $\text{SiO}_2\text{-K}_2\text{O-CaO-P}_2\text{O}_5$ quaternary system was prepared by substituting the Na_2O component with K_2O to avoid $\text{Na}_2\text{Ca}_2\text{Si}_3\text{O}_9$ formation upon thermal treatment since this phase decreases apatite formation kinetics on glass material. To form the glass-ceramic, a modified sol-gel method involving solution precipitation, followed by reagents encapsulation in citric acid was adopted to enable the use of sodium metasilicate as a cheap substitute for traditional alkoxy silane silica precursors. The foam replication method using polyurethane foam as a sacrificial template was used to obtain the scaffold, which on analysis gave a porosity of 92% and an average pore size of $36\pm 6\ \mu\text{m}$. *In vitro* bioactivity evaluation in simulated body fluid for a maximum of 14 days indicated the formation of hydroxyapatite on the sample surface. Phase analysis showed that CaSiO_3 and K_2CaSiO_4 crystals formed in the sintered sample as the main phases, which exhibited biodegradability in simulated body fluid (SBF). Therefore, economically-derived porous bioactive glass-ceramic scaffolds based on the current method (a simple process) are feasible.

Keywords: bioactive glass-ceramic, carbonated hydroxyapatite, bioactivity, foam replication, polyurethane foam, crystallization, biodegradability.

INTRODUCTION

The specific criteria for an ideal scaffold intended for use in tissue regeneration include [1, 2]: a) cell delivery ability; b) outstanding osteoconductivity; c) good biodegradability; d) acceptable mechanical characteristics; e) extremely porous structure; f) irregular shape manufacturing ability; and g) commercialization potential. However, it is challenging to fabricate a material that meets all the foregoing parameters. Bioactive glasses and ceramics have been touted as promising materials for bone tissue regeneration for fulfilling some of these requirements, especially, criteria a to c [3-6]. Bioglass 45S5 (45% SiO_2 , 24.5% Na_2O , 24.5% CaO , and 6% P_2O_5 by weight), a degradable silicate glass with a high calcium concentration that can form a link with both soft and hard tissues, was developed by L. Hench in 1969 and is one of the most important biomaterials for bone defect repair [6]. When Bioglass comes into contact with biological fluids, a layer of carbonated hydroxyapatite, similar to the mineral phase of bone, forms on the surface, and silicon and calcium ions are released, which can stimulate the expression of several genes in osteoblastic cells and cause angiogenesis *in vitro* and *in vivo* [7].

To support load-bearing sites before new bone formation, bioactive glasses and ceramics as scaffolds are expected to possess proper mechanical properties. Sodium-containing bioactive glass, including Bioglass 45S5, despite its clinical success [6], is limited by low fracture toughness. Thus,

they are usually applied in non-load-bearing regions [8]. To toughen them, they are sintered at high temperatures. A major drawback of this strategy, however, is that it may result in full crystallization, which ultimately reduces the bioactivity of the glass [9, 10]. Various studies [11-14] have shown that the resulting crystal phase contains dense sodium calcium silicate ($\text{Na}_2\text{Ca}_2\text{Si}_3\text{O}_9$) which slightly decreases the kinetics of apatite formation on the glass surface. This is due to the slow resorbability of $\text{Na}_2\text{Ca}_2\text{Si}_3\text{O}_9$ in body fluid if sintered at high temperatures [15]. During sintering, densification of the sample occurs, pores' volume decreases and there is an overall reduction in the surface area available for reaction. A simple approach that could prevent full crystallization of the glass is to reduce the sintering temperature. However, insufficient densification could produce an extremely fragile scaffold with poorly packed glass particles. To avoid the formation of $\text{Na}_2\text{Ca}_2\text{Si}_3\text{O}_9$ during the thermal treatment of sodium-containing bioactive glasses, Cannillo and Sola [16] substituted all the Na_2O in Bioglass 45S5 with K_2O to form glass particles by melting the oxide components at $1450\ ^\circ\text{C}$ which were then used for coating alumina. Even though they avoided crystallization of the glass, the resulting compact morphology of the coating gave poor apatite nucleation on its surface. Silva et al. [17] substituted Na_2O with K_2O to form potassium-based Bioglass 45S5 and avoided full crystallization when they melted the oxide precursor up to $1350\ ^\circ\text{C}$. However, the obtained glass presented irregularly shaped particles and poor pore distribution.

These setbacks could be overcome by combining the relatively low-temperature sol-gel processing technique and the foam replication method to fabricate the scaffold and employing K_2O precursors instead of Na_2O to form a

*eressien@bellsuniversity.edu.ng

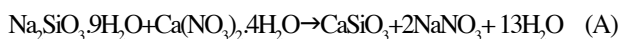
<https://orcid.org/0000-0003-2379-3640>

potassium silicate phase instead $\text{Na}_2\text{Ca}_2\text{Si}_3\text{O}_9$ crystalline phase during devitrification. Glasses manufactured by the sol-gel technique possess the advantages of high specific surface area and pore volume as well as nanoporosity which are key to a high rate of hydroxyapatite formation [18]. During sol-gel processing, the condensation, gelation, and drying stages generate fine colloidal particles in the nanometer size dimension and porous morphology with a large surface area. The replication method gives porous scaffolds that can mimic spongy bone [10] and fulfill criteria e to g highlighted above. Despite these benefits, the replication process has never before been employed to prepare SiO_2 - K_2O - CaO - P_2O_5 bioactive glass-ceramic scaffolds; instead, the SiO_2 - Na_2O - CaO - P_2O_5 system is common. Glasses in the SiO_2 - Na_2O - CaO - P_2O_5 system possess the advantage of forming the $\text{Na}_2\text{CaSi}_3\text{O}_9$ crystalline phase and its attendant ability to improve the mechanical property of resulting the scaffold. To substitute K_2O for Na_2O , the melting method was used [16, 17, 19], apparently to achieve a good degree of crystallization and consequently, appreciable mechanical properties. This study, therefore, aimed to synthesize a bioactive glass-ceramic scaffold in the system SiO_2 - K_2O - CaO - P_2O_5 through a foam replication technique and a modified sol-gel method by solution precipitation and to assess its bioactivity.

MATERIALS AND METHODS

Materials: to prepare the bioactive glass-ceramic scaffold, the following materials were used: sodium metasilicate ($\text{Na}_2\text{SiO}_3 \cdot 9\text{H}_2\text{O}$, Loba Chemie), calcium nitrate tetrahydrate [$\text{Ca}(\text{NO}_3)_2 \cdot 4\text{H}_2\text{O}$, Loba Chemie], dipotassium hydrogen phosphate trihydrate ($\text{K}_2\text{HPO}_4 \cdot 3\text{H}_2\text{O}$, Sigma-Aldrich), citric acid ($\text{C}_6\text{H}_8\text{O}_7$, Sigma-Aldrich), polyvinyl alcohol (PVA, Sigma-Aldrich) and polyurethane (PU) foam of 15 mm thickness cut into 7.5x7.5x15 mm dimension.

Bioactive glass-ceramic preparation: a bioactive glass (composition by wt%: 35 SiO_2 -35 CaO -20 K_2O -10 P_2O_5) was prepared by a modified sol-gel technique involving solution precipitation and precursor encapsulation. In summary, the $\text{Na}_2\text{SiO}_3 \cdot 9\text{H}_2\text{O}$ was dissolved in deionized water and added gradually to $\text{Ca}(\text{NO}_3)_2 \cdot 4\text{H}_2\text{O}$ solution in a conical flask under constant stirring using a magnetic stirrer. The reaction was allowed to continue for 1 h after which the gel formed was poured into a 500 mL beaker and washed with deionized water by swirling the beaker gently to extract the soluble NaNO_3 by-product (Eq. A). Thereafter, the supernatant was discarded by decantation. This procedure was repeated thrice and the obtained gel containing CaSiO_3 was dried at 120 °C for 72 h.



The as-prepared CaSiO_3 powder was added to a solution of 35 wt% citric acid (the encapsulating agent) with constant stirring with a magnetic stirrer unit maintained at 120 °C [14] until it dissolved. After dissolving the CaSiO_3 ,

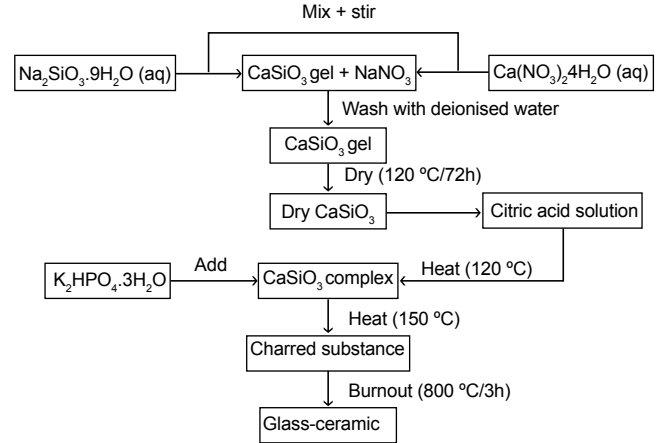


Figure 1: Flowchart summarizing the bioactive glass-ceramic preparation process using a modified sol-gel method.

$\text{K}_2\text{HPO}_4 \cdot 3\text{H}_2\text{O}$ was added and the temperature was adjusted to 150 °C while the stirring was maintained until the mixture was completely burnt. Just before the mixture transformed into a solid mass, the magnetic stirrer bar was withdrawn and the material, thereafter allowed to burn. After cooling to room temperature, the mixture containing the glass was transferred to a furnace for complete burnout at 800 °C for 3 h to destroy the PU template. Part of the resulting monolith was ground into powder for use in preparing the green body. The remainder was labeled BG. The process for obtaining the glass is illustrated in the flowchart presented in Fig. 1.

Preparation of scaffold: the procedure involved the initial preparation of a green body of ceramic foam. Accordingly, a slurry was prepared by adding the bioactive glass-ceramic powder to a 100 mL 0.01 mol/L polyvinyl alcohol (PVA) solution at a 2:3 weight ratio of the bioactive glass-ceramic to PVA solution [10] under vigorous stirring with the aid of a magnetic stirrer for 1 h. Following this, polyurethane foam (dimensions 7.5x7.5x15 mm) was dipped into the slurry and allowed to remain for 15 min. Afterward, the green body was obtained by removing the foam and squeezing out excess slurry. The material was then kept on a smooth surface and allowed to dry ambiently. Thermal treatment to burn out the PU was performed at 400 °C for 2 h, while sintering was carried out at 800 °C for 6 h. The heating rate was 10 °C/min. The bioactive glass-ceramic prepared by using the PU foam as the template was code-named BG_F while that formed without the use of the template was called BG.

The density of the scaffold, ρ_c , was estimated based on the mass and volume of the sintered bodies. The porosity (P) was determined from [10]:

$$P = \left(1 - \frac{\rho_c}{\rho_s}\right) \cdot 100 \quad (\text{B})$$

where ρ_s is the density of 45S5 Bioglass and equals 2.7 g/cm³ [10]. The pore sizes of the scaffolds were measured on their respective SEM micrographs using the ImageJ software. To assess the microstructure of the samples, a scanning electron microscope (SEM, ProX 800-07334, Phenom-

World, Netherlands) was used. The elemental composition of the sample was determined in an energy-dispersive X-ray (EDX) analyzer unit attached to the SEM machine. The operating voltage was 15 kV, while carbon adhesives were used to attach the samples to a sample holder to allow for their visual observation and the samples were sputter-coated with gold. Diffraction patterns of the samples were obtained from an X-ray diffractometer (XRD, D/Max-IIIC, Rigaku, Japan) to enable phase identification in the samples. The machine was operated using a CuK α radiation source with a wavelength of 0.154060 nm at 40 kV and 40 mA in the 2 θ range from 10° to 75°. The strongest diffraction peak in each diffractogram was used to calculate the crystallite size (ζ) of the major phase in the samples, according to the Scherrer equation [18]:

$$\zeta = k\lambda/(\beta \cdot \cos\theta) \quad (C)$$

where k is the Scherrer constant (equal to 0.89), λ is the wavelength of the CuK α X-ray (0.15406 nm), and β is the full width at half maximum (FWHM) of the highest diffraction peak. The chemical characteristics of the bonds in the network structure of the bioactive glass-ceramic samples before and after incubation study in simulated body fluid (SBF) to verify the formation of hydroxyapatite (HA) on the surface of the samples was performed using Fourier

transform infrared spectroscopy (FTIR, Cary 630, Agilent Technol., USA) in the wavenumber range from 4000 to 650 cm^{-1} .

Determination of bioactivity in simulated body fluid (SBF): to study the ability of the samples to induce apatite formation on their surface, they were immersed in SBF (pH 7.4) at 36.5 °C by following a well-established *in vitro* procedure [20]. The following analytical grade reagents were used to prepare the SBF: NaCl, NaHCO₃, KCl, K₂HPO₄·3H₂O, MgCl₂·6H₂O, CaCl₂, tris(hydroxymethyl) aminomethane [Tris-buffer (CH₂OH)₃CNH₂, Sigma-Aldrich, USA]. During the experiment, the samples were placed in clean plastic containers in the SBF (1 g of sample per 100 mL) and kept in an incubator for a duration of 7 to 14 days. At the end of each immersion period, the samples were removed from the solution, rinsed in sufficient amounts of deionized water by gently swirling the contents, and then placed in a desiccator to dry.

RESULTS AND DISCUSSION

Scaffold microstructure and elemental composition: the morphological architecture of the samples is presented in Fig. 2. The sample prepared without using the PU foam template (BG, Fig. 2a) showed glass particles well-distributed on the bioactive glass-ceramic to present a near-homogeneous

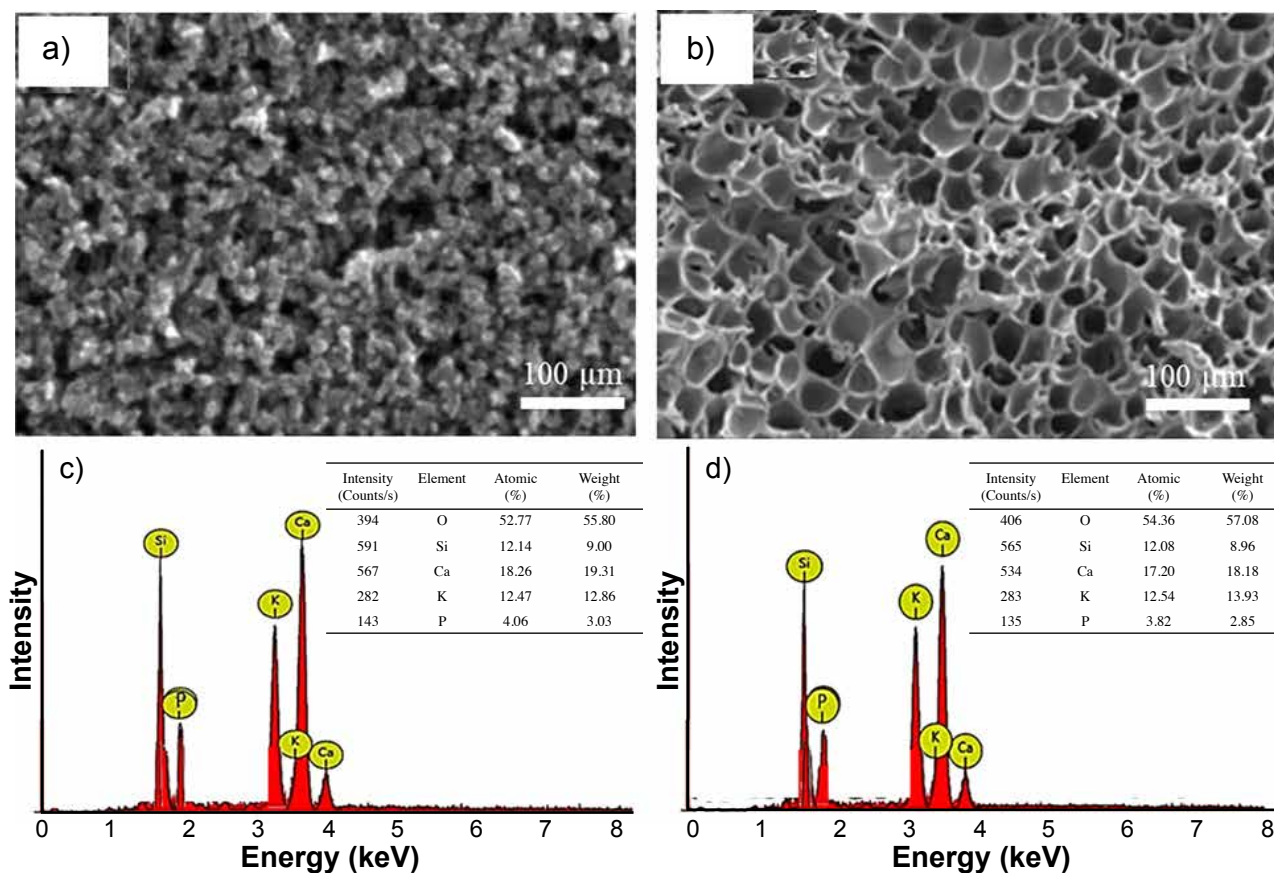


Figure 2: SEM micrographs showing well-distributed particles and pores (a,b) and EDX spectra (c,d) of the glass-ceramic samples sintered at 800 °C for 3 h: a,c) BG; and b,d) BG_F.

surface with a good surface area appearance. However, some of the particles formed clusters and agglomerates, thus giving rise to a few irregularly shaped pore spaces on the surface of the bioactive glass-ceramic. In contrast, a different morphological characteristic was observed in the sample prepared by the replication method using PU foam (BG_F, Fig. 2b). The surface was dominated by a well-defined porous architecture; most of the pores were open and distributed homogeneously over the material surface to present significant microporosity.

The polymer foam template (PU) possessed the desired pore structure and thus served as the sacrificial template during the ceramic coating. Therefore, the final material acquired the microstructure of the sacrificial foam template and hence resulted in a well-ordered glass-ceramic microstructure. BG gave a porosity value of 66% whereas for BG_F the porosity was 92% with pore sizes of $26 \pm 5 \mu\text{m}$ and $36 \pm 6 \mu\text{m}$, respectively. Sufficient porosity of appropriate size and interconnections between the pores create an environment that promotes cell infiltration, migration, vascularization, nutrition, oxygen flow, and waste elimination while enduring external loading pressures [21]. The capacity of cells to penetrate, proliferate, and differentiate, as well as the pace of scaffold degradation, is greatly influenced by the pore distribution and shape of the scaffold [22]. A minimum of $100 \mu\text{m}$ has been proposed as the threshold to adequately achieve these functions [14]. Even though the pore size of the scaffold synthesized in this study did not achieve this cut-off value, the high porosity of 92% obtained could enable enhanced cellular activity, according to Loh and Choong [23]. The application of the PU foam increased the pore size of the bioactive glass-ceramic scaffold from $26 \pm 5 \mu\text{m}$ (in BG) to $36 \pm 6 \mu\text{m}$ (in BG_F) by acting as a template. After the burnout, the scaffold mimicked the pore structure of the PU foam. This pore size ($36 \pm 6 \mu\text{m}$), which was in the sub-macropore category, should provide adequate surface area optimum for protein adhesion and cell attachment on the scaffold [24] and even promote ion exchange between the scaffold and the surrounding biological fluid [25].

The elemental composition of BG and BG_F are shown in Figs. 2c and 2d, respectively. As observed, the concentrations of Si, Ca, K, and P present in the glass-ceramic, as designed in both samples, were in agreement with the EDX results. The CaSiO_3 formed initially (Eq. A) served as the precursor for CaO and SiO_2 at a 1:1 ratio in the samples upon devitrification at $800^\circ\text{C}/3\text{h}$. Also, $\text{K}_2\text{HPO}_4 \cdot 3\text{H}_2\text{O}$ was able to transform into K_2O and P_2O_5 under the same devitrifying condition as depicted in Eq. D. This indicated that the amounts of the starting oxide precursors used as well as the reactions that afforded them were accurate. The absence of a Na peak in the spectrum signified the complete removal of the NaNO_3 side product (Eq. A) during the deionized water-washing stage.



Phase formation in samples: the X-ray diffractograms of

BG and BG_F (Fig. 3) presented three crystalline phases: wollastonite (CaSiO_3), calcite (CaCO_3), and potassium calcium silicate (K_2CaSiO_4). The wollastonite peaks matched the standard PDF (JCPDS 00-043-1460) when indexed in angular positions and reflection indices [18]. The K_2CaSiO_4 peaks matched the JCPDS file 19-943 in angular position and intensity, whereas CaCO_3 was indexed using the JCPDS file 02-0623. The crystallite size obtained by applying Eq. C was 46 nm. K_2CaSiO_4 crystalline phase has been previously formed and identified in a $\text{K}_2\text{O}-\text{CaO}-\text{P}_2\text{O}_5-\text{SiO}_2$ system bioactive glass-ceramic [17]. It is interesting to observe the absence of the $\text{Na}_2\text{Ca}_2\text{Si}_3\text{O}_9$ phase in the diffractograms of the samples, thus validating the approach adopted in this study. K_2CaSiO_4 should enhance the mechanical property of the scaffold while exhibiting appreciable biodegradability kinetics compared with $\text{Na}_2\text{Ca}_2\text{Si}_3\text{O}_9$. The mechanical property and biodegradability of a scaffold should show congruence if it is to be applied at a load-bearing site [10]. The effect of the PU foam template was once again evident as observed in the diffraction patterns of the two samples. The phases formed were similar to those of BG and had an average crystallite size of 33 nm, although they were lower in intensities (Fig. 3b), and appeared to be partially

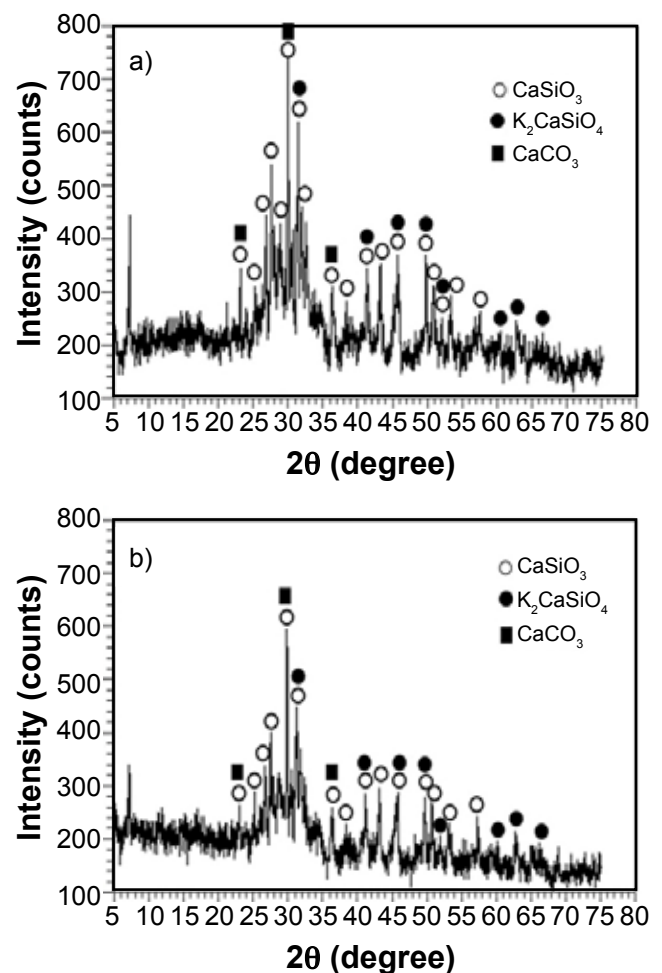


Figure 3: XRD patterns of the samples sintered at 800°C for 3 h showing the presence of crystalline phases: a) BG; and b) BG_F.

crystallized. This may be attributed to differences in porosity, pore and crystallite sizes of the two samples, which led to the better ordering of atoms in the sample during the thermal treatment. This is an encouraging result, given that crystallization is thought to decrease the bioactivity of a glass or glass-ceramic [9], the higher degree of porosity and, consequently, lower crystallinity are properties desirable for achieving higher bioactivity in implant materials [26].

Assessment of bonds: major peaks in the FTIR spectra, depicted in Fig. 4, were used to confirm the composition of the network structure formed in the glass-ceramic samples. In BG (Fig. 4a), a diagnostic peak for SiO₂ was observed at 1068 cm⁻¹ corresponding to siloxane (Si-O-Si) asymmetric stretching vibration [27]. Further vibrational modes of SiO₂ were observed at around 902, 715, and 702 cm⁻¹. The sharp peak around 902 cm⁻¹ was attributed to the symmetric stretching of Si-O in SiO₄⁴⁻ tetrahedron containing two nonbonding oxygen per tetrahedron (Si-O-2NBO) [28], resulting from the presence of K⁺ and Ca²⁺ network modifying cations. The formation of two different tetrahedra was confirmed by the small doublet at 715 and 712 cm⁻¹, which were the torsional vibrational modes of Si-O in SiO₄⁴⁻ [29] due to the presence of K⁺ and Ca²⁺ ions. Diagnostic peaks due to the presence of P₂O₅ were indicated by the PO₄³⁻ asymmetric stretching vibration located at 1006 cm⁻¹ and the symmetric stretching vibrational mode at 932 cm⁻¹ [30]. The bands at around 3450 and 1646 cm⁻¹ were ascribed to O-H stretching and angular vibrations, respectively, of water molecules, an indication of the presence of surface water in the samples. The appearance of the prominent CO₃²⁻ peaks near 1476 and 1406 cm⁻¹ in the spectrum signified CO₂ adsorption by the material during the preparation stage due to the presence of labile ions (K⁺ and Ca²⁺) in the composition [31]. The presence of these peaks confirmed the calcite peaks earlier observed in the X-ray diffractograms in Fig. 3. The FTIR spectrum of BG_F as shown in Fig. 4b indicated similar vibrational modes to BG, but with minor shifts in the O-H stretching and angular vibrations (3250 and 1648 cm⁻¹) as well as the PO₄³⁻ asymmetric stretching vibration (1002 cm⁻¹) to lower frequencies. This appears to be linked with the lower water content in BG_F caused by PU burnout. Also worthy of note is that no carbonaceous bonds associated with the PU foam template were found in the spectrum of BG_F which affirmed the high purity of the scaffold and the efficiency of the sintering procedure.

Bioactivity evaluation in SBF: bioactivity is usually assessed based on a material undergoing specific surface reactions in the presence of physiological fluids to form hydroxyapatite (HA) on the material surface. The scaffolds were immersed in SBF for a duration of 7 and 14 days after which they were investigated for the presence of HA using SEM, EDX, XRD, and FTIR spectroscopy. The microstructural evolution of the samples after the incubation experiment in SBF is presented in the SEM micrographs in Fig. 5. Colonies containing HA granules formed clusters on the surface of the glass-ceramic as observed in the SEM image of BG after soaking in SBF for 7 days (Fig. 5a),

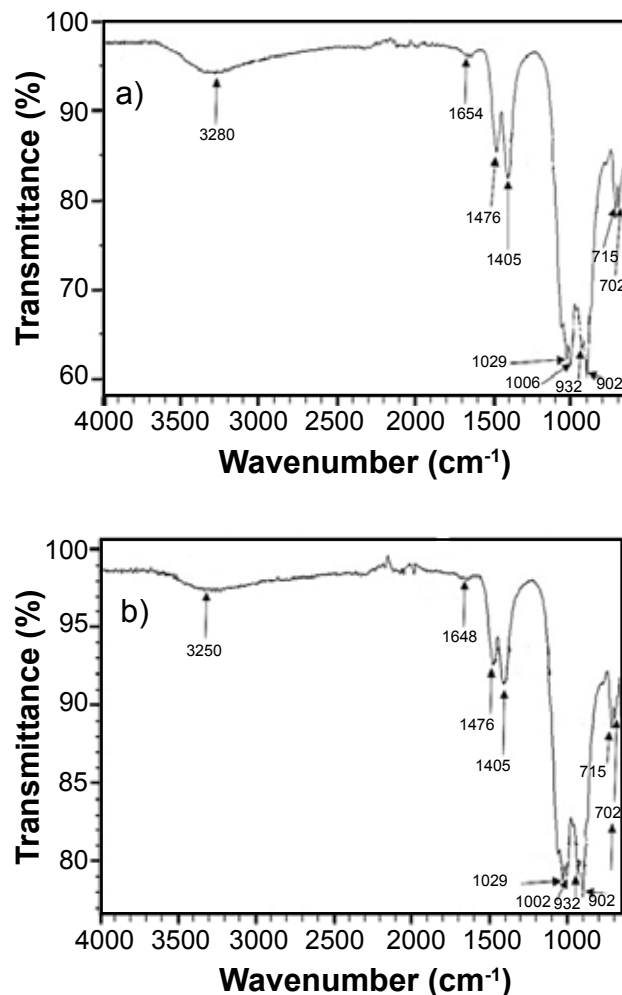


Figure 4: FTIR spectra showing vibrational modes of BG (a) and BG_F (b) samples after sintering at 800 °C for 3 h.

but some portions of the surface not completely covered by HA are still visible. After 14 days in SBF, the surface became enriched with HA balls, which in some areas, also appeared agglomerated (Fig 5b). For BG_F, after 7 days in SBF, the micrograph (Fig. 5c) showed the appearance of HA crystallites on the surface of the scaffold while some areas on the surface of the glass-ceramic were not completely covered by HA. On the 14th day in SBF, the HA crystallites appeared to completely cover the sample surface while some pores initially present on the parent glass-ceramic were retained.

The elemental composition of the sample surfaces after the immersion duration in SBF was also monitored for HA nucleation with the aid of EDX spectra and are presented in Fig. 6. After immersion of BG for 7 days, the K peak disappeared and the Si peak declined slightly in intensity (Fig. 6a). At the same time, the peaks for Ca and P appreciated marginally. A further decline in the Si peak was observed after incubation for 14 days (Fig. 6b), while there was a simultaneous slow increase in P as observed in the table inset. These manifestations were in agreement with a material undergoing surface reaction in physiological fluids

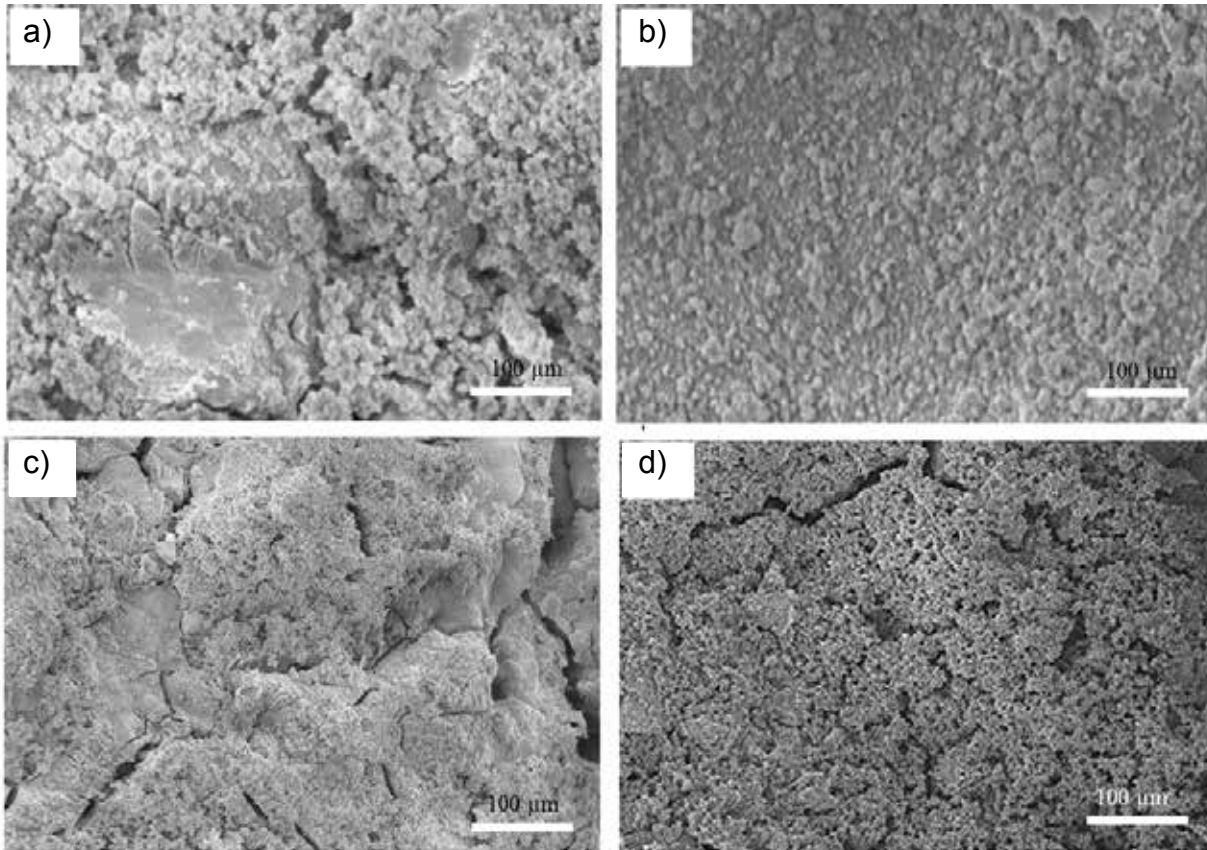


Figure 5: SEM micrographs of BG (a,b) and BG_F (c,d) glass-ceramic samples after immersion in SBF for 7 days (a,c) and 14 days (b,d).

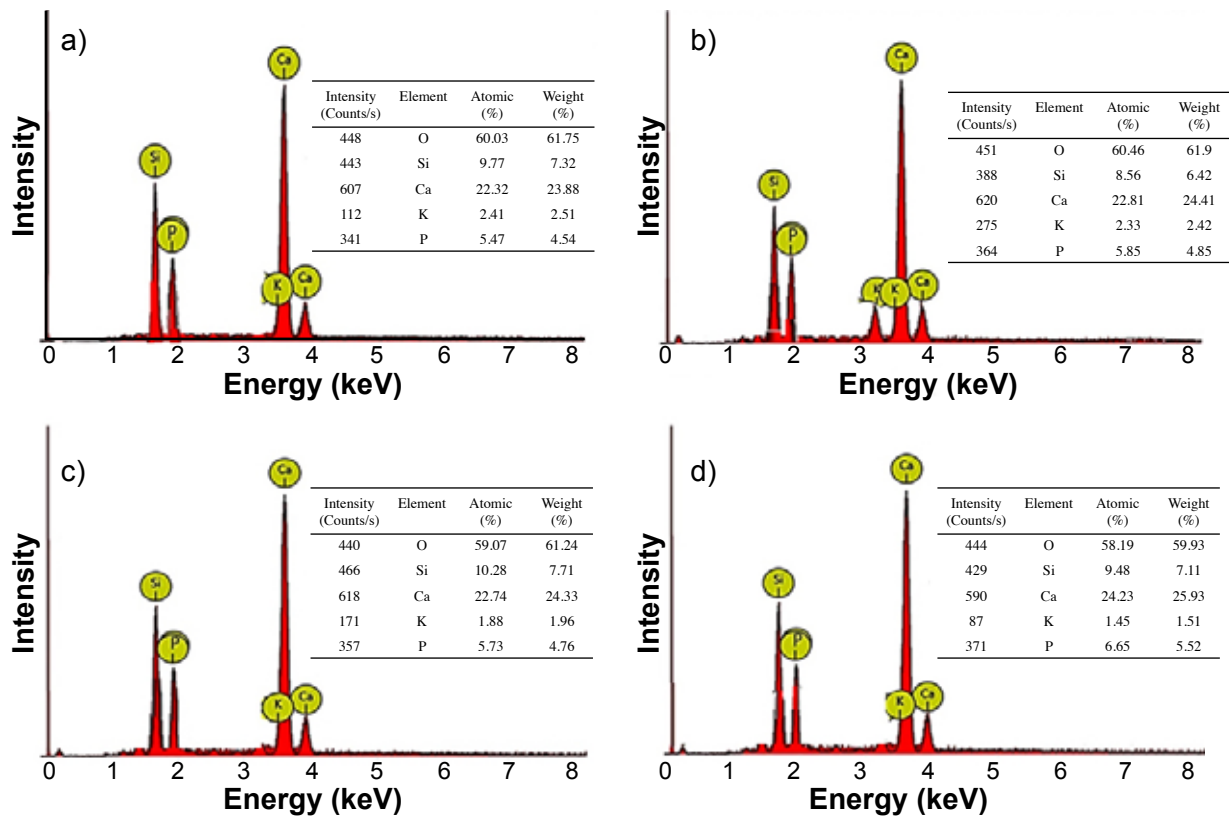


Figure 6: EDX spectra of BG (a,b) and BG_F (c,d) glass-ceramic samples after immersion in SBF for 7 days (a,c) and 14 days (b,d).

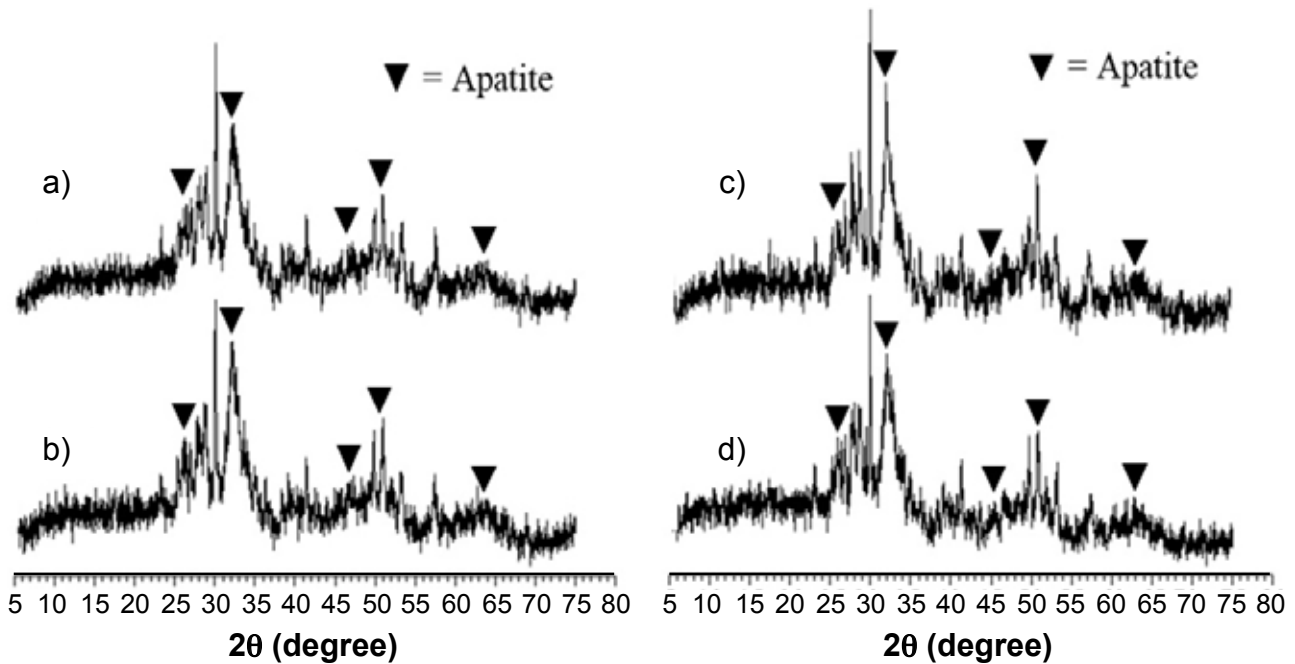


Figure 7: XRD patterns of the glass-ceramic samples after immersion in SBF showing the growth of apatite: a) BG for 7 days; b) BG for 14 days; c) BG_F for 7 days; and d) BG_F for 14 days.

to form HA [12, 32]. During the initial stages in SBF, a glass undergoes a rapid ion-exchange reaction between the glass and the SBF, leading to an exchange of K^+ from the glass and H^+ or H_3O^+ from SBF, consequently, K^+ was depleted from the glass due to its dissolution into the SBF. During the next stages, reabsorption of Ca^{2+} and P from the SBF resulted in an increase in their concentration on the glass surface and hence formed HA [33]. The decrease in Si intensity was attributed to an increase in HA density on the surface of the glass-ceramic as well as degradability in the SBF [10] which led to low detection of Si [18]. A similar reaction was observed for BG_F as was evident in the compositional changes after immersion in SBF for 7 and 14 days, which are depicted in the EDX spectra (Figs. 6c and 6d, respectively).

Further evidence of apatite formation on the samples

during the incubation experiment in SBF was provided by the XRD results in Fig. 7. When the peaks were matched in both angular location and intensity [33], HA peaks were identified in BG after soaking for 7 days (Fig. 7a) at 2θ of 25.8° , 32.0° , 46.6° , 51.2° , and 63.8° corresponding to the reflection indices of the hkl plane at 002, 112, 222, 140 and 304, respectively. After immersion for 14 days, the HA peaks increased in intensity (Fig. 7b) indicating an increase in HA density on the surface of the sample, thus supporting the SEM result in Fig. 5. This trend was sustained in BG_F as observed in the diffractograms (Figs. 7c and 7d) which exhibited similar diffraction patterns to BG. It was equally observed that the silicate peaks declined in intensity upon increased immersion duration in SBF compared with the pristine samples (Fig. 3). This may be associated with

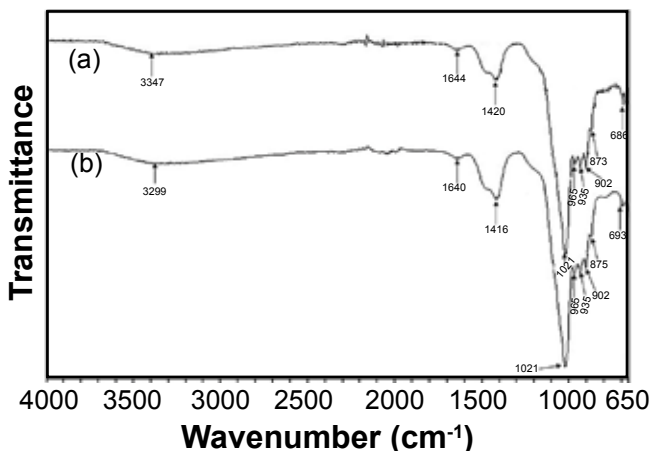


Figure 8: FTIR spectra showing vibrational modes of BG soaked in SBF for 7 days (a) and 14 days (b).

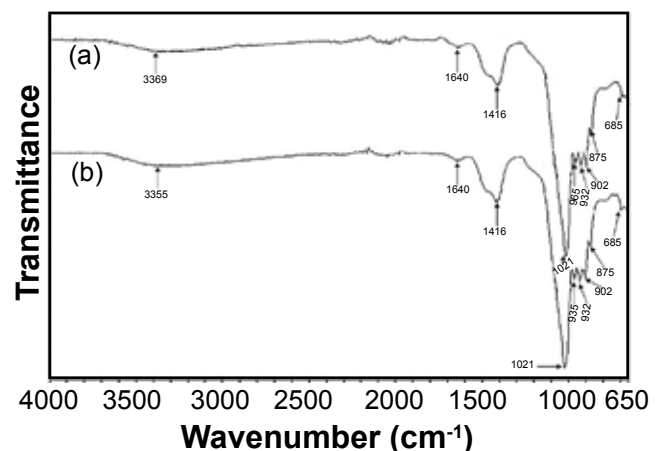


Figure 9: FTIR spectra showing vibrational modes of BG_F soaked in SBF for 7 days (a) and 14 days (b).

the degradation of the silicate peaks as stated earlier. One major concern about glasses in the system $\text{SiO}_2\text{-Na}_2\text{O-CaO-P}_2\text{O}_5$ is that on sintering they crystallize to form combeite ($\text{Na}_2\text{Ca}_2\text{Si}_3\text{O}_9$), which adversely affects their degradability in biological fluids [9-14]. It is quite remarkable, therefore, that the samples herein obtained by substituting Na_2O with K_2O in the composition possessed two important attributes: bioactivity and biodegradability. The parent peaks still observed in the spectrum at high intensity after the immersion experiment were mainly those of CaSiO_3 and CaCO_3 . Even though K_2CaSiO_4 presented some degree of crystallinity after sintering, it became resorbable in SBF as evidenced by its low baseline intensity after the incubation experiment. Thus, crystallinity did not jeopardize the bioactivity of K_2CaSiO_4 . This was in contrast to crystalline $\text{Na}_2\text{Ca}_2\text{Si}_3\text{O}_9$, which decreases the rate of HA formation on a glass surface [11]. The degradation kinetics of a scaffold must match the regeneration kinetics of new bone *in vitro* and/or *in vivo* to have a useful application as an implant [10].

FTIR spectroscopy was used to confirm the presence of bonds related to HA in the samples. For BG, after immersion in SBF for 7 days (Fig. 8a) the vibrational modes showed that the doublet at 1476 and 1405 cm^{-1} fused into a single band centered at 1420 cm^{-1} . At the same time, a shoulder developed at 873 cm^{-1} , suggesting carbonate incorporation to give crystalline HA [34]. Further evidence of the formation of crystalline HA was provided by the emergence of the small peak around 965 cm^{-1} due to the presence of P-O bonds in crystalline HA [35]. The formation of apatite-like crystals was also indicated by the small peak near 686 cm^{-1} in the spectrum resulting from symmetric valence oscillations of the P-O-P bridge bonds, formed by the condensation of the PO_4^{3-} tetrahedron due to better structural ordering [36, 37]. After immersion for 14 days in SBF (Fig. 8b), the vibrational modes of the HA-related bonds did not change significantly, only a slight increase in the intensity of the carbonate band around 1416 cm^{-1} was observed. This was in consonance with the SEM result shown in Fig. 5. A similar trend was observed in the FTIR spectra of BG_F immersed in SBF for 7 and 14 days, as shown in Fig. 9.

CONCLUSIONS

A glass-ceramic scaffold of the $\text{SiO}_2\text{-K}_2\text{O-CaO-P}_2\text{O}_5$ system was designed and synthesized through a modified sol-gel approach that utilized solution precipitation, reagent encapsulation, and foam replication. Na_2O was substituted with K_2O in the composition to prevent crystallization during thermal treatment to $\text{Na}_2\text{Ca}_2\text{Si}_3\text{O}_9$, which reduces bioactivity. A homogeneously porous bioactive glass-ceramic scaffold (porosity: 92%; average pore size: 36 ± 6 μm) with well-distributed pores that retained the pore architecture of the polyurethane foam used as a template for the ceramic coating of the glass was obtained. The porous scaffold induced hydroxyapatite (HA) formation on its surface during *in vitro* bioactivity experiments in simulated body fluid (SBF) for 7 and 14 days which further crystallized through carbonate

incorporation. An important finding is that the potassium calcium silicate crystalline phase (K_2CaSiO_4) formed in the glass-ceramic did not impede its bioactivity but it was resorbed when immersed in SBF. These behaviors imply that the material could be tailored to achieve the desirable properties of bioactivity and degradability at a much significantly better rate than those composed of $\text{Na}_2\text{Ca}_2\text{Si}_3\text{O}_9$ crystals. Equally significant is that the preparation process is cost-effective and facile, i.e., not requiring highly expensive analytical grade reagents, like alkoxysilanes as silica precursors. Hence an economic process for large-scale preparation of porous, bioactive glass-ceramic scaffolds is achievable through the present method.

ACKNOWLEDGEMENT

The authors wish to thank Engr. Nura Adamu of the National Geological Research Laboratory, Nigerian Survey Agency, Kaduna State, Nigeria for the SEM, EDX, XRD, and FTIR spectroscopy analyses of the samples.

REFERENCES

- [1] F.J. O'Brien, Mater. Today **14** (2011) 88.
- [2] J.R. Jones, A.R. Boccaccini, in "Cellular ceramics: structure, manufacturing, processing and applications", M. Scheffler, P. Colombo (Eds.), Wiley-VCH, Weinheim (2005) 550.
- [3] C. Wu, J. Chang, Interface Focus **2** (2012) 292.
- [4] M. Łączka, K. Cholewa-Kowalska, A.M. Osyczka, Ceram. Int. **42** (2016) 14313.
- [5] L. Hupa, K.H. Karlsson, M. Hupa, H.T. Aro, Eur. J. Glass Sci. Technol. A **51** (2010) 89.
- [6] R.J. Jones, Acta Biomater. **9** (2013) 4457.
- [7] O. Peitl, E.D. Zanotto, S.C. Serbena, L.L. Hench, Acta Biomater. **8** (2012) 321.
- [8] H. Arstila, L. Hupa, K.H. Karlsson, M. Hupa, J. Non-Cryst. Solids **354** (2008) 722.
- [9] V.J. Shirliff, L.L. Hench, J. Mater. Sci. **38** (2003) 4697.
- [10] Q.Z. Chen, I.D. Thompson, A.R. Boccaccini, Biomaterials **27** (2006) 2414.
- [11] O. Peitl, G.P. LaTorre, L.L. Hench, J. Biomed. Mater. Res. **30** (1996) 509.
- [12] D.C. Clupper, J.J. Mecholsky Jr., G.P. LaTorre, D.C. Greenspan, J. Biomed. Mater. Res. **57** (2001) 532.
- [13] D.C. Clupper, J.J. Mecholsky Jr., G.P. LaTorre, D.C. Greenspan, Biomaterials **23** (2002) 2599.
- [14] L.A. Adams, E.R. Essien, A.T. Adesalu, M.L. Julius, J. Sci. Adv. Mater. Devices **2** (2017) 476.
- [15] V.J. Shirliff, L.L. Hench, J. Mater. Sci. **38** (2003) 4697.
- [16] V. Cannillo, A. Sola, Ceram. Int. **35** (2009) 3389.
- [17] L.D. Silva, F.C. Puosso, V.O. Soares, O. Peitl Filho, S.D.R. Sabino, F.C. Serbena, M.C. Crovace, E.D. Zanotto, Ceram. Int. **47** (2021) 18720.
- [18] L.A. Adams, E.R. Essien, E.E. Kaufmann, J. Asian Ceram. Soc. **6** (2018) 132.
- [19] D. Bellucci, V. Cannillo, A. Sola, Mater. Lett. **65** (2011) 1825.

- [20] T. Kokubo, H. Takadama, *Biomaterials* **27** (2006) 2907.
- [21] S. Limmahakhun, A. Oloyede, K. Sitthiseripratip, Y. Xiao, C. Yan, *Addit. Manuf.* **15** (2017) 93.
- [22] N. Abbasi, S. Hamlet, R.M. Love, N.-T. Nguyen, *J. Sci. Adv. Mater. Devices* **1** (2020) 5.
- [23] Q.L. Loh, C. Choong, *Tissue Eng. B* **19** (2013) 485.
- [24] C.M. Murphy, M.G. Haugh, F.J. O'Brien, *Biomaterials* **31** (2010) 461.
- [25] L. Morejon, J.A. Delgado, A.A. Ribeiro, M.V. de Oliveira, E. Mendizaba, I. Garcia, A. Alfonso, P. Poh, M. van Griensven, E.R. Balmayor, *Int. J. Mol. Sci.* **20** (2019) 1790.
- [26] P. Kongsuwan, G. Brandal, Y.L. Yao, *J. Manufac. Sci. Eng.* **137** (2015) 31004.
- [27] X. Liu, C. Din, P.K. Chu, *Biomaterials* **25** (2004) 1755.
- [28] V. Aina, G. Malavasi, P.A. Fiorio, L. Munaron, C. Morterra, *Acta Biomater.* **5** (2009) 1211.
- [29] B.C. Babu, S. Buddhudu, *J. Spectrosc. Dyn.* **4** (2014) 5.
- [30] R.L. Frost, R. Scholz, A. López, Y. Xi, *Spectrochim. Acta A Mol. Biomol. Spectrosc.* **124** (2014) 243.
- [31] M. Cerruti, C. Morterra, *Langmuir* **20** (2004) 6382.
- [32] L.L. Hench, R.J. Splinter, W.C. Allen, T.K. Greenlee, *J. Biomed. Mater. Res.* **5** (1971) 117.
- [33] M.E. Fleet, X. Liu, P.L. King, *Am. Mineral.* **89** (2004) 1422.
- [34] L.A. Adams, E.R. Essien, *J. Adv. Ceram.* **5** (2016) 47.
- [35] G.D. Sasso, Y. Asscher, I. Angelini, L. Nodari, G. Artioli, *Sci. Rep.* **8** (2018) 12025.
- [36] Y.M. Moustafa, K. El-Egili, *J. Non-Cryst. Solids* **240** (1998) 144.
- [37] Q. Williams, E. Knittle, *J. Phys. Chem. Solids* **57** (1996) 41.
- (*Rec.* 15/08/2022, *Rev.* 22/10/2022, 14/11/2022, *Ac.* 23/11/2022)



Sedimentation and rheological behavior of reactive and non-reactive magnesium hydroxide pulps for industrial spray dryer processing

E. C. Campos¹, D. H. S. Chaves^{1}, C. M. F. Santos¹, S. D. F. Rocha², V. S. Birchal¹*

¹Universidade Federal de Minas Gerais, Graduate Program in Chemical Engineering, 31270-901, Av. Pres. Antônio Carlos 6627, Belo Horizonte, MG, Brazil

²Universidade Federal de Minas Gerais, Mining Engineering Department, 31270-901, Belo Horizonte, MG, Brazil

Abstract

Two different reactive concentrated magnesium hydroxide (HM) pulps, produced in a lab reactor mill, and a synthetic and non-reactive HM-pulp, for comparative analyses, have been prepared and studied. Sodium polyacrylate was selected as a dispersant for improving the HM pulp fluidity, with concentrations varying from 0.42% to 2.0% on a dry basis. The two reactive pulps differed from each other mainly by the impurity level and for both, a residual MgO amount was detected, implying that the hydration reaction could proceed. Results (with and without dispersant) confirmed the formation of particle clusters as HM concentration rose until a critical value, above which the pulp behaved as a solid. Reactive HM-pulps with high impurities may represent a limiting factor in the drying operation. Among all HM-pulps studied, the purest reactive pulp with 1% dispersant presented the best flow behavior making this reactive pulp the most suitable to be tested in a pilot spray dryer.

Keywords: physical-chemical characterization, rheology, sedimentation, stability, structural particle arrangements.

INTRODUCTION

In the last few decades, the interest in magnesium hydroxide (HM), $\text{Mg}(\text{OH})_2$, has grown due to its use in several industrial processes, such as: alkali agent, adsorbent of heavy metals and organic contaminants in wastewater, and effluent treatments [1, 2]; fire retardant in polymers and epoxy resins [3, 4]; silica removal and desulfurization of environments [2, 5]; bleach and preservative in the papermaking process [6]; fertilizer in the agricultural sector [7]; stabilizer for controlled release of biologically active proteins [8]; and precursor in the production of other magnesium compounds [9]. Caustic magnesia hydration is one of the most known and advantageous routes to obtain HM, especially in countries with natural magnesite ore reserves, such as China, Turkey, Russia, and Brazil, which are responsible for more than half of the world's magnesite mine production [10]. The reaction mechanism comprises three main steps: the magnesium oxide dissolution, the solution supersaturation by magnesium and hydroxyl ions, and the hydroxide precipitation. This latter step represents a barrier in the process yield because HM formed is just deposited on the MgO particle surface, slowing and/or ending the reaction [11, 12]. Therefore, improvements are demanded in HM production, making processes more profitable and feasible to generate particles with the sizes and morphology required by the actual market demand.

Generally, mineral pulps behave as viscoelastic materials with predominant viscous behavior but with solid-like characteristics [13]. Concentrated HM pulps with solid concentration $C_s \geq 35$ wt% are difficult to handle, pump, and process because of their high apparent viscosity ($\eta > 5$ -10 Pa.s at low shear rates) and due to the tendency to stick together in a cake form, making impossible its reconstitution in water [14, 15]. Furthermore, if these pulps are not continuously agitated, particles may aggregate by interconnecting themselves into a lattice structure and due to water expulsion, resulting in irreversible networks that behave as a rigid solid [1, 16, 17]. This problem affects the transportation, processing, and storage of concentrated HM pulps, so, it encourages new advances in producing HM powder with specific properties. A new route for HM production is proposed using an equipment that performs simultaneously the MgO hydration reaction and the particle comminution [18]. The spray dryer is suggested to replace the commonly used rotary dryer to be able to form HM powder with predefined characteristics. Using a lab reactor mill and caustic magnesia with 98.2% of MgO, the technical feasibility of performing the MgO hydration reaction and the particle comminution simultaneously has been confirmed reaching conversions of MgO to HM up to 5% higher than one obtained in a conventional caustic magnesia hydration route (CSTR) under the same operation conditions [18]. The feasibility of using the spray dryer for producing powder from these HM pulps requires knowledge of their sedimentation behavior, their rheology as well as their particle size distribution. There are no studies yet on sedimentation and the rheological behavior of reactive HM

*diegohschaves@outlook.com

<https://orcid.org/0000-0002-4611-9256>

pulps. Reactive pulps prepared from different sources of caustic magnesia may behave differently during continuous operation due to different purity contents.

This work aims to analyze the characteristics and stability of reactive HM pulps produced in a reactor mill equipment for evaluating the feasibility of drying them in a spray dryer. Therefore, two different reactive and concentrated HM-pulps produced in a lab reactor mill were characterized concerning the chemical composition, physical properties (density, particle size, and structure), sedimentation stability, and rheological behavior. For comparison of results, synthetic and non-reactive pulps prepared by a standard commercial HM powder were also characterized using the same methodology. As these pulps have high solid concentrations, problems with their pumping and atomization should be minimized to allow drying operation. Thus, the addition of a dispersant to these pulps for improving their fluidity was also analyzed.

MATERIALS AND METHODS

Preparation of magnesium hydroxide pulps: the HM pulps have been produced in a reactor mill under optimum operating conditions [18]: feed: caustic magnesia suspension varying from 25 to 30 wt% and 0.2 mol/L acetic acid (Labsynth, Brazil); initial temperature=25 °C; operating time=5 h. The reactor mill equipment had an internal volume corresponding to 2.0 L with a diameter of 0.12 m and a height of 0.18 m. Caustic magnesia came from two different Brazilian mineral sources: magnesia A with 91% of MgO and magnesia B with 99% of MgO. HM pulps left the reactor mill in the pH range from 11 to 12 (11.8 on average) and remained at this range due to the buffer effect of HM suspensions [18]. HM-A and HM-B pulps were produced for each test performed since they were reactive and hence could not be stored and/or processed for more than 3 h (stable time scale) at 25 °C. Samples were taken from these pulps to determine: i) solid concentration, $C_s (=m_s/m_{susp})$, by measuring the sample mass (m_{susp}) and the solids mass (m_s), which was made after washing the sample with acetone R.G. (Labsynth, Brazil) and drying it in an oven (Med-Clave, LTE Scient., UK) at 120 °C for 2 h; ii) magnesium hydroxide concentration in dry basis, $X_{HM}=m_{HM}/m_s$ (HM mass/solid mass), by calculating m_{HM} as a sum of the HM mass generated by the MgO hydration reaction plus one already presented in the precursor sample [18]. Mass measurements were made in a high-precision analytical balance (AY220, Shimadzu, USA) in triplicate. Synthetic HM pulps (HM-R) were prepared from a commercial HM powder, analytical standard with 97% of purity and $9.5 \leq \text{pH} \leq 10.5$ (Labsynth, Brazil). To obtain the desired HM-R solid concentration, HM-R powder was added to distilled water inside a glass beaker (Prolab, Brazil) with a mechanical stirrer (713D, Fisatom, Brazil) under a constant agitation of 650 rpm. The NaPA dispersant (KemEcal 211, Kemira Chem., Brazil) had a low molar mass and it came as a light amber aqueous solution with 40% of solid concentration (in mass), pH of

7 to 8, density and viscosity at 25 °C equal to 1300 kg/m³ and 0.045 to 0.070 Pa.s, respectively. This solution was added to HM pulps under a constant agitation of 650 rpm. Preliminary tests performed in a digital rotary viscometer (LVDV-I Prime, Brookfield, USA) defined the working range of the dispersant concentration, which was expressed in dry basis, $X_{disp}=m_{disp}/m_s$. The selected X_{disp} range used in experiments was: 0.42% to 2% for HM-R pulps and 1% to 2% for HM-A and HM-B pulps. This range was in accordance with the recommended literature: $m_{NaPA}/m_s \geq 0.6\%$ (corresponding to $X_{disp} \geq 1.5\%$ for KemEcal 211 solution) [1] and $0.30\% \leq X_{disp} \leq 3.50\%$ [19]. $X_{disp}=3\%$ was also used, when necessary, to complement data.

Solids characterization: the HM pulp characterization included: i) identification of mineral crystalline phases by the X-ray diffraction using a diffractometer (PW 1710, Philips-PANalytical, Netherlands) equipped with copper anode (characteristic $K\alpha$ radiation); ii) measurements, in triplicate, of density at 25 °C by the pycnometric method, using the high precision analytical balance and a calibrated 10 mL glass pycnometer (Prolab, Brazil); iii) determination of particle size distribution by the laser diffraction equipment (Helos12LA, Sympatec, Germany) using the following procedure: filtering (Labsynth, Brazil; filter blue/purple dot) and washing the particle samples with acetone R.G. to avoid further MgO hydration reaction; drying them in an oven (Med-Clave, LTE Scient., UK) at 120 °C for 2 h; dispersion of 1 g of particle sample in a sodium hexametaphosphate solution (Labsynth, Brazil) and homogenization of the dispersion in an ultrasonic system (Vibra-cell, Sonics, USA) with 2.5 s pulsation to minimize particle agglomeration; and carrying out the test in the laser diffraction equipment.

Sedimentation experiments: these experiments were performed by a traditional batch method. After preparing the HM pulp (with or without dispersant), it was well homogenized with the mechanical stirrer (713D, Fisatom, Brazil) at 650 rpm, and a 250 mL aliquot was transferred to a glass graduated cylinder (Prolab, Brazil). This aliquot was then stirred with a glass rod (Prolab, Brazil) to prevent the adherence of particles to the cylinder wall. Since HM pulps were concentrated, Stokes law could not be applied to calculate the particle settling velocity, v_{sed} [20]. This velocity is straightly related to the type of interaction forces between particles/aggregates and can be estimated by the numerical differentiation, using the central difference formula of two points or four points [21].

Rheological behavior experiments: experiments for determining the rheological behavior of HM pulps were performed in a properly calibrated rotary viscometer (LVDV-I Prime, Brookfield, USA) with the R13 adapter for processing small fluid samples (8 mL) and the SC04-18 coaxial cylindrical rotor (range: 0.003 to 10 Pa.s). The experimental procedure for these tests was adapted from the ASTM D2196-05 standard and from the viscometer-specific manual for sticky substances. Two data sets were produced to analyze the rheological behavior of HM pulps at three different temperatures: 27, 35, and 50 °C (± 2 °C). One set

comprised three cycles of runs that generated data to obtain curves of shear stress, τ , as a function of the shear rate, $\dot{\gamma}$, for decreasing and increasing $\dot{\gamma}$ continuously. In this data set, the apparent viscosity, η , and τ were recorded at $\dot{\gamma} = 132, 66, 23.4, \text{ and } 13.2 \text{ s}^{-1}$. The first cycle involved measurements in a descending shear-rate ramp while the second one, which followed immediately the first, was in an ascending shear-rate ramp. The third cycle involved measurements in a descending shear-rate ramp after resting the sample for a few seconds. The other data set included two runs that generated data to obtain curves of τ in the function of time, t , during 20 min at two distinct values of $\dot{\gamma}$ (132 and 60 s^{-1}). Measurements in both sets of experiments were made after the time required for stabilizing the viscosimeter reading (30 to 60 s). These data sets were replicated for each HM pulp used at each temperature, for determining the experimental error.

RESULTS AND DISCUSSION

Chemical characterization: X-ray diffractograms obtained for HM pulps are shown in Fig. 1. For the HM-R (Fig. 1a), brucite was the Mg carrier phase, identified in the characteristic peaks of 2θ ($18^\circ, 33^\circ, 51^\circ, 59^\circ, 63^\circ, 72^\circ, 82^\circ$) using ICDD data. Other minority minerals were also detected as those containing Mg (chlorite, talc, magnesite, dolomite) and Ca (calcite). For HM-A (Fig. 1b) and HM-B (Fig. 1c), brucite was identified in the characteristic peaks of 2θ at $18^\circ,$

$38^\circ, 51^\circ, 59^\circ,$ and $63^\circ,$ and $18^\circ, 33^\circ, 38^\circ, 51^\circ, 59^\circ, 63^\circ, 72^\circ,$ and $82^\circ,$ respectively. In HM-B, the mineral containing Ca was only calcite, while in HM-A dolomite was also detected. As expected, in HM-A and HM-B pulps, residual periclase was identified, indicating that MgO hydration reaction could proceed, slowly or fast, depending on the pulp conditions. There was no trace of periclase in the synthetic HM-R pulp. In addition to the minerals identified in Fig. 1, the presence of iron (Fe), manganese (Mn), and traces of titanium (Ti), copper (Cu), sulfur (S), phosphorus (P), and chlorine (Cl) were confirmed in HM-R. Traces of Fe and Mn were also confirmed in HM-A and HM-B pulps. By the quantitative and qualitative X-ray fluorescence analysis of the HM-R powder, the concentration of HM (calcined form=MgO) was in the range of 97%, corroborating the value supplied by the manufacturer.

Particle size analysis of solids in magnesium hydroxide pulps: the diameters $D_{15.9}, D_{50},$ and $D_{84.1}$ (particle/cluster size diameter for the cumulative distribution of 15.9%, 50%, and 84.1%, respectively) for the solid phase of HM-R, HM-A, and HM-B pulps with their particle size dispersion index, ID, defined by Eq. A are presented in Table I, which also summarizes C_s and X_{HM} values obtained for HM pulps analyzed. It was possible to verify that D_{50} for HM-R particles was up to 28% above D_{50} for HM-A30 and HM-B32 particles. However, this 28% was in the range of experimental error by considering the mean value of $D_{50}=6.7\pm 1.0 \mu\text{m}$ for HM-A (HM-A30 and HM-A34) and $D_{50}=5.6\pm 1.0 \mu\text{m}$ for HM-B

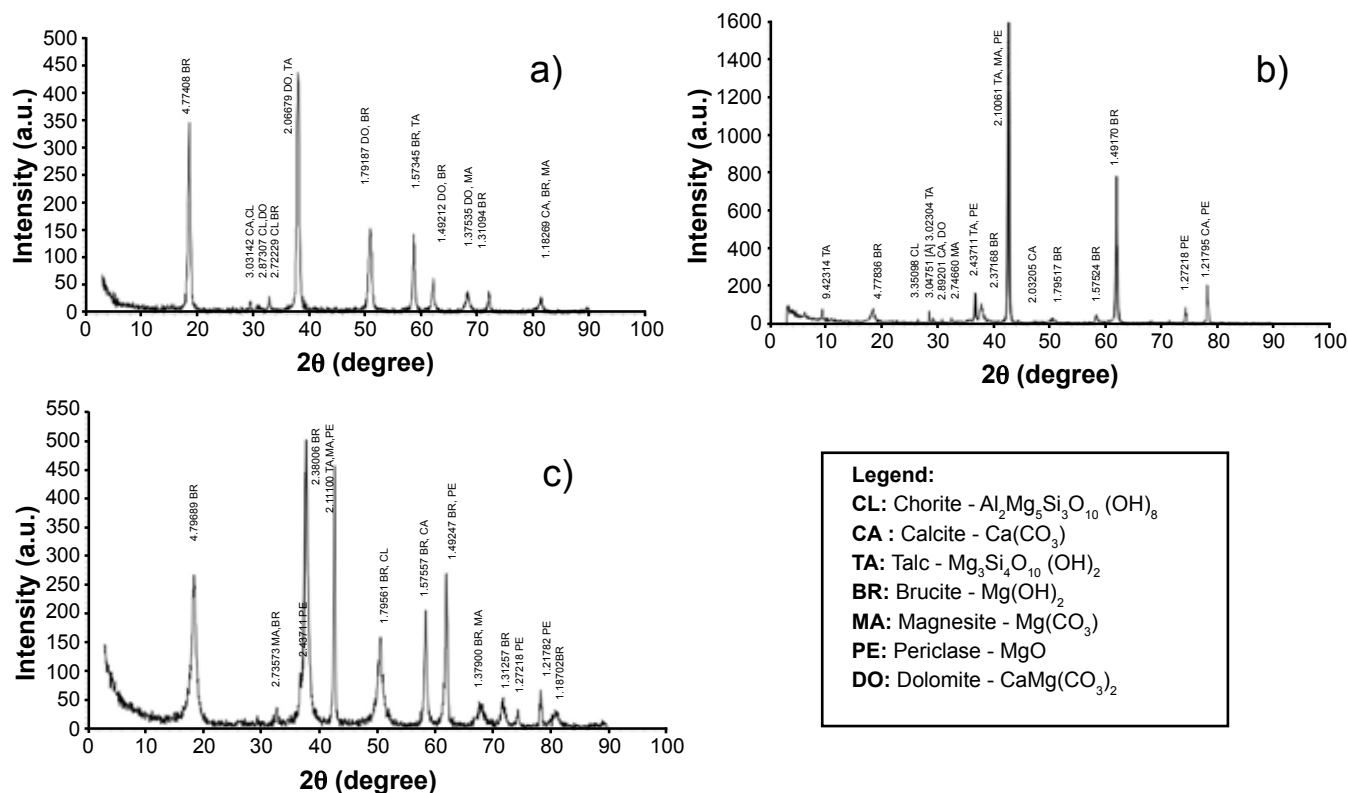


Figure 1: X-ray diffractograms with characteristic peaks of minerals present in: a) HM-R; b) HM-A; and c) HM-B pulps. The number above each diffraction peak is the interplanar distance in Å.

(HM-B32 and HM-B39). Although these three HM pulps presented a similar D_{50} particle size for the solid phase, their particle size dispersion index, ID, was different, indicating that HM-R particles presented the widest particle size dispersion. It is important to emphasize that HM particles were aggregates of primary particles as shown in Fig. 2.

$$ID = \frac{D_{84.1} - D_{15.9}}{2D_{50}} \quad (A)$$

As seen in Fig. 2, HM particles obtained in a CSTR (conventional caustic magnesia hydration route) were aggregated in different structures from those of HM particles produced in the reactor mill. This implied that the combination of the MgO hydration reaction with the particle comminution in a reactor mill affected the particle shape and surface area, and, consequently, the interconnections between particles. Since the HM-R powder was produced by another process route, its particle structural form should be quite different from that of HM-A and HM-B. HM production process is major responsible for first defining the

structural arrangement and surface area of HM nanoparticles [22]. Consequently, the particle surface interactions with NaPA dispersant must differ between HM-R and HM-A or HM-B particles, explaining density ratio trends in Table II.

Magnesium hydroxide pulp density: results at 25 °C for the HM pulp density ratio, $\rho_{\text{susp},X}/\rho_{\text{susp},0}$ (with and without dispersant) are presented in Table II, together with experimental values of $\rho_{\text{susp},X}$ at X_{disp} . The overall error for ρ_{susp} was $\pm 3 \text{ kg/m}^3$ and the maximum error was $\pm 11 \text{ kg/m}^3$. ρ_{susp} increased with the increase in C_s moreover, ρ_{susp} ($C_s=30\text{-}35\%$) values for the three HM pulps were practically equal within an error lower than the maximum experimental one. This indicated the similarity in the mineralogical composition of the three pulps analyzed corroborating the pulp age stability during experiments (less than 3 h). Data from Table II demonstrated that the HM-R density ratio decreased with the dispersant addition (from 1.000 to 0.977 and then to 0.991). Although the HM-A density ratio tended to rise as X_{disp} increased, the values obtained remained in the same range of $\rho_{\text{susp},0}$ following the experimental error (± 0.006). The HM-B ratio increased slightly with X_{disp} . Therefore, these three HM

Table I - Solid characterization of HM pulps analyzed.

HM pulp	C_s (%)	X_{HM} (%)*	$D_{15.9}$ (μm)	$D_{84.1}$ (μm)	D_{50} (μm)	ID
HM-A30	29.6	78.0	1.56	12.91	6.08	0.91 \pm 0.04
HM-A34	33.7	82.4	1.67	14.74	7.24	
HM-B32	32.4	90.3	1.61	12.41	5.91	
HM-B39	38.6	90.8	1.58	10.74	5.25	
HM-R (powder)	N.A.	97.0				0.96
HM-R20	20.0	97.0				
HM-R30	30.0	97.0	2.63	15.60	6.74	
HM-R37	37.0	97.0				

$C_s = m_s/m_{\text{susp}}$; $X_{\text{HM}} = m_{\text{HM}}/m_s$; *: % in dry basis; N.A.: not applicable.

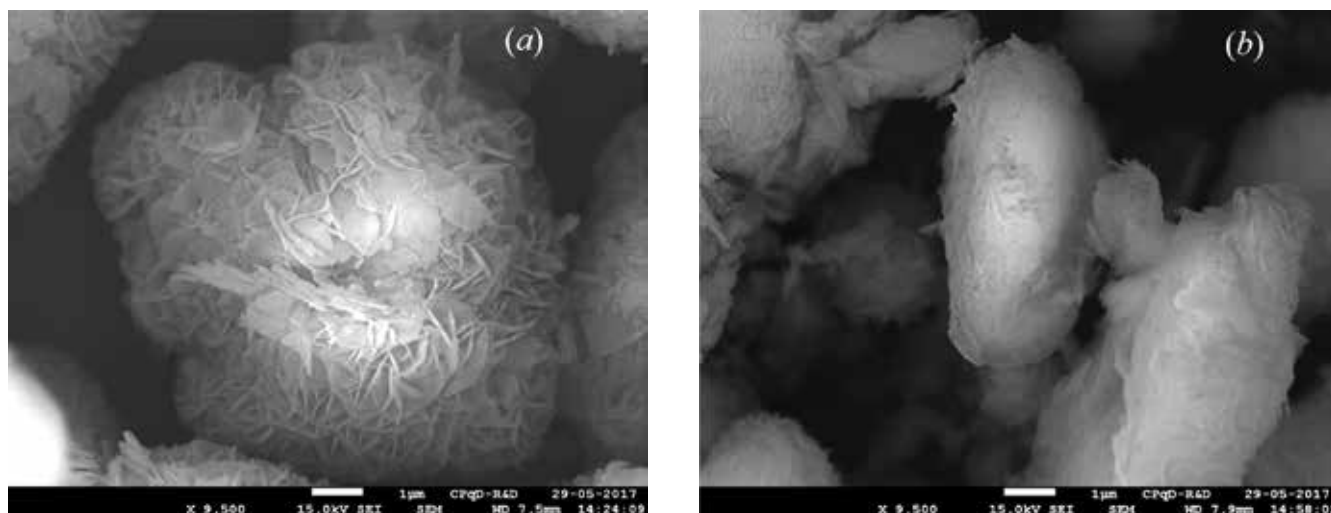


Figure 2: HM particles formed by the hydration of magnesia after 8 h of reaction in a CSTR (a) and reactor mill (b). Backscattered electron images obtained with a scanning electron microscope at 15 kV.

Table II - Densities of the HM pulps with dispersant at a preset dispersant concentration.

HM pulp with dispersant	X_{disp} (%)	$\rho_{susp,X}$ (kg/m ³)	$\frac{\rho_{susp,X}}{\rho_{susp,0}}$
HM-R20-04	0.42	1122	0.987
HM-R20-08	0.84	1124	0.989
HM-R30-1	1.00	1176	0.977
HM-R30-2	2.00	1193	0.991
HM-A30-1	1.00	1208	1.002
HM-A30-2	2.00	1212	1.005
HM-B32-1	1.00	1219	1.010
HM-B32-2	2.00	1221	1.012

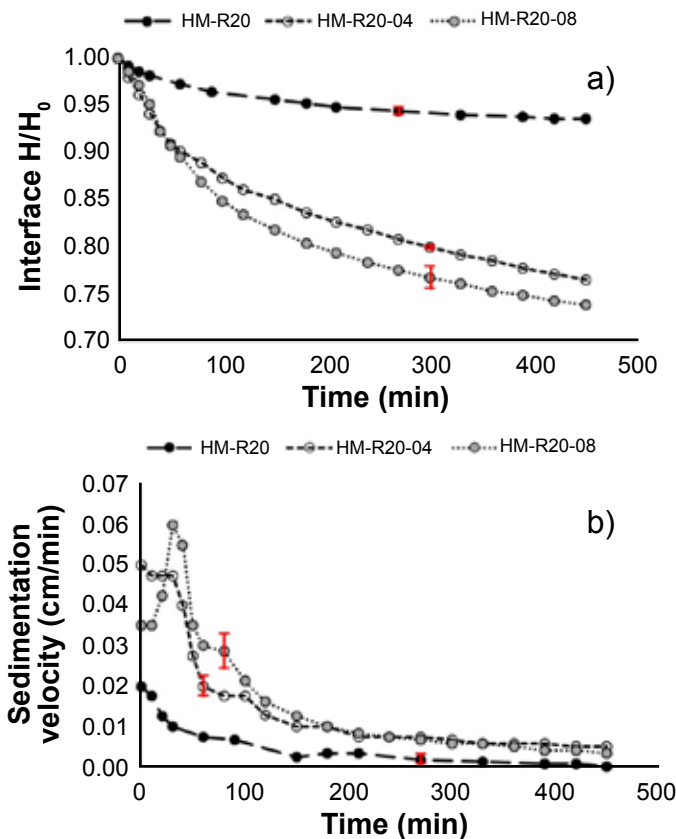


Figure 3: Sedimentation profile (a) and sedimentation velocity (b) curves as a function of time for HM-R20, HM-R20-04, and HM-R20-08 pulps.

pulps behaved differently when the dispersant was added as their values of $\rho_{susp,X}/\rho_{susp,0}$ differed from one another at the same C_s and X_{disp} . As analyzed in the particle size analysis of solids subsection, this difference in behavior may be related to particle morphology (size, shape, structural arrangement).

Sedimentation: the HM pulp sedimentation analysis focused on establishing parameters to well define the system stability, as well as, contributing to a better understanding of the bonds prevailing between particles and/or

aggregates. In this analysis, sedimentation was expressed by its dimensionless parameter, H/H_0 , experimental data points were interconnected by dotted lines without any statistical adjustment, and the experimental error based on replications was displayed, if necessary, in the respective curves obtained. The sedimentation velocity, v_{sed} , decreased exponentially with the increase in the solid concentration, C_s , in accordance with data and trends reported in the literature [21, 23]. For $C_s \geq 0.31$, v_{sed} tended to be negligible (8×10^{-5} cm/s), meaning no sedimentation as a solid phase behavior [17]. Particle interconnections, especially those resulting in rigid three-dimensional networks, destabilize HM pulps, causing changes in their properties. Fig. 3 presents curves for HM-R20 pulps without dispersant, HM-R20-04, and HM-R20-08. As seen in Fig. 3b, the addition of dispersant increased v_{sed} at the initial sedimentation period (increased to $1.7 v_{sed, HM-R20}$ for HM-R20-04 and to $2.5 v_{sed, HM-R20}$ for HM-R20-08 both compared to HM-R20 at $X_{disp}=0$), because the particle mobility was enhanced due to enlarged space between particles promoted by the dispersant. However, preferential channels seemed to be formed for drainage of water expelled from the densest particle structure as the pulp was compressed at the container bottom (shown by peaks obtained).

Fig. 4 presents the v_{sed} vs. t curves for the HM-R30 (Fig. 4a) and for HM-R30-1 and HM-R30-2 (Fig. 4b) pulps. For HM-R30 pulp, the NaPA addition slowed slightly the H/H_0

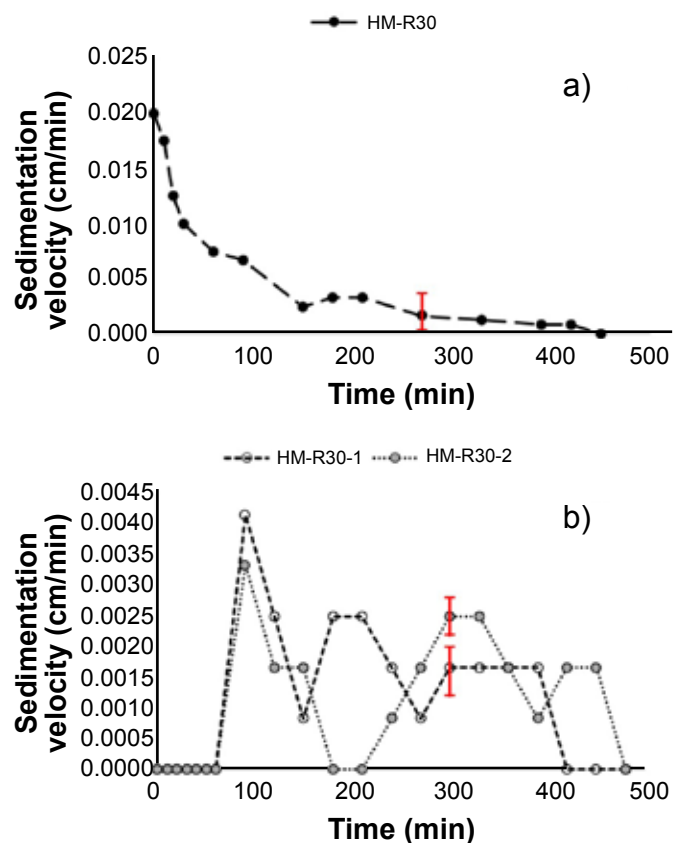


Figure 4: Sedimentation velocity as a function of time for HM-R30 (a), HM-R30-1 and HM-R30-2 (b) pulps.

decay at high dispersant concentrations ($X_{disp} = 1\%$ and 2%). These three curves provided additional information about particle interactions, showing noticeable peaks that resulted from preferential channels for flowing liquid (water). The formation of these channels induced an increase in v_{sed} followed by an abrupt decrease in v_{sed} due to water expulsion. This caused a highly compact pulp with clusters/aggregate consolidation in reticulated structures. As shown in Fig. 4b, an increase in disturbances in v_{sed} was observed at $X_{disp} = 1\%$ and 2% , denoting an increase in the preferential channel formation for water drainage. Due to the dispersant action, the weak particle interconnections were broken easily and rearranged continuously in new structures, resulting in the random formation and collapse of preferential channels. This caused great fluctuations in v_{sed} and restrained particle mobility. Sedimentation becomes significant on the time scale of the experiment since the radii of the aggregates/clusters become considerably large [21].

Fig. 5 shows data of sedimentation curves of HM-A30 without dispersant (Fig. 5a) and HM-A30-2 with $X_{disp}=2\%$ (Fig. 5b). The addition of dispersant resulted in: i) slowing down the interface decay with the drop of v_{sed} ; ii) intensifying peaks and oscillations in the v_{sed} vs. t curve due to the preferential channel formation for water drainage from the compact structure in the container bottom. These trends were similar to those discussed for HM-R30. Although this work did not present HM-A30-1 data, its sedimentation had a transitional behavior between HM-A30 and HM-A30-2, showing that particle interactions were changing from flocculation to deflocculation. Data

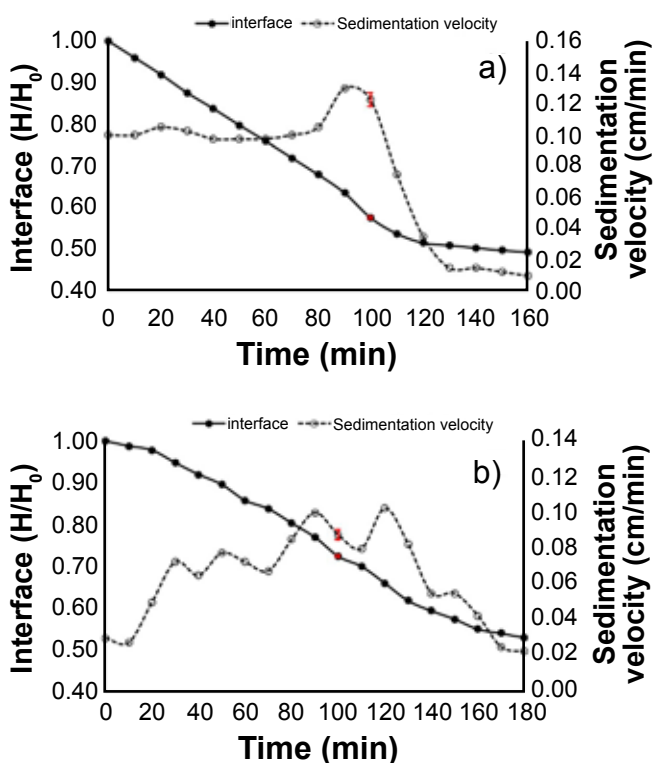


Figure 5: Sedimentation profile and velocity curves as a function of time for the pulps: a) HM-A30; and b) HM-A30-2

sedimentation for HM-A30-2 pulp showed the same trends of deflocculated suspension. The sedimentation curves for HM-A pulps produced in the reactor mill at $C_s = 30\%$ and 34% , exhibited a decrease of 50% in v_{sed} at the initial period as C_s increased. Similar to the HM-R pulp behavior, preferential channels also occurred in these HM-A pulps for drainage of water expelled from reticulated structures developed as the solid phase was compressed, but the v_{sed} oscillation was smoother (Fig. 5a). In contrast, in v_{sed} vs. t curves, a well-defined peak occurred just before the abrupt drop in v_{sed} with a significant deceleration of the solid phase compression. Visual observations confirmed the occurrence of small flocs (turbidity) in the first layer region of the HM-A pulp sample inside the cylinder. Such results suggested that the HM-A pulp sedimentation was characterized by particles that flocculated. HM-A pulps presented the lowest X_{HM} value, i.e., the highest impurity content, as well as, distinct particle morphology, which must have favored flocculation, in which attractive forces overlapped repulsive ones [24]. This corroborated the distinct behavior obtained for HM-A particle sedimentation and interconnections.

For HM-B32 pulp, the conventional sedimentation with a clarified-suspension interface formation was not detected even after 3 h of the experiment. Lumps and volcanoes were seen on the hard pulp surface and inside the dense pulp (with the removal of the pulp from the container after 3 h). The dispersant addition to this pulp, at $X_{disp} = 1\%$, 2% , and even 3% , did not alter such behavior. From these sedimentation data, one can infer that there was a maximum C_s (of which value depended on X_{HM}) at which HM pulps behaved as a rigid solid, with the attraction forces between particles predominating over the repulsion ones. For HM-R pulps ($X_{HM}=97\%$), $C_{s,max}=0.31$ as predicted from sedimentation curves. It was expected that $C_{s,max}>0.34$ for HM-A pulps ($X_{HM}\approx 81\%$) and $0.32<C_{s,max}<0.39$ for HM-B pulp ($X_{HM}\approx 90\%$).

Rheological behavior

Reactive HM-B32 pulps: for HM-B32 pulp without dispersant, although data were limited by the device operation range, τ vs. t data showed that τ increased as the temperature was raised, as well as its value became more dependent on time (Fig. 6a). This behavior should be related with two distinct phenomena occurred in the HM-B32 pulp as the temperature rose: i) acceleration of MgO hydration reaction, which increased HM and reduced H_2O in the pulp, implying in an effective augment of C_s during the experiment; ii) formation of hydroclusters (particle aggregates in chain connections) that tends to enhance the pulp resistance to flow. Note that in concentrated suspensions with C_s close to $C_{s,max}$, a small change in C_s caused significant changes in the structural particle-aggregate [16]. In addition, hydroclusters should occur in concentrated suspensions because of the particle proximity and the hydrodynamic interparticle forces generated during shear flow [16, 21]. The shear flow with the hydrocluster occurrence may retard the rigid solid network formation seen in the sedimentation experiment of this HM-B32 pulp.

For HM-B32-1 pulp, τ decreased progressively with

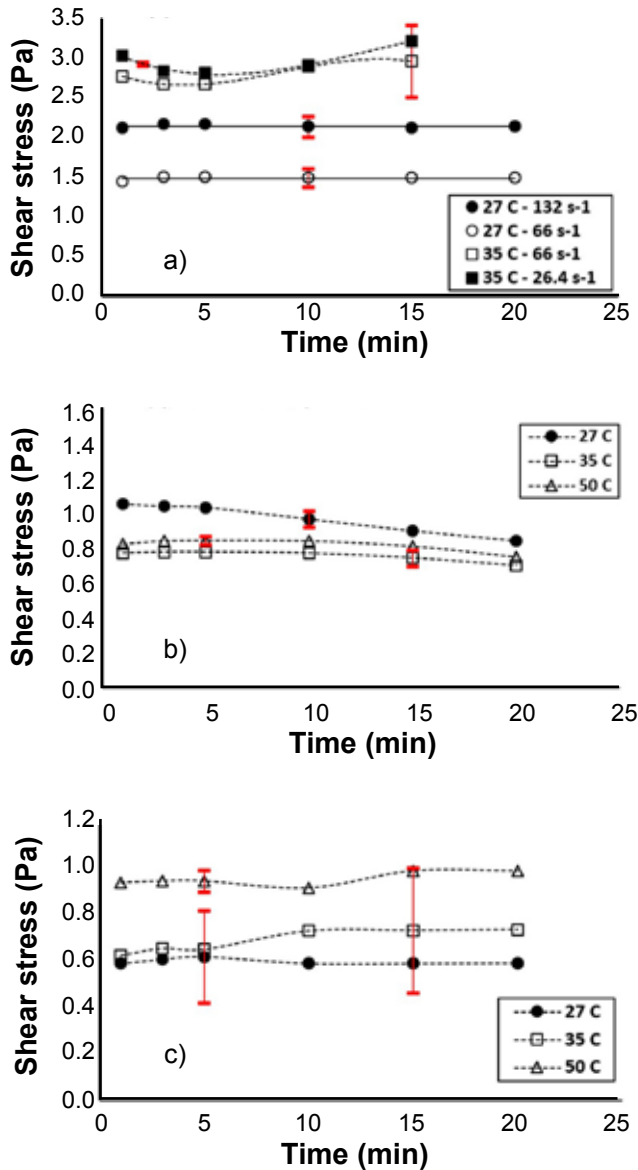


Figure 6: Shear stress as a function of time at constant shear rate and temperature: a) HM-B32 pulp; b) HM-B32-1 pulp at $\dot{\gamma}=66$ s⁻¹; and c) HM-B32-3 pulp at $\dot{\gamma}=66$ s⁻¹ (lines link data without any statistical treatment).

time for both $\dot{\gamma}$ used, as a thixotropic fluid. Fig. 6b presents a typical τ vs. t data for this pulp. Increasing the dispersant concentration from 1% to 2-3%, τ tended to increase slightly with time after 5 min of the experiment at $T>27$ °C (Fig. 6c). Moreover, there was an inversion in τ vs. t curves as the temperature rose, i.e., τ values at 27 °C were lower than those at 35 and 50 °C. At 35 °C, considerable oscillations were detected in τ values enhancing the experimental error as seen in Fig. 6c. Such transitional rheological behaviors observed for both $\dot{\gamma}$ used (66 and 132 s⁻¹) may relate to additional particles-clusters interactions. Note that hydrocluster formation occurs even with dispersant because it depends on hydrodynamic forces developed during the shear flow [25]. Depending on dispersant properties and its concentration on the particle surface, as well as, the type of molecules or ions

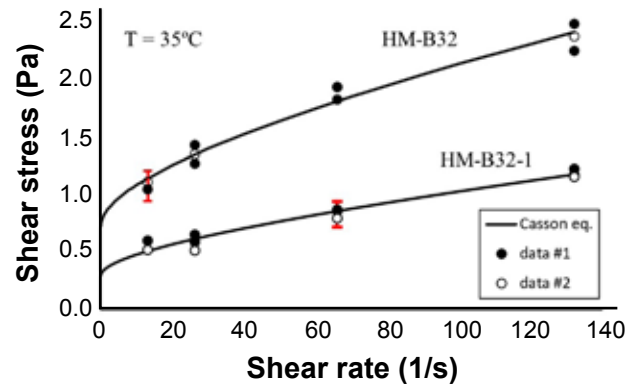


Figure 7: Typical shear stress as a function of shear rate curves at a constant temperature of 35 °C, for HM-B32 and HM-B32-1 pulps (data #1: τ vs. $\dot{\gamma}$ average values for the two first cycles; data #2: τ vs. $\dot{\gamma}$ average values for the last cycle; full line curves: best fitting of Casson model to data).

dispersed in the pulp, additional bridging interactions can appear between these constituents, hindering the particle-cluster mobility [24]. Since these interactions are weaker, they can be formed and broken quickly, giving greater oscillation, complexity, and instability in the pulp flow.

Typical τ vs. $\dot{\gamma}$ curve for HM-B32 and HM-B32-1 pulps are presented in Fig. 7. Experimental data obtained in all three cycles (descending τ - $\dot{\gamma}$ ramp; ascending τ - $\dot{\gamma}$ ramp; pulp rest/descending τ - $\dot{\gamma}$ ramp) did not differ from each other following the statistical analysis based on the experimental replication error, meaning that the hysteresis loop in τ vs. $\dot{\gamma}$ curve was statically insignificant for these two pulps. Based on the statistical analysis, the Casson model (Eq. B) fitted well these τ vs. $\dot{\gamma}$ data for the three temperatures analyzed. Data from Fig. 7 at 35 °C presented a typical fitting behavior for these two pulps. In Eq. B, τ_{0C} is the critical shear stress required for shearing the material and η_C is the apparent fluid viscosity, following the Casson model (subscript C). Both variables are the Casson model parameters, determined by fitting Eq. B to τ vs. $\dot{\gamma}$ data. Values of τ_{0C} are related to particle-cluster interactions (solid-like characteristics of the pulp) and η_C the viscous flow behavior (liquid-like characteristics of the pulp). For HM-B32 pulp, τ_{0C} and η_C varied from 0.43 to 1.81 Pa and from 4.9 to 2.1 mPa.s, respectively, as the temperature rose from 27 to 50 °C; on the other hand, for HM-B32-1 pulp, τ_{0C} and η_C varied from 0.37 to 0.45 Pa and from 2.5 to 1.1 mPa.s, respectively, as the temperature rose from 27 to 50 °C. A comparison between τ_{0C} values for HM-B32 and HM-B32-1 corroborated that the addition of $X_{disp}=1\%$ contributed to reducing: i) τ_{0C} , mainly at $T>27$ °C, improving the pulp condition to start flowing; and ii) η_C , improving the pulp condition to flow and implying a low apparent viscosity at high $\dot{\gamma}$. It is important to stress that the HM-B32 and HM-B32-1 pulp rheological behavior depended on time. Therefore, τ_{0C} and η_C values presented were restricted to a small-time interval of $t=3$ h after their production in the reactor mill equipment. Because of the instabilities in the shear flow for HM-B32-2 and HM-B32-3

pulps due to the additional particle-cluster interactions, τ vs. $\dot{\gamma}$ data depended also on the previous pulp shearing history (τ vs. $\dot{\gamma}$ curves in cycles 1, 2, and 3 differed from each one). These two pulps were considered unstable and eliminated from this analysis.

$$\tau^{1/2} = \tau_{0C}^{1/2} + (\eta_C \cdot \dot{\gamma})^{1/2} \quad (\text{B})$$

Reactive HM-A30 pulps: the τ vs. t and τ vs. $\dot{\gamma}$ data obtained for HM-A30 pulps without and with NaPA dispersant showed a remarkable dependency on the previous pulp shearing history with great oscillations in τ values at higher values of $\dot{\gamma}$ and temperature T . As confirmed by sedimentation experiments, HM-A30 was the most heterogeneous pulp, behaving as flocculated suspensions. The elevated pulp heterogeneity (different particle-flake mobilities) associated with high $\dot{\gamma}$ (high centrifugal force) and T (low liquid phase viscosity) enabled particle migration to the rotating rotor wall. This generated a liquid lubricant layer with low solid concentrations on this rotating wall, induced by particles sliding on this wall. Such behavior caused disturbances in the pulp flow, oscillations, and negative deviations from the actual τ value. The τ vs. $\dot{\gamma}$ data for these HM-A30 pulps, mainly at 50 °C, resembled those data from the characteristic rheogram of flocculated suspensions that have this particle sliding behavior [26]. Heterogeneity, oscillations, and instability detected in the shear flow of the reactive HM-A30 pulps must prevent their further operation in the spray dryer. Therefore, these pulps must be conditioned with different additive agents to improve their homogeneity and fluidity, avoiding any flocculation disturbances in the flow regime.

Non-reactive HM-R pulps: five HM-R pulps were analyzed regarding their shear flow behavior: HM-R20, HM-R20-04, HM-R20-08, HM-R30-1, and HM-R30-2. For HM-R30 pulp no data were obtained even at 50 °C because of its high flow resistance that exceeded the device reading scale, corroborating its low particle mobility identified in sedimentation experiments. The τ vs. t data for these pulps were characterized by decreasing τ along the time, except at higher T and $\dot{\gamma}$ in which τ oscillated about a constant value. The τ vs. $\dot{\gamma}$ data adjusted well to the Casson model (Eq. B), except data obtained at 50 °C that oscillated from one to another replication increasing the experimental error. These τ vs. $\dot{\gamma}$ data at 50 °C seemed to depend on the previous pulp shearing history (τ vs. $\dot{\gamma}$ in cycles 1, 2, and 3 differed slightly from each one); however, such differences among data were in the range of experimental error. Therefore, the adjustment of these τ vs. $\dot{\gamma}$ data at 50 °C to Eq. B provided average values of the Casson model parameters within a high experimental error. Based on τ_{0C} and η_C values obtained by the fitting analysis, the following trends could be drawn for the HM-R pulps: i) a significant reduction in τ_{0C} occurred with the dispersant addition, improving the necessary condition for starting flow (similar to a trend observed for HM-B30 pulps); ii) for HM-R30-1 pulp, τ_{0C} and η_C reached values of 0.75, 1.09, and 0.70 Pa and 2.6, 0.7, and 1.7 mPa.s, respectively, as the temperature rose from 27 to 50 °C; and

iii) an increase in X_{disp} from 1% to 2% in the HM-R30 pulps resulted in increasing τ_{0C} and reducing η_C . This meant that the HM-R30-2 pulp presented a great resistance to start flowing but, after overcoming τ_{0C} , this pulp flowed more easily. Such behavior implied a change of particle-cluster interactions at $X_{disp}=2\%$ in a way to restrain their mobility at the flow startup, corroborating the earlier discussion about the rheological behavior of HM-B32-2 and HM-B32-3 pulps. In the range of the operation conditions analyzed, a comparative analysis between the rheological behavior of HM-R30-1 and HM-B32-1 pulps confirmed the lowest τ_{0C} and η_C values for HM-B32-1 pulp during a short operating time ($t \leq 3$ h) and the most stable flow behavior for this pulp based on the replication τ vs. $\dot{\gamma}$ experimental data.

Preliminary experiments developed confirmed the feasibility of drying HM pulps in the spray dryer under specific operating conditions. However, to make the spray drying stage viable concerning the proposed process route, HM-powder must be produced continuously, without interruption due to the atomizer clogging. For that, the pulp must be fed in the spray dryer in an intermittent mode under rigid temperature control [27].

CONCLUSIONS

Two concentrated and reactive magnesium hydroxide (HM), $Mg(OH)_2$, pulps, HM-A (more impure) and HM-B (purer), were produced by caustic magnesia hydration in a reactor mill equipment, and they were characterized chemically and physically to evaluate the feasibility of drying them in a spray dryer. As discussed, the dispersant addition to these HM-concentrated pulps should be carefully analyzed since there was a restricted range of NaPA concentration at which this dispersant could improve the pulp flow. For non-reactive HM-R pulps, the fluid flow analysis confirmed the formation of hydroclusters. Their behavior aided in better understanding the reactive HM pulp fluid flow behavior since X_{HM} (HM mass/solid mass) was maintained constant during each experiment and its value could be easily varied from a diluted pulp to a concentrated one. As HM-A pulp became more concentrated, hydroclusters were also formed, hindering its flow. However, the heterogeneity of the HM-A pulp was the predominant restriction for operating it in the spray dryer. This HM-A pulp presented high impurities in its composition, resulting in the lowest X_{HM} value (from 78% to 82%). Reactive HM-pulps with high impurities ($X_{HM} < 90\%$) must be conditioned with different additive agents to improve their homogeneity and fluidity, before testing these pulps in the spray dryer stage. Although comparable to the one of a synthetic and non-reactive HM-pulp at ambient temperature, the flow behavior of HM-A and HM-B changed as the temperature increased due to the progress of the MgO hydration reaction. Both the water reaction consumption and the increase in HM contributed to concentrating more HM-B pulp. Considering all the above, this study allowed defining that, among all HM-pulps studied, HM-B32 pulp (HM-B with 32% solids) with 1% NaPA dispersant (HM-B32-1)

was the most stable one for a short processing period and presented the best flow behavior making this pulp the most suitable to be tested in a pilot spray dryer.

ACKNOWLEDGMENTS

The authors are immensely and sincerely grateful to Professor Maria Laura Passos for her precious contributions to this work. The authors are also grateful to the National Council for Scientific and Technological Development (CNPq) and the Research Support Foundation of the Minas Gerais State (FAPEMIG) for financial support.

REFERENCES

- [1] K. Tong, X. Song, S. Sun, Y. Xu, J. Yu, *Colloids Surf. A Physicochem. Eng. Asp.* **436** (2013) 1111.
- [2] Q. Wu, P.L. Bishop, T.C. Keener, J. Stallard, L. Stile, *Water Sci. Technol.* **44**, 1 (2001) 161.
- [3] A. Pilarska, K. Bula, K. Myszka, T. Rozmanowski, K. Szwarz-Rzepka, K. Pilarski, Ł. Chrzanowski, K. Czaczyk, T. Jesionowski, *Open Chem.* **13**, 1 (2015) 161.
- [4] S.D.F. Rocha, V.S.T. Ciminelli, *Polímeros* **11**, 3 (2001) 116.
- [5] H.N. Costa, C.C. Noberto, L.A. Almeida, R.E.F.Q. Nogueira, A.E.B. Cabral, *Cerâmica* **67**, 384 (2021) 399.
- [6] A. Thakore, J.O.B. Ringrose, A. Gibson, M. Wajer, *Pulp Pap. Canada* **106**, 5 (2005) 46.
- [7] J.H.M. Viana, A.M. Coelho, A. Thomazini, M.P.F. Carvalho, *An. Acad. Bras. Cien.* **93**, 3 (2021) e20201614.
- [8] A.A. Pilarska, Ł. Klapiszewski, T. Jesionowski, *Powder Technol.* **319** (2017) 373.
- [9] A. Pilarska, E. Markiewicz, F. Ciesielczyk, T. Jesionowski, *Dry. Technol.* **29**, 10 (2011) 1210.
- [10] U.S. Geological Survey, “Mineral commodity summaries” (2022).
- [11] S.D.F. Rocha, M.B. Mansur, V.S.T. Ciminelli, *J. Chem. Technol. Biotechnol.* **79**, 8 (2004) 816.
- [12] V.S. Birchal, S.D.F. Rocha, M.B. Mansur, V.S.T., Ciminelli, *Can. J. Chem. Eng.* **79**, 4 (2001) 507.
- [13] D.M. Núñez Ramírez, L. Medina-Torres, F. Calderas, R.H. Lara RH, H. Medrano Roldán, O. Manero, *Miner. Eng.* **121** (2018) 122.
- [14] H. Aral, M.R. Houchin, P.R. Strode, R. Van Merckestein, P. Bush, US Patent 5906804A (1999).
- [15] H. Sano, N. Matsuno, K. Okina, US Patent 3957674A (1976).
- [16] S. Mueller, E.W. Llewellyn, H.M. Mader, *Proc. R. Soc. London A* **466**, 2116 (2010) 1201.
- [17] J.Z.Q. Zhou, T. Fang, G. Luo, P.H.T. Uhlherr, *Rheol. Acta* **34** (1995) 544.
- [18] C.M.F. Santos, A.F.B. Andrade, K.C. Ferreira, S.D.F. Rocha, *Braz. Appl. Sci. Rev.* **3**, 4 (2019) 1882.
- [19] R.J. Falcione, R.R. McManis, J.A. Aufman, US Patent 4230610A (1980).
- [20] A.P.G. Lockwood, J. Peakall, N.J. Warren, G. Randall, M. Barnes, D. Harbottle, T.N. Hunter, *Chem. Eng. Sci.* **231** (2021) 116274.
- [21] B.A. Di Giovanni, F.M. Mahdi, V.M. Starov, R.G. Holdich, *Chem. Eng. Res. Des.* **90**, 9 (2012) 1168.
- [22] G. Balducci, L.B. Diaz, D.H. Gregory, *CrystEngComm* **19**, 41 (2017) 6067.
- [23] B. Camenen, D.P. Van Bang, *Cont. Shelf Res.* **31**, 10 (2011) 106.
- [24] F.S. Ortega, V.C. Pandolfelli, J.A. Rodrigues, P.A. Sepúlveda, *Cerâm. Ind.* **2**, 5-6 (1997) 34.
- [25] J. Warren, S. Offenber, H. Toghiani, C.U. Pittman Jr., T.E. Lacy, S. Kundu, *ACS Appl. Mater. Interfaces* **7**, 33 (2015) 18650.
- [26] N.G. Triantafillopoulos, *Measurement of fluid rheology and interpretation of rheograms*, Kaltec Scient., Livonia (1988) 37.
- [27] M.L. Passos, A.L.G. Trindade, J.V.H. D’Angelo, M. Cardoso, *Dry. Technol.* **22**, 5 (2004) 1041.
(*Rec. 04/11/2022, Ac. 07/12/2022*)



Tailoring the properties of Y_2O_3 via synthesis parameters varied during the PVA-assisted sol-gel route

J. C. C. Carvalho¹, G. F. C. Bispo¹, T. S. Lilge², C. S. Bezerra², A. B. Andrade²,
Z. S. Macedo^{1,2}, M. E. G. Valerio^{1,2*}

¹Federal University of Sergipe, Materials Science and Engineering Department, São Cristovão, SE, Brazil

²Federal University of Sergipe, Physics Department, Materials Preparation and Characterization Laboratory, 49100-000, São Cristovão, SE, Brazil

Abstract

The effect of synthesis parameters on the microstructural behavior and morphology during the yttrium oxide (Y_2O_3) formation is reported. Y_2O_3 crystals were produced by a modified sol-gel route assisted by polyvinyl alcohol solution varying the calcination temperature and solution pH. The crystalline phase formation was investigated using X-ray powder diffraction combined with the Rietveld refinement method. The microstructural properties were analyzed by using the Williamson-Hall formalism. The calcination temperature followed the thermal events observed in the differential thermal analysis combined with the thermogravimetric analysis of the precursor xerogel. It was seen that the combination of PVA and pH variation can be used to minimize the calcination time and temperature. The morphological analysis showed samples with different sizes and appearances depending on pH and calcination temperature. Therefore, it was shown that the parameters in the synthesis process can be used to tailor the properties of Y_2O_3 , such as crystallite size, degree of structural ordering, and morphology, and consequently, improve the desired application.

Keywords: Y_2O_3 , sol-gel method, thermal treatment, pH solution.

INTRODUCTION

The control of synthesis parameters has been of material science interest because they can change structure and morphology properties. For example, the particle size of compounds is susceptible to calcination parameters such as heating and cooling rate, plateau time, and pressure of synthesis [1]. Other features such as particle morphology depend on the synthesis method and pH solution besides synthesis conditions. All these parameters must be considered in the production of fine powders to enhance industrial applicability. However, most of the literature on material synthesis is worried only about the production of bulk without proper control of these parameters. For chemical synthesis, this can be troublesome since the pH of the solution plays an important role in the thermal events, phase formation, particle size, and particle morphology as well as luminescent properties [2, 3].

Yttria, Y_2O_3 , is a well-known compound that has been attracting the attention of researchers due to its possible applications in sensors, optoelectronics devices, solar cells, anticancer activity, and lasers, among others [4-8]. As a yttria matrix, this material is commonly employed for incorporation of other rare-earth ions which present interesting optical properties and applications. For example, Nd-doped Y_2O_3

nanocrystals synthesized by sol-gel route were investigated for application in temperature sensing of biological systems [4]. In the literature, doped- Y_2O_3 nanoparticles have been synthesized via the PVA-assisted sol-gel method for employment in luminescence applications [9]. However, the influence of pH in the synthesis was not investigated. Results from the sol-gel route have shown an increase in the relative sensitivity as temperature sensing with the increase in crystallite size, indicating that the synthesis method can be employed for the control of optical parameters [4]. Another paper [10] shows that the crystallite size of Sm-doped Y_2O_3 changed with agitation conditions during the synthesis by the sol-gel method influencing the photoluminescence response. Also, undoped Y_2O_3 , synthesized by the combustion process with different calcination temperatures, demonstrated the best response for application in low-dose X-ray conversion sensors due to the highest crystallite size [11]. Analyses of the pH effect in Bi-doped Y_2O_3 synthesized by the coprecipitation method reveal that changes in crystallite size and microstrain depend on pH variation [12].

Among the eco-friendly routes used for production, the following can be highlighted: sonochemical green synthesis [13], ultrasonic-microwave [14], microwave-hydrothermal [15], and coconut water-assisted sol-gel route [16]. Through the sol-gel route, it is possible to control the synthesis parameters and combine precursors for accelerating the chemical reactions during the process. The polyvinyl alcohol (PVA) content in oxides' synthesis influences the crystallization of materials [17], providing a route with OH

*megvalerio@academico.ufs.br

●<https://orcid.org/0000-0003-1707-1078>

groups that stabilize the metals in the polymer, thus reducing the precipitation of undesirable phases and the temperature to obtain the oxides. This paper presents the synthesis of undoped Y_2O_3 by a modified sol-gel method assisted by a PVA solution controlling the synthesis parameters. We pretend to produce Y_2O_3 varying two parameters: solution pH and calcination temperature. These parameters have demonstrated influence in particle morphology as well as microstructural deformations. The controlled synthesis can enable the industrial applicability of this route in the future.

EXPERIMENTAL

Y_2O_3 powders were synthesized via the sol-gel method assisted by polyvinyl alcohol (PVA) solution. The starting salts were yttrium nitrate [$Y(NO_3)_3$] and nitric acid (Alphatec, R.G.). PVA solution was prepared by dissolving PVA in distilled water at a concentration of 10% under magnetic stirring at 80 °C until the solution became homogeneous and transparent. Yttrium nitrate was dissolved in distilled water and PVA solution was dropwise added keeping a molar proportion of 2:1 [18]. A solution of HNO_3 (Neon, 65%) was used to adjust the initial pH value (~3) to approximately 0. The solution was heated and stirred at 150 °C for 2 h to obtain the gel phase. The sample was dried at 100 °C for 24 h, obtaining then a dried xerogel that was homogenized in an agate mortar. The calcination temperatures were estimated by using thermal analyses of xerogel. The differential thermal analysis (DTA) and thermogravimetry (TG) were performed from room temperature up to 1200 °C in a simultaneous system (SDT 2960, TA Instr.), with a heating rate of 10 °C/min under synthetic dry air flow. Based on the thermal analysis, the samples were calcined in an electric furnace with different plateau temperatures (600 and 1000 °C) for 1 h in an open atmosphere.

Structural analysis of the samples was performed using a conventional X-ray diffractometer (XRD, D8 Advanced, Bruker) with $CuK\alpha$ radiation, operating at 40 kV and 40 mA, over a 2θ range from 15° to 90° with steps of 0.02°. All measurements were carried out at room temperature and atmospheric pressure. The crystalline phases were identified by comparison using a standard XRD pattern from the Inorganic Crystal Structure Database (ICSD). In addition, Rietveld refinement was carried out using FullProf software [19] with the pseudo-Voigt function as the profile function. The refinement routine is described in detail in previous work [20]. From these analyses it was possible to investigate the crystallite size (D) and the microstructural deformation (lattice strain) by using the Williamson-Hall formalism [21]:

$$\beta \cdot \cos\theta = \frac{k\lambda}{d} + 4\epsilon \cdot \sin\theta \quad (A)$$

where k is the shape coefficient for the reciprocal lattice point (k=0.9 was used), λ is the X-ray wavelength, θ corresponds to the peak position of the identified crystalline phase, and D and ϵ are the effective crystallite size and the

effective strain, respectively. The β represents the full width at half maximum (FWHM) of the diffraction peaks. The peak broadening was corrected by:

$$\beta = \sqrt{\beta_{exp}^2 - \beta_{inst}^2} \quad (B)$$

where β_{exp} and β_{inst} are the broadenings of the measured line and the instrument, respectively [20]. β_{inst} was determined from the XRD pattern of silicon powder standard by the angular dependence equation proposed by Caglioti *et al.* [22]. The profile parameters $U=0.02806$, $V=-0.04376$, and $W=0.0292$ were obtained from Rietveld refinement of silicon powder standard:

$$\beta = \sqrt{U \cdot \tan^2\theta + V \cdot \tan\theta + W} \quad (C)$$

The morphology of the calcinated samples was analyzed through scanning electron microscopy (SEM, JSM-6510LV, Jeol). The microscope operated at 20 kV of accelerating voltage and the images were obtained at 5000x magnification.

RESULTS AND DISCUSSION

Firstly, thermal analyses were performed of Y_2O_3 xerogel before the calcination process. Fig. 1 shows the DTA/TG results of the Y_2O_3 xerogel. The curve analysis was divided into five different stages containing the main events. In the first stage, the mass loss from 100 to 200 °C was about 11%, and it was associated with loss of absorbed water by the xerogel. In the second stage, between 200 and 400 °C, a series of thermal events occurred associated with mass loss that was related to a breakdown of the PVA polymer chains and the loss of the organic matter [18, 23]. The thermal events in the TG curve above 400 °C were less evident. DTG (derivative of TG) curve showed an abrupt variation in the mass between 400 and 500 °C (third stage), accompanied by an exothermic peak associated with a large mass loss, at approximately 465 °C. This event may be related to the decomposition of PVA and precursor salts [18]. The fourth stage occurred at around 600 °C, where it was possible to observe an exothermic event, that can be associated with the

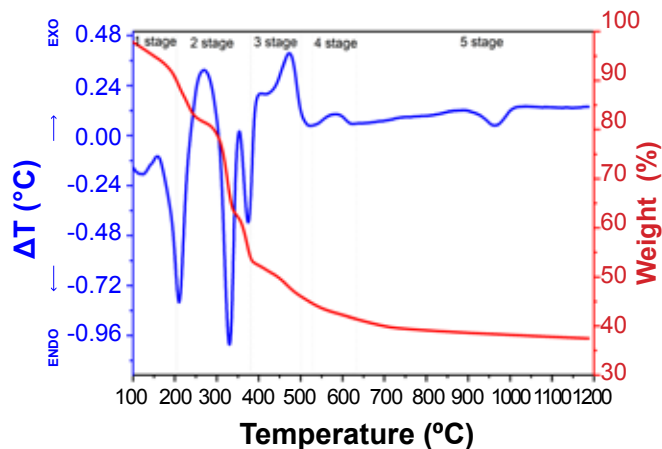


Figure 1: DTA and TG curves of the yttrium oxide precursor xerogel.

initial stage of the Y_2O_3 crystallization. Above 650 °C (fifth stage), there was no significant mass loss, indicating that the crystallization process was concluded and the increasing of the temperature could act only for a full ordering of the crystal lattice. The endothermic event observed in the DTA curve between 700 and 900 °C can be associated with the ordering of the crystal lattice or due to a structural change in Y_2O_3 . Since Y_2O_3 requires some special thermodynamic conditions like very high temperature and high pressure to produce structural changes [24], this last possibility was overruled.

Fig. 2a shows the XRD patterns of the Y_2O_3 samples produced with the variation of pH solution and calcined at 600 and 1000 °C. The diffraction peaks were compared with the ICSD file 82420 for the Y_2O_3 phase of cubic structure and space group Ia-3 (206) [25]. The results showed that all samples present only this Y_2O_3 phase without the presence of additional phases. Another advantage compared with recent works which synthesized Y_2O_3 through the sol-gel method is the reduction of the time for 1 h of calcination in this present work. Several works report the Y_2O_3 formation with heat treatment above 2 h [26-29]. The time and temperature reduction for oxide crystallization using a PVA solution is discussed in the literature [18]. The PVA content in the synthesis process provides a route with OH groups that stabilize the metals in the polymer, thus reducing the precipitation of undesirable phases and the calcination temperature [17]. In the present work, in a solution containing nitrates, PVA could also have acted as a fuel, accelerating the process of materials formation during calcination [30]. However, fast nucleation can lead to disordering in the crystal lattice [31]. It was also possible to observe a narrowing effect in the width of diffraction peaks as the calcination temperature increased. This behavior can be attributed to either the crystallite size increase or microstrain, which could also contribute to the peak narrowing and displacement of the XRD patterns [25]. For better visualization, the main peak of the phase (plane 222) was highlighted for all samples and is presented in Fig. 2b. In addition to peak broadening for samples calcined at 600 °C, a shift in this peak can also be seen, which was dependent on the solution pH. For the sample with pH~0, a shift to smaller angles was observed, while for the less acidic pH, the opposite occurred, for larger angles. As can be seen, the temperature is an important parameter for Y_2O_3 production because it directly interferes with crystallization processes, since at 1000 °C, the XRD pattern corresponded to the reference pattern. Therefore, these structural effects were closely linked to the synthesis parameters for the material preparation such as those used in this work: heat treatment or pH variation. To investigate the effects in the Y_2O_3 crystal lattice ordering, the lattice parameters were determined by using Rietveld refinement applied to the raw XRD data. The structural parameters obtained from Rietveld refinement for the Y_2O_3 samples, such as cell parameters, unit cell volume, and agreement factors are shown in Table I and compared to the literature data [25]. The values of lattice parameters found from the refined structure for the samples

were similar to the ones reported by Maslen *et al.* [25] for single crystalline/microcrystalline Y_2O_3 , except for the samples calcined at 600 °C. For these samples, highlighted for the sample produced at pH 3, the lattice parameter and unit cell volume were slightly higher than those observed for the samples calcined at the highest temperature. That is in agreement with the displacement of the diffraction peak position observed in Fig. 2b.

The microstrain (ϵ) contribution in the narrowing width of the XRD peaks and the crystallite size (D) for all the samples were calculated from the Williamson-Hall (W-H) formalism [21] and are shown in Table II. The W-H plot was done by plotting $\beta\cos\theta$ versus $\sin\theta$, and it was possible to find the crystallite size from the intercept with the vertical axis and the microstrain was given from the slope of the straight line (Fig. 3). The narrowing of XRD peaks associated to the

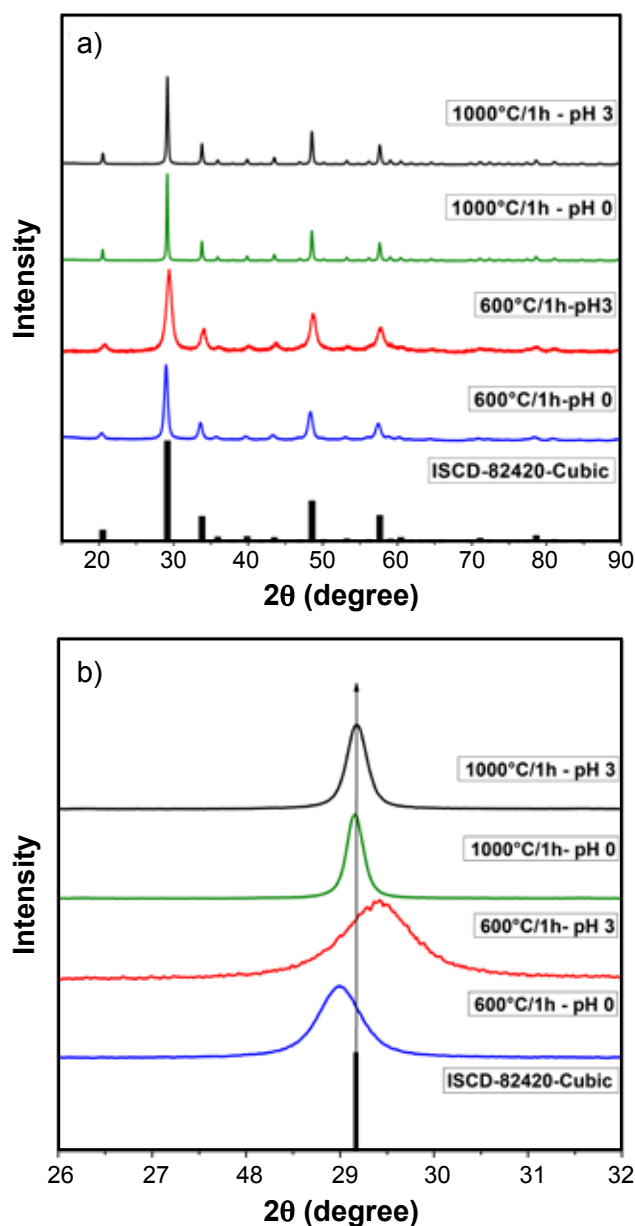


Figure 2: XRD patterns of Y_2O_3 synthesized at different parameters: a) general view; and b) expanded view of the diffraction peak (222).

Table I - Parameters for the Rietveld refinement of Y_2O_3 compared to the lattice parameters of ICSD file 82420.

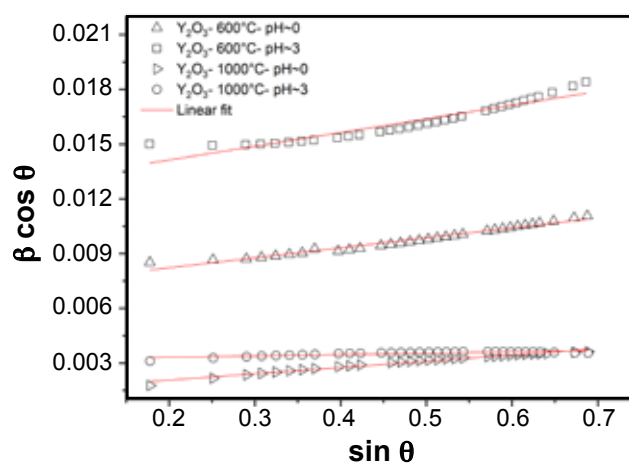
Sample	χ^2	R_{Bragg} (%)	R_{WP} (%)	Lattice parameter $a=b=c$ (Å)	Unit cell volume (Å ³)
600 °C - pH~0	2.26	5.33	11.9	10.6236(5)	1198.99(0.11)
600 °C - pH~3	1.67	6.20	16.8	10.6486(14)	1207.48(0.28)
1000 °C - pH~0	3.42	5.25	10.3	10.6061(1)	1193.08(0.03)
1000 °C - pH~3	2.84	4.87	8.74	10.6091(3)	1194.11(0.03)
Y_2O_3 [25]	-	-	-	10.5981(7)	1190.38

increase of crystallite size of samples synthesized by sol-gel route is discussed in the literature [32]. As can be seen in Table II, the broadening and the displacement observed in the XRD peak (Fig. 2b) were not only due to the structural microstrain. There was a combined effect of structural microstrain and crystallite size. The smaller calculated microstrain factor was found for the samples calcined at 1000 °C. These results meant that higher calcination temperatures could result in a coalescence of the crystallites with a subsequent increase of particle size, causing a better ordering in the crystal lattice, as observed in Table I by the relaxation in the unit cell volume of the Y_2O_3 unit cell. Now, comparing the results for changing the chemical environment differences can also be seen. The more acidic environment (pH~0), the faster the calcination process due to the interaction of PVA with HNO_3 ions (used to adjust the pH value). The sample synthesized at 1000 °C with pH 3 had the highest degree of structural ordering, which corroborated the XRD pattern (Fig. 2b) since fast nucleation can cause distortions in the structure. The pH of the solution influenced the crystallite size, in which there was a significant increase for the more acidic pH. It is reported in the literature that the highest crystallite size in Y_2O_3 particles is an important parameter for several applications, such as temperature sensing [4], down conversion properties [10], low-dose X-ray conversion sensors [11], and others. However, these works used longer times of calcination (from 2 to 5 h). Therefore, the pH variation can be used for improving the properties of Y_2O_3 , consequently, the applications, besides minimizing the calcination time of Y_2O_3 .

Fig. 4 shows the images for Y_2O_3 obtained by scanning electron microscopy. It was possible to visualize agglomerates for all samples, however with some differences. At the highest temperature (1000 °C), there was the begging of the spherical shape of particles, while at 600 °C, the small particles had an irregular assembly. Another difference observed was the

Table II - Microstrain factor (ϵ) and average crystallite size of Y_2O_3 samples.

Parameter	600 °C pH~0	600 °C pH~3	1000 °C pH~0	1000 °C pH~3
ϵ	0.0015	0.0019	0.0010	0.0002
D (nm)	20.1(5)	11.0(2)	115(3)	44(1)

Figure 3: Williamson-Hall plot for Y_2O_3 samples.

particle size: samples calcined at 600 °C were smaller than those calcined at 1000 °C. A possible explanation is that the polymer chains covered the Y_2O_3 nuclei, limiting the reaction space and decreasing the contact between neighboring nuclei [18]. It was seen in the thermal analysis graph (Fig. 1) that the highest percentage of mass loss occurred up to approximately 600 °C. Above this temperature, stabilization occurred, which was associated with the material's crystallization process. Therefore, the sample calcined at 600 °C may have contained traces of organic matter and, consequently, influenced the morphology of the particles. The variation in morphology for Y_2O_3 has already been reported in the literature. The Y_2O_3 samples obtained by the sol-gel method with PVA without pH control have well-defined, coalesced spherical particles [9]. However, it should be considered that the samples were calcined at 1000 °C for 5 h, which probably favored the coalescence process. Another work [33] explored the Y_2O_3 produced by the sol-gel route and associated the change in morphology with the variation in parameters, such as starting acids and calcination temperature (800 and 1100 °C for 4 h) resulting in different shapes: needles, platelets, or spheres. The synthesis of Er-doped Y_2O_3 when changing the calcination temperature (600, 850, and 1000 °C for 5 h) was investigated for application in temperature sensing [29]. The authors found a dependence between the relative sensitivity with the particle size. However, in addition to using longer calcination times, neither of the works above explored the pH variation.

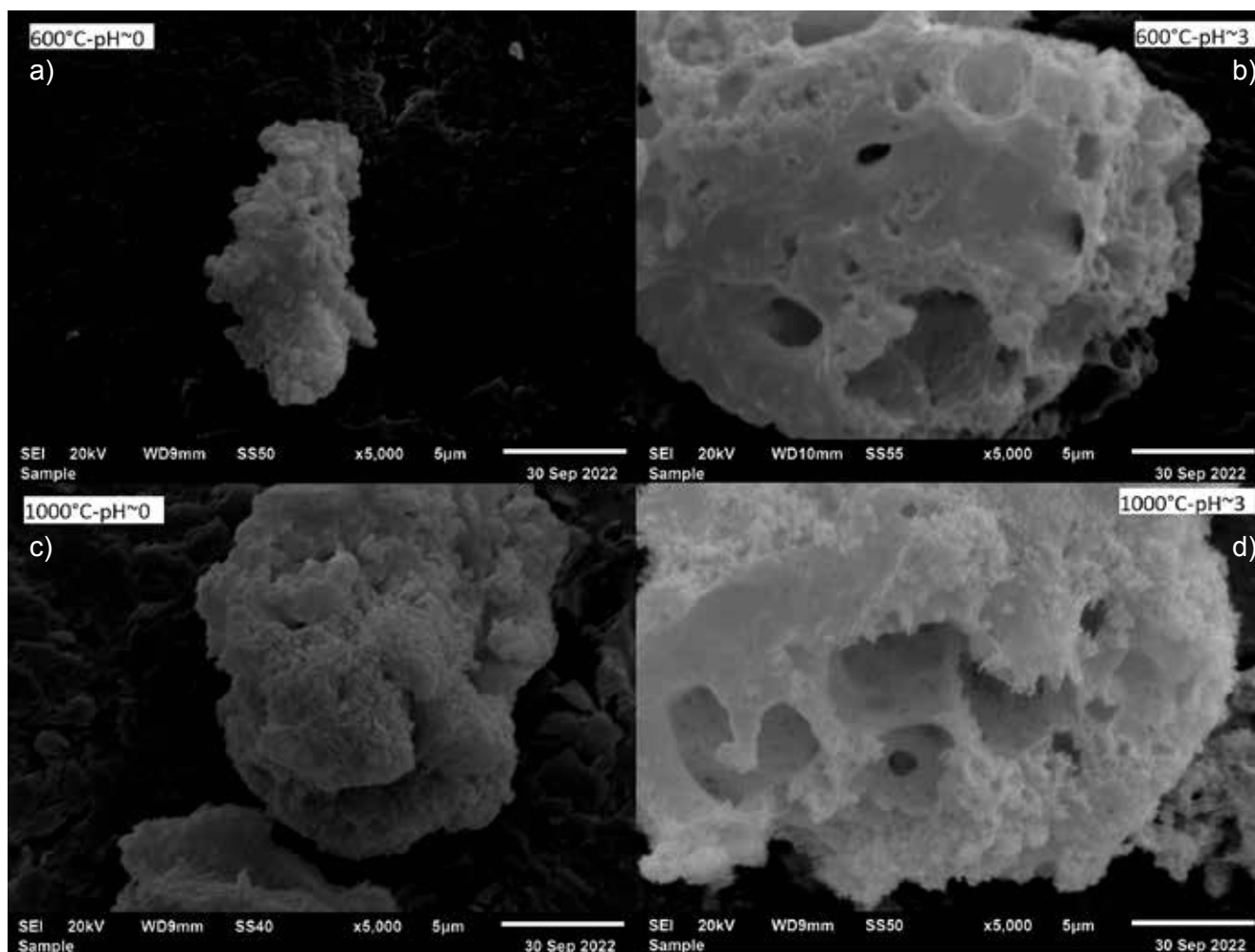


Figure 4: SEM images of Y_2O_3 particles synthesized at 600 °C (a,b) and 1000 °C (c,d) with pH~0 (a,c) and pH~3 (b,d)

As can be seen in Fig. 4, the pH variation also revealed differences in the morphology. The first one was the increase of the particles with the increase of pH ($pH \sim 3 > pH \sim 0$). Another difference was the porosity appearance of the Y_2O_3 synthesized with pH~3. This behavior was visualized for both calcination temperatures. In the literature, the change in morphology and microstructure with the variation of precipitation agent when obtaining Y_2O_3 calcined for 3 h was investigated [34]. The authors observed a spongy morphology for particles containing NH_4OH as precipitating agent. The porosity behavior of particles of Y_2O_3 doped with Yb, Er, and Zn was investigated for application in a dye-sensitized solar cell (DSSC); this behavior increases the photovoltaic response of the Y_2O_3 used on TiO_2 photoanode [35]. The authors [36] noted a high porosity of the films, and this behavior is desirable because it favors efficient diffusion of the dye in cells. Therefore, the calcination temperature and pH variation during the Y_2O_3 formation can be used for tailoring the desired application.

CONCLUSIONS

According to the results presented, it is concluded that

the sol-gel route modified with PVA was satisfactory in the production of Y_2O_3 , minimizing the time of calcination. The thermal analysis combined with XRD results showed that from 600 °C the crystalline phase of cubic Y_2O_3 was formed. The results obtained from Rietveld refinement combined with Williamson-Hall formalism showed that the synthesis parameters directly interfered with the crystallite size and structural deformation in the crystal lattice. There was a significant increase in the crystallite size for the more acidic pH ($pH \sim 0$). As well as the structural properties, the morphology was also influenced by temperature and pH. Therefore, the control of the synthesis parameters is important because different kinds of Y_2O_3 particles can be produced and, thus, adjusting the properties according to the desired application.

ACKNOWLEDGMENTS

The authors gratefully acknowledge the CNPq, CAPES, FINEP, and FAPITEC-SE, Brazilian funding agencies, for financial support. Jéssica C. C. Carvalho also thanks to CNPq for the master in materials science and engineering scholarship (Edital 02/2016/COPES/POSGRAP/UFS).

This research used facilities of the Multiuser Centre for Nanotechnology at UFS (CMNano-UFS), a non-profit organization member of the National Multiuser Centres sponsored by Financiadora de Estudos e Projetos (FINEP). The CMNano technical staff is acknowledged for their assistance during the experiments under proposal number #008/2019.

REFERENCES

- [1] C.S. Bezerra, A.B. Andrade, P.J.R. Montes, M.V.S. Rezende, M.E.G. Valerio, *Opt. Mater.* **72** (2017) 71.
- [2] R. Thomatieli-Santos, M. Bernardi, A. Hernandez, *J. Sol-gel Sci. Technol.* **42** (2007) 173.
- [3] D.F. Farias, C.M. de Abreu, S.M.V. Novais, Z.S. Macedo, *J. Lumin.* **194** (2018) 535.
- [4] M.A. Gomes, I.S. Carvalho, L.F.A. Domingos, A.C.B. Silva, J.F.M. Avila, J.J. Rodrigues, M.A.R.C. Alencar, M.E.G. Valerio, Z.S. Macedo, *Opt. Mater.* **89** (2019) 536.
- [5] D. Nunes, A. Pimentel, M. Matias, T. Freire, A. Araújo, F. Silva, P. Gaspar, S. Garcia, P.A. Carvalho, E. Fortunato, R. Martins, *Nanomaterials* **9**, 2 (2019) 234.
- [6] S. Chen, J. Lin, J. Wu, *Appl. Surf. Sci.* **293** (2014) 202.
- [7] P.C. Nagajyothi, M. Pandurangan, M. Veerappan, D.H. Kim, T.V.M. Sreekanth, J. Shim, *Mater. Lett.* **216** (2018) 58.
- [8] J. Kong, D.Y. Tang, B. Zhao, J. Lu, K. Ueda, H. Yagi, T. Yanagitani, *Appl. Phys. Lett.* **86**, 16 (2005) 161116.
- [9] G.A. Sobral, M.A. Gomes, J.F.M. Avila, J.J. Rodrigues, Z.S. Macedo, J.M. Hickmann, M.A.R.C. Alencar, *J. Phys. Chem. Solids* **98** (2016) 81.
- [10] L. Lamiri, B. Kahouadji, M. Berd, A. Abdellatif, L. Benchallal, L. Guerbous, S. Ouhenia, A. Souici, L. Amieur, A. Zoukel, M. Samah, *J. Rare Earths* **41** (2023) 51.
- [11] P. Praveenkumar, T. Subashini, G.D. Venkatasubbu, T. Prakash, *Sens. Actuator A Phys.* **297** (2019) 111544.
- [12] E. Lee, J.J. Terblans, H.C. Swart, *Vacuum* **157** (2018) 237.
- [13] N. Basavegowda, K. Mishra, R.S. Thombal, K. Kaliraj, Y.R. Lee, *Catal. Lett.* **147** (2017) 2630.
- [14] J. Bi, L. Sun, Q. Wei, K. Zhang, L. Zhu, S. Wei, D. Liao, J. Sun, *J. Mater. Res. Technol.* **9**, 5 (2020) 9523.
- [15] J. Kaszewski, B.S. Witkowski, L. Wachnicki, H. Przybyłńska, B. Kozankiewicz, E. Mijowska, M. Godlewski, *J. Rare Earths* **34**, 8 (2016) 774.
- [16] M.A. Gomes, A.C.B. Silva, J.F.M. Avila, M.A.R.C. Alencar, J.J. Rodrigues, Z.S. Macedo, *J. Lumin.* **200** (2018) 43.
- [17] J. Feng, T. Liu, Y. Xu, J. Zhao, Y. He, Y. Ceram. Int. **37**, 4 (2011) 1203.
- [18] S.K. Saha, P. Pramanik, *Nanostruct. Mater.* **8**, 1 (1997) 29.
- [19] J. Rodriguez-Carvajal, *Physica B Condens. Matter* **192**, 1 (1993) 55.
- [20] A.B. Andrade, N. Ferreira, M.E.G. Valerio, *RSC Adv.* **7** (2017) 26839.
- [21] G.K. Williamson, W.H. Hall, *Acta Metall.* **1**, 1 (1953) 22.
- [22] G. Caglioti, A. Paoletti, F.P. Ricci, *Nucl. Instrum.* **3**, 4 (1958) 223.
- [23] K.F. Suzart, A.B. Andrade, Z.S. Macedo, M.E.G. Valerio, *J. Lumin.* **203** (2018) 385.
- [24] R. Dai, Z. Wang, Z. Zhang, Z. Ding, *J. Rare Earths* **28** (2010) 241.
- [25] E. Maslen, V. Streltsov, N. Ishizawa, *Acta Crystallogr. B Struct. Sci. Cryst. Eng. Mater.* **52**, 3 (1996) 414.
- [26] N. Wang, J. He, K. Ye, X. Song, T. Li, *Infrared Phys. Techn.* **93** (2018) 77.
- [27] I. Benammar, R. Salhi, J.L. Deschanvres, R. Maalej, *J. Mater. Res. Technol.* **9**, 6 (2020) 12634.
- [28] P.M. Kakade, A.R. Kachere, P.D. Sahare, A.V. Deshmukh, S.D. Dhole, S.R. Jadhkar, N.T. Mandlik, *J. Alloys Compd.* **928** (2022) 167106.
- [29] A.S. Laia, A.C.B. Silva, M.A. Gomes, Z.S. Macedo, M.E.G. Valerio, J.J. Rodrigues, M.A.R.C. Alencar, *J. Alloys Compd.* **926** (2022) 166816.
- [30] M. Stoia, M. Barbu, M. Stefanescu, P. Barvinschi, L. Barbu-Tudoran, *J. Therm. Anal. Calorim.* **110**, 1 (2012) 85.
- [31] T.S. Lilge, C.S. Bezerra, G.F.C. Bispo, A.B. Andrade, Z.S. Macedo, M.L. Moreira, M.E.G. Valerio, *Dalton Trans.* **49** (2020) 8540.
- [32] M. Junaid, M.A. Khan, A. Majeed, H. Alkhalidi, M.S. Attia, M.A. Amin, M.A. Iqbal, *Ceram. Int.* **48**, 15 (2022) 21651.
- [33] A. Dupont, C. Parent, B. Le Garrec, J.M. Heintz, *J. Solid State Chem.* **171**, 1 (2003) 152.
- [34] E.E. Kaya, S. Gurmen, *Physica E Low Dimens. Syst. Nanostruct.* **115** (2020) 113668.
- [35] F.L. Chawarambwa, T.E. Putri, S.H. Hwang, P. Attri, K. Kamataki, N. Itagaki, K. Koga, D. Nakamura, *Opt. Mater.* **123** (2022) 111928.
- [36] M. Ahmad, D.A. Pandey, N. Rahim, *Renew. Sust. Energy Rev.* **77** (2017) 89.

(Rec. 14/11/2022, Rev. 27/12/2022, Ac. 07/01/2023)



Study of rhombohedral tricalcium phosphate in hexagonal crystal structure family on the sample prepared by the sol-gel route and the effect of calcination temperature

J. Ady^{1,2}, S. D. A. Ariska¹, D. I. Rudyardjo^{1,2}, S. Anindriya²*

¹*Airlangga University, Faculty of Science and Technology, Department of Physics, 60115 Surabaya, Indonesia*

²*Airlangga University, Faculty of Science and Technology, Biomedical Engineering Study Program, 60115 Surabaya, Indonesia*

Abstract

The effect of the calcination temperature at 800 and 1000 °C on the stable formation of the tricalcium phosphate with rhombohedral structure in the system of the hexagonal crystal family was determined, while its precursor was made from limestone obtained from nature in the Lumajang district, Indonesia. The rhombohedral tricalcium phosphate samples were prepared by sol-gel routine, then examined by several tests, such as, Fourier transform infrared spectroscopy to study the deficiency of -OH, X-ray diffraction test to study the microstructure of the tricalcium phosphate with the rhombohedral structure in a hexagonal crystal system, differential scanning calorimetry and thermogravimetry tests to study thermal characteristics, scanning electron microscopy and energy dispersive spectroscopy to study the surface topography and to obtain the atomic ratio Ca/P ~1.5. Finally, the UV-vis test found the optical energy gap, E_g , from ~5.34 to ~5.41 eV for the sample calcined at 800 °C and E_g ~5.19 to ~5.21 eV at 1000 °C.

Keywords: tricalcium phosphate, sol-gel, temperature, rhombohedral, research, structure.


INTRODUCTION

In crystallography, there are six crystal families, one is the hexagonal crystal family, which includes two crystal systems (hexagonal and trigonal) and two lattice systems (hexagonal and rhombohedral). Meanwhile, the rhombohedral crystal structure is depicted inside the hexagonal crystal system. Tricalcium phosphate is one of several ceramic compounds derived from hydroxyapatite that has a stable crystal structure in a hexagonal system. Tricalcium phosphate (TCP) is an attractive material or biomaterial such as bone phosphate of lime (BPL) with low solubility in the white solid form. In the general commercial product, TCP is produced by treating hydroxyapatite (HA_p) with phosphoric acid and slaked lime. TCP or BPL have three recognized polymorphs, namely: 1) rhombohedral (β -TCP), 2) monoclinic (α -TCP), and 3) hexagonal (α' -TCP) forms. The rhombohedral TCP has a crystal denser than monoclinic or hexagonal TCP in its own stable temperature, however, are less dense at high temperature. They are potentially used in medicine, such as for bone substitutes either in dense or porous forms [1-3]. The melting point of TCP is about ~1670 °C [4], and it was indicated the effective sintering temperature at about ~1113 °C when it was calculated by using 2/3 of the melting temperature [5, 6]. The solid phases of TCP in three existing

forms namely β -, α -, and α' -TCP always made from low, near, and same sintering temperatures [7].

There are several methods of the synthesis of polymorphic tricalcium phosphates; among others, they are prepared by solid-state reaction and wet methods or wet chemical precipitation (sol-gel) route [8-12]. The novelty of this research is to provide raw material for artificial bone based on tricalcium phosphate with a rhombohedral crystal structure by utilizing natural limestone available in Indonesia. In several previous tricalcium phosphate studies using the sol-gel technique, the $CaCO_3$ compounds have been used as a precursor in the sol-gel route, but many studies use fabricated $CaCO_3$ compounds with varying levels of purity. Meanwhile, the use of $CaCO_3$ compounds from natural materials is rarely carried out in similar studies. Therefore, the novelty of this study is related to: 1) the use of a novel $CaCO_3$ material as a precursor in the sol-gel route for the sample preparation of tricalcium phosphate derived from the mineral limestone (natural raw material) in the Lumajang region, East Java, Indonesia; 2) this research study focused on the microstructure of tricalcium phosphate in the rhombohedral crystal system which is a family of hexagonal crystal structure with the level of stability of the crystal structure affected by heating temperature; and 3) the search for the potential use of the novel materials of $CaCO_3$ as an artificial bone bioceramic derived by a limestone mineral in Lumajang with the rhombohedral system crystal characteristics. In this focus, the rhombohedral tricalcium phosphate was prepared from limestone ($CaCO_3$) that was obtained from nature in the Lumajang district, with the use

*jan-a@fst.unair.ac.id

 <https://orcid.org/0000-0002-5408-580X>

of a wet method in sol-gel routine, and after that influenced by calcination temperature at 800 and 1000 °C. The sol-gel technique was preferred in this research due to the simplicity of the method regarding the preparation handling and because it provides a nanometer scale for the crystal size. In other words, this preparation technique always produces a finely powdered sample in the nanosized form [13, 14]. Previously, there are several appropriate tests to justify the rhombohedral tricalcium phosphate in the hexagonal crystal structure form already formed by sol-gel technique, such as: 1) FTIR test: it was used to study the functional group [15-17], especially for deficiency of the hydroxyl functional group (-OH) analysis when temperatures of 800 and 1000 °C were applied on sample; 2) XRD test [18-20]: it was used to analyze the lattice system of crystal, through studies of the crystallite size, strain, dislocation density, crystallinity, and the preferential plane of the rhombohedral tricalcium phosphate in the hexagonal crystal structure; 3) DSC-TGA test [21, 22]: it was used to analyze the thermal responses including information of specific heat capacity, mass reduction, enthalpy of fusion and melting; 4) SEM-EDX test [23-27]: it was used to analyze the surface morphology and the atomic ratio Ca/P ~1.5; and finally, 5) UV-vis test [28, 29]: it was used to analyze the optical energy gap (E_g) of the rhombohedral tricalcium phosphate sample with Tauc formula to determine the E_g value.

This study is relevant for giving information about the effect of temperature, exactly at 800 and 1000 °C for stable structure formation of tricalcium phosphate sample in the hexagonal crystal system through a particular study, when the sample was prepared by a sol-gel routine with the use of a limestone precursor obtained from Indonesia. Therefore, the aim of this study is to provide information on temperature leverage as a reinforcing parameter to improve the microstructure of the tricalcium phosphate with rhombohedral structure in a hexagonal crystal system, which is prepared by a sol-gel route and when the effects of temperature at 800 and 1000 °C are applied to this sample, from its gel to the dry phases. Moreover, some parameters of interest were studied by using several examinations, such as looking for the lattice plane of the rhombohedral tricalcium phosphate in the hexagonal crystal structure through its study from XRD results for the determination of the crystallite size, strain, dislocation density, and the crystallinity degree. Subsequently, a functional group of the rhombohedral tricalcium phosphate sample was studied from FTIR results and then studied to find the atomic ratio and their profile surfaces through analysis of SEM-EDX results. Previously, the DSC-TGA thermograms were used to study the specific heat capacity, mass reduction, fusion and melting enthalpies. Finally, the optical energy gap was studied by using the UV-vis result to provide information about thermal characteristics as an insulator.

EXPERIMENTAL

Preparation of rhombohedral tricalcium phosphate samples: the sample was prepared by sol-gel route with

the wet reaction method. First, the calcium oxide (CaO) was made from limestone (CaCO_3) obtained from nature in the Lumajang district, Indonesia, with a calcination technique at 1100 °C in a laboratory furnace (tabletop-type vertical muffle furnace) for 3 h. Second, the calcium oxide was mixed with water to produce the calcium hydroxide [$\text{Ca}(\text{OH})_2$]. Third, the sol-gel route was conducted to find the rhombohedral tricalcium phosphate or calcium and hydroxyl deficiencies in hydroxyapatite form with a Ca/P ratio of ~1.5: i) hydrolysis step: mixing 0.6 M water with 1.6 M of $\text{Ca}(\text{OH})_2$ and 1.2 M of H_3PO_4 (ACS reagent, ≥ 85 wt% in water) using a hot plate magnetic stirrer for 2 h; ii) condensation step: dropping the ethanol into the previous solution that was produced by the hydrolysis step and keep going to mix using the hot plate magnetic stirrer for 15 to 20 h [30-32]; iii) aging step: the gel form of the sample produced by condensation step in the sol-gel route was aged for 20 h at room temperature (~27 °C); iv) drying step: the fine powder of the rhombohedral tricalcium phosphate sample was obtained when its gel form was heated at 800 and 1000 °C.

Examinations of the rhombohedral tricalcium phosphate samples: there were several types of tests used for sample analysis, such as X-ray diffraction analysis (XRD, XPert MPD, Philips; 2θ range: 20-80°, step size: 0.017°, scan step time: 10.15 s), Fourier transform infrared spectroscopy (FTIR, IRPrestige 21, Shimadzu; wavenumber range: 4000-400 cm^{-1} , resolution: ~4 cm^{-1} , mirror speed: ~2.8 mm/s, total of ~10 scans), scanning electron microscopy-energy dispersive X-ray spectroscopy (SEM-EDX, Inspect-S50, FEI), differential scanning calorimetry-thermogravimetric analysis (DSC-TGA, STA PT 1600, Linseiss; temperature range: 27 to 995 °C, heating rate: 25 °C.min⁻¹, atmosphere: air), and ultraviolet-visible spectroscopy (UV-vis, UV-1800, Shimadzu; wavelength range: 190 to 800 nm, scan speed: fast, sampling interval: 0.5 nm). 1) FTIR: this test examined the hydroxyl functional group deficiency of hydroxyapatite compound [$\text{Ca}_5(\text{PO}_4)_3(\text{OH})$] that became tricalcium phosphate compound [$\text{Ca}_3(\text{PO}_4)_2$]. In this effort, the scan parameters were analyzed by using the standardized points of the angular frequency in all spectrum obtained from FTIR on the integrated transmittance count and wavenumber range, to study their type of vibration, where every type of vibration was studied to define the kind of the functional group of -OH, $-\text{PO}_4^-$, and $-\text{PO}_4^{3-}$. 2) SEM-EDX: this test examined the surface morphology and atomic ratio of the rhombohedral tricalcium phosphate sample, Ca/P ~1.5. In this effort, the step line of the scanning of SEM was used to define the surface morphology of the tricalcium phosphate sample. Meanwhile, the integrated intensity count and spread of electron in the energy level was defined to find the atomic ratio of the tricalcium phosphate sample. 3) XRD: this test examined the crystal system of the rhombohedral tricalcium phosphate by determining some inherent parameters, such as the study of the crystal lattice system which included the crystallite size, strain,

dislocation density, crystallinity, and the preferential plane orientation of the rhombohedral crystal structure in the hexagonal crystal structure. In this effort, every data obtained from XRD scan parameters on the integrated intensity count and full-width at half maximum (FWHM) were analyzed by using the Gaussian method. 4) DSC-TGA: this test examined the thermal responses through the study of some inherent parameters of rhombohedral tricalcium phosphate, such as analysis of the heat flow, specific heat capacity, change of mass, enthalpy of crystallization and fusion reactions via the endothermic and exothermic process. In this effort, the results of the thermogram on the integrated heat flow and time/temperature obtained from DSC-TGA were used to define the thermal parameters, such as heat capacity, mass reduction, enthalpy of fusion and melting quantities. 5) UV-vis: this test examined the optical energy gap of the rhombohedral tricalcium phosphate using Tauc's equation [33, 34]. In this effort, every data obtained from UV-vis spectra were plotted in the absorbance and wavelength, and this curve was used to define the optical energy gap of the tricalcium phosphate sample by using the Tauc plot approach.

RESULTS AND DISCUSSION

FTIR data analysis for rhombohedral tricalcium phosphate functional group: the functional group information of rhombohedral tricalcium phosphate in the hexagonal crystal structure was confirmed by using data analysis from the FTIR test result, where, deficiency of the hydroxyl functional group (-OH) was obtained for samples calcined at 800 and 1000 °C. The wavenumber of -OH was indicated to occur at the point ~3446.6 cm⁻¹ with a bit of existence characteristic of transmittance value or big value of absorbance appeared, such as shown in Fig. 1a. In the other words, this indicated that a low vibration occurred with a weak angular frequency for samples calcined at 800 and 1000 °C. The FTIR spectra, such as shown in Fig. 1a, indicated a change from Ca(OH)₂ to Ca₃(PO₄)₂. Therefore, these FTIR spectra denoted that the rhombohedral tricalcium phosphate effectively was formed by temperature effect at 800 and 1000 °C. Meanwhile, their anion of the functional group of orthophosphate (PO₄³⁻) was confirmed as asymmetric bending (~566.6 and ~608.9 cm⁻¹) or

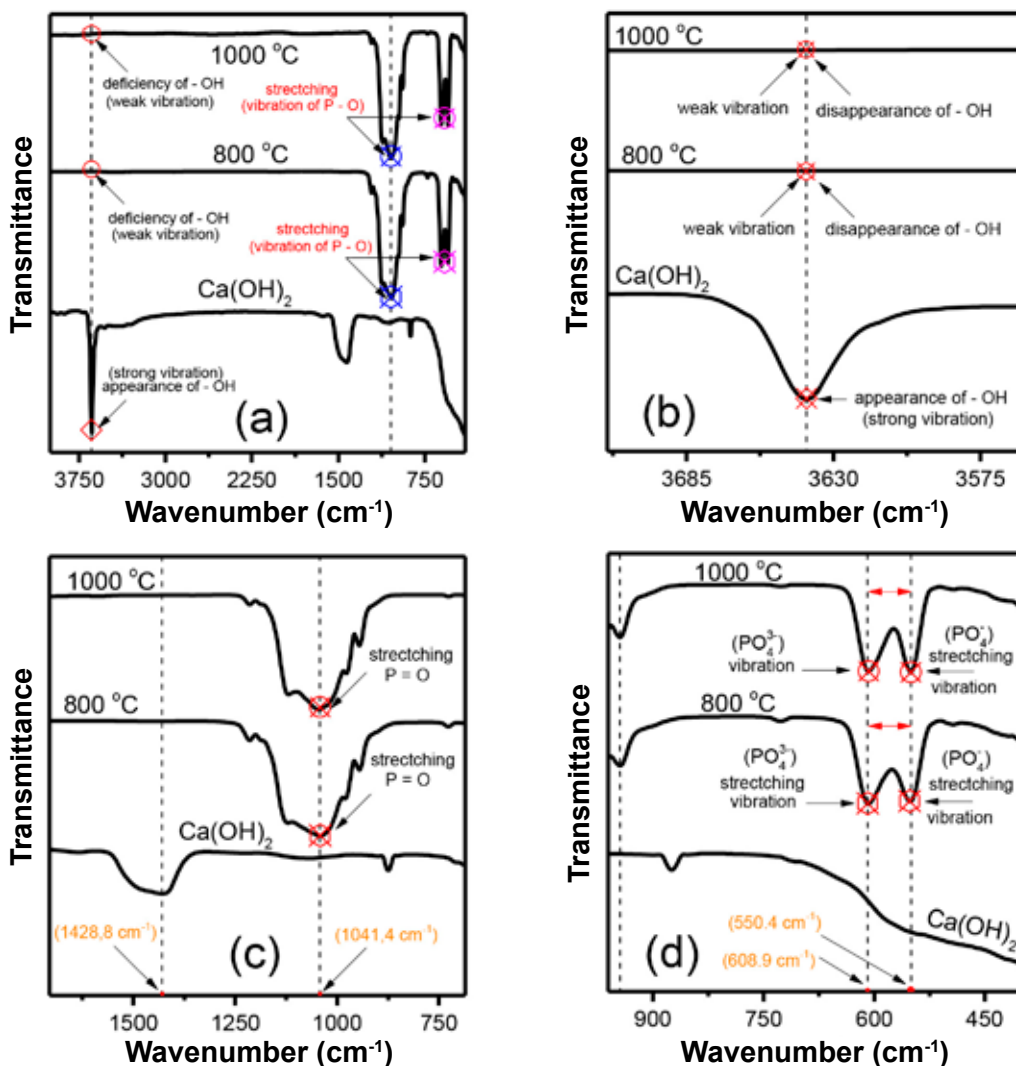


Figure 1: FTIR spectra of samples over the entire range (a) and for specific ranges (b-d) of tested wavenumber.

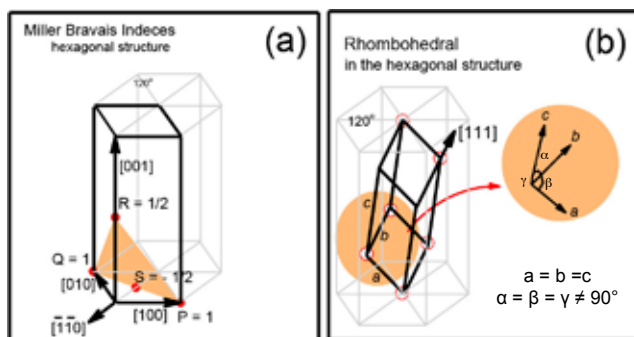


Figure 2: Schematics showing Miller indices (a) and rhombohedral structure (b) in the hexagonal structure.

asymmetric stretching (~ 1041.4 , ~ 962.4 , and ~ 900.1 cm^{-1}) and with strong frequency vibration value. Moreover, the anion functional group of PO_4^- was confirmed to occur at the point ~ 550.4 cm^{-1} . Particularly, all FTIR spectra for these samples with the specific wavenumber and transmitted values are shown in Figs. 1b to 1d.

XRD data analysis for rhombohedral tricalcium phosphate in the hexagonal crystal structure: several analyses were conducted by using the XRD results to reveal the crystalline features of the rhombohedral tricalcium phosphate samples in the hexagonal crystal structure, as follows.

Miller indices (hkl) and constant lattice plane determinations for the crystalline samples: lattice planes'

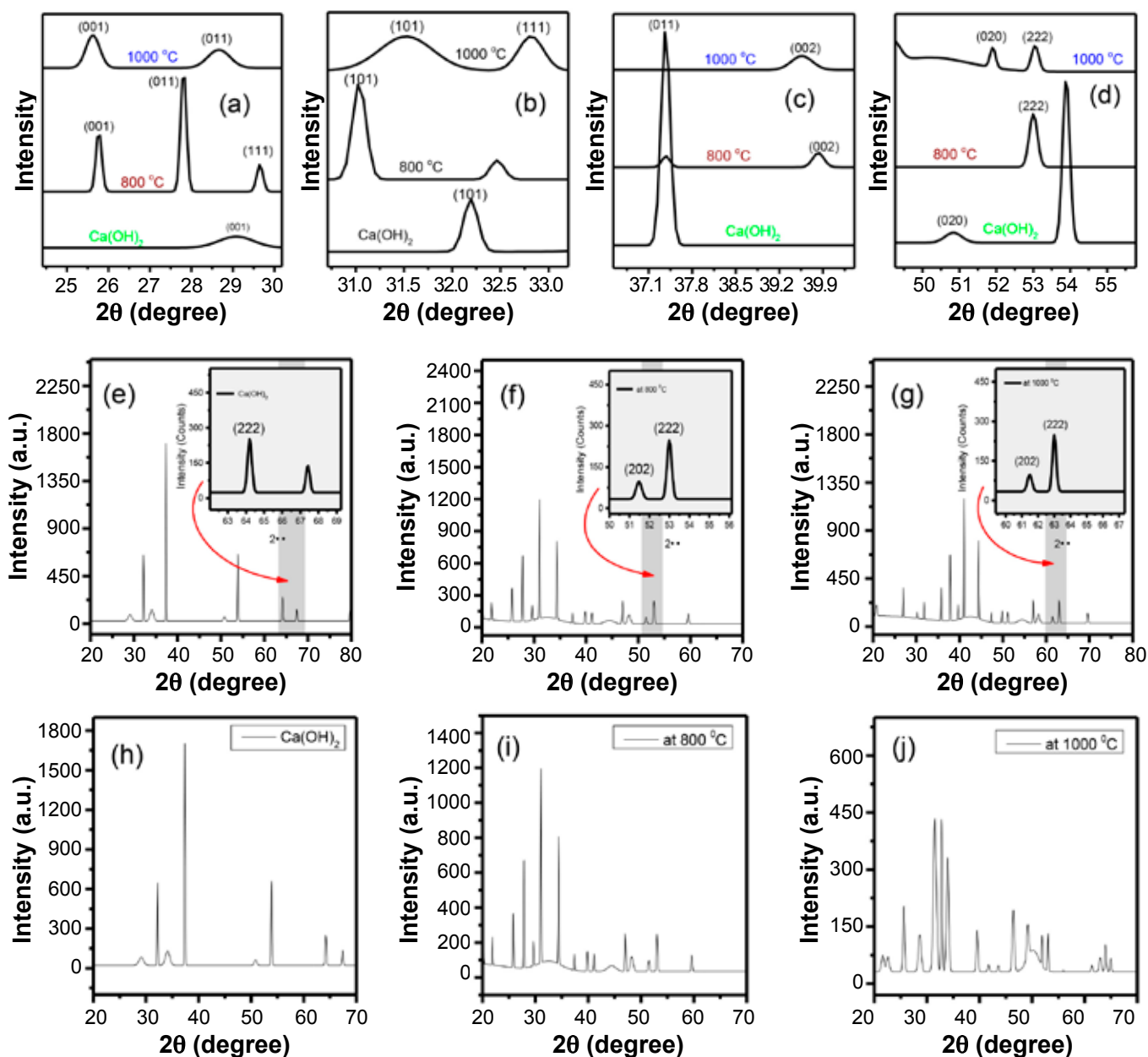


Figure 3: Refinement of the XRD patterns for combined curves of samples at Bragg's angle interval of: a) 25° to 30°; b) 30° to 33°; c) 37° to 40°; and d) 50° to 55°. Diffractograms from 20° to 80° for: e) Ca(OH)_2 ; f) sample heated at 800 °C; and g) sample heated at 1000 °C. Gaussian fitted diffractograms for: h) Ca(OH)_2 ; i) sample heated at 800 °C; and j) sample heated at 1000 °C.

family of the rhombohedral structure of tricalcium phosphate is given by particular Bravais lattice defined by three integers h, k, and l, and denoted as Miller indices with notation (hkl). However, with hexagonal and rhombohedral lattice systems, it is possible to use the Bravais-Miller lattice system, which uses four indices h, k, i, and l or with notation (hkil) that obey the constraint [35, 36]:

$$h + k + i = 0 \tag{A}$$

where h, k, and l define the Miller indices and i is a redundant index. As follows, the interplanar spacing (d_{hkl}) for the hexagonal system is given by:

$$d_{hkl} = \frac{a}{\sqrt{\frac{4}{3}(h^2+k^2+h.k)+\frac{a^2}{c^2}l^2}} \tag{B}$$

where a and c are defined as lattice constants and d_{hkl} is corresponding with the crystallite size (D), peak broadening (β), and crystallite strain (ϵ) parameters. Particularly, D can be determined by using the Scherrer equation and Williamson-Hall plot method [37-39]. Therefore, the Miller indices and lattice constants of the rhombohedral tricalcium phosphate in the hexagonal crystal structure were calculated by using Eqs. A and B. Previously, the XRD pattern obtained was showing the specific peaks of the crystal and amorphous patterns. By means of peak refinement with the Gaussian distribution method in the software used, it was found the specific peak values with Miller indices (001) as a lattice plane orientation for a hexagonal crystal structure with 3-fold symmetry, such as shown in Fig. 2a. Meanwhile, the Miller indices (011) and (111) were described particularly for rhombohedral in the hexagonal crystal structure, as shown schematically in Fig. 2b [40].

The Miller indices of the rhombohedral tricalcium phosphate in the hexagonal crystal structure appeared in the XRD pattern of this sample, as shown particularly for specific Bragg angles in Figs. 3a to 3d. The Miller indices (001) appeared at $2\theta \sim 25.76^\circ$ and $\sim 25.61^\circ$ for samples heated

at 800 and 1000 °C, respectively, whereas, for Ca(OH)_2 they appeared at $2\theta \sim 29.07^\circ$. The peak (001) looked like shifted when the temperature at 800 and 1000 °C was applied if compared with the peak (001) of Ca(OH)_2 . In the same way, Miller indices for rhombohedral lattice planes (011) and (111) were defined at $2\theta \sim 27.78^\circ$ and $\sim 29.66^\circ$ for the sample heated at 800 °C. Subsequently, for (011) and (111) of the sample heated at 1000 °C, they were confirmed sequentially at $2\theta \sim 31.52^\circ$ and $\sim 32.81^\circ$. Overall, the Miller indices of rhombohedral tricalcium phosphate in the hexagonal crystal structure were found, such as shown in the particular Bragg angle in Figs. 3a to 3d. Meanwhile, the X-ray diffractograms for Ca(OH)_2 and samples heated at 800 and 1000 °C from 20° to 80° are shown in Figs. 3e to 3g and the Gaussian fitted diffractograms are shown in Figs. 3h to 3j. Entirely, the specific Miller indices corresponded with the interplanar spacing from the rhombohedral tricalcium phosphate sample, and according to Eq. B, they were appropriated with the lattice plane orientation to the hexagonal crystal structure model shown in Fig. 4.

Peak broadening, crystallite size, strain, and dislocation density of rhombohedral tricalcium phosphate: in 1918 Scherrer derived a formula relating the mean of the volume average of crystallite size, D, of a powder to the broadening, β , of its powder diffraction peaks ignoring other effects such as strain [41, 42], as described by:

$$D(\beta, \theta) = \frac{K \cdot \lambda}{\beta \cdot \cos \theta} \tag{C}$$

where θ is the usual Bragg angle, λ is the radiation wavelength, and K is a constant that depends on the assumption in the theory. Particularly, the refinements of X-ray patterns for the samples Ca(OH)_2 , heated at 800 and 1000 °C are shown in Figs. 5a to 5c. The refinement curves obtained by using the Gaussian method were used to determine several corresponding parameters in Eqs. C and D, such as a crystallite size $D(\beta, \theta)$, broadening β , and strain ϵ . The formulation in Eq. D was attributed to G. K. Williamson and his student, W. H. Hall. Subsequently, by

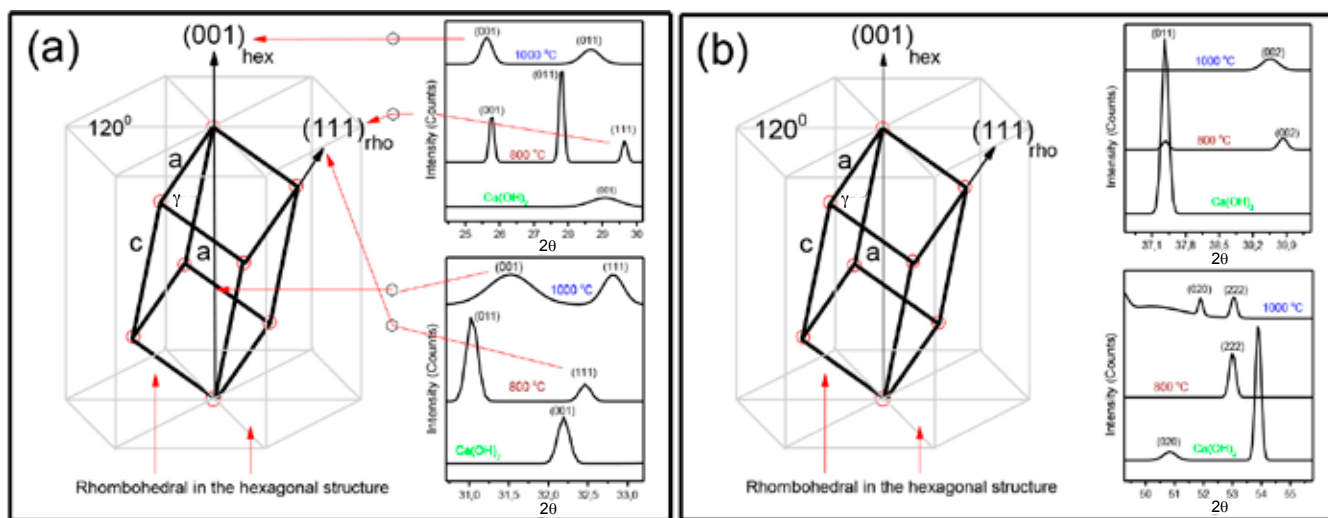


Figure 4: Representation of rhombohedral Miller indices in the 2θ range from: a) $\sim 24.4^\circ$ to $\sim 33.2^\circ$; and b) $\sim 36.5^\circ$ to 55.6° .

using a software (Origin Pro) approximation to determine the FWHM values that varied quite differently with respect to Bragg angle θ , the crystallite broadening parameter β was found. These all parameters found were related to the specific Miller indices for rhombohedral tricalcium phosphate in the hexagonal crystal structure described previously.

$$\beta \cdot \cos\theta = 4\varepsilon \cdot \sin\theta + \frac{K \cdot \lambda}{D(\beta, \theta)} \quad (D)$$

Particularly, Figs. 6a to 6c denote specific Miller indices (001) at different Bragg angle values for sample $\text{Ca}(\text{OH})_2$, heated at 800 and at 1000 °C. The Miller indices (001) is one of three lattice plane orientations for hexagonal crystal structure, with the rhombohedral crystal structure inside with 3-fold symmetry, [100], [010], and [110], such as shown in Fig. 2. The quantities of several parameters are shown in Table I, where the crystallite size D , strain ε , and dislocation density δ values were calculated by using Eqs. A and D. Previously, the data were plotted (Fig. 5d), after fitted by the linear equation in the curve $\beta \cos\theta$ vs. $4\sin\theta$, and then from the linear regression the slope and intercept values were found (Fig. 6d). The curve slope gave the crystallite strain value and from

curve intercept the crystallite size value was found. All values of the crystallite size D , strain ε , and dislocation density δ of the rhombohedral tricalcium phosphate sample are displayed in Table I. The slope of linear regression in Fig. 6d tended to decrease with the crystallite strain, resulting in negative values for the samples $\text{Ca}(\text{OH})_2$ and heated at 800 °C. Conversely, for the sample heated at 1000 °C, it tended to increase with the crystallite strain and had a positive value. Consequently, the crystallite strain was proportional to the crystallite dislocation density value, however, it was reciprocal to the crystallite size value.

SEM-EDX analysis for rhombohedral tricalcium phosphate in the hexagonal crystal structure: the SEM-EDX results for two samples that are comparable, those heated at 800 and 1000 °C, are shown. Previously, the surface profile of samples calcined at 800 and 1000 °C looked different from one another, as shown in Figs. 7a and 7b. Both seemed like a white cloud, however, the sample calcined at 1000 °C looked denser than the sample calcined at 800 °C. This indicated that the increase in temperature from 800 to 1000 °C influenced the grain size of the rhombohedral tricalcium phosphate sample which became denser. Meanwhile, the quantities

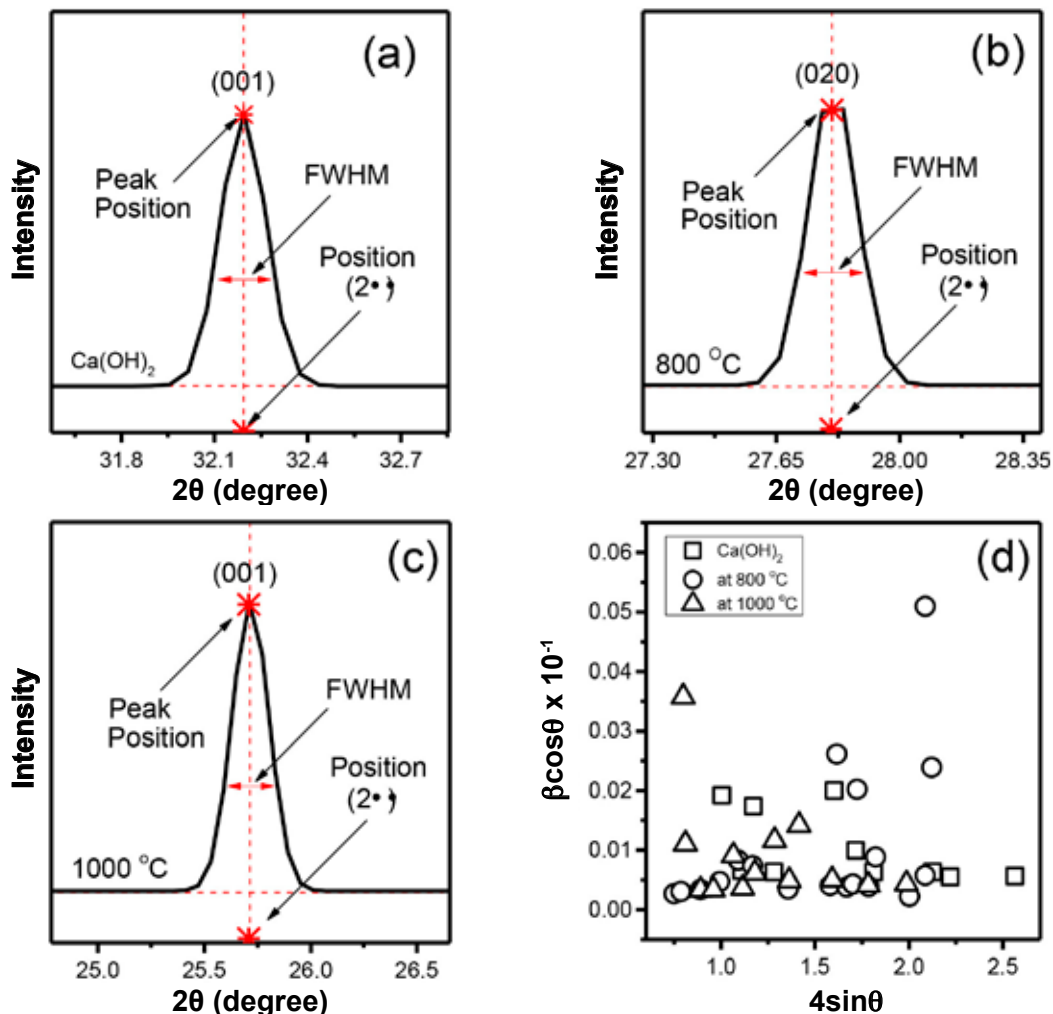


Figure 5: XRD peak at particular Bragg's angle and Miller indices for $\text{Ca}(\text{OH})_2$ (a), sample heated at 800 °C (b) and at 1000 °C (c), and W-H plot, $\beta \cos\theta$ versus $4\sin\theta$ (d).

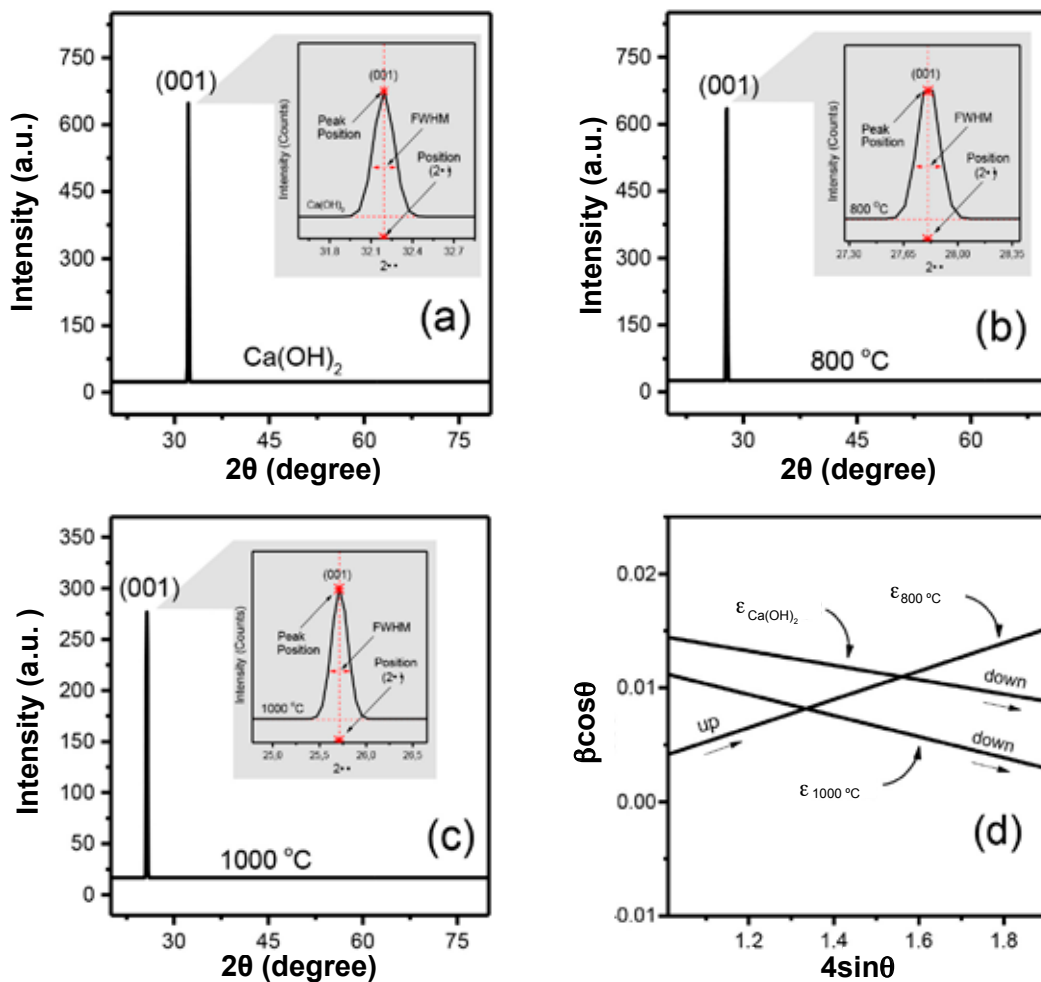


Figure 6: XRD peak for the specific Miller indices at (001) for Ca(OH)₂ (a), sample heated at 800 °C (b) and at 1000 °C (c), and W-H plot for crystallite strain determinations, $\epsilon_{Ca(OH)_2}$, $\epsilon_{800^\circ C}$, and $\epsilon_{1000^\circ C}$.

Table I - Crystallite size (D), strain (ϵ), dislocation density (δ), and crystallinity of samples calculated by using the XRD data.

Sample	D (nm)	ϵ	δ (nm ⁻²)	Crystallinity (%)
Ca(OH) ₂	69.3	-0.001±0.003	0.21	65.7
Heated at 800 °C	86.7	0.012±0.006	0.83	71.3
Heated at 1000 °C	73.0	-0.008±0.007	0.18	69.1

of elements in the samples of rhombohedral tricalcium phosphate obtained by EDX analysis are shown in Table II. The atomic ratio Ca/P ~1.3 and mass ratio Ca/P ~1.4 of the sample heated at 800 °C were found whilst for the sample heated at 1000 °C the atomic ratio Ca/P ~1.43 and mass ratio Ca/P ~1.7. Therefore, the nearly rhombohedral tricalcium sample was formed with a chemical formula β -Ca₃(PO₄)₂ or β -TCP for both samples calcined at 800 and 1000 °C. In other words, the high calcination temperature, particularly at 800 and 1000 °C, was effective to form the rhombohedral tricalcium phosphate, which previously was proven by XRD analysis in this study.

DSC-TGA analysis of gel sample: the thermal analysis of the gel sample was examined by using the DSC-TGA

equipment and it was set up looking for the effective calcination temperature. 800 and 1000 °C were chosen to conduct different treatments on the sample to obtain the rhombohedral tricalcium phosphate. However, these temperatures had to be compared with other references, before being used as an effect in the sample. The recorded thermogram of DSC plotted as heat flow versus temperature and TGA curve are shown in Fig. 8. On a DSC curve, endothermic and exothermic processes occur that can be described by the enthalpy changes during glass transition, melting, and crystallization. Simultaneously, the mass reduction with temperature (TGA curve) can be obtained. In particular temperature ranges of the thermogram of DSC-TGA gave the endothermic and exothermic process,

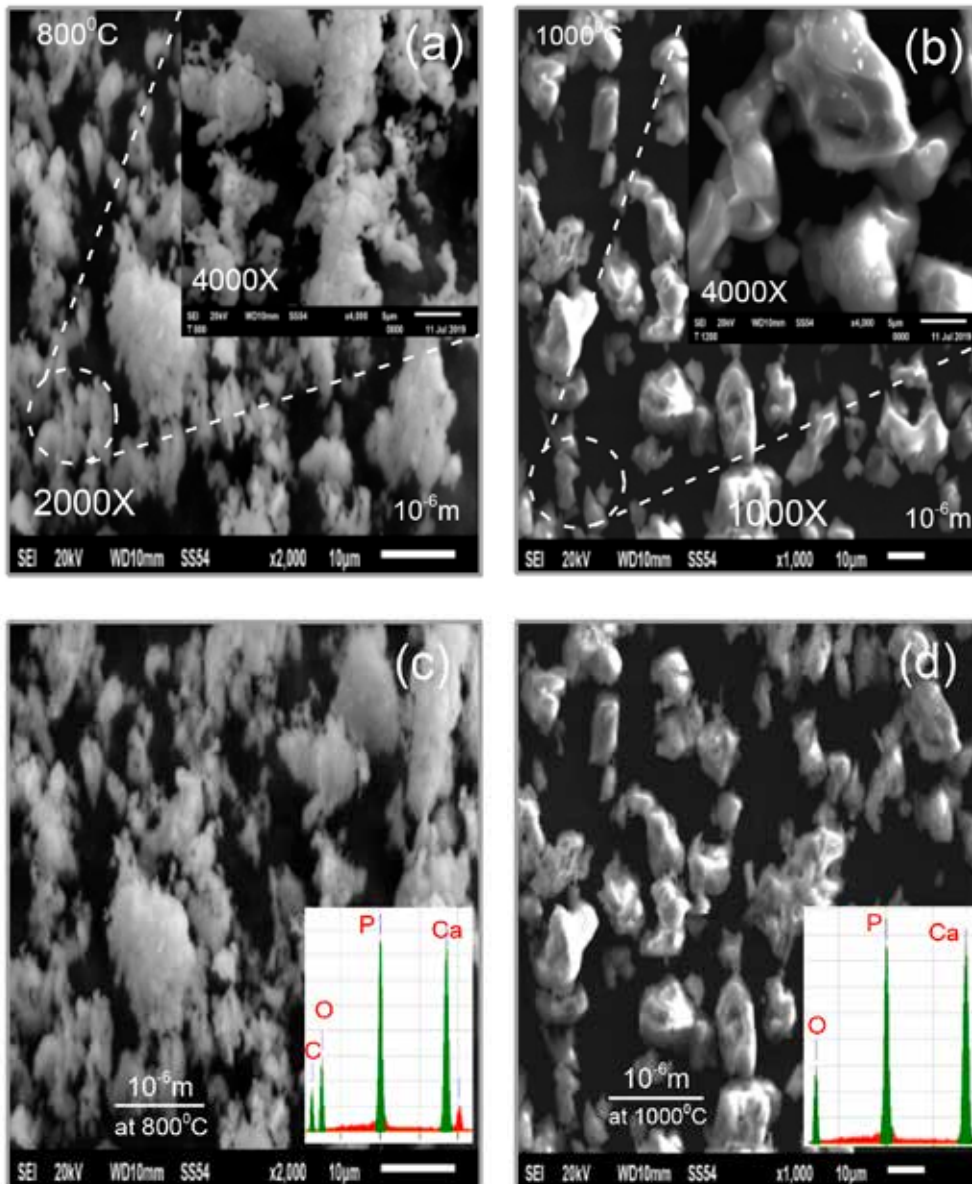


Figure 7: SEM images of samples heated at 800 °C (a,c) and 1000 °C (b,d); EDX spectra are included in (c,d).

Table II - Quantities of elements of samples obtained from the EDX test.

Element	Mass (%)	Atomic (%)	Error (%)
Sample heated at 800 °C			
O	36.08	39.68	0.30
P	14.13	7.02	0.06
Ca	19.72	8.98	0.10
C	30.07	44.32	0.08
Sample heated at 1000 °C			
O	41.42	53.32	0.27
P	17.08	11.12	0.06
Ca	29.86	15.87	0.09
C	11.64	19.69	0.09

denoted by the peak-to-peak shifting. In Fig. 8a, the initial peak appeared for an endothermic reaction in the DSC and TGA thermogram curves at about 60 to 128 °C, and an exothermic reaction occurred at about 130 to 159 °C. After that, sequentially in the temperature range from 146 to 184 °C for endothermic reaction and ~190 to ~240 °C for exothermic process occurred (Fig. 8b). Furthermore, at about 354 to 402 °C for endothermic reaction and about 406 to 460 °C for exothermic process occurred (Fig. 8c). Finally, in the temperature range from about 614 to 748 °C for exothermic reaction and about 758 to 855 °C for endothermic process occurred (Fig. 8d). Therefore, based on these results and compared with appropriate references related to the topic, the study of rhombohedral tricalcium phosphate in hexagonal crystal structure was influenced by the chosen temperatures of 800 and 1000 °C, when the sample was previously prepared by the sol-gel route. Meanwhile, the

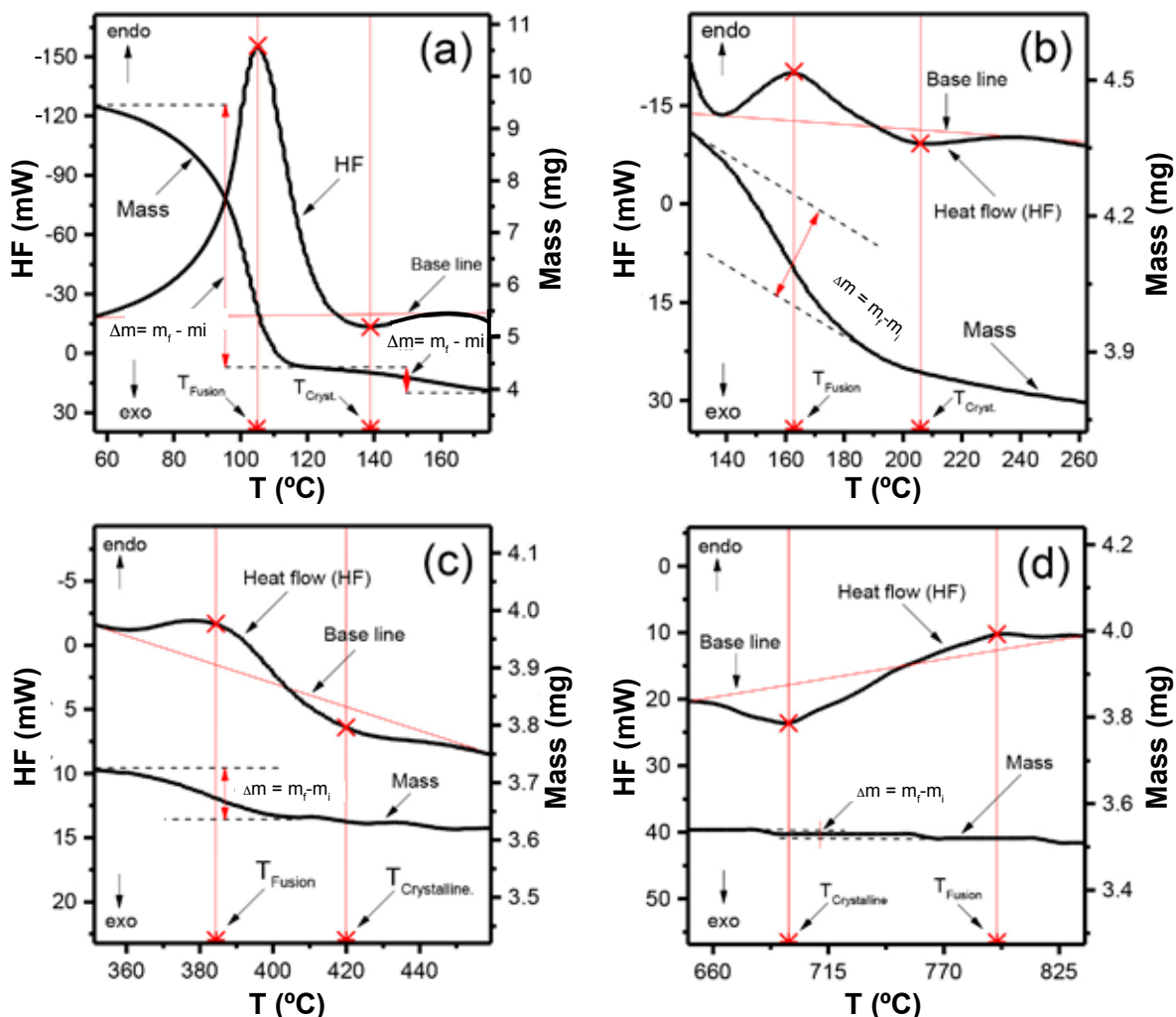


Figure 8: DSC-TGA thermograms of gel sample in the specific temperature ranges.

Table III - Results of melting point (T_i and T_p), enthalpy of fusion (ΔH_f), enthalpy of crystallization (ΔH_c), and specific heat capacity (C_p) of gel sample.

T_i (°C)	T_f (°C)	ΔH_f (J.g ⁻¹)	ΔH_c (J.g ⁻¹)	C_p (J.g ⁻¹ .°C ⁻¹)
91.12	131.13	1290.34	42.45	4.43
359.06	465.76	57.87	27.06	0.58
617.28	653.15	8.01	123.13	12.89
937.87	960.15	8.78	10.98	6.21

values of melting point, enthalpy of fusion, enthalpy of crystallization, and specific heat capacity of the samples treated at 800 and 1000 °C were calculated by using the DSC-TGA results and are shown in Table III.

Figs. 9a and 9c show the melting and crystallization points as a function of time or temperature. Every endothermic peak is the point of melting or fusion. Otherwise, each exothermic peak is a point of crystallization, such as denoted by the red sign in Figs. 9a and 9c, whilst each endothermic peak area is the quantity

of enthalpy of fusion or melting, and each exothermic peak area is a quantity of enthalpy of crystallization, as denoted by hatched areas in Fig. 9b. For a specific mass reduction in the TGA curve at the temperature range from ~27 to ~190 °C showed that the DTG (derivative of TGA) curve was instantaneously shifted following the mass change (Fig. 9d). This result indicated the crystalline structure of the sample was changed as a function of temperature and the chemical bond changed when heat flowed in (absorbed by the endothermic process) or out (released by the exothermic process) [43, 44]. Table III shows the results of initial, T_i , and final, T_p , melting or fusion temperatures, enthalpy of fusion, ΔH_f , and crystallization, ΔH_c , and specific heat capacity, C_p . These results indicated that the gel phase of the rhombohedral tricalcium phosphate sample became a dry powder, and justified the temperature range from ~937.87 to ~960.15 °C. Therefore, based on this analysis, the temperatures chosen were 800 and 1000 °C in this work and then their effects on the rhombohedral tricalcium phosphate inside the hexagonal crystal structure were studied.

UV-vis analysis for rhombohedral tricalcium phosphate in the hexagonal crystal structure: analysis of the optical

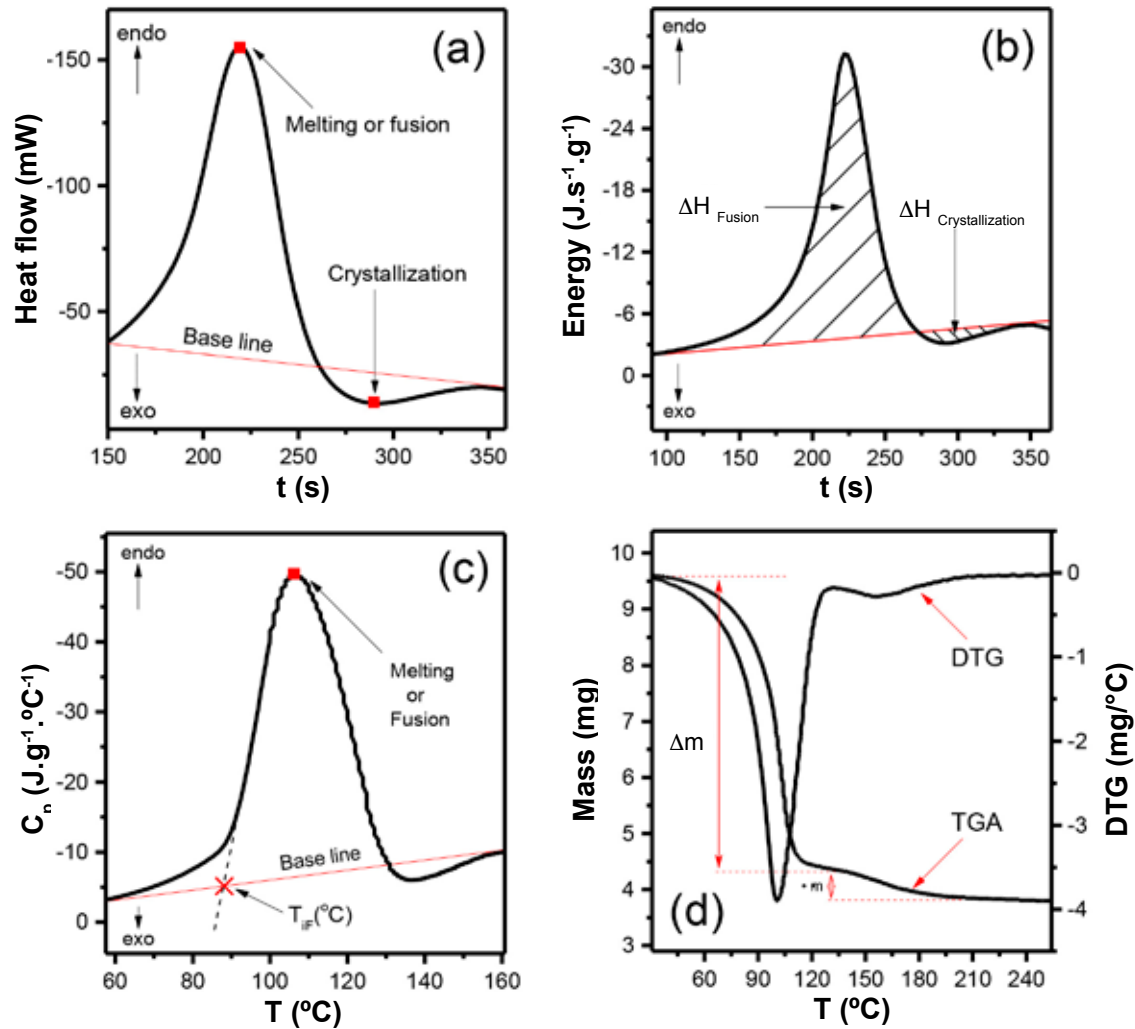


Figure 9: Curves of heat flow versus time (a), energy versus time (b), C_p versus temperature (c), and TGA and DTG thermograms (d).

properties of the rhombohedral tricalcium phosphate sample in this work was conducted by using UV-vis spectroscopy. This is one of the important characterization techniques to understand the interaction between the matrix and filler inside a synthesized sample and to analyze the effects to enhance the properties of a composite sample. Therefore, this technique was used in this work to look for the optical band gap of the rhombohedral tricalcium phosphate sample. In the beginning, the UV-vis spectroscopy gave the absorption spectra of samples in duplicate for sample calcined at 800 °C (Figs. 10a and 10b) and at 1000 °C (Figs. 10c and 10d). The optical band gap of rhombohedral tricalcium phosphate samples was found by using the Tauc plot and using Eq. E:

$$(\alpha \cdot h \cdot \nu)^\gamma = A(h \cdot \nu - E_g) \quad (E)$$

where α is the absorption coefficient, h is Planck's constant, ν is the frequency of the incident photon, A is a proportionality constant determined by the index of refraction, and E_g is the optical band gap energy. The important term is the exponent γ , which denotes the nature of the electronic transition. There are some terms for the exponent γ in Eq. E; when $\gamma=2$, it is a

direct allowed transition, when $\gamma=1/2$, it is an indirect allowed transition, when $\gamma=2/3$, it is a direct forbidden transition, and when $\gamma=1/3$, it is an indirect forbidden transition. However, typically, the allowed transitions are dominated by the basic absorption processes giving either direct or indirect transitions [45, 46]. Thus, the basic procedure for Tauc analysis is to acquire the absorbance data of a sample from UV-vis spectral information, as shown in Fig. 10, where the band gap transition energy is defined. By plotting the $(\alpha h\nu)^2$ versus $h\nu$ (considering $\gamma=2$ in Eq. E), a graph such as those shown in the insets of Fig. 10 is obtained. Extrapolation of the linear curve of the plot onto the x-axis gave the optical band gap or edge energy, just as Tauc's equation was used in 1968 to calculate the absorption edge or band gap energy [47, 48].

By twice plotting curves of the $(\alpha h\nu)^2$ versus $(h\nu)$ for the sample calcined at 800 °C, the optical band gap energy (E_g) was found to be ~ 5.34 and ~ 5.41 eV (Figs. 10a and 10b). Meanwhile, for the sample calcined at 1000 °C, the determined E_g values were ~ 5.19 and ~ 5.21 eV (Figs. 10c and 10d). Therefore, rhombohedral tricalcium phosphate samples are responsive under UV-vis light. However, it is still unclear to define that it can behave as a photocatalyst under UV-vis

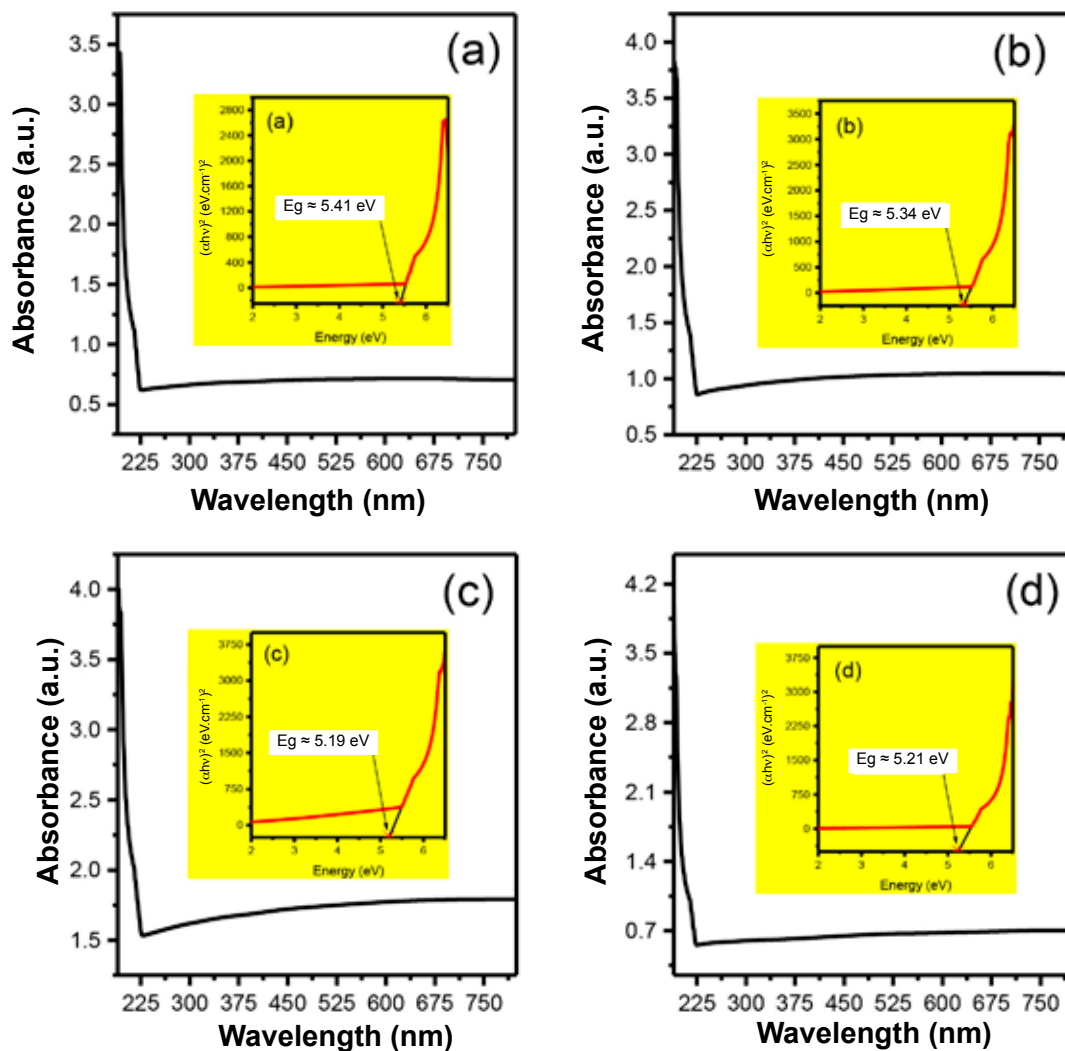


Figure 10: UV-vis absorption spectra of rhombohedral tricalcium phosphate samples calcined at 800 °C (a,b) and at 1000 °C (c,d)

light, probably due to oxygen deficiencies compared with hydroxyapatite $[\text{Ca}_5(\text{PO}_4)_3(\text{OH})_2]$ that can have photocatalytic activity under UV light, due to the reported optical band gap energy of all samples varied greatly ($E_g \sim 5.34$ to ~ 5.41 eV, and ~ 5.19 to ~ 5.21 eV). However, the optical energy gap of the rhombohedral tricalcium phosphate sample tended to decrease when the calcination temperature increased from 800 to 1000 °C.

CONCLUSIONS

The sample of rhombohedral tricalcium phosphate in the hexagonal crystal structure prepared by a sol-gel route was influenced by the calcination temperature and was studied by several tests, such as FTIR, XRD, SEM-EDX, DSC-TGA, and UV-vis spectroscopy. The information of deficiencies of the hydroxyl functional group of -OH was shown by FTIR and this indicated the results of a tricalcium phosphate when calcination temperatures at 800 and 1000 °C were applied to this sample. The rhombohedral structure in the hexagonal crystal system of the sample was confirmed by XRD, where the Miller indices showed the rhombohedral lattice plane orientation

at two points (011) and (111). The temperatures used at 800 and 1000 °C were confirmed by DSC-TGA and effectively influenced and made the sample of tricalcium phosphate with a stable structure in the rhombohedral system. The atomic ratio Ca/P ~ 1.5 of the rhombohedral tricalcium phosphate sample was found by EDX and its surface topography looked like white clouds using SEM. Finally, the optical energy gap of the rhombohedral tricalcium phosphate sample had quite large values of $E_g \sim 5.34$ - 5.41 eV, when calcined at 800 °C, and $E_g \sim 5.19$ - 5.21 eV, when calcined at 1000 °C. These results indicated that the optical band gap of the rhombohedral tricalcium phosphate sample tended to be wide and to decrease when the calcination temperature increased.

ACKNOWLEDGMENTS

We thank especially the Ministry of Research, Technology, and Higher Education of Indonesia for providing all support.

REFERENCES

- [1] A.I. Ibrahim, N.R. Al-Hasani, V.P. Thompson, S. Deb, J.

- Clin. Exp. Dent. **12**, 4 (2020) 317.
- [2] A. Seifert, J. Groll, J. Weichhold, A.V. Boehm, F.A. Müller, U. Gbureck, *Adv. Eng. Mater.* **23**, 5 (2021) 1.
- [3] N. Laohavisuti, B. Boonchom, W. Boonmee, K. Chaiseeda, S. Seesanong, *Sci. Rep.* **11**, 1 (2021) 1.
- [4] W.M. Haynes, *Handbook of chemistry and physics*, 97th ed., CRC Press (2016) 121.
- [5] K. Rubenis, S. Zemjane, J. Vecstaudza, J. Biteniekis, J. Locs. *J. Eur. Ceram. Soc.* **41**, 1 (2021) 912.
- [6] S. Grasso, M. Biesuz, L. Zoli, G. Taveri, A.I. Duff, D. Ke, A. Jiang, M.J. Reece, *Adv. Appl. Ceram.* **119**, 3 (2020) 115.
- [7] M. Yashima, A. Sakai, T. Kamiyama, A. Hoshikawa, *J. Solid State Chem.* **175**, 2 (2003) 272.
- [8] H. Chair, H. Labjar, O. Britel, *Morphologie* **101**, 334 (2017) 124.
- [9] D. Moreno, F. Vargas, J. Ruiz, M.E. López, *Bol. Soc. Esp. Ceram. V.* **59**, 5 (2020) 2.
- [10] T.V. Safronova, I.I. Selezneva, S.A. Tikhonova, A.S. Kiselev, G.A. Davydova, T.B. Shatalova, D.S. Larionov, J.V. Rau, *Bioact. Mater.* **5**, 2 (2020) 423.
- [11] A.P. Periyasamy, M. Venkataraman, D. Kremenakova, J. Militky, Y. Zhou, *Materials* **13**, 8 (2020) 1838.
- [12] G.J. Owens, R.K. Singh, F. Foroutan, M. Alqaysi, C. Han, C. Mahapatra, H. Kim, J.C. Knowles, *Prog. Mater. Sci.* **77** (2016) 1.
- [13] P. Owczarz, M. Orczykowska, A. Rył, P. Ziółkowski, *Food Chem.* **271** (2019) 94.
- [14] A.E. Danks, S.R. Hall, Z. Schnepp, *Mater. Horizons* **3**, 2 (2016) 91.
- [15] M. Anugrahwati, M.D.P. Nasution, F.I. Fajarwati, *J. Pijar Mipa* **17**, 1 (2022) 73.
- [16] E. Isparnadi, M. Hidayat, A. Aulanni'am, N. Permatasari, *Int. J. Chemtech Res.* **8**, 6 (2015) 718.
- [17] R. Jing, A. Varveri, X. Liu, A. Scarpas, S. Erkens, *Road Mater. Pavement Des.* **22**, 5 (2019) 1.
- [18] L. Ma, M. Li, S. Komasa, S. Yan, Y. Yang, M. Nishizaki, L. Chen, Y. Zeng, X. Wang, E. Yamamoto, S. Hontsu, Y. Hashimoto, J. Okazaki, *Materials* **15**, 6 (2022) 2306.
- [19] Y. Tang, X. Qiu, X. Gong, Y. Tang, *Acta Mater. Compos. Sin.* **39**, 1 (2022) 169.
- [20] Í.E.L. Viana, R.M. Lopes, F.R.O. Silva, N.B. Lima, A.C.C. Aranha, S. Feitosa, T. Scaramucci, *J. Dent.* **92** (2020) 103263.
- [21] M. Zheng, D. Fan, X.K. Li, Q.B. Liu, J.B. Zhang, *Key Eng. Mater.* **373-374** (2008) 710.
- [22] H. Zhang, S. Xu, Y. Xiong, R. Gao, X. Li, *J. Mech. Eng.* **55**, 15 (2019) 81.
- [23] S.A. Silva, R.E.F.Q. Nogueira, J.M.C. Teixeira, J.S.V. Albuquerque, E.B. Duarte, *Matéria* **24**, 1 (2019) 1.
- [24] T. Tariverdian, A. Behnamghader, P.B. Milan, H. Barzegar-Bafrooei, M. Mozafari, *Ceram. Int.* **45**, 11 (2019) 14029.
- [25] T. Furihata, H. Miyaji, E. Nishida, A. Kato, S. Miyata, K. Shitomi, K. Mayumi, Y. Kanemoto, T. Sugaya, T. Akasaka, *J. Biomed. Mater. Res. B Appl. Biomater.* **108**, 7 (2020) 34632.
- [26] M. Taherimehr, R. Bagheri, M. Taherimehr, *Ceram. Int.* **47**, 11 (2021) 15458.
- [27] Y.M. Sahin, Z. Orman, S. Yucel, *J. Aust. Ceram. Soc.* **56**, 2 (2020) 477.
- [28] D.H. Yang, M.S. Bae, L. Qiao, D.N. Heo, J.B. Lee, W.J. Lee, J.H. Park, D.W. Lee, Y. Hwang, I.K. Kwon, *Macromol. Res.* **20**, 7 (2012) 754.
- [29] J.A.R. Pasqual, L.C. Freisleben, J.C. Colpo, J.R.J. Egea, L.A.L. dos Santos, V.C. de Sousa, *J. Mater. Sci. Mater. Med.* **32**, 4 (2021) 38.
- [30] R. Bento, A. Gaddam, J.M.F. Ferreira, *Materials* **14**, 16 (2021) 4515.
- [31] T.N.M. Bernards, M.J. van Bommel, E.W.J.L. Oomen, A.H. Boonstra, *J. Non. Cryst. Solids* **147-148** (1992) 13.
- [32] O.E. Shapovalova, A.S. Drozdov, E.A. Bryushkova, M.I. Morozov, V.V. Vinogradov, *Arab. J. Chem.* **13**, 1 (2020) 1933.
- [33] M.A. Almessiere, Y. Slimani, U. Kurtan, S. Guner, M. Sertkol, S.E. Shirsath, S. Akhtar, A. Baykal, I. Ercan, *Ultrason. Sonochem.* **58** (2019) 104638.
- [34] A. Vilvanathaprabu, B. Ravikumar, *J. Phys. Conf. Ser.* **1644**, 1 (2020) 12034.
- [35] P. Phatai, C.M. Futralan, S. Utara, P. Khemthong, S. Kamonwannasit, *Results Phys.* **10** (2018) 956.
- [36] S. Kannan, F. Goetz-Neunhoffer, J. Neubauer, A.H.S. Rebelo, P. Valério, J.M.F. Ferreira, *J. Biomed. Mater. Res. B Appl. Biomater.* **90**, 1 (2009) 31299.
- [37] A.C.B. Jesus, J.R. de Jesus, R. Lima, K.O. Moura, J.M.A. Meneses, J.G.S. Duque, C. Meneses, *Ceram. Int.* **46**, 8 (2020) 11149.
- [38] M. Horchani, A. Omri, A. Benali, M.S. Eddine, A. Tozri, E. Dhahri, M.P.F. Graça, M.A. Valente, B.F.O. Costa, S.K. Jakka, *J. Solid State Chem.* **308** (2022) 122898.
- [39] S.K. Sen, U.C. Barman, M.S. Manir, P. Mondal, S. Dutta, M. Paul, M.A.M. Chowdhury, M.A. Hakim, *Adv. Nat. Sci. Nanosci. Nanotechnol.* **11**, 2 (2020) 5004.
- [40] N.W. Ashcroft, N.D. Mermin, *Solid state physics*, Rinehart Winston, New York (1976).
- [41] D. Louër, J.P. Auffrédic, J.I. Langford, D. Ciosmak, J.C. Niepce, *J. Appl. Crystallogr.* **16**, 2 (1983) 183.
- [42] D. Balzar, N. Audebrand, M.R. Daymond, A. Fitch, A. Hewat, J.I. Langford, A. Le Bail, D. Louër, O. Masson, C.N. McCowan, N.C. Popa, P.W. Stephens, B.H. Toby, *J. Appl. Crystallogr.* **37**, 6 (2004) 911.
- [43] A.L.C.S. Nascimento, G.M.B. Parkes, G.P. Ashton, R.P. Fernandes, J.A. Teixeira, W.D.G. Nunes, M. Ionashiro, *J. Anal. Appl. Pyrolysis* **135** (2018) 67.
- [44] M. Ciecinińska, P. Goj, A. Stoch, P. Stoch, *J. Therm. Anal. Calorim.* **139**, 3 (2020) 1763.
- [45] F.P.N. Inbanathan, P. Kumar, K. Dasari, R.S. Katiyar, J. Chen, W.M. Jadwisieniczak, *Materials* **14**, 12 (2021) 3307.
- [46] J.B. Coulter, D.P. Birnie, *Phys. Status Solidi Basic Res.* **255**, 3 (2018) 1700393.
- [47] M. Sheik-Bahae, D.C. Hutchings, D.J. Hagan, E.W. Van Stryland, *IEEE J. Quantum Electron.* **27**, 6 (1991) 89946.
- [48] S. Muhammadiyah, Y. Kurniawan, M.A.K. Purbayanto, Y. Darma, *Mater. Res. Express* **5**, 6 (2018) 66303.
- (Rec. 09/08/2022, Rev. 16/11/2022, 31/12/2022, Ac. 07/01/2023)

Mesh reinforcement in masonry mortar coatings: a systematic literature review

V. A. Coelho^{1*}, F. G. S. Silva²

¹Federal University of Bahia, Polytechnique School, Post-Graduation Program in Civil Engineering,
R. Aristides Novis 2, 40210-630, Salvador, BA, Brazil

²Federal University of Bahia, Polytechnique School, Department of Structural and Construction Engineering,
Salvador, BA, Brazil

Abstract

Mortar coatings have a major influence on a building's aesthetics, valorization, and habitability, with significant effects on the mechanical behavior of masonry walls. Multiple types of meshes can be embedded in plaster to enhance both masonry and coating's mechanical behavior, restrain crack formation, enhance the bonding between layers, and increase the wall's seismic resistance. The reinforcement technique has simple execution and is suitable for many applications, including the strengthening of non-load bearing walls, façade performance improvement, and restoration of historical buildings. However, there is an absence of guidelines and specifications for design and execution, resulting in high variability in field applications due to the many variables involved and few in-depth studies. This paper presents a systematic review of the effects of mesh reinforcement in cementitious mortar coatings and its major applications. Mortar and mesh parameters and influences, the status of analytical and simulation models, and suggestions for future research are described.

Keywords: coating, reinforced, façade, cracking, composite.


INTRODUCTION

Masonry elements are susceptible to the occurrence of several pathological manifestations that reduce the building's overall performance and durability due to its nature, composed of multiple layers of different materials, and exposition to multiple deterioration agents. There is also the influence of design specifications, construction techniques, quality control, and, sometimes, a lack of specific building codes [1, 2]. Such a scenario raises concerns about building safety, especially for historic buildings [3]. Coatings have major relevance to a construction's performance, influencing the aesthetics, security, comfort, and valorization of buildings. This system characterizes the external visual, customizes the inner rooms, regulates waterproofing, thermic and acoustic insulation, fire safety, and many other factors involved in maintainability and usage [4, 5]. Mortar coatings also enhance the mechanical behavior of masonries by slenderness reduction, cross-section increase, and stress distribution [6, 7]. Masonry performance can be improved even more if reinforcing meshes are embedded in the coating layer, a technique known for its low cost, ease of execution, and high compatibility with multiple materials [8-10]. This procedure provides greater mechanical strength for masonries under multiple load conditions and many studies suggest it is suitable for repair, retrofitting, and reinforcement applications, as well as seismic strengthening

of non-structural infill walls [7, 11-13].

Cementitious mortars are known for their high rigidity, showing little or no plastic deformation. Hence, the coatings suffer from the occurrence of cracking when subjected to tensile stresses, caused by various phenomena, and the use of reinforcing elements can provide more than just higher tensile strength. Visible cracking results from the propagation of microcracks along paths of lower resistance in the cementitious microstructure, and the mesh wires act as resisting cores since more energy is needed to pass through its surroundings, restraining the opening and propagation of cracking [14, 15]. Also, the reinforcement distributes stresses along the mortar layer [14, 16-19], and may be used to enhance the bonding with the masonry or between multiple layers to reduce the risk of coating spalling and falling due to the high specific surfaces of the meshes [20]. Microstructural understanding of the reinforcements is also very important, since the mortar's rheology and reinforcement's geometrical features, as well as the chemical compatibility between them, are strongly connected to the bonding and behavior of the composite [21]. A good interlocking combination between mortar and reinforcement is known to provide great results in retrofitting applications, being able to enhance the energy absorption, displacement, and load capacity of wallets by more than 100% [22]. The technique is described in some international standards, albeit in an incipient way [20, 21, 23]. The Brazilian Standards (NBR), for example, recommends the use of metallic mesh reinforcement to avoid cracking in transition zones between different materials subjected to differential deformation and as support for thick coating layers [24-26]. However, the normative prescriptions

*mrvoelho@gmail.com

 <https://orcid.org/0000-0003-3595-9433>

are superficial and very limited. There is also an absence of guidelines and specifications for the design and execution of such procedures, resulting in high variability in real applications and endorsing the need for in-depth studies about efficiency, methodology, and performance [20, 22]. Also, the development of analytical and simulation models for reinforcement design is hampered due to the intrinsic heterogeneity of such materials and the numerous amount of variables that affect its behavior, such as mesh's material, wire diameter, durability, grid format and spacing, mortar's type and mechanical properties, the use of connectors, type of masonry, and loading conditions [20, 27].

The potential benefits of coating reinforcements, added to the increasing need for an upgrade of existing buildings due to deterioration, deficient maintenance, and the need for compliance with new performance standards, have inspired more in-depth research on the topic [28-30]. Mesh reinforcements are suitable for strengthening and repair of structural, historical, and non-structural masonries. However, the high number of influent factors and test procedures hinders a clear understanding of the technique's state of development, specifications, and potential applications. The main goal of the present systematic review is to present a wider understanding of the reinforcement of masonry cementitious mortar coating with these elements, observing how the mesh, masonry, and mortar properties affect the system performance under different applications. Such understanding is fundamental to the development of further studies focused on the optimization of the technique and examination of the microstructural relationship between mesh and mortar matrices aspiring for enhanced performance of mortar coatings. Along these lines, this review used a variant of the 'population, phenomena of interest and context' (PICO) framework [28] as a guide to establishing the following research question: what are the effects of mesh reinforcement in cementitious mortar coatings?

METHODOLOGY

The standards of the 'preferred reporting items for systematic review and meta-analysis' (PRISMA) [31] were

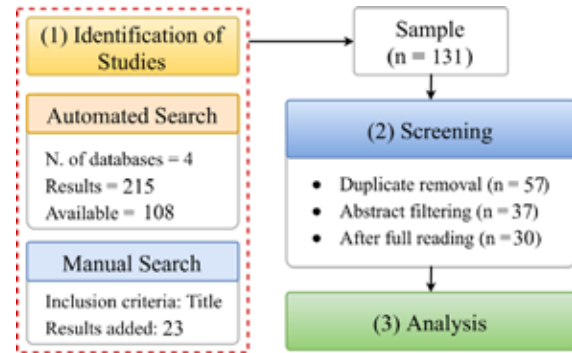


Figure 1: Flow diagram of the review steps.

adopted as guides for this systematic review. The study is divided into three main steps shown in Fig. 1 and further explained: 1) identification and collection of potentially relevant studies; 2) screening, assessment, and filtering accordingly to inclusion and exclusion criteria; and 3) information gathering, analysis, and synthesis. Automated searches were performed on SCOPUS, Web of Science, SciELO, and Engineering Village databases along with a manual search on Google Scholar for increased coverage. The automated search filters included journals, conference, and review papers, along with book chapters, without further restrictions such as publication year. The Google Scholar query included doctoral dissertations due to the database's coverage. The keywords, strings used, number of returned results, and those available to full-text access in each database are presented in Table I. The number of documents from the manual search in Google Scholar represents those whose titles were related to the research question and so were retrieved. The screening process consisted of duplicates removal (using the Mendeley Desktop software) and application of the following exclusion criteria during abstract analysis, followed by full-text reading: 1) meshes not used in cementitious mortar layer; 2) studies focused on the analysis of other materials (e.g. cement substitution); 3) concrete reinforcement techniques (e.g. carbon fiber reinforced polymers); and 4) parts of wider studies already included in the final sample.

The data collection occurred through the full reading

Table I - Search databases, strings, and the number of results for automated and manual search.

Database	String	Returned results	Available results
Engineering Village	(mortar OR plaster) AND (mesh) AND (coat*)	78	30
SciELO	[(mortar) OR (plaster)] AND (mesh) AND (coat*)	3	3
Scopus	TITLE-ABS-KEY [("mortar" OR "plaster") AND ("mesh") AND ("coat*")]	82	40
Web of Science	ALL=[(mortar OR plaster) AND mesh AND coat*]	52	35
Google Scholar	Allintitle: mortar mesh coating; mortar mesh reinforcement; plaster mesh coating; plaster mesh reinforcement; mortar mesh reinforced; plaster mesh reinforced		23
Total		215	131

of the texts and sought information regarding geometrical and material characteristics of mortars and meshes, type of masonry and analysis (experimental, analytical, or simulation), experimental design, and resulting mechanical behavior from the mesh incorporation (e.g. changes in tensile strength, cracking behavior, failure modes, etc.). The data were grouped according to the proposed system application (e.g. façade cracking, masonry strengthening, etc.). Publication year, origin country, and type of publication (e.g. journal, conference paper) were collected to perform a quantitative analysis of the results. Authors' comments were also observed to construct an overview of the body of knowledge involving meshes in mortar layers. Network maps of keywords and co-authorship relations from the final sample documents were drawn using the VOSviewer software [32]. For the keyword map, 'author keywords' were selected and filtered for synonyms and variations of form, resulting in 88 keywords. In the co-authorship map, the author's circle size used the number of occurrences as a proportion, grouped by origin country manually.

RESULTS

The search was conducted on Feb 11, 2022. The starting sample of 131 documents was reduced to 37 after duplicate removal and abstract screening. From these, seven were removed after full-text reading because they were not related to the research proposal. The removed documents and the reasons for their elimination are detailed in Table II. The final sample for analysis consisted of 30 documents, detailed in Table III. In this review, the different kinds of stones used for masonry building (e.g. cobblestone, sandstone) were considered simply as 'stone' while the varied kinds of bricks were discriminated. Likewise, applications were grouped according to their main purposes such as: composite design, reinforcement of façade coatings (against cracking and detachment), masonry strengthening (load bearing and rehabilitation), and seismic strengthening and retrofitting, illustrated in Fig. 2. The design of composite elements for structural repair or design of load-bearing elements, as well as concerns about the durability of the composite, constitutes a wider area of knowledge and are beyond this review's scope. For more information in such scenarios, the authors

recommend consulting specific publications and reviews [38-41]. The strengthening and retrofitting documents were grouped together for discussion due to similarities in tests and analysis.

The network of keywords, presented in Fig. 3, highlights masonry as the most occurring keyword, with strengthening, mortar, composite, retrofit, reinforced mortar, seismic, and coating also appearing intensively. This indicated the most common uses of mesh reinforcements in mortar layers. The keyword mesh is scattered among others that indicated the type of reinforcement, showing a high variability for the kind of material employed in such applications. The co-authorship map (Fig. 4) revealed that most of the documents analyzed were from Italy. These documents were centered on masonry strengthening with an emphasis on the seismic performance of wall frames. A common theme explored in other European documents is motivated by building guidelines concerning safety under seismic activity [13], especially in the case of older masonry structures with architectural heritage [16, 42]. The second country with more documents was Brazil, with research spread among individual groups, with one or two publications each, including one document in association with Portuguese authors. Most of the documents were associated with the effects of mesh reinforcements in building façades, while three focused on masonry strengthening, and one on reinforced mortar plates, a type of composite. The documents from Egypt, Singapore, and Saudi Arabia examined the mechanical behavior of composite plates with different kinds of meshes. Fig. 5 summarizes the number of documents per application, exhibiting a major debate in the literature over strengthening applications. The use of meshes in façade coating appears next, with relatively new studies (the oldest document dates from 2015), followed by composite and retrofitting. The strengthening and retrofitting documents are discussed together, as they are very similar and, in some cases, complementary. It is worth noting that composite applications other than coatings are vast and not the focus of this review, so the findings described in the following sections consider the results of composite specimens as an analysis of individual coating layers.

Table II - Excluded documents after full reading and reasons.

Type ⁰	Reason for removal	Ref.
JP	Numerical study on the structural behavior of masonry vaults under seismic activity	[33]
JP	Finite element analysis of chimneys' structural behavior under seismic activity	[18]
JP	Study focused on analysis of insulation materials	[34]
JP	Study focused on the evaluation of insulation plaster	[35]
CP	Part of a wider study already included	[36]
JP	Reinforcement in horizontal joints, not coating	[37]
JP	Method for concrete structure reinforcement	[29]

⁰: CP: conference paper; JP: journal paper.

Table III - Included studies and main characteristics.

Type ⁰	Country	Application	Mesh material	Mesh opening (diameter) (mm) ¹	Masonry ²	Analysis ³	Face ⁴	Coating thickness (mesh position) (mm) ⁵	Ref.
JP	Saudi Arabia	Composite	Woven galvanized steel	3.15x3.15 (0.63); 6.3x6.3 (0.63); 12x12 (0.63)	NA	EX	NA	12.5 (-)	[14]
CP	Brazil	Composite	Polymer (rhomboid); metallic (3 types)	-	NA	EX	NA	20 (10)	[43]
JP	Singapore	Composite	Bamboo fiber	10x10 (-); 15x15 (-); 20x20 (-)	NA	EX	NA	19 (-)	[44]
JP	Spain	Composite	Epoxy coated vegetal fiber	24x8 (var.)	NA	EX, AN	NA	10 (5)	[19]
JP	Brazil	Façade coating	Galvanized steel ^A	25x25 (1.24); 1/2", 1" (0.56); 1" (0.18); 2" (1.24)	NA	EX	NA	50 (33)	[21]
CP	Brazil	Façade coating	Electrowelded steel wire; alkali-resistant fiberglass; polymer (rhomboid)	25x25 (-); 10x10 (-); 20 (-)	NA	EX, AN	2	35 (17.5)	[20]
JP	Brazil	Façade coating	Electrowelded galvanized steel; steel (hexagonal); high-density polyethylene	25x25 (1.24); 12.7x12.7 (0.56); 13 (0.4)	HB	EX	1	25 (10); 50 (30)	[27]
JP	Brazil	Façade coating	Electrowelded galvanized steel; steel (hexagonal); high-density polyethylene	25x25 (1.24); 25.4x25.4 (0.71); 13 (0.4)	NA	EX	NA	50 (15); 50 (25); 50 (30)	[17]
CP	Brazil	Façade coating	Electrowelded galvanized steel	25x25 (1.24)	NA	EX	NA	50 (var.)	[15]
JP	Portugal, Brazil	Masonry strengthening	Welded steel bars	100x100 (4.2)	HB	EX	2	30 (15)	[6]
JP	Italy	Masonry strengthening	Alkali-resistant fiberglass-A; unidirectional steel strip-B	A-23x23 (2.13); A-40x40 (1.25); B-4.25 (warp)	SB	EX, SM	2	12-30 (-)	[45]
CP	Italy, United Kingdom	Masonry strengthening	Alkali-resistant fiberglass	30x35 (-); 50x50 (-)	SB, ST	EX, SM	1, 2	20-30 (-)	[30]
JP	Italy	Masonry strengthening	Alkali-resistant fiberglass	66x66 (2.19; 3.11)	SB, ST	EX	2	30 (0)	[46]
JP	Italy	Masonry strengthening	Alkali-resistant fiberglass	33x33 (3.8); 66x66 (3.8); 99x99 (3.8)	SB	EX	1	30 (0)	[3]
JP	Italy	Masonry strengthening	Alkali-resistant fiberglass	66x66 (3.8)	SB, ST	EX, SM	2	30 (15)	[16]
JP	Italy	Masonry strengthening	Alkali-resistant fiberglass-A; steel-B	A-33x33 (-); A-66x66 (-); A-99x99 (-); B-150x150 (5.0); B-200x200 (6.0)	SB	EX	2	30 (0)	[47]

(to be continued)

Type ⁰	Country	Application	Mesh material	Mesh opening (diameter) (mm) ¹	Masonry ²	Analysis ³	Face ⁴	Coating thickness (mesh position) (mm) ⁵	Ref.
DT	Brazil	Masonry strengthening	Welded steel bar	10x10 (5.0)	HB	EX	2	20-50 (0)	[48]
JP	Brazil	Masonry strengthening	Electrowelded steel wire	50x50 (2.77)	SB	EX, SM, AN	NA	20 (0)	[11]
JP	Italy	Retrofitting	Electrowelded steel wire; hot-rolled ribbed steel	50x50 (2); 200x200 (6)	HB	EX	2	25 (12.5)	[42]
JP	Iran, Australia	Retrofitting	Steel (hexagonal); polymer; alkali-resistant fiberglass	20 (-); 6x6, 15x15 (-); 6x6 (-)	SB	EX	2	20 (0)	[22]
JP	Iran	Retrofitting	Crimped steel wire	- (3.0)	SB	EX	1	30 (0)	[10]
JP	Italy	Seismic strengthening	Alkali-resistant fiberglass	5x5.9 (-)	HB	EX, SM	1	20 (0)	[12]
JP	Italy	Seismic strengthening	Alkali-resistant fiberglass	5x5.9 (-)	HB	EX	1	20 (0)	[49]
JP	Italy	Seismic strengthening	Alkali-resistant fiberglass; stainless steel cord	66x66 (3.56)	ST	EX, SM	1, 2	30 (0)	[50]
JP	Italy	Seismic strengthening	Alkali-resistant fiberglass	66x66 (3.46)	SB	EX	1	30 (0)	[51]
JP	Lebanon, Spain	Seismic strengthening	Bitumen coated fiberglass; basalt fibers; steel wire	25x25 (-); 25x25 (-); 13x13 (0.5)	HB, SB, ST	EX	1, 2	8 (5)	[13]
JP	Turkey	Seismic strengthening	Square galvanized steel	25.4x25.4 (1.5)	HB	EX	2	25 (5)	[7]
JP	Turkey	Seismic strengthening	Square steel	16x16 (1.1)	HB	EX	1	15-30 (0)	[52]
JP	Turkey	Seismic strengthening	Square steel	16x16 (1.1)	HB	EX	1	15-30 (0)	[23]
JP	China, USA	Seismic strengthening	Polypropylene	50x50 (8)	SB	EX	NA	10 (-)	[9]

⁰: CP: conference paper; JP: journal paper; DT: Doctoral thesis; ¹: (-) missing information; (var.) variable data; ²: masonry type: HB: hollow brick; SB: solid brick; ST: stone; NA: not applicable; ³: AN: analytical; EX: experimental; SM: simulation; ⁴: number of coated faces, if applicable; ⁵: total thickness of mortar layer and mesh distance from the base; ⁶: varied types of metal mesh (square, hexagonal and rhomboid).

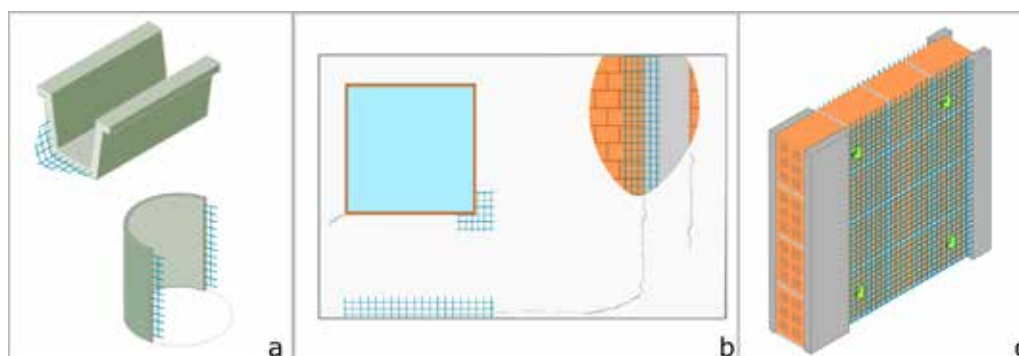


Figure 2: Illustrations of mesh uses in composite design (a), façade coating reinforcement for cracking control (b), and masonry strengthening for load-bearing scenarios (c).

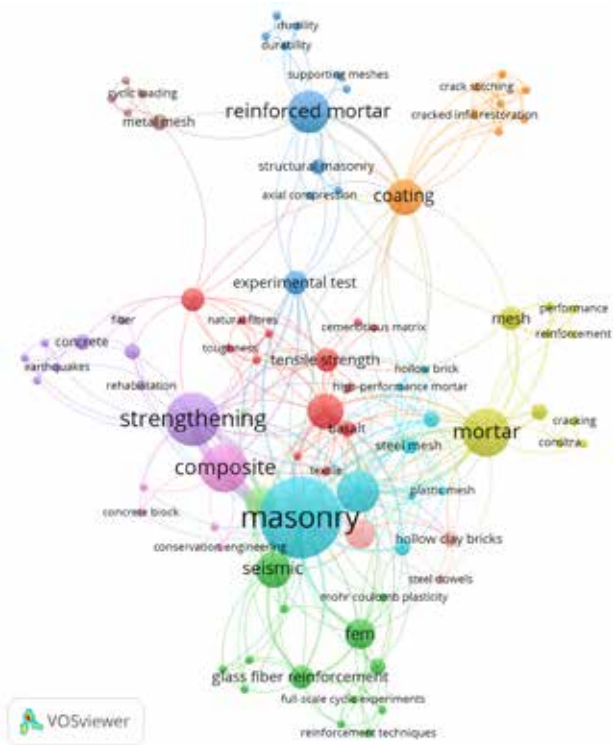


Figure 3: VOSviewer of co-occurrence by keywords map.

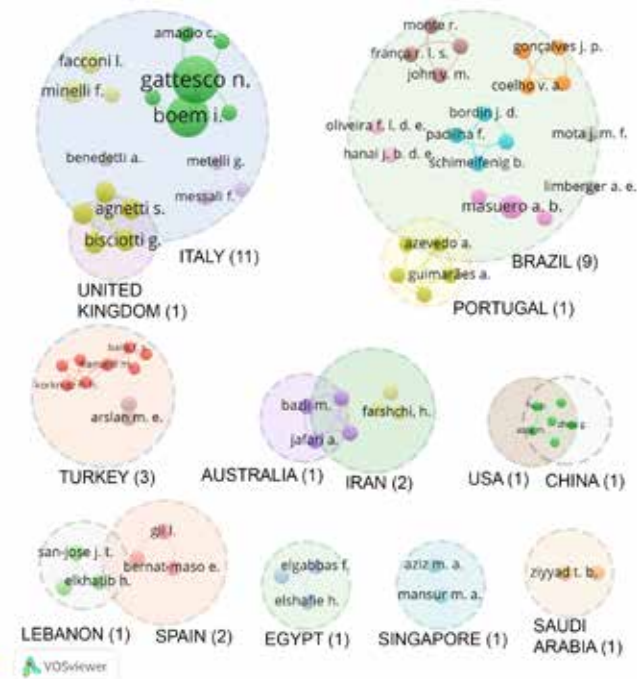


Figure 4: VOSviewer of co-authorship by authors map manually grouped by country.

Composites

A ferrocement element is composed of a combination of Portland cement mortar with a reinforcement mesh layer, somewhat similar to reinforced concrete but with a much smaller thickness (usually around 25 mm). Usually,

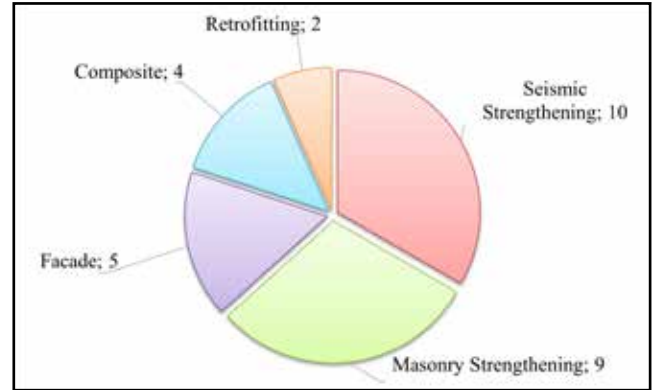


Figure 5: Number of documents per application.

the meshes are metallic, but there are no restrictions for the material used, such as plastic, fabric, glass, basalt, and other alkali-resistant fibers [14, 40]. By this definition, the materials described as composites in the documents analyzed, composed of mesh-reinforced mortar plates, are individual cases of ferrocement, also known as the fabric-reinforced cementitious matrix (FRCM) or reinforced mortars [19, 43]. All documents presented only experimental analysis, except for [19], which also proposed adjustments for an analytical model describing the tensile behavior of FRCM with three stages of deformation.

Reinforcement design: four of the five analyzed studies used high compressive strength mortar (39 to 75 MPa). The plates' thickness varied between 10 and 40 mm, meshes opening from 3.15x3.15 mm to 24x8 mm, and mesh wire diameter between 0.5 and 2.5 mm. The elastic modulus of vegetal fiber reinforcements varied between 4.87 and 38.74 GPa (after resin coating, if used) and ultimate stress between 91.9 and 630 MPa. Steel wire meshes presented 200 GPa for elastic modulus and 350 MPa for ultimate stress. No study that tested multiple materials (vegetal, metal, and polymer) presented full mesh characterization for comparison.

Mechanical behavior: the consulted studies showed good behavior of composites with steel and vegetal meshes, considering each particularity and treatment for synergy with the cementitious matrix. Steel meshes are often preferred, but some vegetal alternatives indicate benefits through low cost, lower densities, and sustainability concerns. Mansur and Aziz [44] investigated bamboo fiber mesh reinforcement and mentioned important aspects of the use of vegetal meshes in cementitious matrices such as fiber treatment with sealants to reduce water absorption and shrinkage. Fiber degradation within the matrix can be avoided with the use of resin coatings that also contributes to bond strength and stiffness. Better results of bonding strength were found with epoxy coating in comparison with polyester [19]. One or two layers of bamboo or hemp mesh promoted higher ultimate tensile strength compared to non-reinforced mortar specimens (19.3% to 275%). Flax, sisal, and cotton mesh reduced the property between 5% and 39%, even with epoxy coating [19, 44]. In general, smaller mesh openings produced the highest flexural strength [44]. Bavastri and Limberger [43]

observed increments in ultimate flexural strength between 3.47% and 13.1% using small opening sizes, while a wider grid provided a negligible 0.35% increase (the opening values were not supplied). This effect was likely due to the higher number of wires in the composite, as suggested by the findings of Shannag and Ziyad [14], where the difference between small and medium grids (3.15 and 6.3 mm steel square mesh) become almost negligible with four layers. The same study found at least the double peak strength when using four instead of two layers. The wider grid used by Bavastri and Limberger [43] was a weaved hexagonal steel mesh, known as a 'chicken net', and its negligible influence could be associated with its great deformability and variation in strength between the orthogonal directions.

Cracking, deformation, and microstructure: regarding cracking, higher energy absorptions were associated with smaller grids, better matrix-reinforcement interaction, and higher stiffness of the meshes. Those composites with low elastic modulus mesh (cotton, bamboo, and weaved steel) produced wider cracking at ultimate strength, presented higher deformations, and even reduced the cracking stress needed for the first crack to appear [14, 19, 43, 44]. Mansur and Aziz [44] observed higher cracking strength with an increase in casting pressure and with the use of a water sealant in bamboo meshes, as such treatments reduced the swelling and shrinking of fibers inside the matrix due to early water absorption, a major problem related to the use of vegetal fibers that compromises the surface interaction and bonding between mesh and mortar. Also, surface treatments may affect the mechanical properties of the fibers, where the fluidity and ability of the resin to penetrate the internal structure of the yarns must be analyzed and controlled [19]. Failure by mesh rupture was observed for steel, polymer, hemp, flax, and cotton (wire diameter between 0.5 and 1.5 mm), indicating good bonding between matrix and reinforcement. Differently, bamboo and sisal showed failure by mortar slip, associated with weaker bonding and possibly the higher diameter (2.5 mm) of the sisal fibers [14, 19, 43]. Such findings suggest that, although the tensile behavior is strongly influenced by the number of fibers and the failure mode becomes gradually more ductile, spalling and detachment of the mortar cover is possible at high reinforcement ratios [14, 19]. Shamseldein et al. [29] observed a tensile strength growing tendency of mortars reinforced with basalt fibers as more layers were added and more resistant elements became part of the material cross-section. However, there seems to be a limit to be defined beyond which delamination starts to occur depending on the mesh properties. The use of fiber-added mortars may be impaired since longer fibers prevent the mortar flow through the mesh, leading to imperfections and poor bonding. Most authors did not evaluate the influence of reinforcements on the mortar absorption properties. However, Bavastri and Limberger [43] reported a reduction in the capillary absorption of mortars using metallic meshes with small openings. This effect should be studied more since the property influences the durability of the coating.

Façade coating

The use of meshes in façade coatings is supported by the recurrent occurrence of pathological manifestations and the importance of the system for building design, quality, and performance [2, 4, 5]. The mortar coatings are susceptible to differential deformations as they are composed of juxtaposed layers with different properties. The resulting stress state often causes fractures, cracking, and detachments [21]. Reinforcement meshes are applied in various situations, especially corners of openings and transition zones between different materials, acting as distributors of punctual stresses and giving ductility to the coating, reducing the large cracking to smaller, distributed, and sometimes harmless, microcracks [17, 27]. Only one study [20] presented an analytical model for the determination of the coating stress state, considering the occurrence of cracking in the structure under the coating. The others performed experimental analysis under flexural, impact, and thermal loadings in test specimens and panels.

Reinforcement design: the main types of meshes used in façade reinforcement are electrowelded metallic with a square opening (EMS), weaved metallic with a hexagonal opening (WMH), expanded metal with a diamond opening (EMD), polymer meshes with various openings, and alkali-resistant fiberglass with a square opening (AFG). The WMH and EMD were initially produced for animal fencing or light applications, where the free passage of light and air is desired (e.g. guardrails and doors). They are highly deformable, and this may compromise their performance in mortar coatings in comparison to others. The EMS has opposite characteristics, being structurally strong with good uniformity in spacing and diameter, but harder to handle [21]. Five studies verified the EMS since it is the one recommended by the Brazilian standard NBR 13755 [24]. The mesh openings varied from 2x2 to 25x25 mm, with diameters from 0.18 to 1.65 mm [21]. The EMS with 1.24 mm wire and 25x25 mm opening presented the highest tensile strength, an order of magnitude higher than the polymer meshes, with reported wire strength between 400 and 600 MPa. The studied WMH presented a sensible gain of strength with smaller mesh openings and wire diameter due to the higher number of wires in a same-size specimen [17, 21, 27]. AFG meshes were close in strength to EMS, although they had smaller openings.

The mortars utilized had flexural strength varying from 0.61 to 2.79 MPa, with a reported elastic modulus of 7.58 GPa [20, 21]. Mortar strength seems to significantly affect reinforcement behavior [27]. Some authors [21] suggest that the closer the elastic moduli between mesh and mortar, the better the interaction between both. Others [17], however, argue that the proximity between matrix and reinforcement can be a problem since the mesh won't be able to increase the mortar resistance to deformation, as seen from the contrary behavior found between EMS and polymer meshes. Although mortar thickness exerts a significant influence on the performance of façades, especially regarding safety, adherence, and cracking behavior, there was no discussion regarding the property. Most studies tested with 50 mm,

yet none explained why this size was adopted. A possible reference is the Brazilian standard NBR 13755 [24], which establishes limits for the thickness of a single coating layer between 20 and 50 mm. Only two documents tested with a smaller thickness, but the difference between materials and test conditions is such that any comparison is hindered. The major mesh position was in 2/3 of the layer from the base, followed by the middle of the layer [20, 21, 27]. Some authors [17] found more contribution for flexural strength using the mesh in the external part of the layer, while others [15] found no significant variation along the height.

Mechanical behavior: mortars reinforced with WMH or polymer meshes presented the same or lower performance compared to unreinforced specimens. This effect is associated with their higher deformability, relative lower resistance, and possible geometric incompatibilities, also explained as lower bonding due to the mesh format when the mesh strength, material, and wire diameter were the same as EMS [17, 21]. The studies that compared different meshes suggested higher performance of the EMS reinforcement, with flexural strength between 20% and 100% higher than others, signs of good bonding with cementitious matrix, and the smallest loss in shear strength, independently of the mortar type [17, 21, 27].

Cracking, deformation, and microstructure: Musse et al. [27] tested a prone-to-cracking, low-strength mortar (flexural strength of 0.8 MPa), with the exposition of wall panels, reinforced with EMS, WMH, and polymer mesh, to thermal loadings. They evaluated the cracking behavior through thermography, maximum crack opening, and the ratio between total crack length and the panel area (known as cracking index, CI) relative to the unreinforced panels. The results (Table IV) showed that EMS presented the best tension distribution, with increased CI under high thermal loadings but with smaller crack openings. The polyethylene mesh produced fewer cracks, but with wider openings. Similar behavior is noticed in the shear strength parallel to the reinforcement and on the impact test results, with the square steel presenting the smallest crack openings under the impact (less than 0.05 mm). The same study also reported that cracking induced by thermal loading could be detected in non-reinforced panels using thermography, however, no cracking was observed if the panels were reinforced. The

main failure mode in flexural tests consists of mortar cracking followed by mesh rupture. After mortar cracking, EMS and AFG presented good residual load capacity, and polymer meshes showed the lowest, very close to unreinforced situations [20, 21]. Accordingly to the model presented by Junginger et al. [20], mesh reinforcements are unable to provide enough resistance to prevent the crack formation in coating if the crack propagates from the concrete structure behind it. Although it can be useful for crack opening control and mortar detachment avoidance. EMD meshes may also have problems associated with corrosion due to the lack of galvanization in most samples, leading to expansive stresses and degradation of the mortar matrix. It is also noteworthy that WMH meshes may need a more fluid mortar, to ensure the impregnation of its thin wires avoiding adherence problems [21].

Strengthening and retrofitting

The behavior of masonry walls depends on the relationship between its component's properties and the efforts to which they are subjected. Reinforced coatings can be used to improve the performance of these elements in rehabilitation and retrofitting or to provide higher strengths under special load conditions, such as seismic activity [11-13]. The mesh reinforcement is usually applied in discrete parts of the buildings and may be used as emergency repair or as a permanent strengthening method [30]. Some noteworthy applications of mesh in cementitious coatings include the reinforcement of load-bearing masonry in buildings constructed with non-structural blocks, especially in cases of old popular housing buildings [48] when bricks and mortar have low adherence [42] or for reinforcement of cave dwellings [9]. And as retrofit for historic buildings, when the use of epoxy resins is not allowed or suitable, as in stone masonry or reversible applications [3, 30, 47, 49]. The revised documents also covered masonry rehabilitation, the increase of load capacity on structural bearing walls [11, 46], retrofit due to seismic activity [3, 7, 10, 12, 13, 22, 30, 45, 47, 49, 50], coating influence in compressive strength [6], and reinforcement of arches and masonry vaults [51]. A recent study also covered a detailed characterization of AFG meshes for reinforcement use [51].

Table IV - Summary results of different mesh types (data from [27]).

Test specimen (dimensions)	Property	Mesh type		
		Square steel	Polyethylene	Weaved steel
Prismatic (7.5x7.5x28.5 cm)	Relative flexural strength	+48%	+46%	+22%
	Relative shear strength	-1.7%	-29.5%	-26.7%
Masonry, 38 °C (2.5 cm coating)	Relative CI	-7.51%	+14.16%	+23.17%
	Crack opening	0.1, 0.3 mm	0.7 mm	0.4 mm
Masonry, 80 °C (5.0 cm coating)	Relative CI	+64.04%	+27.61%	+39.81%
	Crack opening	0.1 mm	0.3 mm	0.2 mm

CI: cracking index.

Although a lot of work has been done about the use of mesh reinforcements for masonry strengthening, there is, apparently, a lack of guidelines for the selection and dimensioning of such retrofitting methods, as noted in a study [22] that also presented a brief list of studies in the area. Regarding the use of similar dimensioning methods (e.g. reinforced concrete coating), significant adaptations need to be made, considering the differences in stiffness, strength, load-bearing capacity, and masonry contribution [46]. As a possible effect of this gap, the majority of analyzed studies (73.7%) proposed analytical models [11, 13, 46, 51] or finite elements simulations varying from simplified considerations in 2D to refined 3D models with masonry and mesh discretization [3, 11, 12, 30, 45, 50].

Reinforcement design: in 76% of the studies, the reinforcement was applied to both internal and external faces of masonry. The reinforcement layers were usually connected through the bricks, providing a beneficial confinement effect that opposes the crack's opening and propagation under compression efforts [51]. Fig. 6 shows a histogram of the reported coating thickness. Layers between 25 and 30 mm are the most used, with almost half of the studies within 10 to 20 mm. Although thicker layers are related to a higher mechanical strength of test walls, other variables such as mesh opening and the use of connectors are more significant for performance [6, 13, 45]. 94% of the studies employed connectors to fix the meshes, like L or U-shaped fiberglass stripes, metal bolts, or steel hooks, fixed mechanically or chemically by use of mortar or epoxy. These anchorage points are a critical part of the system as they prevent detachment during loading stages [42, 45], keep the correct geometry of the mesh inside the mortar during casting, and are important to the stress distribution and ductility of the walls [46], especially under discrete cracking repairs [10]. Tests and finite elements models (FEM) results showed that the lack of connectors, or the use of inadequate ones, can disable the reinforcement and the resulting masonry behavior become similar to an unreinforced situation [12, 46]. Stress concentration can also occur around connectors, leading to local failure of blocks [11]. Some authors [3, 12, 47] used an additional mesh layer and steel washers in the vicinity to avoid such occurrences, and deep studies of the design and influence of connectors are widely recommended.

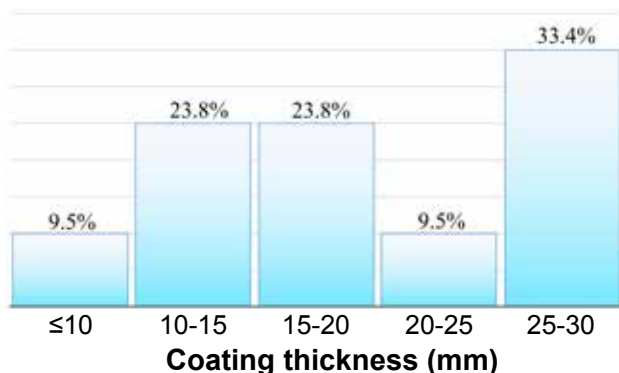


Figure 6: Histogram of reported coating thickness.

Regarding mesh position, 58% of the reported results were over the base, directly over the bricks, or with a thin mortar layer (less than 10 mm thick). 25% were at the half of mortar width and 17% at 2/3 of the layer width from the base. The masonry walls and prisms were tested under static and dynamic scenarios for compressive strength [6, 11, 48], shear strength [7, 12, 42, 50, 53], diagonal compression [22, 30, 45-47, 50], transversal loading [3, 13], and horizontal loading in the case of masonry vaults [51].

Fig. 7 shows the distribution of the reported coatings' strengths. Comparative studies suggest that stronger coatings provide slightly higher mechanical performance [30]. On the other hand, the behavior under load is significantly affected: sudden failure of masonry and coating debonding were reported with weak coatings (compressive strength < 5 MPa), stronger coatings (around 23 MPa) presented successive and distributed cracking until failure, and stiffer coatings (36 MPa) specimens failed due to stress concentration in few cracks [11, 13]. The most employed reinforced material was AFG with square openings, varying between 5x5.9 mm and 99x99 mm, and diameters from 2.19 to 3.56 mm. Tensile strength was found between 530 to 1700 MPa and elastic modulus from 30 to 72 GPa. The best results were found with mesh openings between 33 and 66 mm [3, 12, 30, 45-47, 50, 51]. EMS is widely used, although the possibility of corrosion is a point of concern [46]. The openings varied from 50 to 200 mm, with wire diameters from 2 to 5 mm. The reported tensile strength was between 700 to 1040 MPa. Elastic modulus was not informed [6, 11, 42, 47, 48]. The crimped steel mesh used by Ghobadi et al. [10] had an average ultimate stress of 458 MPa. Polymer, basalt fibers, and hot-rolled ribbed meshes, with similar properties, were also used [9, 13, 22, 42].

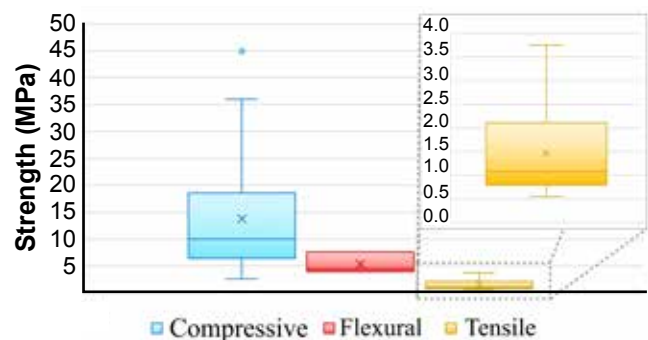


Figure 7: Distribution of reported coating mortar strengths.

Mechanical behavior: the observed results showed that mesh reinforcement coatings can effectively strengthen masonry walls under different load conditions. Strength gains with reinforcement varied between 20% to 400% in compression [11, 22], 20-200% in shear [30, 42], and 600% for transversal bending [3, 13]. Higher values are associated with the application of masonries with openings, unreinforced, or intrinsically weaker [42, 47].

Cracking, deformation, and microstructure: the reinforcement influence is even more evident during the

deformation stages. The presence of meshes significantly affects the ductility of the walls [46], rising the load needed for the first crack [3], counteracting crack openings [47], and providing stiffer and stronger responses even in pre-damaged specimens [49]. The crack pattern also suffered significant changes when reinforcements were present. In general, unreinforced specimens presented cracks along the entire wall thickness, oriented vertically or diagonally depending on the load direction, mostly through brick joints, followed by the typical sudden resistance drop of brittle rupture [6, 11, 30, 46-48]. Differently, reinforced specimens exhibited smaller distributed cracking, beginning in the coating layer, next to the mesh wires, or between brick joints, then progressing through masonry [6, 22]. It is evident that the rupture mode is dependent on reinforcement properties, but the most reported occurrences include ductile behavior associated with higher deformation, monolithicity, significant residual strength [11, 30, 47, 48, 50], minimal brick damage [42], and load support by the textile until debonding or rupture [13, 22]. In the case of transversal bending, the specimens showed a single horizontal crack in the mid-height while unreinforced, but several parallel cracks if reinforced. The rupture only happened after mesh breakage [3]. It is observed that the total mesh strength is slightly different from the sum of individual wires, showing that the transversal mesh wires play an important role in the reinforcement's behavior. Nodes' connection also plays an important role in slippage avoidance and stress distribution but can lead to excessive cracking and debonding if the mesh opening is too small, due to the bond weakening between mortar layers as the effective surface area is reduced. The coating's failure pattern is also dependent on the effective bond length of the reinforcement, ranging from mesh slippage with mortar failure to complete mobilization of the reinforcement and composite failure only after wire rupture. Thus, the minimum length to avoid slippage should be determined by direct pull-out and lap-splice tests as it is highly dependent on the material and mesh geometry [16].

Modeling: the proposed analytical models showed good predictions on ultimate loads for design purposes, although some correction factors may be needed to match experimental observations [11, 46]. The FEM simulations produced good results with experimental and literature results, with errors within 10% and 20% [30, 45]. The models vary from simpler adaptations with 2D elements [12] to more complex involving associations of different materials and discrete mesh modeling [30]. Some FEM analysis suggests that thinner walls have more gains with reinforcement. Also, higher tensile resistance mortar coating and thicker layers should increase the first crack loading, while the higher tensile strength of mesh reflects in the ultimate bending resistance [3].

DISCUSSION

Although the results showed a high variability of test procedures and type of specimens depending on the desired

application, is evident that mesh reinforcement promotes a better mechanical performance of mortar layers and masonries under different stress conditions, highlighting the potential for multiple applications. The reinforcement is associated with higher energy absorption and stress distribution along the layer, inducing ductile deformations in materials highly known for their brittle behavior. The reinforcement also contributes to higher energy dissipation capacity under seismic loads [7, 14, 19, 27, 43, 44, 46]. The technique execution is simple, relatively cheap, and does not require skilled labor [49]. The procedures for ferrocement applications, for example, are very similar to the known execution of reinforced concrete elements [49]. Some attention is needed for use in mortar coatings regarding the maintenance of geometrical criteria, as deformable meshes may end up folded, crumpled, or in the wrong position during mortar casting, compromising the reinforcement [21, 27]. Such occurrences can be prevented by using suitable connectors, whose relevance for system performance was already highlighted by the strengthening studies [42, 45, 46, 54].

Mesh positioned in the external part of the mortar layer (2/3 of its thickness) provided the best results in many scenarios involving coating mechanical and cracking performance, which can be attributed to mesh action in the tensile region of the composite. Such location is also logically interesting for façade applications since the external part is the most requested by thermal or impact loads. The middle of the layer is also an interesting position, as the thicker cover acts as a barrier for aggressive agents and protects the mesh from damage, enhancing durability. Some studies found little or no variation between these locations, but it is arguable if other effects, such as mortar properties and bonding conditions, were so influential that the position effect became negligible [15, 17]. Differently, most masonry reinforcement studies positioned the mesh directly over the base, as their main concern was the masonry's mechanical behavior. Such a position may be more appropriate for retrofitting situations, due to the removal of the previous coating and better fixation of the reinforcement [3, 30, 49]. Given the multitude of possibilities, design variables must be evaluated in detail for each application. A small opening mesh, for example, might be the best option for coating crack containment and composite tensile strength, but may also compromise the bonding area between mortar layers and result in premature detachment and spalling [14, 19]. Similarly, given one type of material, the mesh geometry, stiffness, wire diameter, and number of layers are of great concern. The WMH (also known as 'chicken mesh'), for instance, showed low contributions under different applications, while the EMS provided good results in most cases, so deep research is encouraged [17, 21, 22, 27, 43, 46].

The use of small grids yields good properties for composite applications, including high flexural strength and energy absorption. Also, the use of stiffer reinforcements provided better cracking control, as the stress needed for

the first crack increased. An important point to be studied is the interaction between mesh and matrix, especially in the case of vegetal fibers, where some surface treatment may be needed to ensure chemical compatibility with the matrix. It is clear that the masonry type influences the failure mode of specimens, as hollow bricks behave differently from solid ones and rocks under stress, but the observed results suggest that it does not affect the effectiveness of the reinforcement, although different values of resistance increment were registered [13, 30, 46]. Several successful reinforcement applications were reported using multiple types of mortar. Properties such as mechanical strength and stiffness are highly dependent on the desired application, but a good bonding relationship with the chosen mesh is essential for all cases, especially if the reinforcement acts in the transition between different base materials. Direct-pull tests for the determination of bond length are highly encouraged [16, 21]. Some documents reported variations in performance when additions were incorporated into the mortars, but such results are out of the review scope [11, 48].

The use of connectors is predominant in strengthening applications because an independent behavior between the reinforced coating and masonry is not tolerated in such situations. However, attention is needed to possible stress concentration around the connection points, which could lead to premature failure. For façade applications, the use of connectors is an unexplored area, although some studies mentioned the use for detachment prevention and load support in the case of thick coatings. The behavior under load for strengthening applications appears to be directly connected to the mortar's mechanical strength. According to the findings, weak coatings should be avoided, as they resulted in sudden failure and mortar debonding. On the other hand, high-strength mortars present few cracks, with high stress concentration. Each situation should be accessed individually from a security point of view since the occurrence of successive and distributed cracking, obtained with medium-strength coatings, can be a useful and desired warning sign. For future research in masonry strengthening, it is suggested the study of reinforcement stability under fire situations [48], more in-depth analysis of seismic out-of-plane capacity [13], a better understanding of the coating-masonry interface and bond lengths [3, 30], and the possible use of localized rebars in addition to the meshes in regions of stress concentration [42].

For façade design, it is important to observe the elasticity modulus of the reinforcement, as highly deformable meshes may not be able to control or prevent mortar cracking. The use of stiffer meshes usually results in more cracks but with smaller openings than a flexible mesh, demonstrating better stress distribution along the layer. Another relevant interaction to be studied is the relation between mesh opening and the adherence between mortar layers, because although smaller openings provide better tensile strength, the reduced mortar contact area may compromise the adherence of the whole layer. Such relations are still open and should be investigated by further research. Façade reinforcement

can be applied in many ways, ranging from isolated applications (e.g. corners of openings or cracked regions) to full coverage of a wall panel (e.g. as support to a thick coating). Unfortunately, there are few guidelines to support the decision-making, which makes the process largely dependent on the designer's experience. The reviewed documents suggest an incipient state of the theoretical understanding, focusing on the analysis of mesh materials and their influence on the coating mechanical properties, and there are still numerous questions about the reinforcement technique that need further studies to be fully understood.

The interactions between mesh and mortar matrix at the microstructural level are extremely relevant to the performance of coatings in all applications described governing effects such as bonding, stress distribution, and cracking resistance. Few studies explored these details, focusing more on the macro effects of the reinforcements, which highlights the need for more research for future optimization of the technique. The findings indicate the need for standards and guidelines related to mesh reinforcements in mortar coatings. Some references revealed mentions of the technique in coating and tiling-related standards, such as the Australian standard AS 3958.1 [55], British standard BS 5385 [56], and Brazilian standard NBR 7200 [26]. Complementary technical recommendations may also be found in masonry and composite-related standards and seismic codes [12, 21]. It was also observed a lack of analytical and simulation models for façade coatings compared to the other applications. The development or adaptation of existent models needs to care for the different phenomena acting on façades, especially due to the relevance that cracking occurrence has to this application, representing another potential area of study.

CONCLUSIONS

A systematic review on the use of mesh reinforcement in cementitious mortar layers, involving the analysis of 30 documents identified through a search in five databases without date restriction was conducted. The findings were associated with composite development, façade coating, and masonry strengthening or retrofitting. Most research was conducted on masonry and seismic strengthening, and the most recent findings from all applications agree that it is still much to be researched and developed. From the results, the following conclusions can be derived: i) there is a need for guidelines for the selection and design of mesh reinforcements; a multitude of combinations of materials and influential variables are associated with the technique, highlighting the need for deep studies in both macro and micro scale in each application to the establishment of parameters for design; ii) FEM simulations and wider applications could benefit from a better understanding of the behavior between mesh and mortar matrix, especially in respect to bonding and stress distribution; the computational simulation is relatively new for façade applications, with no models proposed by the consulted references; iii) the use of

meshes in mortar coatings is an effective, relatively cheap, and simple method for masonry retrofitting, reinforcement, and rehabilitation in diverse circumstances, including out-of-plane and seismic loads, or emergency repairs; the results showed great potential for changes in the failure modes of reinforced masonry, varying from sudden failure with mesh debonding to great stress concentration with fewer cracks; iv) for composite development, reinforcements with small grid opening and high elasticity modulus are preferred for the resulting higher tensile strengths; however, the relation between mortar matrix and the diameter of the wires, minimum mesh opening, and the number of layers need further studies, to ensure the avoidance of spalling and detachment; v) the study of mesh reinforcement's influence in façades is relatively new, and there is still much to explore concerning coatings' performance, design, and durability; the influence of coating thickness, and the relation between mesh opening and adherence between mortar layers, as well as that between mesh's deformability and cracking control, are of high interest for the application and demand for further research; also, no mention was made for mesh positioning, the texts suggest that usage is still very empirical, with few theoretical propositions; thus, further research is needed; and vi) there are significant changes in mechanical strength according to each application; most of composite studies used high compressive strength mortar with more than 39 MPa, while façade coatings stayed around 6 MPa; strengthening applications presented greater variation, ranging in between these two due to the multitude of materials involved. Such observations and future research possibilities presented could be of great value for the improvement of standards and formulation of guidelines on the use of mesh reinforcement in mortar coatings. The authors highlight that, although the present research was made as comprehensive as possible, it is not exhaustive on the topic, as the analyzed sample may not include other related documents that explore the research question but were not accessible or do not include the chosen keywords. Also, future studies should cover more in-depth aspects of the variables cited, including the reinforcement-matrix bonding interaction, coating failure mode, and mesh development for each application.

ACKNOWLEDGMENTS

The authors express their gratitude to the Coordenação de Aperfeiçoamento de Pessoal de Nível Superior - Brasil (CAPES) and the Federal University of Bahia (UFBA) for the financial support.

REFERENCES

- [1] R.A. Oliveira, F.A.N. Silva, C.W.A. Pires, A.A.C. de Azevedo, *Amb. Constr.* **17** (2017) 175.
- [2] E. Bauer, E.K. Castro, M.N.B. Silva, *Cerâmica* **61**, 358 (2015) 151.
- [3] N. Gattesco, I. Boem, *Compos. B Eng.* **128** (2017) 39.
- [4] I. Flores-Colen, J. de Brito, *Constr. Build. Mater.* **24** (2010) 1718.
- [5] E. Bauer, J.S. Souza, L.M.G. Mota, *Amb. Constr.* **21** (2021) 23.
- [6] A. Azevedo, J.Q. Delgado, A. Guimarães, F.A. Silva, R. Oliveira, *Rev. Constr.* **18**, 1 (2019) 123.
- [7] S. Pul, M.E. Arslan, *Constr. Build. Mater.* **211** (2019) 899.
- [8] L.N. Koutas, Z. Tetta, D.A. Bournas, T.C. Triantafyllou, *J. Compos. Constr.* **23**, 1 (2019).
- [9] F. Zhang, X. Liu, J. Xue, H. Mahmoud, P. Hu, G. Zhou, *J. Struct. Eng.* **147**, 12 (2021).
- [10] M.S. Ghobadi, R.A. Jazany, H. Farshchi, *Eng. Struct.* **178** (2019) 665.
- [11] F.L. de Oliveira, J.B. de Hanai, *IBRACON Estrut. Mater.* **1**, 2 (2008) 158.
- [12] L. Facconi, F. Minelli, *Constr. Build. Mater.* **231** (2020) 117.
- [13] M. Harajli, H. El Khatib, J.T. San-Jose, *J. Mater. Civ. Eng.* **22**, 11 (2010) 1171.
- [14] M.J. Shannag, T.B. Ziyad, *Constr. Build. Mater.* **21** (2007) 1198.
- [15] E.F. Trombini, A.B. Masuero, in *Proc. Feira Inov. Tecnol. UFRGS, Un. Fed. Rio Grande Sul, Porto Alegre* (2015).
- [16] N. Gattesco, I. Boem, *Compos. Struct.* **165** (2017) 209.
- [17] B. Schimelfenig, F. Padilha, J.D. Bordin, C.V. da Silva, *Matéria* **23**, 3 (2018) e-12200.
- [18] R.I. Ivanov, *IOP Conf. Ser. Mater. Sci. Eng.* **951** (2020) 12017.
- [19] L. Mercedes, L. Gil, E. Bernat-Maso, *Constr. Build. Mater.* **175** (2018) 161.
- [20] M. Junginger, V.M. John, R.L.S. França, R. Monte, in *Proc. XII Simp. Bras. Tecnol. Argamas., S. Paulo* (2017).
- [21] G.R. Antunes, A.B. Masuero, *Constr. Build. Mater.* **121** (2016) 559.
- [22] A.V. Oskouei, A. Jafari, M. Bazli, R. Ghahri, *Constr. Build. Mater.* **169** (2018) 578.
- [23] M. Kamanli, H.H. Korkmaz, A. Unal, F.S. Balik, F. Bahadir, M.T. Cogurcu, *Earthq. Struct.* **8** (2015) 761.
- [24] NBR 13755, "Revestimentos cerâmicos de fachadas e paredes externas com utilização de argamassa colante: projeto, execução, inspeção e aceitação: procedimento", *Ass. Bras. Norm. Téc.* (2017).
- [25] NBR 13749, "Revestimento de paredes e tetos de argamassas inorgânicas: especificação", *Ass. Bras. Norm. Téc.* (2013).
- [26] NBR 7200, "Execução de revestimento de paredes e tetos de argamassas inorgânicas: procedimento", *Ass. Bras. Norm. Téc.* (1998).
- [27] D.S. Musse, V.A. Coelho, J.P.D. Gonçalves, F.G.S. Silva, *Ambient. Constr.* **20**, 3 (2020) 467.
- [28] C. Lockwood, Z. Munn, K. Porritt, *Int. J. Evid. Based Healthc.* **13** (2015) 179.
- [29] A. Shamseldein, F. Elgabbas, H. Elshafie, *Ain Shams Eng. J.* **13**, 1 (2021).
- [30] G. Castori, E. Speranzini, M. Corradi, S. Agnetti, in *Proc. Int. Conf. Struct. Dyn., GR, Athens* (2020).

- [31] M.J. Page, D. Moher, P.M. Bossuyt, I. Boutron, T.C. Hoffmann, C.D. Mulrow, L. Shamseer, J.M. Tetzlaff, E.A. Akl, S.E. Brennan, R. Chou, J. Glanville, J.M. Grimshaw, A. Hróbjartsson, M.M. Lalu, T. Li, E.W. Loder, E. Mayo-Wilson, S. McDonald, L.A. McGuinness, L.A. Stewart, J. Thomas, A.C. Tricco, V.A. Welch, P. Whiting, J.E. McKenzie, *BMJ* **372** (2021) 160.
- [32] N.J. van Eck, L. Waltman, *Scientometrics* **84** (2010) 523.
- [33] N. Gattesco, I. Boem, *Bull. Earthq. Eng.* **17** (2019) 4027.
- [34] S. Malanho, M.R. Veiga, *J. Build. Eng.* **28** (2020) 101021.
- [35] M. Schuss, U. Pont, A. Mahdavi, *Energy Procedia* **132** (2017) 508.
- [36] H. Korkmaz, S. Korkmaz, in *Proc. 8th Int. Conf. Civ. Archit. Eng.* (2010).
- [37] L. Turanli, A. Saritas, *Constr. Build. Mater.* **25** (2011) 1747.
- [38] B.J. Mariam, J.A. Susan, *Mater. Today Proc.* **42** (2020) 1100.
- [39] Y. Yardim, *Period. Polytech. Civ. Eng.* **62** (2018) 1030.
- [40] C.K. Ma, N.M. Apani, C.S.Y. Sofrie, J.H. Ng, W.H. Lo, A.Z. Awang, W. Omar, *Constr. Build. Mater.* **133** (2017) 502.
- [41] R. Mohana, S. Prabavathy, S.M.L. Bharathi, *J. Clean. Prod.* **291** (2021) 13.
- [42] F. Messali, G. Metelli, G. Plizzari, *Constr. Build. Mater.* **141** (2017) 619.
- [43] E.Y.N. Bavastri, A.E. Limberger, in *Proc. 60th Congr. Bras. Concr., Foz Iguacu* (2018).
- [44] M.A. Mansur, M.A. Aziz, *Int. J. Cem. Compos. Lightweight Concr.* **5** (1983) 165.
- [45] A. Benedetti, *Int. J. Archit. Herit.* **13** (2019) 1029.
- [46] N. Gattesco, I. Boem, *Constr. Build. Mater.* **88** (2015) 94.
- [47] N. Gattesco, I. Boem, A. Dudine, *Bull. Earthq. Eng.* **13** (2015) 1703.
- [48] J.M.F. Mota. “Reforço de alvenaria resistente com argamassa armada com adição de metacaulim”, Dr. thesis, Un. Fed. Pernambuco, Recife (2015).
- [49] F. Facconi, F. Minelli, E. Giuriani, *Constr. Build. Mater.* **160** (2018) 574.
- [50] N. Gattesco, C. Amadio, C. Bedon, *Eng. Struct.* **90** (2015) 143.
- [51] N. Gattesco, I. Boem, V. Andretta, *Eng. Struct.* **172** (2018) 419.
- [52] S.Z. Korkmaz, M. Kamanli, H.H. Korkmaz, M.S. Donduren, M.T. Cogurcu, *Nat. Hazards Earth Syst. Sci.* **10** (2010) 2305.
- [53] L. Facconi, F. Minelli, E. Giuriani, in *Proc. 16th Int. Brick Block Mason. Conf. IBMA* (2016) 1191.
- [54] J.M.F. Mota, R.A. Oliveira, in *Proc. 55th Congr. Bras. Concr., Gramado* (2013).
- [55] AS 3958.1, “Ceramic tiles, part 1: guide to the installation of ceramic tiles”, *Stand. Austral.* (2007).
- [56] BS 5385-2, “Wall and floor tiling: design and installation of external ceramic, natural stone and mosaic wall tiling in normal conditions: code of practice”, *Brit. Stand. Inst.* (2015).
- (*Rec.* 08/07/2022, *Rev.* 18/11/2022, 01/01/2023, *Ac.* 08/01/2023)



Synthesis of TiO₂/ZnO photoanodes on FTO conductive glass for photovoltaic applications

V. F. Nunes^{1*}, F. M. Lima¹, E. S. Teixeira¹, P. H. F. Maia Júnior¹, A. F. L. Almeida², F. N. A. Freire¹

¹Federal University of Ceará, Department of Science and Engineering Materials, 60440554, Fortaleza, CE, Brazil

²Federal University of Ceará, Department of Mechanical Engineering, 60455760, Fortaleza, CE, Brazil

Abstract

For oxide semiconductors for application in dye-sensitized solar cells (DSSCs), titanium dioxide conjugated with zinc oxide thin films was synthesized and characterized. The UV (ultraviolet) spectrum characterization showed a peak of absorbance at around 355 nm, with a band gap of 3.25 eV and reflectance around 85%. Such characteristics allowed the fabrication of DSSCs with N719 dye, under simulated light of 100 mW/cm². The highest efficiency of 1.17% was at 5% titanium dioxide and 4 h of dye immersion.

Keywords: ZnO, DSSC, titanium oxide, dye time.

INTRODUCTION

Photovoltaic (PV) energy is a viable option for renewable energy, supplying demands for houses, cars, and industries. Countries such as India intend to make commercial cars green by 2030 [1]. Dye-sensitized solar cells (DSSCs) are part of the third generation of photovoltaic solar cells. The DSSC constitutes a photoanode, a counter electrode, a dye, and an electrolyte [2]. The photon excited in the dye circulates through the photoanode, the external circuit, and back to the electrolyte. The photoanode is on a transparent conductor oxide, such as fluorine tin oxide (FTO), graphite, or platinum. Zinc oxide has many advantages for the photoelectric effect, such as low-cost, non-toxicity, high visibility, light transmittance, and low resistivity after doping [3]. Oxides are optional to the Si-based photovoltaic technologies that are already established. However, the lower electron injection into the ZnO can reduce the photocurrent efficiency (PCE) [4]. Anand et al. [5] produced 1.652 mA with DSSC based on the ZnO nanoflower shape. The energy conversion was at 1.61% with ZnO/ruthenium-based dye [6]. These results can be improved when combining ZnO with other oxide semiconductors. Many works have mixed ZnO with oxides containing elements such as tin (Sn), titanium (Ti), aluminum (Al), cobalt (Co), and gallium (Ga), amongst others [7-18]. TiO₂ is a viable option with ZnO due to similarities between the two oxides, like the band gap energy value, around 3.0 eV for TiO₂ and 3.2 eV for ZnO [19]. The blend between ZnO and TiO₂ has high electron injection, besides the high electron-hole separation in the TiO₂ [20]. The adsorption dye time of the films can also affect the performance of the solar cells. The dye adsorption may enhance the electron density and electron transfer in


the film and the electrolyte interface [21]. The time for dye immersion should be enough to cover the layer of the film and avoid the deterioration of the cell, due to the formation of Zn²⁺/dye aggregates that lower electron injection [22, 23].

In this work, TiO₂-ZnO thin films were synthesized on FTO to improve the photocurrent activity and the effect of dye adsorption time on the film's efficiency. The main novelty of this work is the simple, low-cost, environmentally friendly, and simple synthesis of crystallite thin films. Methods that deposit zinc oxides and titanium oxides are spray pyrolysis, spin coating, hydrothermal deposition, and doctor blade. The present methodology uses none of the usual additional chemical reactants or/and supportive elements, like heat and vacuum, nor expensive deposition devices, which reduces the total cost of the solar cell. Since cost and efficiency are crucial for the photovoltaic industry advancement, this methodology can enhance the DSSC's technology, lowering the overall production costs. Titanium dioxide/zinc oxide thin films were synthesized by simply dipping the glass into the precursor solution and waiting until complete evaporation of the solvent, without any additives, at room temperature, and with no auxiliary or additional devices. The characterization of the DSSCs indicated the performance of the assembled cells.

EXPERIMENTAL

Synthesis of the TiO₂/ZnO films: all reagents were used without further purification: TiO₂ (rutile, Sigma-Aldrich) and ZnO (Vetec). 0.05 g of ZnO powder was dispersed in 10 mL of deionized water and then placed in an ultrasonic bath for 30 min. Three different suspensions of ZnO with 5, 10, and 15 wt% of rutile (TiO₂) were prepared, which were then used to cover a fluorine-doped tin oxide (FTO) glass (Solaronix) until complete evaporation of the water. The layers of the oxides that remained on the FTO were then submitted to thermal treatment at 450 °C for 30 min.

* vanjafnunes@gmail.com

 <https://orcid.org/0000-0003-2458-5616>

Characterization of the films: the films of ZnO/TiO₂ were characterized by X-ray diffraction (DMAXB, Rigaku) with CuK α radiation between 20° and 70° (2 θ). The UV-vis analysis of the films was performed between 220 and 700 nm by spectroscopy (UV-2600, with integrating sphere ISR-2600Plus, Shimadzu). Also, scanning electron microscopy (SEM) was performed (Quanta FEG 450, FEI) at 50000 times magnification and 20 kV.

DSSC fabrication: the films of titanium dioxide/zinc oxide were deposited on FTO, as the electrode, and the counter electrode was platinum (Solaronix) deposited also on FTO. The films, before being connected with the counter electrode, were immersed in N719 dye (Solaronix) at a concentration of 3x10⁻⁴ M. The films were immersed in the dye for 4 and 24 h, for the three concentrations, and then sandwiched and coupled with the counter electrode. The electrolyte used between them was Iodolyte AN-50 (Solaronix). The assembled cells were electrically characterized on a potentiostat (Autolab PGSTAT302N, Metrohm) under 100 mW/cm² illumination, for measurement of the I-V curves.

RESULTS AND DISCUSSION

SEM analysis: Figs. 1 and 2 show the images obtained by scanning electron microscopy (SEM) of the nanocrystallite blend of titanium oxide and zinc oxide. The combination created the nanocrystallite films with the thickness listed in Table I, which was calculated using the SEM images (Fig. 1) and the following equations [24, 25]:

$$\alpha \approx F_{(K-M)}(R) = \frac{(1-R)^2}{2R} \quad (A)$$

$$\alpha = \frac{1}{d} \cdot \ln \frac{(1-R)^2}{T} \quad (B)$$

There was no substantial difference between the SEM images, with the formation of agglomerates for all percentages of Ti(IV), probably due to the high adhesion forces between the particles [26]. The values for thickness varied between 6 and 20 μ m; Homcheunjit et al. [24] also observed differences in thickness from 8 to 20 μ m, when depositing thin films by spray pyrolysis and dip coating. These results showed the importance of finding an optimum thickness. When it is too thick, the film at 15%, there are conglomerates that block the electron passage through the film and may increase the resistance to the photocurrent flow. Otherwise, if the film is too thin, the film does not absorb the dye, causing a lower flux of photon-excited electrons in the photoanode through the external circuit. The concentration of titanium affects the building of the crystallite layers, which can affect the porosity of the nanocrystallites, and, as noted by Zhou et al. [27], there must be an equilibrium between porosity and cell efficiency. The higher TiO₂ concentration presented less evident porous (Fig. 1a), which may have

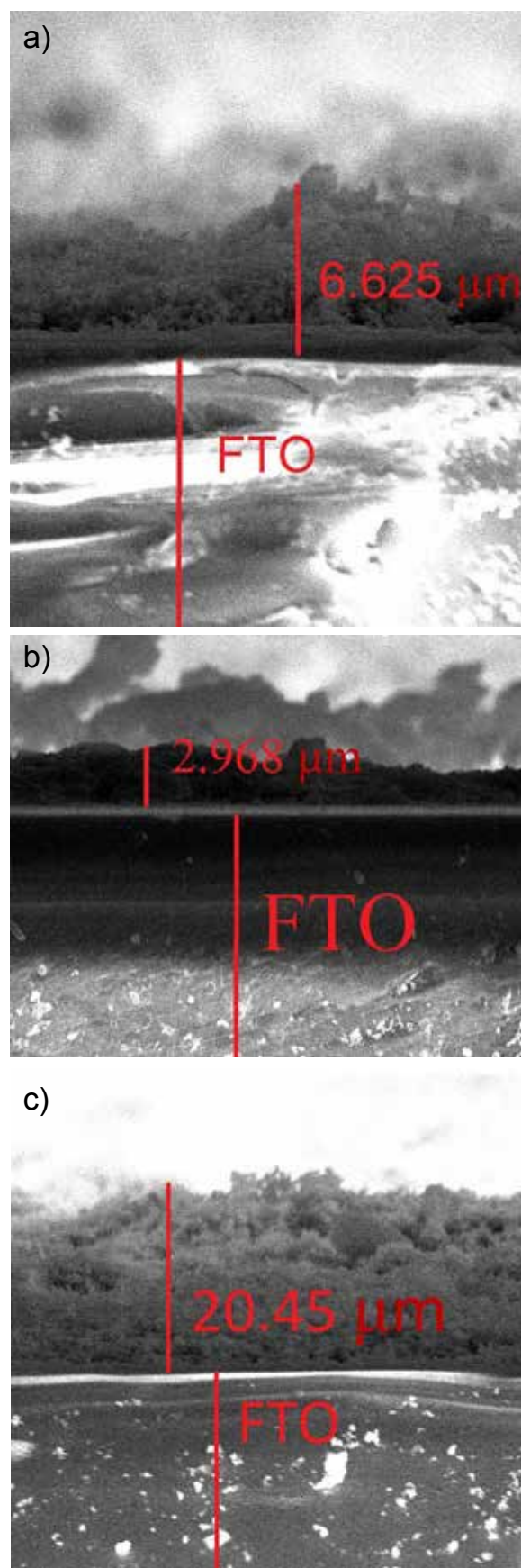


Figure 1: SEM images of the cross-section of the films with: a) 5% Ti(IV); b) 10% Ti(IV); and c) 15% Ti(IV).

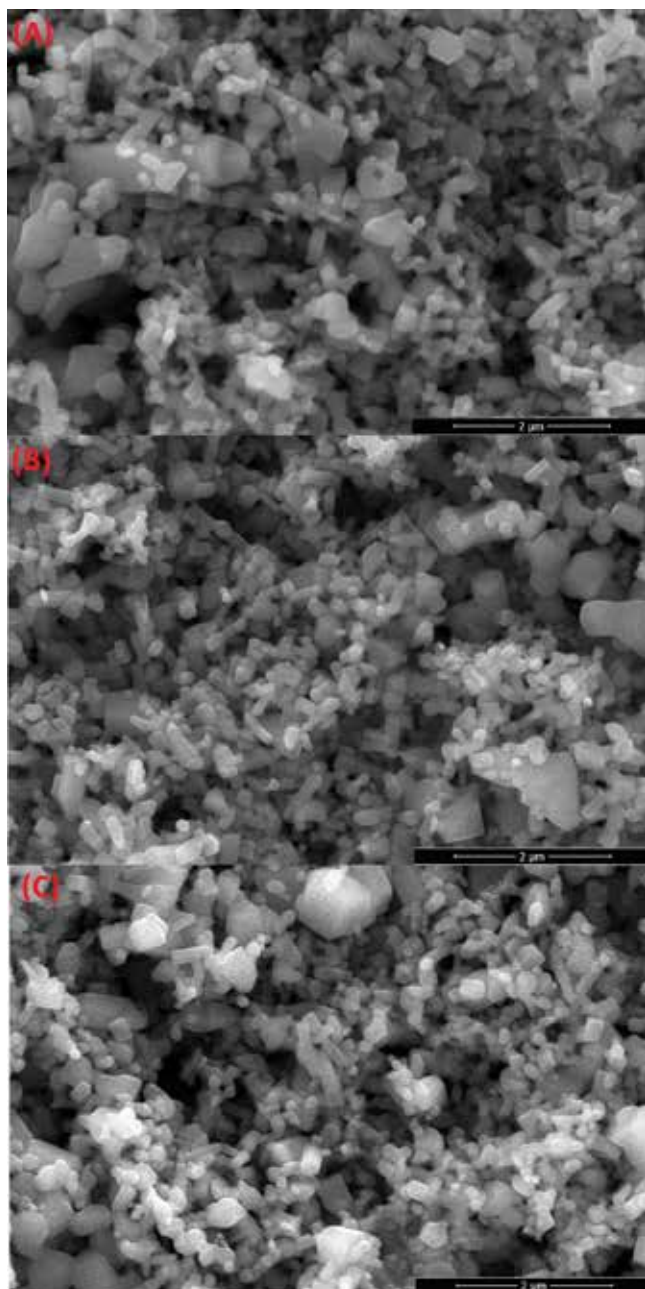


Figure 2: SEM micrographs for the thin films with: a) 5% TiO₂; b) 10% TiO₂; and c) 15% TiO₂.

Table I - Thickness of the TiO₂/ZnO thin films.

Thin film (%TiO ₂)	5%	10%	15%
Thickness (μm)	6.62	2.97	20.45

negatively influenced the short current density of the cell at 15% concentration [27].

X-ray diffraction (XRD): the XRD patterns showed the wurtzite structure for the zinc oxide, corresponding to the ICSD file 67848 (Fig. 3). The characteristic peaks corresponded to the crystalline planes (100), at around 31.7°, (002), 34°, (101), 36.2°, (102), 47.5°, (110), 56.5°, (103), 62.7°, and (112), 67.8°. The more prominent peak was the

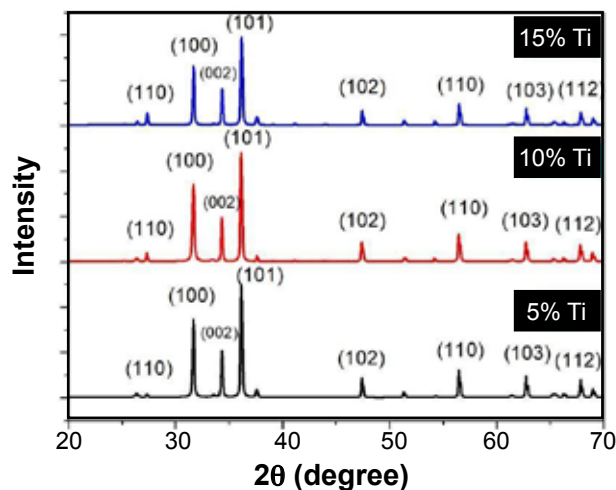


Figure 3: XRD patterns of the synthesized films, at the three different percentages.

(101), 36.2°, as also observed by Bhushan et al. [28]. At a higher percentage of titanium dioxide, the intensity of the (002) peak decreased. The three characteristic peaks, (100), (002), and (101), all had narrow widths, which attested to the crystallinity of the synthesized films [29]. The (110) peak at around 26° identified the rutile phase of the TiO₂ [30].

From the XRD data, the Scherrer equation ($D = k\lambda/\beta\cos\theta$) was used to calculate the crystallite size (D), where k is 0.9, λ is the wavelength (1.5406 Å), β is the broadening of the diffraction line at the half intensity, and θ is the Bragg's diffraction angle [31]. According to this data, by increasing the mass percentage of titanium dioxide, the average crystallite size also increased, from 53.1 nm at 5% to 54.8 nm at 10% and 55.8 nm at 15% Ti(IV). Aksoy et al. [23] obtained crystallite sizes of 34 nm for the powder and 46 nm for the thin film, both of pure ZnO, indicating that the annealing treatment of 400 °C was responsible for the increase in the average size. The authors calculated the grain sizes of titanium dioxide heated between 100 to 600 °C, for the anatase and rutile phases, with results between 49.27 to 61.91 nm [32]. The present results, at 450 °C, were close to the results between 400 and 500 °C. For larger grain sizes, there is an increase in the crystallinity of the structures [31]. Other techniques like spray pyrolysis, co-precipitation, DC magnetron sputtering, sol-gel, spin coating, and thermal synthesis obtained sizes of 34.7, 32, 23.66, 42-47, and 14 nm [1, 18, 33-35]. The large crystallite sizes in this work can be explained by the high concentration of titanium dioxide, above 10%, and the heat treatment at 450 °C [17]. Table II lists the specific surface area (SSA) [20]. The values for the crystallite sizes (D) and the ZnO density (ρ) were used for the calculation (Eq. C). The SSA indicates the amount of TiO₂ in the ZnO matrix. Higher SSA points to improved electron transport and photovoltaic efficiency, as was noticed by the better efficient cell at 5% TiO₂, with an SSA of 20.1 m²/g. The lower value of the SSA can also explain the lower incorporation of the Ti⁴⁺ and, consequently, higher thickness.

$$SSA = \frac{6000}{\rho \cdot D} \quad (C)$$

Table II - SSA and dimension for the nanostructures.

TiO ₂ (%)	5	10	15
Crystallite size (nm)	53.1	54.8	55.8
SSA (m ² /g)	20.1	19.5	19.2

UV-vis studies: the absorbance plot demonstrated peaks at the UV region for the films (Fig. 4a). The peaks were at around 250 nm with 5% titanium. For the 10% and 15% titanium-doped films, there was also a peak at about 355 nm, associated with the presence of Ti⁴⁺ [36]. There was a peak at around the same wavelength value (~350 nm) for the isolated alcohol N719 dye solution (Fig. 4b) that indicated that the oxide conduction band was close to the dye conduction band, making possible the electron transition inside the cell. Also, for the 5% Ti, the film had higher absorption in the UV region. Upadhyay *et al.* [37] also reported a sharp band on the spectrum at less than 400 nm. The smaller crystallite

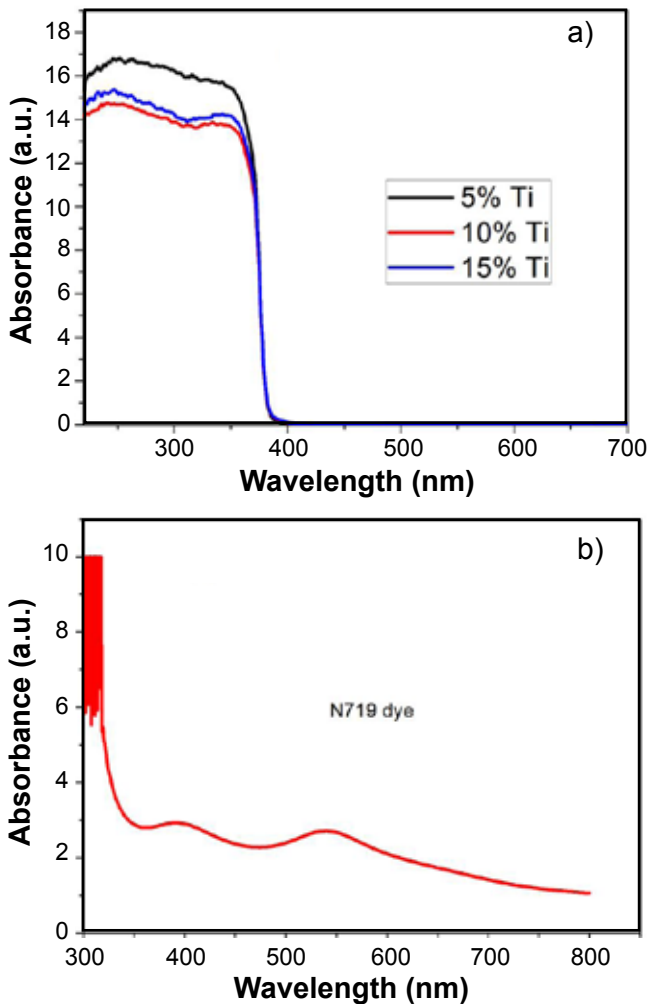


Figure 4: Absorbance spectra of: a) nanostructures; and b) isolated dye solution.

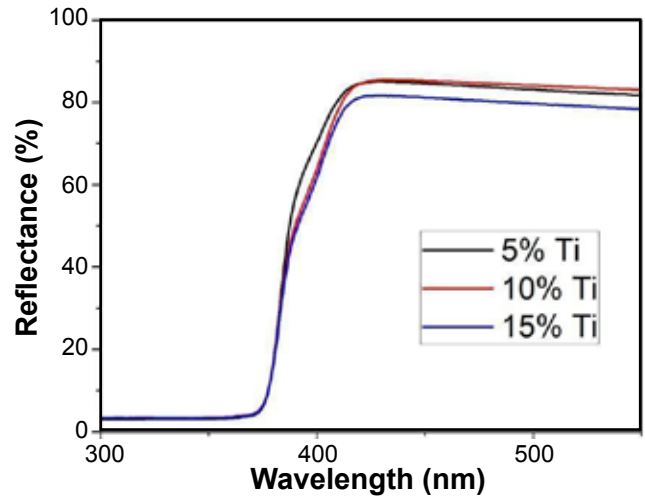


Figure 5: Reflectance spectra of the photoanodes.

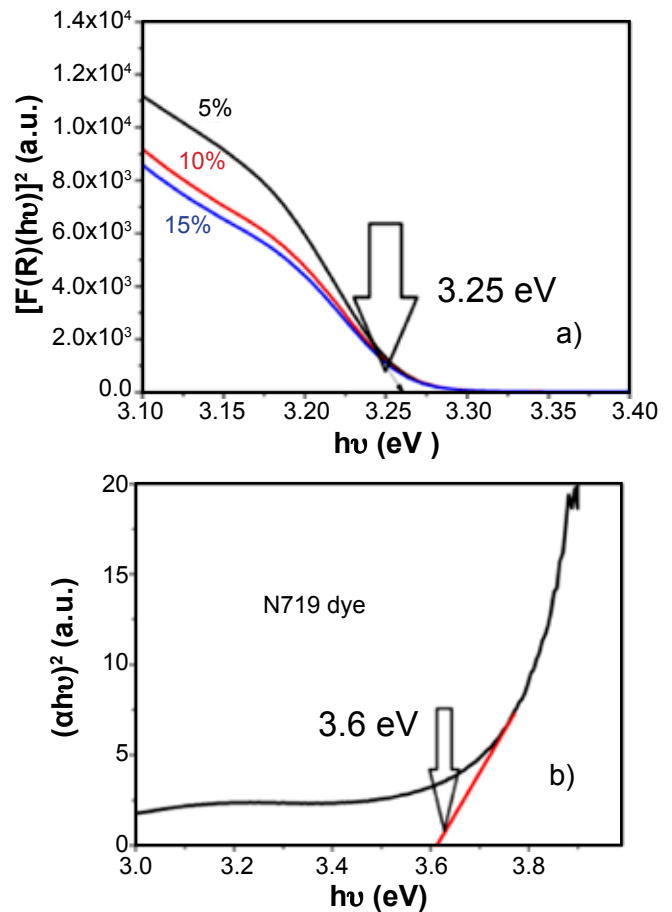


Figure 6: Tauc plots of the Kubelka-Munk function for: a) semiconductor layers; and b) N719 dye.

size agreed with the maximum absorbance at 5% TiO₂ [1]. The reflectance for all samples was around the same value, about 83% (Fig. 5). The Ti(IV) percentages did not alter the reflectance of the ZnO, with a slight decrease for the ZnO at 15% TiO₂. Das *et al.* [21] observed similar values of reflectance for Al/ZnO treated at 800 °C. The Kubelka-Munk function $F(R)$ was used to calculate the band gap for

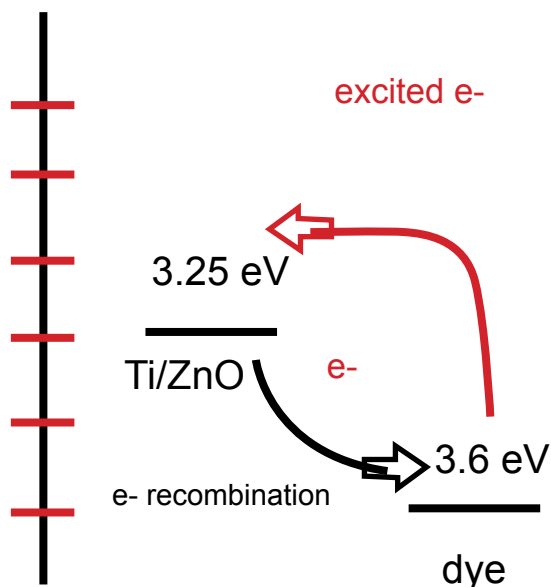


Figure 7: Schema of electron transition and recombination inside the cell.

the films [38]. A plot of $[F(R)(h\nu)]^2$ as a function of photon energy, $h\nu$, made possible the determination of the band gap energy (E_g) from the curve extrapolation to the x-axis. The band gap was around 3.25 eV for the three films (Fig. 6). Ali et al. [36] found 3.255 eV for Ti-doped ZnO by the sputter deposition technique [39]. Also, it was found 3.17 and 3.30 eV for ZnO-TiO₂ composites prepared by sol-gel at 15% and 25% TiO₂. The layers of ZnO/TiO₂ and N719 dye had levels of band gap between 3.25 and 3.6 eV, respectively (Fig. 7). It can help the electron transition. At the same time, it can increase the recombination rate which reduces cell efficiency.

The photoluminescence (PL) spectra in Fig. 8 show a quenching peak for the films at about 385 nm, with the peak for the 5% film shifted closer to the visible, which helps improve efficiency. Katta et al. [40] observed a PL peak at 405 nm for a non-doped TiO₂. The blend of the titanium oxide helped to shift the ZnO PL spectrum. Fig. 9 indicates the Urbach energy between 1.5 and 1.6 eV for the three TiO₂/ZnO blends. The increase in the Urbach energy from 5% to 15% TiO₂ revealed an increase in the formation of oxygen vacancies and the number of sites of trapping states

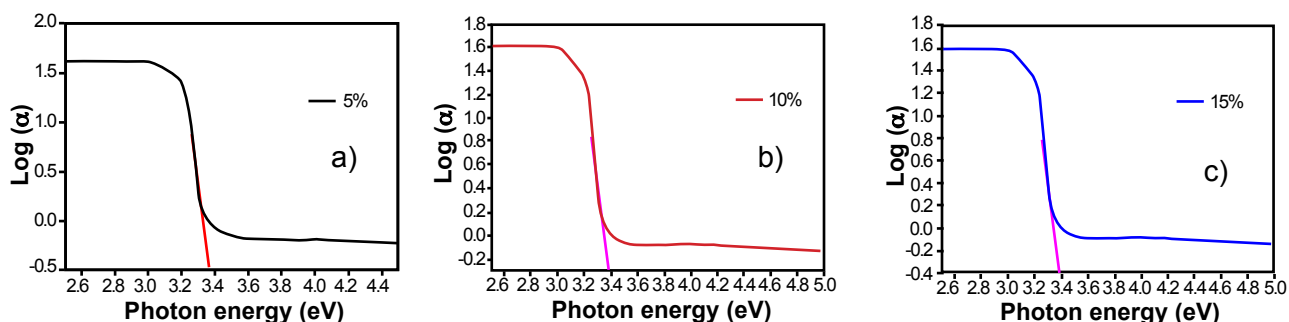


Figure 9: Graphs of absorption coefficient (α) versus photon energy ($h\nu$) for the determination of Urbach energy for the blend TiO₂/ZnO nanofilms.

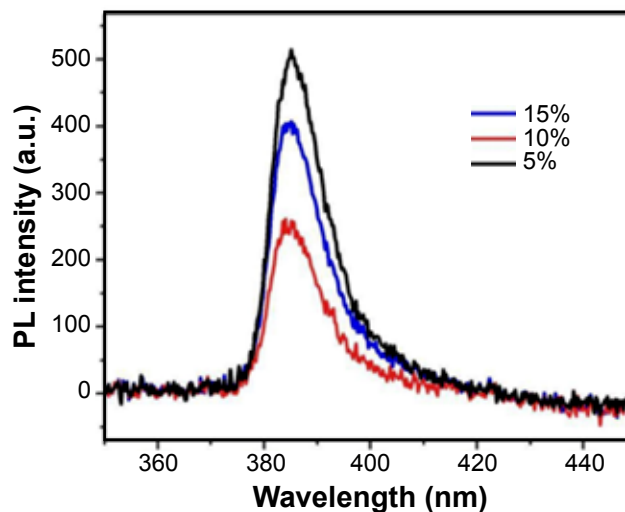


Figure 8: PL fluorescence spectra of TiO₂/ZnO films.

which can form dye aggregations and increase the resistance to the electron flux [40].

Nyquist plot: Fig. 10 shows the Nyquist plot for the thin films at different dye loading times, 4 and 24 h. The imaginary part plotted against the real part exhibited semicircular shapes for the 24 h plot (Fig. 10b), but for 4 h (Fig. 10a), the plot did not close the arc. In both cases, the values indicated high resistance in the interfaces.

Photovoltaic tests: the efficiency observed by Das et al. [21] for a sample obtained by co-precipitation and CuO was around 0.89%. The incorporation of TiO₂ improved the short-circuit current density (J_{sc}) and the overall efficiency (η). The presence of the titanium improved the light-harvesting efficiency, with lower charge rate recombination, and increased the transfer of electrons from the ZnO to the FTO, improving the J_{sc} and the open-circuit voltage (V_{oc}) [41]. From the data collected, the optimum value of Ti(IV) in these synthesis conditions was at 5 wt%, with an efficiency of 1.17% and J_{sc} of 4.58 mA/cm² (Fig. 11). The efficiency was close to the ones found by Pham et al. [42], where a conversion of 0.7% was reached for SnO₂@TiO₂ shells applied to DSSCs with an aqueous electrolyte. Ako et al. [43] created TiO₂/ZnO core-shell nanostructures photoanodes with a η value of 0.53%. The increase in the fill factor (FF) to 0.56 (at 10 wt% TiO₂) suggested lower recombination between the photoanode and the I₃⁻/I₃⁻ [15].

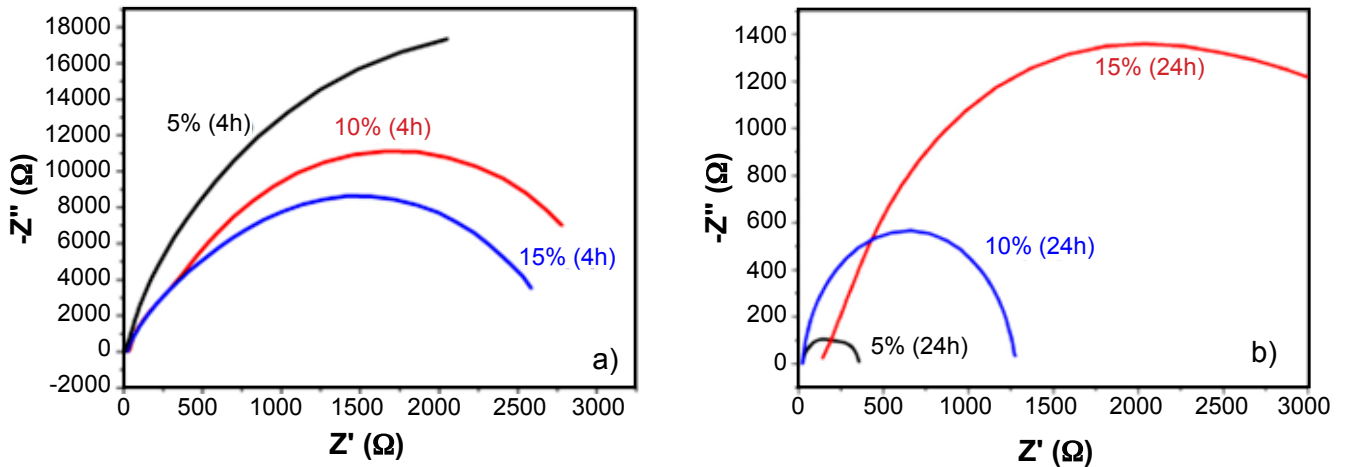


Figure 10: Nyquist plots of thin films for 4 h (a) and 24 h (b) dye immersion time

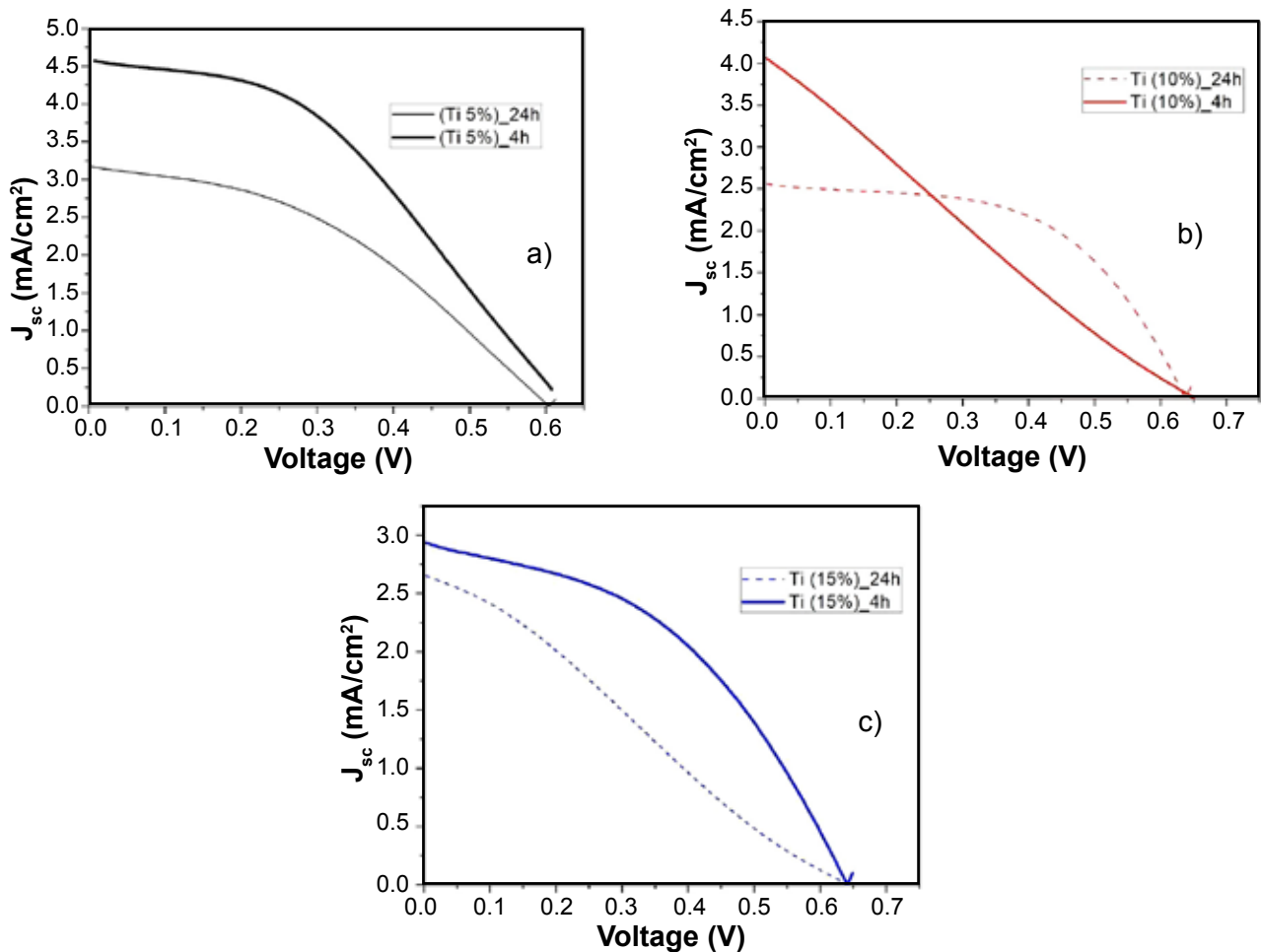


Figure 11: Short-circuit current density (J_{sc}) versus voltage for 5 wt% (a), 10 wt% (b), and 15 wt% (c) TiO₂/ZnO.

Efficiency and fill factor were according to Tyagi *et al.* [41]. Table III relates the photovoltaic parameters found for the cells with photoanodes on the dye for 4 and 24 h. The shorter time on dye was beneficial for the increase in short-circuit current density for all the percentages of TiO₂, increasing the efficiency, except for the 10% TiO₂ film. The decrease in efficiency was due to the lowering of FF, from 0.56 to 0.23, indicating that the average voltage and J_{sc} of this cell did not

follow the maximum current and voltage, with a steep along the way, decreasing in values (Fig. 11b). At 15 wt% TiO₂, the efficiency value almost doubled, led by the higher J_{sc} and a higher fill factor, from 0.28 to 0.43 (Fig. 11c). The benefits of the lower dye immersion time were usual for large crystallite sizes. When the crystallite is large, more dye time can create aggregates that hinder the flow of excited electrons through the cell. The formation of agglomerates can increase the

Table III - Photovoltaic parameters for TiO₂/ZnO films.

Sample	V _{oc} (V)	FF	J _{sc} (mA/cm ²)	η (%)
Ti 5% 24 h	0.61	0.40	3.17	0.77
Ti 5% 4 h	0.63	0.40	4.58	1.17
Ti 10% 24 h	0.64	0.56	2.56	0.88
Ti 10% 4 h	0.65	0.23	4.05	0.63
Ti 15% 24 h	0.64	0.28	2.65	0.45
Ti 15% 4 h	0.65	0.43	3.00	0.84

V_{oc}: open-circuit voltage; FF: fill factor; J_{sc}: short-circuit current density; η: cell efficiency.

resistance to electron mobility, lowering the J_{sc} values [44].

Table IV compares the best efficiency for this work and photovoltaic efficiencies obtained by other authors, using TiO₂ and other elements, showing the methodology for the film's synthesis works for the photovoltaic application. Tyagi et al. [41] found photovoltaic parameters for non-doped ZnO-based DSSCs from 0.16% to 0.64% efficiency and a current density of 1.62 mA/cm². Mehmood et al. [45] obtained higher efficiency for the ZnO-based DSSCs doped with titanium (1%) and Cu, reaching 2.38% efficiency. Katta et al. [40] also concluded that for the doped TiO₂, the photocurrent density was three times higher than the non-doped photoanode. Yang et al. [46] obtained an efficiency of 3.61% for 1D ZnO@C@MoS₂ nanoarrays on conductive glass. Yu and Zi [47] decorated ZnO hollow microspheres with TiO₂ nanotubes with an efficiency of 7.40%. Thus, these works reaffirm that the semiconductor oxides can improve their characteristics when incorporated with n-type materials. The recombination between the TiO₂/electrolyte caused low efficiency, as indicated by the semicircles in Fig. 10 [48]. This recombination happened due to the back recombination of charges between the dye and the counter electrode FTO [49]. Also, in accordance with Ekmekci et al. [50], the overall efficiency of the DSSC was better for a lower concentration of titanium. Table IV indicates that this work methodology reached the levels of efficiency obtained by more sophisticated, complex, and expensive deposition methods. The present work was on par with the current efficiency in the research community.

Table IV - Efficiency values for different DSSCs.

Efficiency (%)	Ref.
1.17	This work
0.70	[27]
0.89	[15]
0.53	[28]
2.38	[44]
7.56	[17]

CONCLUSIONS

TiO₂/ZnO thin films were synthesized by simply dipping the FTO into the precursor suspensions and waiting until

complete evaporation of the liquid (water), without any additives at room temperature and with no auxiliary or additional devices. This method proved, by analysis such as X-ray diffraction, SEM, absorbance, and band gap, the formation of nanocrystalline-type wurtzite ZnO. The films presented good transmittance and reflectance on the UV-vis spectrum. However, the combination of these films with the N719 dye had poor photovoltaic performance, higher being 1.17%. Future works could improve this value by changing the dye, used in the photovoltaic cell, or the concentration of the TiO₂/ZnO combination.

ACKNOWLEDGMENTS

The authors would like to acknowledge the Brazilian research agency Coordenação de Aperfeiçoamento de Pessoal de Nível Superior-CAPES for the financial support, the Laboratório de Filmes Finos e Energias Renováveis-LAFFER for the assistance throughout the research. Also, the authors want to thank the CNPq (Process: 402561/2007-4) Edital MCT/CNPq n° 10/2007. The authors would like to thank the Central Analítica-UFC (funded by Finep-CT-INFRA, CAPES-Pró-Equipamentos, and MCTI-CNPq-SisNano2.0) for microscopy measurements.

REFERENCES

- [1] M. Bhogaita, D. Devaprakasam, Solar Energy **214** (2021) 517.
- [2] H. Widiyandari, S. Wijyanti, A. Prasetyo, A. Purwanto, Opt. Mater. **107** (2020) 110077.
- [3] F. Yang, J. Song, X. Chen, X. Lu, J. Li, Q. Xue, B. Han, X. Meng, J. Li, Y. Wang, Solar Energy **228** (2021) 168.
- [4] K. Kighuta, A.-Y. Gopalan, D.E. Lee, G. Saianand, Y.-L. Hou, S.S. Park, K.P. Lee, J.C. Lee, W.J. Kim, J. Environ. Chem. Eng. **9** (2021) 106417.
- [5] A. Anand, S. Mittal, V. Leeladevi, D. De, Mater. Today Proc. **27**, 1 (2022) 227.
- [6] M. Biçer, M. Gökçen, E. Orhan, Opt. Mater. **131** (2022) 112691.
- [7] M. Abdelfatah, H.Y. Salah, M.I. El-Henawey, A.H. Oraby, A. El-Shaer, W. Ismail, J. Alloys Compd. **873** (2021) 159875.
- [8] V. Ganesh, I.S. Yahia, S. Alfaify, M. Shkir, J. Phys. Chem. Solids **100** (2017) 115.
- [9] B.B. Çirak, Ç. Eden, Ç. Erdoğan, Z. Demir, K.V. Özdokur, B. Caglar, S.M. Karadeniz, T. Kilingç, A.E. Ekinçi, Ç. Çirak, Optik **203** (2020) 163963.
- [10] A. Yildiz, T. Serin, E. Öztürk, N. Serin, Thin Solid Films **522** (2012) 90.
- [11] M. Ajili, M. Castagné, N.K. Turki, Superlattices Microstruct. **53** (2013) 213.
- [12] H. Aydin, H.M. El-Nasser, C. Aydin, A.A. Al-Ghamdi, F. Yakuphanoglu, Appl. Surf. Sci. **350** (2015) 109.
- [13] L. Xu, G. Zheng, F. Xian, J. Su, Mater. Chem. Phys. **229** (2019) 215.
- [14] M.I. Khan, M. Naeem, G.M. Mustafa, S.A. Abubshait,

- A. Mahmood, W. Al-Masry, N.Y.A. Al-Gharadi, S.M. Ramay, *Ceram. Int.* **46** (2020) 26590.
- [15] Y. Caglar, S. Aksoy, S. Ilican, M. Caglar, *Superlattices Microstruct.* **46** (2009) 469.
- [16] V.F. Nunes, E.S. Teixeira, P.H.F. Maia Júnior, A.F.L. Almeida, F.N.A. Freire, *Cerâmica* **68**, 385 (2022) 120.
- [17] V.F. Nunes, F.M. Lima, E.S. Teixeira, P.H.F.M. Júnior, A.F.L. Almeida, F.N.A. Freire, *Matéria* **26**, 4 (2021) e13112.
- [18] A. Badawi, M.G. Althobaiti, E.E. Ali, S.S. Alharthi, A.N. Alharbi, *Opt. Mater.* **124** (2022) 112055.
- [19] R. Gosh, R.P. Sahu, R. Ganguly, I. Zhitomirsky, I.K. Puri, *Ceram. Int.* **46** (2020) 3777.
- [20] T.D. Malevu, *Phys. B* **621** (2021) 413291.
- [21] A. Das, R.R. Wary, R.G. Nair, *Solid State Sci.* **104** (2020) 106290.
- [22] W.-C. Chang, C.-H. Lee, W.-C. Yu, C.-M. Lin, *Nanoscale Res. Lett.* **7** (2012) 688.
- [23] S. Aksoy, K. Gorgum, Y. Caglar, M. Caglar, *J. Mol. Struct.* **1189** (2019) 181.
- [24] R. Homcheunjit, P. Pluengphon, A. Tubtimtae, P. Teesetsopon, *Phys. B* **637** (2022) 413885.
- [25] M. Patel, A. Chavda, I. Mukhopadhyay, J. Kim, A. Ray, *Nanoscale* **8** (2016) 2293.
- [26] A. Hidayat, A. Taufiq, Z.A.I. Supardi, S.M. Jayadininggar, U. Sa'adah, N.A. Astarini, T. Suprayogi, M. Diantoro, *Mater. Today Proc.* **44** (2021) 3395.
- [27] K. Zhouiri, M. Spencer, K. Nulph, P. Appiah-Kubi, K.A.S. Fernando, *Solar Energy* **241** (2022) 343.
- [28] M. Bhushan, R. Jha, R. Bhardwaj, R. Sharma, *Mater. Today Proc.* **48** (2022) 629.
- [29] A.H. Javed, N. Shahzad, M.A. Khan, M. Ayub, N. Iqbal, M. Hassan, N. Hussain, M.I. Rameel, M.I. Shahzad, *Solar Energy* **230** (2021) 492.
- [30] R. Sekar, R. Sivasamy, B. Ricardo, P. Manidurai, *Mater. Sci. Semicond. Process.* **132** (2021) 105917.
- [31] M. Thirumoorthi, J.T.J. Prakash, *Mater. Sci. Eng. B* **248** (2019) 11440.
- [32] F.M. Lima, F.M. Martins, P.H.F. Maia Júnior, A.F.L. Almeida, F.N.A. Freire, *Rev. Matér.* **23** (2017) e11965.
- [33] E. Kouhestanian, S.A. Mozaffari, M. Ranjbar, H.S. Amoli, *Org. Electron.* **86** (2020) 105915.
- [34] T. Marimuthu, N. Anandhan, R. Thangamuthu, S. Surya, *J. Alloys Compd.* **693** (2017) 1011.
- [35] D.S. Biron, V. dos Santos, C.P. Bergmann, *Mater. Res.* **23** (2020) e20200080.
- [36] M.M. Ali, M.J. Haque, M.H. Kabir, M.A. Kaiyum, M.S. Rahman, *Results Mater.* **11** (2021) 100199.
- [37] G.K. Upadhyay, J.K. Rajput, T.K. Pathak, V. Kumar, L.P. Purohit, *Vacuum* **160** (2019) 154.
- [38] S. Aksoy, O. Polat, K. Gorgun, Y. Caglar, M. Caglar, *Phys. E* **121** (2020) 114127.
- [39] C. Bairam, Y. Yalçin, H.I. Efkere, E. Çokduygular, Ç. Çetinkaya, B. Kinaci, S. Özçelik, *Phys. B* **616** (2021) 413126.
- [40] V.S. Katta, A. Das, R.D. K. G. Cilaveni, S. Pulipaka, G. Veerappan, E. Ramasamy, P. Meduri, S. Ashtana, D. Melepurath, S. Santosh, K. Raavi, *Sol. Energy Mater. Sol. Cells* **220** (2021) 110843.
- [41] J. Tyagi, H. Gupta, L.P. Purohit, *Opt. Mater.* **115** (2021) 111014.
- [42] B. Pham, D. Willinger, N.K. McMillan, J. Roye, W. Burnett, A. D'Achille, J.L. Coffey, B.D. Sherman, *Sol. Energy* **224** (2021) 984.
- [43] R.T. Ako, D.S.U. Peiris, P. Ekanayake, A.L. Tan, D.J. Young, Z. Zheng, V. Chellappan, *Sol. Energy Mater. Sol. Cells* **157** (2016) 18.
- [44] H.A. Deepa, G.M. Madhu, V. Venkatesham, *Mater. Today Proc.* **46** (2021) 4579.
- [45] B. Mehmood, M.I. Khan, M. Iqbal, A. Mahmood, W. Al-Masry, *Int. J. Energy Res.* **45** (2021) 2445.
- [46] F. Yang, Y. Gao, P. Zhao, Y. He, Y. Wang, *Mater. Lett.* **324** (2022) 132716.
- [47] L. Yu, Z. Zi, *Mater. Sci. Semicond. Process.* **149** (2022) 106881.
- [48] S. Erten-Ela, Y. Ueno, T. Asaba, Y. Kubo, *New J. Chem.* **41** (2017) 10367.
- [49] S. Erten-Ela, A.C. Cakir, *Energy Sources A* **37** (2015) 807.
- [50] M. Ekmekci, C. Ela, S. Erthen-Ela, *Appl. Ceram. Technol.* **16** (2019) 727.
- (*Rec.* 21/07/2022, *Rev.* 27/10/2022, 16/01/2023, *Ac.* 21/01/2023)



Instruções para Autores (Instructions for Authors)

Encaminhamento de Contribuições

As contribuições devem ser submetidas por meio da URL: <https://mc04.manuscriptcentral.com/ce-scielo>.

Tipos de contribuição

Trabalhos técnico-científicos originais e artigos revisão. Todas as contribuições serão submetidas à análise por relatores. Toda submissão deve conter pelo menos dois nomes e endereços eletrônicos de relatores (que não sejam da instituição dos autores), e e-mails de todos os autores.

Preparação da contribuição

As contribuições devem:

A- Ser redigidas com editor de texto MSWORD (.doc ou .docx) em português ou inglês, em formato A4, em uma coluna com margens 1,5 cm acima e abaixo, 2,5 cm à esquerda e 1,5 cm à direita, espaço simples, com fonte Times New Roman 10, sem formatação especial.

B- Ser submetidas por meio da URL: <https://mc04.manuscriptcentral.com/ce-scielo>.

C- Conter

título em português

título em inglês

nomes dos autores

afiliação, endereço, e-mail

resumo (máximo 300 palavras)

palavras-chave (pelo menos duas)

abstract (máximo 300 palavras)

keywords (pelo menos duas)

texto em português na seguinte ordem:

- INTRODUÇÃO

- EXPERIMENTAL (ou MATERIAIS E MÉTODOS)

- RESULTADOS E DISCUSSÃO

- CONCLUSÕES

- AGRADECIMENTOS (se necessário)

- APÊNDICE (se necessário)

- REFERÊNCIAS

- Tabelas, numeradas sequencialmente com algarismos romanos, com legendas na parte superior em português e em inglês. As tabelas devem ser inseridas no texto.

(Tabelas não devem ter formatação especial, como cores e sombreamento. As tabelas devem ter preferencialmente três linhas horizontais, como no exemplo:

Tabela 1 - Limites de Atterberg das amostras.

[Table 1 - Atterberg limits of the samples.]

Amostra	Limite de liquidez (%)	Limite de plasticidade (%)	Índice de plasticidade (%)
A	38,5	20,5	18,0
B	40,0	19,0	21,0
C	37,5	19,8	17,7
D	38,9	18,8	20,1
E	34,8	17,8	17,0

- Figuras numeradas sequencialmente com algarismos arábicos, com legendas na parte inferior em português e em inglês. As figuras devem ser preferencialmente inseridas no texto.

As figuras (incluindo gráficos, desenhos, fotos e micrografias) devem ter bom contraste e dimensões que permitam a leitura após redução (recomenda-se dimensões de 12 cm x 8 cm ou 12 cm x 12 cm).

Gráficos feitos no software Origin devem ter traço de eixos 4, números com font 30 negrito, nomes nos eixos com font 36 negrito, símbolos tamanho 12, e devem ser colados no MSWORD com colar especial.

As equações devem ser indicadas sequencialmente no texto com letras maiúsculas.

Exemplo de equação:

$$\Theta(t, T) = \int_{t_0}^t \frac{1}{T} \exp\left(-\frac{Q}{kT}\right) dt \quad (A)$$

D - Ter as referências assinaladas sequencialmente no texto com algarismos arábicos, entre colchetes, e apresentadas no final da contribuição. As referências não devem ser linkadas (referência cruzada) ao texto. Expressões do tipo et al., e cols., e similares, não devem ser empregadas nas referências. Evitar referenciar sites, dissertações de mestrado e teses de doutorado. Referenciar os periódicos em que os trabalhos de dissertação e tese foram publicados.

Como formatar as referências:

Artigos em periódicos

(Nomes dos autores separados por vírgulas, nome do periódico, volume em negrito, número (opcional), ano entre parêntesis, página inicial-página final.)

Exemplos:

[1] A.H.A. Pereira, D.Y. Miyaji, M.D. Cabrelon, J. Medeiros, J.A. Rodrigues, Cerâmica 60, 355 (2014) 449-456.

[2] R. Muccillo, E.N.S. Muccillo, J. Eur. Ceram. Soc. 34, 4 (2014) 915-923.

Livros

(Nomes dos autores separados por vírgulas, título do livro, edição, nome da editora, local da edição, ano entre parêntesis, número da página referenciada.)

Exemplos:

[1] I.R. de Oliveira, A.R. Studart, R.G. Pileggi, V.C. Pandolfelli, Dispersão e empacotamento de partículas - princípios e aplicações em processamento cerâmico, Fazendo Arte Editorial, S. Paulo, Brasil (2000) 25.

[2] P. Souza Santos, Ciência e Tecnologia de Argilas, 3ª ed., Vol. 1, Edgard Blücher, S. Paulo, SP (1992) 397.

[3] J.S. Reed, Principles of ceramics processing, John Wiley, New York, EUA (1995) 254.

Artigos em anais de congressos

(Nomes dos autores separados por vírgulas, nome do congresso, nomes do(s) editor(es), editora, local do congresso, volume, ano entre parêntesis, número da página referenciada.)

Exemplos:

[1] E.C.F. Souza, S.R.M. Antunes, S.A. Pianaro, A.J. Zara, A.C. Antunes, Anais XIII CBECIMAT, Curitiba, PR (1998) 2437.

[2] M.A. Quintela, F.D. Santos, C.A. Pessoa, J.A. Rodrigues, V.C. Pandolfelli, Proc. Unified Int. Tech. Conf. Refractories, UNITECR'05, Orlando, EUA (2005) 380.

[3] M. Kleitz, L. Dessemond, M.C. Steil, F. Thevenot, Proc. Materials Research Society Symposium, Eds.: R.A. Gerhardt, S.R. Taylor, E.J. Garboczi, Materials Research Society, Pittsburgh, EUA, 411 (1996) 269.

Custo e separatas

Não há cobrança aos autores. Um arquivo pdf contendo a forma final do artigo será enviado ao autor responsável pela submissão.

Processo de publicação

1- o artigo é encaminhado para análise de relatores, membros ou não do Conselho de Editores (sistema de avaliação cego-simples - anonimato dos nomes dos relatores aos autores);

2- os pareceres dos relatores são encaminhados ao autor com "aceito para publicação" (o artigo aprovado pelos relatores é agendado para publicação), com "sugestão de revisão" (o artigo é encaminhado ao autor para revisão e quando providenciada, encaminhado aos relatores para nova análise), com "não aceito para publicação" (o artigo não é publicado; se houver pedido de reconsideração, esta é enviada aos relatores e o artigo pode, posteriormente, ser enviado a novos relatores).

3- artigos aprovados são editados graficamente no layout da revista Cerâmica. Artigos submetidos nos padrões da revista (contidas nas Instruções para Autores) são agendados preferencialmente.

4- visando aumentar a internacionalização da revista, artigos submetidos em inglês terão prioridade de publicação.

Submission of papers

Contributors should submit their papers (.doc or .docx MSWord files) at: <https://mc04.manuscriptcentral.com/ce-scielo>.

Types of contributions

Original papers and state-of-the art review articles. All papers will be blind peer reviewed.

Manuscript preparation

- All manuscripts should be written in English. A Portuguese version of the abstract and captions of foreign contributions in English will be provided by the Editors.

- The manuscript should follow the instructions:

a) single-space typing, font Times New Roman, font size 10, one column without any special formatting, on A4-size (210 mm x 297 mm) pages, margins 1.5 cm top, right and bottom, 2.5 cm left;

b) the manuscript should contain title, name, affiliation(s) and e-mail address(es) of all author(s), an abstract with no more than 300 words, and at least two keywords.

c) the standard sequence for papers should be followed: Title, Authors names, Affiliations, Abstract, Keywords, Introduction, Experimental (or Materials and Methods), Results and Discussion (or Results), Discussion, Conclusions, Acknowledgements (if pertinent), References. Footnotes should be avoided.

d) tables should be inserted in the text.

e) illustrations: 9 or 18 cm wide and 18 cm maximum height. The line drawings should be large enough (3 - 5 mm) to remain legible after reduction for printing. Any scale markers should be inserted on micrographs.

f) figures should be preferentially inserted in the text.

g) equations, indicated in the text by capital letters, should be represented as shown below:

$$\Theta(t, T) = \int_{t_0}^t \frac{1}{T} \exp\left(-\frac{Q}{kT}\right) dt \quad (A)$$

h) references should be non-linked and consecutively numbered in the text using square brackets and listed by number in the Reference list. Examples:

[1] I.R. Oliveira, V.C. Pandolfelli, Ceram. Int. 36, 1 (2010) 79-85.

[2] W.D. Kingery, H.K. Bowen, D.R. Uhlmann, Introduction to Ceramics, 2nd ed., John Wiley & Sons, New York, USA (1975) p. 293.

[3] M. Kleitz, L. Dessemond, M.C. Steil, F. Thevenot, in Proc. Mat. Res. Soc. Symp., Vol. 411, Eds. R.A. Gerhardt, S.R. Taylor, E.J. Garboczi, Materials Research Society, Pittsburgh, USA (1996) pp. 269-275.

Page charges and offprints

There will be no page charges. A pdf file of the paper will be sent to the corresponding author.

Synthesis of delafossite CuCrO_2 via solution combustion method and its acid functionalization for biodiesel production <i>M. C. Viegas, G. P. de Figueredo, S. F. Rodrigues, A. A. Cabral, M. A. M. Castro, M. M. Oliveira</i>	1
Technological properties of a self-bloating clay and expanded-clay aggregate for the production of lightweight concrete <i>A. V. Rodrigues, S. R. Bragança</i>	6
Impact of fuel quantity on luminescence properties of $\text{Sr}_3\text{Al}_2\text{O}_6:\text{Eu}$ by combustion synthesis <i>W. T. Barbosa, C. M. Álvarez-Docio, R. Garcia-Carrodegas, M. V. L. Fook, M. A. Rodríguez, R. E. Rojas-Hernandez</i>	17
The influence of compositional variability of dimension stone residues on the properties of rustic porous ceramic tiles <i>A. C. A. Prado, R. L. M. Feitosa, M. A. Neves, S. P. Taguchi</i>	23
Bioactive $\text{SiO}_2\text{-K}_2\text{O-CaO-P}_2\text{O}_5$ glass-ceramic scaffold prepared using polyurethane foam template <i>E. R. Essien, D. O. Nwude, V. E. Okolie, L. A. Adams</i>	30
Sedimentation and rheological behavior of reactive and non-reactive magnesium hydroxide pulps for industrial spray dryer processing <i>E. C. Campos, D. H. S. Chaves, C. M. F. Santos, S. D. F. Rocha, V. S. Birchal</i>	39
Tailoring the properties of Y_2O_3 via synthesis parameters varied during the PVA-assisted sol-gel route <i>J. C. C. Carvalho, G. F. C. Bispo, T. S. Lilge, C. S. Bezerra, A. B. Andrade, Z. S. Macedo, M. E. G. Valerio</i>	48
Study of rhombohedral tricalcium phosphate in hexagonal crystal structure family on the sample prepared by the sol-gel route and the effect of calcination temperature <i>J. Ady, S. D. A. Ariska, D. I. Rudyardjo, S. Anindriya</i>	54
Mesh reinforcement in masonry mortar coatings: a systematic literature review <i>V. A. Coelho, F. G. S. Silva</i>	66
Synthesis of TiO_2/ZnO photoanodes on FTO conductive glass for photovoltaic applications <i>V. F. Nunes, F. M. Lima, E. S. Teixeira, P. H. F. Maia Júnior, A. F. L. Almeida, F. N. A. Freire</i>	79